Structural analyses by advanced X-ray scattering on GaP layers epitaxially grown on silicon for integrated photonic applications

Yanping Wang

To cite this version:

Yanping Wang. Structural analyses by advanced X-ray scattering on GaP layers epitaxially grown on silicon for integrated photonic applications . Materials Science [cond-mat.mtrl-sci]. Université Bretagne Loire; INSA RENNES, 2016. English. NNT : . tel-01450671v1

HAL Id: tel-01450671
https://hal.science/tel-01450671v1

Submitted on 14 Feb 2018 (v1), last revised 31 Jan 2017 (v2)

Thèse

UNIVERSITE
BRETAGNE
LOIRE

THESE INSA Rennes
sous le sceau de Université Bretagne Loire
pour obtenir le titre de
DOCTEUR DE L'INSA DE RENNES
Spécialité : Physique - Optoélectronique

présentée par
Yanping WANG
ECOLE DOCTORALE : SDLM
LABORATOIRE : : FOTON-OHM/INSA de Rennes

Structural analyses by advanced X-ray scattering on GaP layers epitaxially grown on silicon for integrated photonic applications

Thèse soutenue le 17.06.2016
devant le jury composé de :

Gilles PATRIARCHE
Directeur de Recherche CNRS, C2N, Marcoussis / *Président*
Chantal FONTAINE
Directrice de recherche CNRS, LAAS, Toulouse / *rapporteur*
Olivier THOMAS
Professeur des Universités, IM2NP, Université d'Aix-Marseille / *rapporteur*
Jean DECOBERT
Ingénieur de Recherche, III-V Lab, Palaiseau / *examinateur*
Charles RENARD
Chargé de Recherche, C2N, Orsay / *examinateur*
Antoine LETOUBLON
Maître de conférences, FOTON-OHM, INSA de Rennes / Co-encadrant de thèse
Olivier DURAND
Professeur des Universités, FOTON-OHM, INSA de Rennes / Directeur de thèse

Structural analyses by advanced X-ray scattering on GaP layers epitaxially grown on silicon for integrated photonic applications

Yanping WANG

Acknowledgement

Firstly, I would like to deeply acknowledge my supervisor prof. Olivier Durand for giving me the opportunity to perform my PhD project in his research group and for his continuous support during my thesis. His precious guidance, advices, pedagogy and encouragements have helped me to fulfill the thesis. I really appreciate his solid knowledge and that he treats everything seriously and methodically, which guided me not only in doing the research, but also in everyday life.

As well, I express my sincere gratitude to my second supervisor Dr. Antoine Létoublon for instructing me in the X-ray diffraction experiments with great enthusiasm. He has shared with me not only his knowledge but also the precious inspiring ideas on research. I'm very grateful to him for his guidance in the world of X-ray diffraction that makes me go forward in the right direction.

I want to thank Chantal Fontaine, Olivier Thomas, Jean Decobert, Gilles Patriarche and Charles Renard for having accepted to be the members of my dissertation committee, for their time, their patience and their critiques during my final defense. A special thanks to Chantal and Olivier for their precise review of the manuscript and providing many valuable comments that improved this dissertation.

I'm thankful to Charles Cornet, for giving me all his patience and precisions when telling me about the sample growth, teaching me use the Atomic Force Microscope, and helping me writing the journal papers. My thanks also goes to Alain Le Corre, Yoan Léger, Laurent Pedesseau, Mickael Coqueux, Julien Lapeyre, Isabelle Eyeillard, Alexandrine Le Saint and all the other colleagues in our laboratory, for giving me their help when I need. It was a great pleasure to pass these years in such a warm and nice group.

I have had the chance to participate in three measurement campaigns at the European Synchrotron Radiation Facility, respectively on the BM02 beamline and on the ID01 beamline. I'm thankful to the staff of the BM02 team and the ID01 team, especially Nathalie Boudet, Jean François Berar, Tobias Tschulli, Gilbert Chahine, Vincent Favre-Nicolin and Joël Eymery, for their help during and after the experiments. I also acknowledge Valérie Demange from ICSR for providing us the access to their X-ray Diffractometer.

Many collaborators contributed to this research. In particular I would like to thank Anne Ponchet, Julien Stodolna from CEMES, Gilles Patriarche, Mounib Bahri, Ludovic Largeau from LPN for the beautiful TEM images, as well as Pascal Turban and Simon Charbonnier from IPR for the STM analyses, without which I wouldn't have had a thorough understanding of the structure of the GaP epilayer.

Finally, I'm deeply indebted to my parents for their selfless love and unconditional support throughout my whole life and my study.

Table of Contents

List of abbreviations

AFM	Atomic Force Microscopy
APB	Antiphase Boundaries
APD	Antiphase Domain
BF	Bright Field
CL	Correlation Length
CMOS	Complementary Metal Oxide Semi-conductor
CTR	Crystal Truncation Rod
DF	Dark Field
DFT	Density Functional Theory
EIC	Electronic Integrated Circuits
FCC	Face Centered Cubic
HAADF	High-Angle Annular Dark-Field
HCP	Hexagonal Close Packed Structure
IB	Integral Breadth
LED	Light-Emitting Diode
MBE	Molecular Beam Epitaxy
MEE	Migration Enhanced Epitaxy
MOCVD	Metal Organic Chemical Vapor Deposition
MOVPE	Metal Organic Vapor Phase Epitaxy
MT	Microtwin
OEIC	Optoelectronic Integrated Circuits
QF	Quality Factor
r.m.s.	Root Mean Square
RC	Rocking-curve
RELP	Reciprocal Lattice Point
RHEED	Reflection High-Energy Electron Diffraction
RLN	Reciprocal Lattice Node
ROI	Region of Interest
RSM	Reciprocal Space Map

SEM	Scanning Electron Microscopy
SOI	Silicon-on-Insulator
STEM	Scanning Transmission Electron Microscopy
STM	Scanning Tunneling Microscopy
TDS	Thermal Diffusion Scattering
TEM	Transmission Electron Microscopy
UHVCVD	Ultra High Vacuum Chemical Vapor Deposition
WHL	Williamson-Hall like
XRD	X-ray Diffraction

Remark: all the vectors are represented by a ***bold italic*** letter.

General introduction

Transmission of optical signals via optical fibers instead of electronic signals by metal wires permits transmission over longer distances, at higher data rates, with lower power consumption, and without electromagnetic interference. Optical computers, using photons for computing, will compute thousands of times faster than any electronic computer can ever achieve. Optical fibers are now well established for efficient data communication, while on-chip data processing is still performed based on electronic integrated circuits (EIC), although the processor clock rates have been limited by the interconnect problem for years[1]. Optical interconnects offered by optoelectronic integrated circuits (OEIC) is considered as a solution to overcome this bottleneck of modern electronic integrated circuits.

Silicon photonics, a technique integrating photonic devices and circuits onto silicon-on-insulator (SOI) waveguide platform[2–4], opens the route for high performance and very large-scale integration (VLSI) photonics. Silicon has been long ago the most important semi-conductor material for microelectronic industry, owing to its natural abundance, low cost, high purity and availability of large single crystals. Silicon photonics shows advantages such as compatibility with the low-cost and mature complementary metal oxide semi-conductor (CMOS) manufacturing, possibility of realizing compact optical devices, high bandwidth, wavelength multiplexing and immunity to electromagnetic noise, etc. Pioneered in the year of 1980s,[5,6] silicon photonics is booming since 2000 and largely applied in light emitters[7–9], waveguides[10–12], modulators[13,14], photodetectors[15,16].

Nevertheless, silicon shows poor optical properties because its indirect bandgap precludes the efficient light emission. Many strategies have been demonstrated to efficiently enhance the light emission of silicon, such as porous silicon[17–19], Erbium doping[20,21], Si nanocrystals[22–26], Erbium doped silicon nanocrystals[27–30], Germanium photodetectors on Si[16,31,32], etc. Challenges of Si-based lasers are loss of efficiency, difficulty of high-density integration, and far lower performances in comparison with the III-V compound semi-conductors, which show higher nonlinearity, higher speed, more efficient light detection at infrared wavelengths, etc. Heterostructure of III-V on silicon has then been proposed, taking advantage of the mature and low-cost Si technology and the high performance of III-V materials, allowing an ultimate platform for on-chip optical interconnects.

Three main approaches have been developed and applied to realize the integration of III-V compound semiconductor on top of a SOI wafer: flip-chip, bonding, and heteroepitaxy. For flip-chip integration, III-V optoelectronic component processed on the III-V wafer are flipped and bonded on the silicon platform through soldering.[33] Bonding techniques, including direct bonding and adhesive bonding, allows the integration of III-V thin film onto the SOI substrates and fabrication of optoelectronic devices afterwards. Low temperature O_2 plasma-assisted bonding[34,35] has been recently developed to overcome the problem of thermal expansion coefficient differences, which is a key challenge in conventional direct bonding at high-temperature. Though such hybrid techniques have showed interesting results, the requirement of stringent alignment not only limits the integration density but also makes them time-consuming and expensive.

Heteroepitaxy is now the most promising and attractive technique allowing a low-cost, highly integrated, and large-scale monolithic integration of III-V material on Si. As candidates, III-V materials such as GaAs[36–38], InP[39,40], InAs[41–43], AlSb[44] have been reported successfully grown on silicon. However, most III-V compounds present large lattice mismatch with silicon, for example, 4% for GaAs and 8% for InP, which results in quite a large density of treading dislocations.[45,46] The luminescence efficiency and long-life performance of optical devices will be strongly reduced by these defects.

Gallium phosphide (GaP), an indirect band gap semiconductor material, due to the very small lattice mismatch with Si (0.37% at room temperature), has been proposed as an ideal buffer material grown on silicon substrate to overcome the problem of misfit dislocations. Incorporation of other substance like Indium(In), Arsenic(As) and Nitrogen(N) enables the modification of band structure to create novel direct band gap materials lattice-matched to GaP, making GaP/Si platform an efficient pseudo-substrate allowing monolithic integration of direct band gap III-V semiconductors towards Si substrate.

Yonezu and co-workers at the University of Toyohashi in Japan demonstrated the heteroepitaxial growth of GaAsPN and GaNP layers on Si substrate covered with a thin GaP initial layer of high structural perfection.[47] A Dislocation-free double heterostructure InGaPN/GaPN light-emitting diode (LED) grown on Si by solid source molecular beam epitaxy (SS-MBE)[48] and a Si/GaP/GaPN/GaP/Si structures for OEICs by two chamber MBE[49] were also obtained by their group. Volz and his group from Philipps-University in Marburg (Germany) has achieved the defect free GaP nucleation on Si,[50] and the growth of Ga(NAsP) multi-quantum wells on GaP substrate without any formation of misfit dislocations by metal organic vapor phase epitaxy (MOVPE). [51,52] Grassman et al. from the Ohio State University also reported the growth of GaP thin films on Si substrates without any defects, using MBE[53] or metal organic chemical vapor deposition (MOCVD)[54,55].

Our laboratory is skilled in growing GaP-based optical devices such as InP/GaP quantum dots (QDs)[56], GaAsP(N)/GaP(N) quantum wells (QWs)[57], GaP/GaAsPN/GaP PIN diodes[58], etc., as well as Ultra High Vacuum Chemical Vapor Deposition (UHVCVD) MBE growth of GaP on Si[59]. The aim of the thesis work is the structural analysis and development of analytical methods for the structural improvement of the GaP/Si platform, mainly focusing on the characterization of crystal defects such as microtwins and antiphase domains using X-ray diffraction, combined with complementary microscopic techniques. The dissertation is organized as following:

Chapter 1 describes some crystal defects commonly presented in heteroepitaxial thin layers such as the stacking faults (SF), microtwins (MT), antiphase domains (APD), lattice strain and relaxation, mosaic tilt, etc. Then basic principles and techniques of X-ray scattering are introduced, including reciprocal space map, $\omega/2\theta$ scan, ω scan, and pole figures. Finally, crystal defect behaviors in reciprocal space and their characterization by X-ray diffraction are briefly presented.

Chapter 2 briefly introduces the Si substrate surface cleaning and the heteroepitaxial growth of GaP/Si thin layers in the UHVCVD-MBE chamber, the X-ray diffraction setups using Synchrotron and laboratory sources, and complementary microscopy techniques for structural analyses such as the Atomic Froce Microscopy (AFM), Transmission Electron Microscopy (TEM) and Scanning Tunneling Microscopy (STM).

Chapter 3 is dedicated to the development of MT quantification methods, aiming to improve the GaP/Si platform structural properties through the growth condition optimization. Two quantification methods are developed using X-ray diffraction pole figures and rocking-curve scans, in order to measure the MT volume fraction. These methods, along with complementary microscopy techniques, are used to optimize the growth conditions involving growth temperature, Migration Enhanced Epitaxy (MEE) procedure and two-step growth sequence. Quasi MT-free GaP/Si pseudo-substrates have been obtained after growth optimization.

Chapter 4 presents the evaluation of antiphase domains, based on the analyses of X-ray diffraction reciprocal space images and TEM techniques. Si substrate surface preparation and growth parameters like growth temperature, Ga coverage at the initial growth stage and use of AlGaP marker layers are optimized to improve the GaP/Si interface quality and to reduce the APDs density. The APD formation and annihilation mechanisms related to the growth conditions are also discussed.

Finally, Chapter 5 summarizes all the results obtained during the thesis, including the structural analyses of the GaP/Si layer and the optimization of growth parameters towards the defect elimination. Moreover, some perspective works based on experiments of Coherent Bragg Imaging and Nanodiffraction microscopy are briefly introduced, along with the preliminary analyses, providing new analytical means to a complete structural evaluation of the GaP/Si platform.

Chapter 1 Advanced X-ray scattering on crystal defects

Why and how can we use X-ray scattering to investigate the crystal structure of the GaP epitaxial layers? The first part provides a brief introduction to the common crystal defects like point defects, dislocations, stacking faults, twin boundaries and antiphase boundaries. Then the introduction is extended to the structural figures and defects encountered in the GaP/Si heteroepitaxial system such as strain and relaxation, misfit dislocations, mosaic tilt, microtwins, as well as antiphase domains. In the second part, X-ray scattering principles and reciprocal space are presented: the construction of the Ewald Sphere and different typical ways of reciprocal space exploration such as linear scans, reciprocal space maps, pole figures, etc. Finally, based on the representation of the real space structure in reciprocal space, some practical examples are given on the characterization of heteroepitaxial thin layer structure by X-ray scattering.

1.1 Crystal defects in heteroepitaxial thin layers

1.1.1 Crystal defects

A crystal is composed of regular repetition of atoms or molecules in all directions. The smallest group of atoms or molecules that is repeated is called the unit cell. The periodic arrangement framework is called the crystal lattice and each lattice point is associated with a unit cell. Therefore, one of the main properties of a crystal is the long-range order. However, perfect crystal doesn’t exist in nature. Crystal defects are atomic arrangement mistakes that break the long-range order and may involve: single atoms (point defects), row of atoms (linear defects), plane of atoms (planar defects) and bulk of atoms (volume defects).

a Point defects

Point defects occur when an atom is missing or irregularly placed in the lattice structure. There are several types of point defects, as shown in Figure 1.1. Vacancies are lattice sites which should be occupied by an atom, but are vacant. They are present at an equilibrium concentration in all crystalline materials at any temperature.[60] In most cases the solid diffusion in crystal is dominated by vacancies since an empty site is needed as target for the diffused atom. Besides vacancies, self-interstitial atoms are another type of intrinsic defects appearing in a pure material, when an atom occupies a lattice site that should be empty. They are found in several metals and semiconductors like Si[61] in low concentrations because they result in high stress and high energy state around them. Extrinsic defects are caused by foreign atoms. Small atoms such as carbon, nitrogen, hydrogen and oxygen usually fill in an interstitial site since they introduce less distortion to the lattice. These are called interstitial impurities and are very common in solid solutions and alloys. For example, dilute nitride III-V-N semiconductor alloys have been widely studied because of their electronic and optoelectronic properties. Among them, GaP(N) is created based on GaP and changes the band gap characteristic of GaP, which makes it possible to use the indirect-gap GaP/Si thin film platforms in photonic and photovoltaic applications.

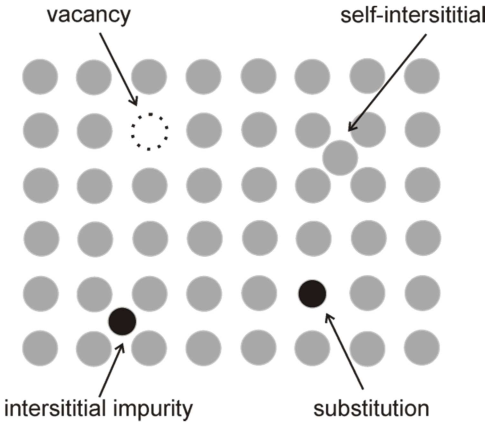

Figure 1.1 A schematic representation of typical point defects in a crystal

b Linear defects

Dislocations are linear defects within a crystal and were discovered by Orowan, Polanyi and Taylor[62] in the year of 1934. There are basically two types of dislocation: edge dislocation and screw dislocation, but in most case they exist as a combination of both types and form a "mixed dislocation". Edge dislocation, as shown in Figure 1.2 a), can be considered as the insert of an extra half-plane of atoms in the crystal. The termination of the half-plane is called a dislocation line, where the surrounding inter-atomic bonds are strongly distorted. The direction and magnitude of the lattice distortion is represented by the Burgers vector ***b***,[63] that is defined as the vector linking the start point to the end point of a clockwise "rectangle" that is not closed around the dislocation line but should be otherwise closed in a perfect crystal lattice, as indicated by the red lines in Figure 1.2 b).

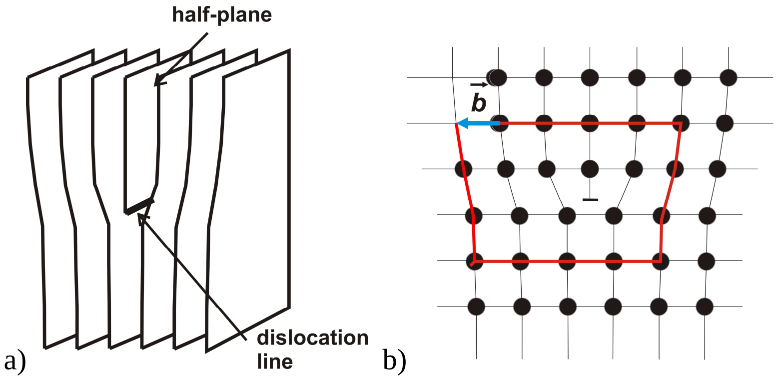

Figure 1.2 a) A schematic representation of edge dislocation and b) the definition of the Burgers vector ***b***.

It is more difficult to visualize the screw dislocations. The screw dislocation can be created by applying a shear stress to the bloc of crystal, in order to slice the bloc along an atomic plane, stop at the dislocation line, and displace one part by a Burgers vector ***b*** parallel to the dislocation line. When the applied shear stress is increased, the atoms bonds at the dislocation line are broken, the dislocation line moves towards the direction perpendicular to ***b*** and the bloc is finally plastically deformed. Figure 1.3 shows a typical screw dislocation in a three-dimensional view.

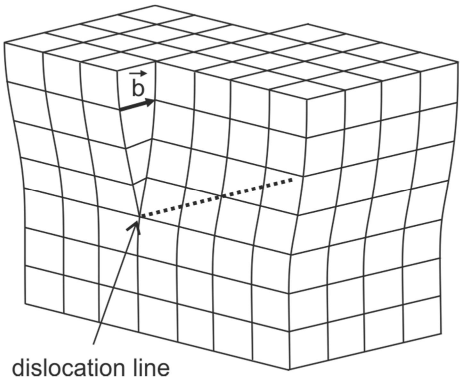

Figure 1.3 A schematic illustration of screw dislocation

In III-V semiconductor thin films epitaxially grown on Si substrate, the most commonly linar defects are the misfit and treading dislocations due to the lattice mismatch between the III-V material and the Si. The GaP is dedicated to prevent these dislocations, because the very small lattice mismatch.

c Planar defects

Planar defects mainly include stacking faults, grain boundaries and antiphase boundaries.

Stacking faults are found especially in close-packed structures where atomic layers are arranged obeying a certain stacking order. Let’s note the first layer configuration as A. When stacking the second layer B, the atoms cannot be arranged directly one on top of another, but over the depressions of the first layer. The third layer can be placed so that the atoms are directly above those of the layer A, to form the ABABAB sequence order as shown in Figure 1.4 a). This is a hexagonal close packed structure (HCP). Otherwise, they can arrange themselves as configuration C (Figure 1.4 b), to form the ABCABCABC sequence order. This is a face centered cubic structure (FCC). When the long-range stacking sequence is disrupted and becomes for example ABC□BCABC or ABC*BABC, there is a stacking fault. The former, where a plane C is missing, is called an intrinsic stacking fault and the latter, where an extra *B plane is inserted, is called an extrinsic stacking fault.

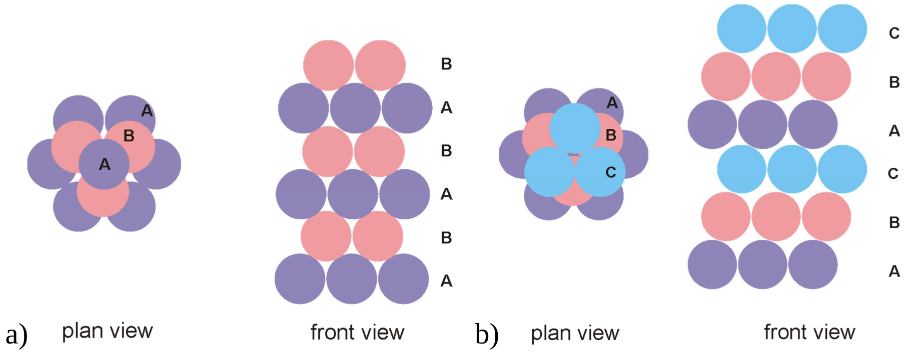

Figure 1.4 Stacking sequence in closed packed structures: a) HCP, b) FCC.

It is important to introduce the Shockley partial dislocations when discussing the stacking fault. A perfect dislocation may decompose into two partial dislocations if the energy state of the sum of the partial dislocations is lower than that of the original one. Figure 1.5 a) shows the first two (1-11) layers compactly stacking in the direction of [1-11] for the FCC structure. The Burgers vector $\boldsymbol{b}$ = a/2[110] is disassociated into two Shockley partials $\boldsymbol{b}_1$ = a/6[121] and $\boldsymbol{b}_2$ = a/6[21-1].

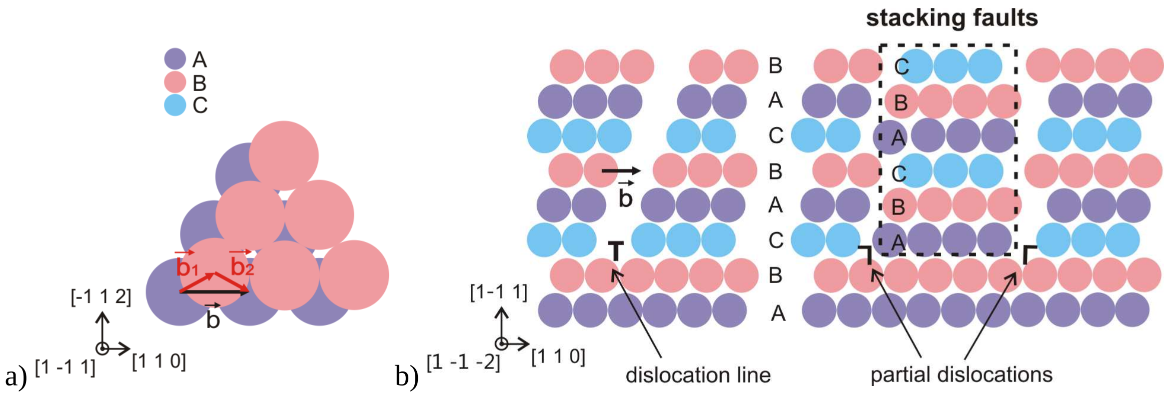

Figure 1.5 a) Decomposition of dislocation $\boldsymbol{b}$ into a pair of partial dislocations $\boldsymbol{b}_1$ and $\boldsymbol{b}_2$ in a FCC structure, b) formation of stacking faults from the partial dislocations

It is evident that the two adjacent layers are displaced one over the other by a vector $\boldsymbol{b}_1$ or $\boldsymbol{b}_2$ in the (1-11) plane. When a shear stress is applied, instead of forming a perfect dislocation $\boldsymbol{b}$ which results in the sequence order AB□CABCABC in the [1-11] direction (Figure 1.5 b) left), it is energetically preferable to slip into two partial dislocations and therefore creating the stacking faults such as AB|ABCABC[64] (Figure 1.5 b) left).

There is a special stacking fault named twin, whose main characteristic is the mirror symmetry of the stacking sequence, just like ABCABCA|ACABC, as shown on the hith resolution TEM image of a GaP layer[65] in Figure 1.6. The twinned domain contains 4 monolayer atoms in the C, A, A, C positions, limited by the twin boundaries indicated by the blue lines in the figure.

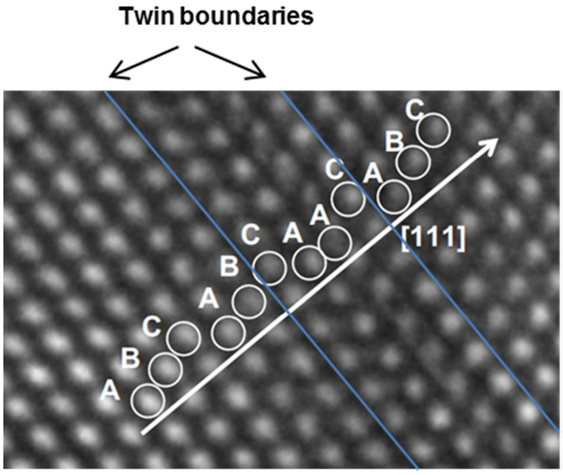

Figure 1.6 High resolution TEM image of the GaP layer. Open circles labeled with ABC show stacking order along the [111] direction. The CAAC sequence corresponds to a four monolayer twin domain, with its boundaries indicated by the blue lines. [65]

Phase boundaries are interfaces separating two crystal grains of same chemical composition but of different crystal structures. One of the very common phase boundaries is the antiphase boundary. Antiphase boundaries have been discovered in sphalerite (also called zinc blende) structure[66] around the year 1970. Sphalerite structure is a characteristic of most III-V or II-VI compounds. It can be considered as a FCC close packed stacking of type-A atoms combined with another FCC lattice of type-B atoms and offset by a quarter of a body diagonal in the [111] direction. The structure has two types of lattice sites and exhibits polarity in the [111] direction, since atom A and atom B are linked by a polar covalent bond representing unequal electron sharing between them. If in one domain, all the sites of the nominal FCC are occupied by atoms B and the offset FCC is constituted by atoms B, this domain is called an antiphase domain (APD). The polarity in the APD is inversed. The boundaries between the APD and the nominal phase are antiphase boundaries (APB), as illustrated in Figure 1.7. [67]

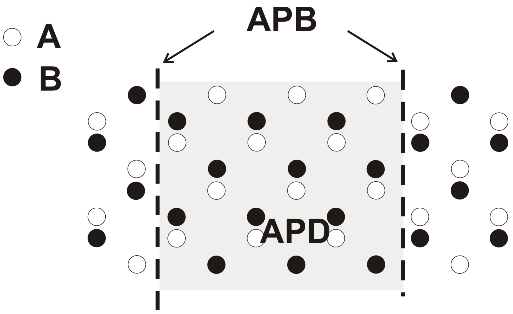

Figure 1.7 Illustration of antiphase domain and antiphase boundaries in zinc blende structure, projection in the [110] direction.

d Volume defects

Volume defects are small regions in the crystal where defects are present, such as voids that can be thought of clusters of vacancies, precipitates that are small bulks of accumulated impurities. In my thesis, we are only interested in the antiphase domains and twinned domains, formed from the antiphase boundaries and twin boundaries.

1.1.2 Defects in hetoroepitaxial GaP/Si thin layers

Epitaxy is the growth of a crystalline overlayer of one material, or compound, on the crystalline surface of another crystalline material, or compound, such that the in-plane crystalline orientation of the overlayer is well-defined with respect to the in-plane crystalline orientation of the substrate. It is commonly used in the high quality growth of integrated crystalline layers or nanostructures, especially for compound semiconductors. Homoepitaxy consists in the epitaxial growth of a layer composed of the same material as the substrate, whereas heteroepitaxy consists in the epitaxial growth of a material different from the substrate, such as the growth of GaP thin films on silicon substrate. Besides the common defects discussed above, and due to the presence of an interface (both structural and chemical), heteroepitaxial layers may display some specific crystalline defects, owing to the lattice mismatch, misorentation, interface quality, etc.

a Lattice strain of the epilayer

From Figure 1.8, we can easily see that all the most commonly used cubic III-V compounds, have a lattice constant much larger than the silicon one.

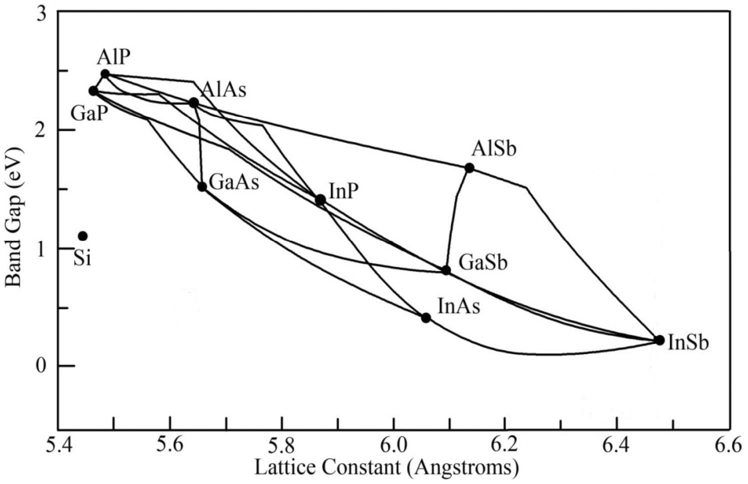

Figure 1.8 Band Gap energy versus lattice constants for silicon and most common III-V semiconductors

Table 1.1 lists some basic parameters of the GaP and the Si that are useful for the following discussions.

Table 1.1 Some basic parameters for GaP and Si

		GaP	Si
300K	Lattice constant	0.54506 nm	0.54309 nm
	C_{11}	140.5 GPa	166.0 GPa
	C_{12}	62.0 GPa	64.0 GPa
	Energy gap	2.26 eV	1.12 eV
	Thermal expansion coefficient	4.65×10^{-6}/K	2.6×10^{-6}/K
800K	Thermal expansion coefficient	$\sim5.5\times10^{-6}$/K	$\sim4.2\times10^{-6}$/K

The lattice mismatch is defined by Equation 1-1[68], with a_f and a_s being the lattice constant of respectively the thin film and the substrate:

$$f = \frac{a_f - a_s}{a_s}. \qquad \text{Eq. 1–1}$$

In the case of a GaP thin film heteroepitaxially grown on Si, the lattice mismatch is estimated to be about 0.36% at room temperature and the film material can be elastically strained to accommodate the lattice parameter of the substrate under the critical thickness (defined in the following), as shown in Figure 1.9 a) and in Figure 1.10 a). We call this growth mode “coherent growth” or “pseudomophic growth”. This is the case of the GaP grown on Si at the initial stage of growth.

For GaP pseudomophically grown on nominal Si(001) substrate, the strain of the GaP lattice structure is tetragonal (Figure 1.9 a)). Assuming $e_\perp$ and $e_{//}$ the strain in vertical and lateral directions:

$$e_\perp = \frac{a_\perp - a_f}{a_f}, e_{//} = \frac{a_s - a_f}{a_f}, \qquad \text{Eq. 1–2}$$

According to the elastic theory:

$$e_\perp = -\frac{2C_{12}}{C_{11}} e_{//}, \qquad \text{Eq. 1–3}$$

where C_{12} and C_{11} are elastic constants of GaP. With a_f =0.54506 nm, a_s=0.54309 nm, C_{11}=140.5 GPa, C_{12}=62.03 GPa, $a_\perp$ for fully strained GaP is calculated to be 0.5467 nm.

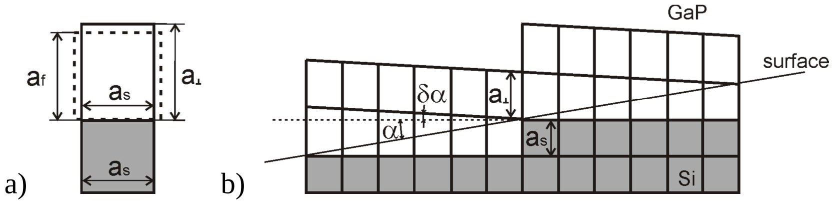

Figure 1.9 2D presentation of lattice strain of GaP epilayer grown on a a) nominal Si substrate, b) vicinal Si substrate misoriented by α°

In case of vicinal Si substrate misoriented by α°, the lattice deformation is triclinic. If the lattice mismatch is small, this deformation can be characterized by the angle δα (the tilt angle between the [001] orientation of GaP and that of Si) and is calculated using the following equation: [69]

$$tan(\delta\alpha) = ((a_{\perp} - a_s)/a_s) \times tan(\alpha) \qquad Eq.\ 1\text{–}4$$

For α = 6°, δα is calculated to be 0.041°. This value is quite small and can be neglected. Therefore, the ou-of-plane lattice parameter of GaP epilayer growth on Si substrate misoriented of 6°, is considered to be the same as the GaP grown on nominal substrate, that is, 0.5467 nm.

b Lattice relaxation and misfit dislocation

For III-V materials with larger lattice mismatch with the Si, or as the GaP film thickness increases, the rising strain energy exceeds the energy of dislocation formation. It is then energetically more favourable to generate dislocations, in order to relieve the elastic strain, which leads to a relaxation (Figure 1.10 b)).[70] This type of dislocation is called the misfit dislocation.

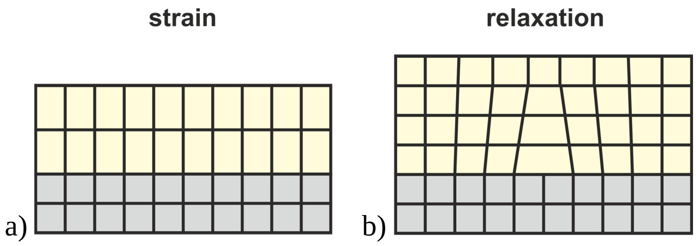

Figure 1.10 A 2D schematic representation of a) elastic strain and b) plastic relaxation at the interface of a heteroepitaxial thin layer grown on a lattice mismatched substrate.

For every misfit dislocation, there are always two threading dislocations at the two ends that thread to the layer surface, as illustrated by the example in the SiGe/Si thin film in Figure 1.11 a). The treading dislocations can be obviously evidenced by a cross-sectional TEM image. Figure 1.11 b) shows a cross-sectional TEM image of an InP/GaP/Si structure, presenting a large number of treading dislocations. [71]

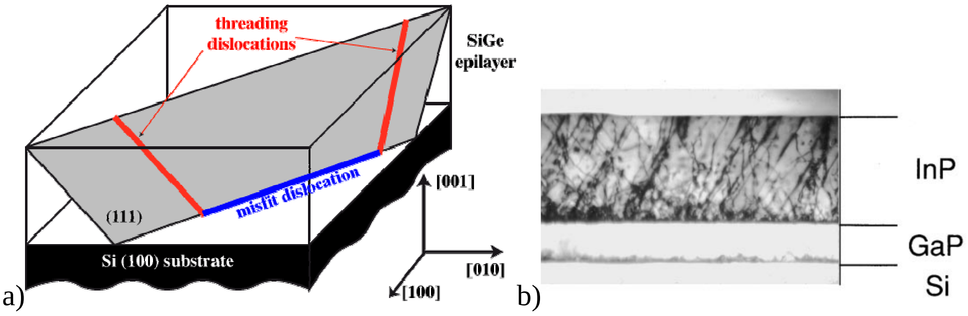

Figure 1.11 a) schematic illustration of misfit dislocation and treading dislocations in the system SiGe/Si, b) cross-sectional TEM image of InP/GaP/Si structure showing a large number of treading dislocations generating from the InP/GaP interface.[71]

The growth thickness beyond which the plastic relaxation occurs through the introduction of misfit dislocations is called the critical thickness. For the GaP/Si(001) system, the critical thickness is estimated to be about 90 nm by Soga[72], between 45 nm and 95 nm by Takagi[69], and 64 nm by Skibitzki[73]. GaP layer grown on Si below the critical thickness is theoretically fully strained and free of misfit dislocations. It has to be noticed that most of the GaP layers studied in this thesis has a thickness small enough to prevent the misfit (threading) dislocatios, as well as micro-cracks due to the difference of thermal expansion coefficients between the GaP and the Si.

c Mosaicity characteristics

The heteroepitaial thin layers usually consist of small single-crystalline blocks, typically of size of a few micrometers, which are randomly slightly misoriented with respect to each other. We call this mosaicity in crystal, as shown in Figure 1.12. The average sizes of the mosaic blocks in vertical and lateral directions are called coherence lengths. Out-of-plane rotation perpendicular to the layer surface is called “mosaic tilt” and in-planed rotation around the surface normal is “mosaic twist”. In practice, the vertical coherence length is commonly determined by the layer thickness in heteroepitaxial layers, and the lateral one is related to the planar defects.

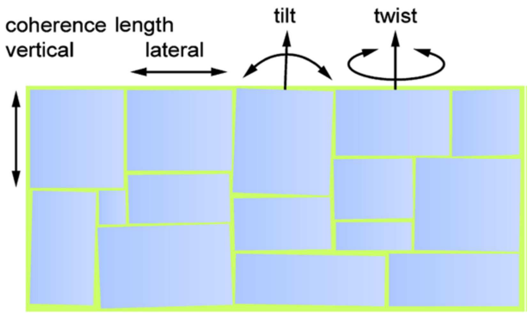

Figure 1.12 Characteristic parameters of mosaicity in single crystals [64]

d Antiphase domains and antiphase boundaries

The APDs in GaP on Si were firstly observed by Morizane on Si substrate oriented in the [100] and [110] directions,[74] and were found to be generally formed due to the polar-on-non polar materials growth and is favored by the presence of single stepped Si surface or the imperfect coverage of Ga or P at the initial Si surface.[67] It was suggested that the APDs could be partially avoided via double stepped Si(001) surface, realized by using a vicinal Si substrate with a miscut of a few degrees towards the [110] direction.[45,54,75] The APD density in the epilayer could be characterized by APD volume percentage in the whole layer (the APD volume fraction), or the mean distance between two adjacent APBs defined as APD correlation length (CL) as shown in Figure 1.13 a). Indeed, Figure 1.13 a) schematically presents the emerging APD with APBs emerging to the layer surface, which are detrimental to the surface roughness, efficient tunnel junction for tandem solar cells[58,75,76] and suitable carrier injection across the interface for integrated photonic devices. Therefore, it is of great importance to suppress the APD generation at the GaP/Si interface, or makes them annihilate during the growth. Figure 1.13 b) shows another type of APD, called self-annihilated APD. We find that the APDs can be suppressed by APBs' merging.

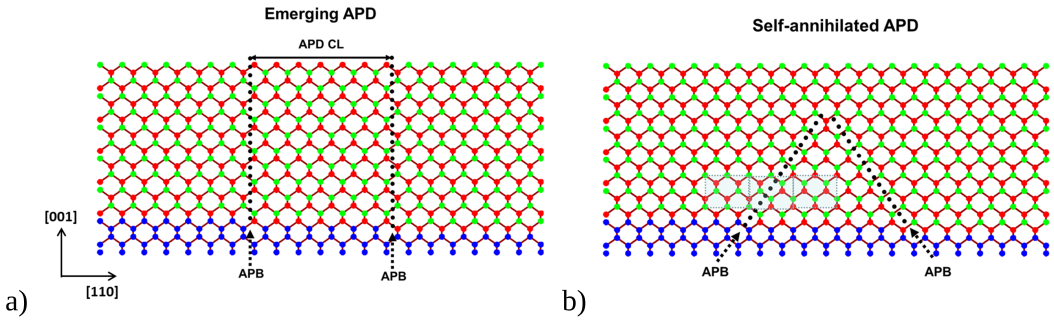

Figure 1.13 a) Schematic representation of an emerging APD in GaP layer grown on mono-atomic stepped Si substrate. The lateral correlation length related to APD (CL) is defined by the distance between two adjacent APB; b) schematic representation of a self-annihilated APD.

e Microtwins

In zinc blende GaP/Si heterogeneous epitaxial system, a twinning domain can be considered as a 180°C rotation of the {111} planes of the main phase around a [111] type axis. Microtwin (MT) is defined as a sequence of small twinning domains. As shown in Figure 1.14 a), the nominal GaP {111} planes are inclined by 54.7° from the (001) plane and the MT planes are inclined by 15.9°. Four MT variants can be obtained due to the fourfold symmetry of the zinc blende GaP crystalline structure, called MT (111), (1-11), (11-1) and (11-1), labelled by their boundaries planes. For example, Figure 1.14 a) represents the MT (11-1) since their boundaries lye on the (1-11) planes, and with an axis of rotation [11-1]. A more simple notation is given by Skibitzki research group[73], as illustrated in Figure 1.14 b). In this figure, the sample displays a miscut along the [110] direction, giving rise to a stepped surface. The MTs elongated in the real space parallel to the atomic step edges are labelled MT-A and MT-C, and those perpendicular to the steps are labeled MT-B and MT-D. They correspond respectively to MT (11-1), (111), (1-11) and (-111).

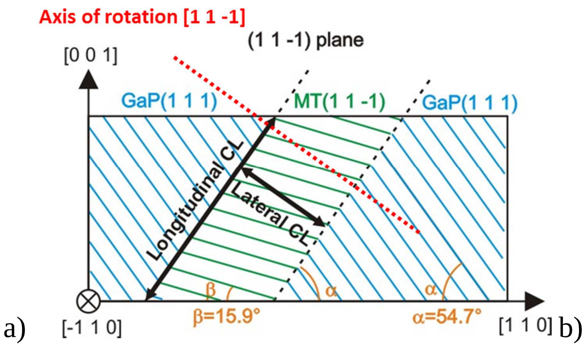

Figure 1.14 a) Geometrical stretch of nominal GaP (111) and MT (11-1) plane inclinations in a thin film of GaP. b) Skibitzki notation of MT variants. MT-A, C, B, D correspond respectively to MT- (11-1), (111), (1-11) and (-111).

Two factors are used to characterize the MT density. The first one is the MT volume fraction, i.e. the percentage of MT domains in the whole GaP layer. The second one is the correlation length (CL) in the lateral and longitudinal direction, giving rise to the average MT size (Figure 1.14 a)).

1.2 X-ray scattering in reciprocal space

1.2.1 Reciprocal space and reciprocal lattice point

In real-space, the crystal unit cell can be defined by three basis vectors $\mathbf{a}_1$, $\mathbf{a}_2$ and $\mathbf{a}_3$ and therefore the lattice points are represented by the vectors $\boldsymbol{R_n} = n_1\boldsymbol{a_1} + n_2\boldsymbol{a_2} + n_3\boldsymbol{a_3}$, with n_1, n_2 and n_3 integers. The reciprocal space is defined by a set of basis vectors $\mathbf{a_1}^*$, $\mathbf{a_2}^*$ and $\mathbf{a_3}^*$, with

$$\boldsymbol{a}_1^* = \frac{\boldsymbol{a_2}\times\boldsymbol{a_3}}{\boldsymbol{a_1}\cdot\boldsymbol{a_2}\times\boldsymbol{a_3}},\ \boldsymbol{a}_2^* = \frac{\boldsymbol{a_3}\times\boldsymbol{a_1}}{\boldsymbol{a_1}\cdot\boldsymbol{a_2}\times\boldsymbol{a_3}},\ \boldsymbol{a}_3^* = \frac{\boldsymbol{a_1}\times\boldsymbol{a_2}}{\boldsymbol{a_1}\cdot\boldsymbol{a_2}\times\boldsymbol{a_3}}. \qquad \text{Eq. 1–5}$$

In terms of a crystallographic plane (hkl) in real-space, we define a vector in reciprocal space as $\boldsymbol{G} = h\boldsymbol{a}_1^* + k\boldsymbol{a}_2^* + l\boldsymbol{a}_3^*$. It is easy to prove that the vector is perpendicular to the (hkl) plane and the magnitude of the vector is the inverse of the inter-planar distance d_{hkl}, i.e. |$\boldsymbol{G}$| = 1/d_{hkl}. Such reciprocal vector is constructed for each plane (hkl) and the point at the end of each such vector is a reciprocal lattice point (RELP), noted thereafter as: HKL. All directions in real-space are preserved in reciprocal space. The scale of the reciprocal space, called reciprocal length, is the inverse of the corresponding real-space length. For example, an orthogonal real-space unit cell with basis vectors $\mathbf{a_1}$ = (a, 0, 0), $\mathbf{a_2}$ = (0, b, 0) and $\mathbf{a_3}$ = (0, 0, c), the reciprocal space vectors are also orthogonal and are respectively $\mathbf{a_1}^*$= (2π/a, 0, 0), $\mathbf{a_2}^*$= (0, 2π /b, 0) and $\mathbf{a_3}^*$= (0, 0, 2π /c).

1.2.2 Diffraction conditions

a Bragg’s condition

X-ray diffraction from a crystal can be considered as scattering from atoms located at a set of crystallographic planes (hkl). Assuming θ the value of both incident angle and emergent angle, $\boldsymbol{k_i}$ and $\boldsymbol{k_s}$ are reduced scattering vectors along, respectively, the incident and scattered directions, with | $\boldsymbol{k_i}$ | = | $\boldsymbol{k_s}$ | = 1/λ. The scattering vector is defined by $\boldsymbol{S} = \boldsymbol{k_s} - \boldsymbol{k_i}$, as illustrated in Figure 1.15. The direction of $\boldsymbol{S}$ is perpendicular to (hkl) planes with the magnitude |$\boldsymbol{S}$| = $\frac{2\sin\theta}{\lambda}$.

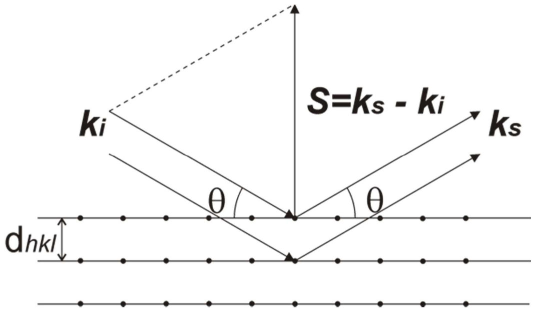

Figure 1.15 Illustration of X-ray scattering geometry from the (hkl) planes

The family of planes diffracts X-rays when the Bragg’s condition is satisfied:

$$2d_{hkl}\, sin\,\theta = \lambda, \qquad Eq.\ 1\text{–}6$$

where λ is the wavelength of the incident x-ray. In this condition, |$\boldsymbol{S}$| $= \frac{2\sin\theta}{\lambda} = \frac{1}{d_{hkl}}$ with $\boldsymbol{S}$ a vector of reciprocal lattice, that is, $\boldsymbol{S} = \boldsymbol{G}$.

That is to say, the X-ray diffraction is observed when and only when the scattering vector is a reciprocal lattice vector. This is the Laue Condition, which is exactly equivalent to the Bragg Condition.

b Ewald Sphere construction

A useful way to find the direction of X-rays diffracted by the crystal and visualize the diffraction in reciprocal space is provided by the Ewald Sphere construction (Figure 1.16). Let us consider the reciprocal lattice for a given crystal fixed at the origin of the reciprocal space O. Monochromatic X-ray beam arrives on the crystal with an incident angle ω and is scattered. Now, we construct a virtual sphere of radius 1/λ centered at C, such that ***CO*** coincides with $\boldsymbol{k}_i$. By definition, the scattering vector ***S*** starts at O and points to the sphere surface. When the incident beam changes its direction with respect to the crystal, the sphere rotates around the origin O. According to Laue Condition, the X-ray is diffracted when ***S*** is a reciprocal lattice vector, in other words, when the RELP is located at the Ewald Sphere surface. The incident and diffracted angles corresponding to the RELP can be then determined. Moreover, the rotation of Ewald Sphere defines a limiting sphere of radius 2/λ centered at O, which covers the region of reciprocal space accessible to X-rays of a given wavelength λ. Therefore, higher diffraction order can be reached only by using X-rays with higher energy (smaller wavelength).

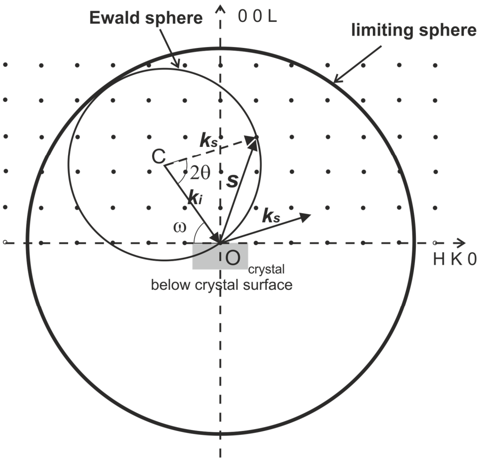

Figure 1.16 Illustration of Ewald Sphere construction, Projection on 2D.

1.2.3 Reciprocal space map and line profile scans

The characterization of crystal properties by X-ray scattering can be realized by the measurement of the scattered intensity I for all possible values of ***S***. The distribution of I(***S***) in the reciprocal space, is called a Reciprocal Space Map (RSM). RSM around a RELP HKL, involving the intersection between the RELP and the Ewald Sphere surface, gives information on the HKL planes and furthermore the crystal microstructure. The RSM is a powerful method for structural characterization of heterostructures. [77]

Figure 1.17 schematically represents a RSM around 224, with respect to the Ewald Sphere described above. It has to be noticed that only the RELP marked with a black solid dot can be studied by conventional X-ray techniques, since the two grey semi-spheres covers the region where incident or emerging beam is below the crystal surface, and the RELP outside the limiting sphere are inaccessible to the X-ray beam. Such measurement is generally acquired using a conventional ω-2θ diffractometer, with the incident X-ray beams fixed when the sample rotates to change the ω angle and the detector arm rotates to change 2θ. Three typical linear scan types are depicted in the figure: ω scan where only ω angle changes and the 2θ angle is kept at a constant value, ω/2θ scan where the sample rotation angle Δω and the detector rotation angle Δ2θ are coupled such that Δ2θ=2×Δω, and 2θ scan where the sample is fixed and the detector arm rotates around a 2θ Bragg position. The RSM is usually done by performing a series of ω/2θ scan at different ω settings. It is important to distinguish two ω scan types, that is, rocking-curve scan and transverse scan: rocking-curve scan is performed with an open-detector and transverse scan is high resolution ω scan performed with channel-cut in the diffracted beam path in order to differentiate contributions orthogonal and parallel to the sample surface. The transverse scans are more accurate in the characterization of a thin film with mosaic structure.

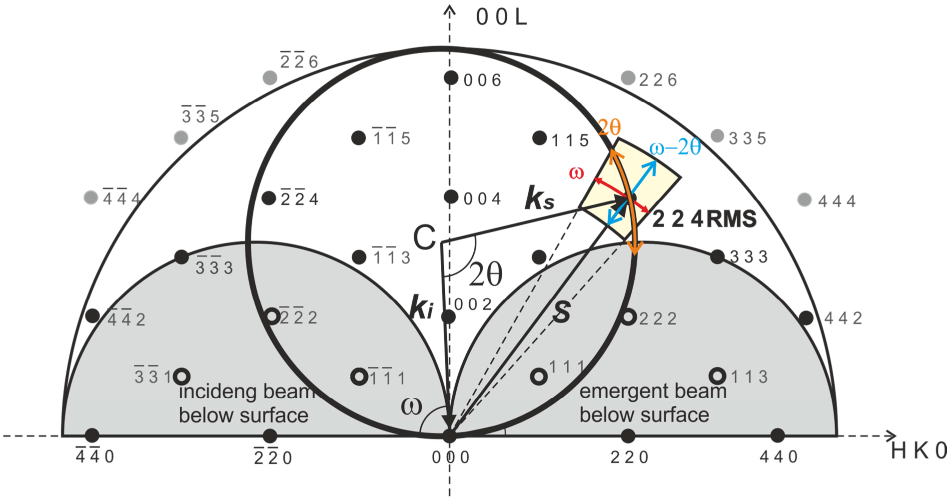

Figure 1.17 Different scan type presented in Ewald Sphere

1.2.4 Pole figure

A conventional symmetric ω/2θ scan permits investigating only the planes oriented parallel or nearly parallel to the thin-film sample surface, or in other words, the planes whose normal ***n*** coincides the scattering vector, as shown Figure 1.18 a). For tilted planes that are oriented in other directions, there are two ways to bring the normal vector into the scattering vector direction. The first way is illustrated in Figure 1.18 b), consisting of a ϕ rotation to bring the plane normal ***n*** onto the scattering plane (Δϕ =0 if ***n*** is initially in the scattering plane, which is the case in the figure), which is followed by a ω scan to bring ***n*** parallel to the scattering vector (here Δω=α). This is a conventional asymmetric ω/2θ scan and it is performed with a Bragg-Brentano diffratometer, with a linear source, while the direction distribution accessible with this method is small. It is commonly used when the orientation direction is given, for example, in the study of lattice parameter of GaP layer grown on a Si(001) substrate misoriented of 6° towards the [110] direction. Another method, as illustrated in Figure 1.18 c), can be considered as turning the ***n*** firstly by a ϕ rotation then make a ψ rotation (rotation perpendicular to the scattering plane). So this time Δϕ=90° and Δψ=α. This method requires a 4-circle diffractometer with a point source (Figure 1.19). The ω and 2θ angles are fixed at the Bragg position of the plane of interest, and then a 360° rotation around ϕ is performed with successive ψ values. A wide range of direction distribution of diffraction planes is reachable, showing a great advantage for detection (111) plane twins.

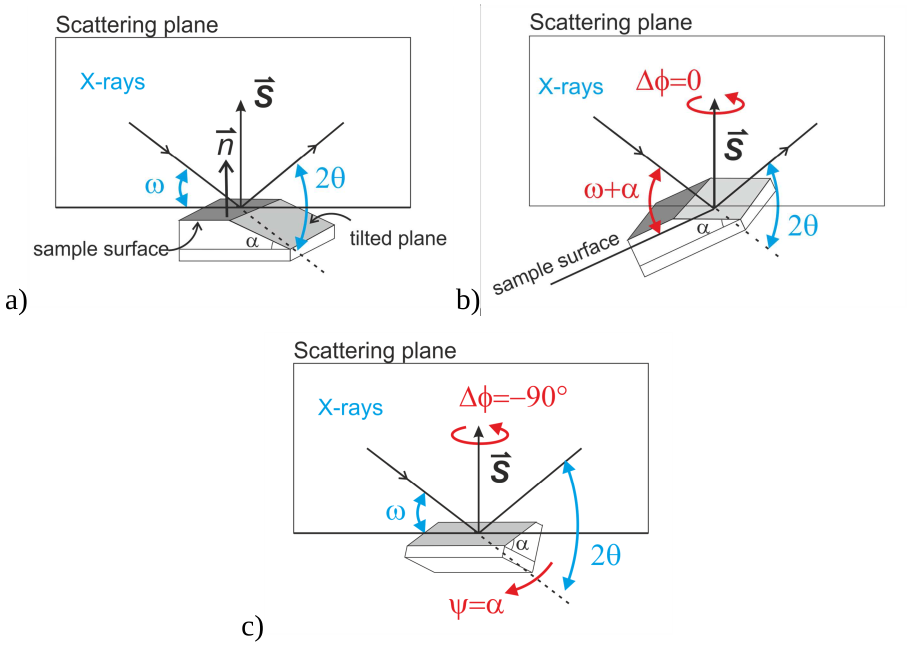

Figure 1.18 Measurement of crystalline planes of different orientations. a) Conventional ω/2θ scan to study the planes parallel to the sample surface, b) asymmetric ω-2θ using ω offset to compensate the crystalline plane tilt, c) 4-circle measurement using ψ offset to compensate the tilt.

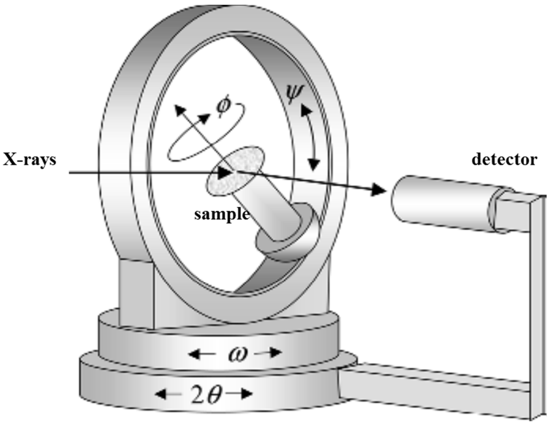

Figure 1.19 Scheme of a four-circle diffractometer with variable azimuth ϕ and tilt angle ψ [78]

The intensity I(ϕ,ψ) recorded in the 4-circle measurement can be represented on a 3D reference sphere. Figure 1.20 illustrates the spherical projection of crystal planes on the reference sphere for a cubic lattice crystal. The crystal is placed at the center of a reference sphere. The intersection between the plane normal and the sphere is called a pole. The origin of azimuth angle ϕ is fixed at the radius along the [010] direction and ψ is defined as the angle between the plane normal and [001] direction. The poles of all the planes form a spherical projection of the coordinates (ϕ,ψ). Such a spherical projection allows conservation of the angle between planes, which can be measured from the great-circle distance between the two corresponding poles and the sphere radius. In Figure 1.20, poles corresponding to several representative faces are marked on the reference sphere with a black point.

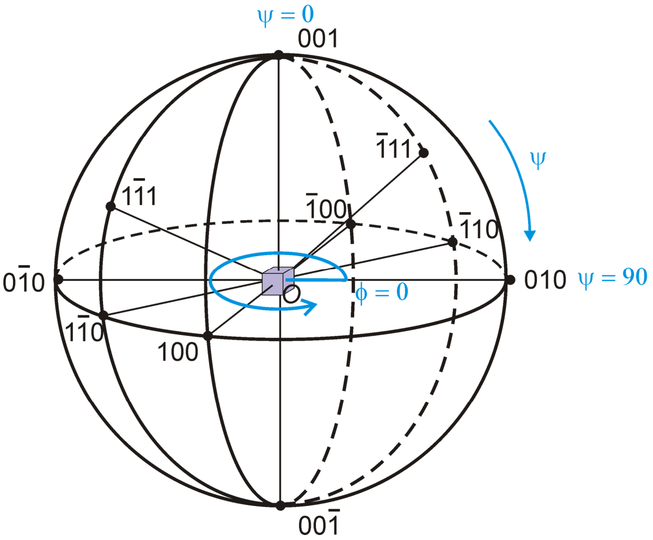

Figure 1.20 Spherical projection of a cubic crystal

Although the spherical representation is obvious to understand, it is always preferential to work with a 2D representation of (ϕ,ψ) coordinates for convenience, in condition that all the angle relationships between planes can be conserved. Hence, the stereographic projection is commonly employed, using the equatorial plane as projection plane. Figure 1.21 describes the stereographic projection principle of all the poles in “northern hemisphere”. For any pole P at the reference sphere, when being linked with the South Pole, the piercing point P’ is considered as its projection on the equatorial plane, which is characterized by the initial azimuth angle ϕ and the distance r from the sphere center. The relationship between r and ψ can be described by the Equation 1-7.

$$r = R \cdot tan({}^{\psi}/_{2}) \qquad Eq.\ 1\text{–}7$$

Figure 1.21 b) shows the stereographic projection of the poles in Figure 1.17, and we call this a pole figure. A four-circle measurement displays such a pole figure.

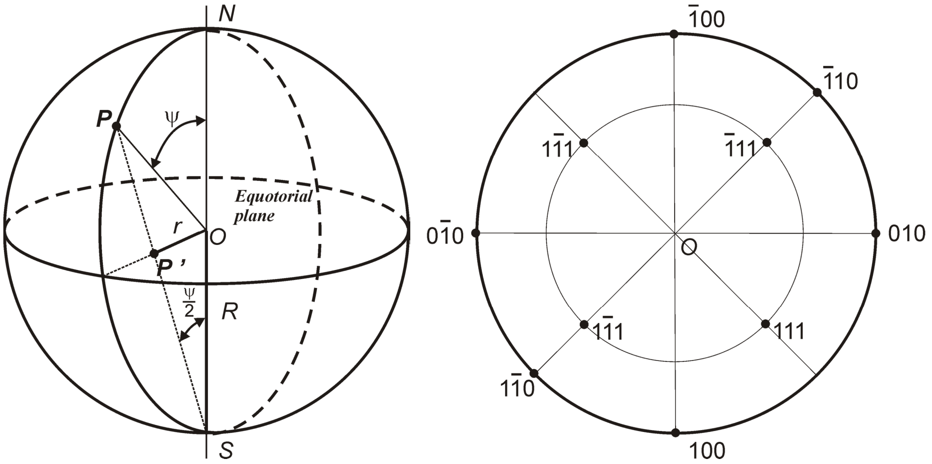

Figure 1.21 Stereographic projection

1.3 Analysis of heteroepitaxial layers by X-ray scattering techniques

The X-ray diffraction patterns are indeed the intersection of the Ewald sphere with the reciprocal space lattice nods corresponding to the studied structure. By definition, the reciprocal space scale is inversely proportional to the real space scale. So that a 3D infinitely great volume is interpreted in reciprocal space as a 0D point without any volume; a 2D plane becomes a line in reciprocal space, whose direction is perpendicular to the plane. Contrarily, a real-space 0D point is expressed by a 3D volume and a 1D line by a 2D plane in reciprocal space. Now let’s think of a perfect thin layer with limited lateral size a and a thickness T, composed of a series of crystalline planes with regular inter-plane distances, as shown in Figure 1.22. Its interpretation in reciprocal space should have an elongated form, in the way that the lateral and longitudinal sizes are respectively inversely proportional to a and T, taking into consideration that the X-rays beam is monochromatic.

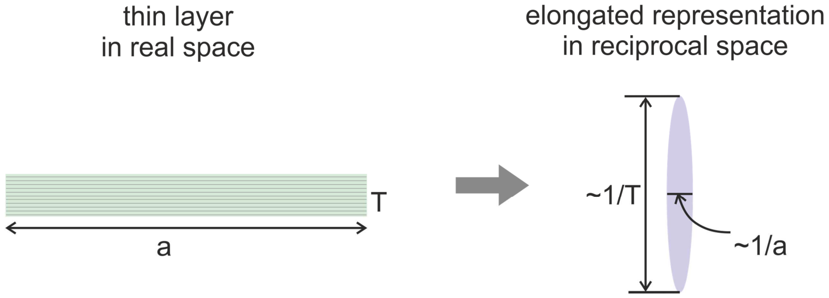

Figure 1.22 A thin film with a lateral limited size a and a thickness T in real space and its interpretation in reciprocal space.

Therefore, the traditional 00L ω/2θ scans along the longitudinal direction, is sensitive to the variation of lattice parameter in the out-of-plane direction due to the lattice strain, while the 00L transverse scans on the perfect thin layers grown along the [00L] direction should display a very thin peak, and any defect (such as small crystallites, lattice misorientation (“tilt”) and planar defects) that disturbs the lateral long range order brings a broadening effect on the transverse scans.

1.3.1 Determination of epilayer strain and relaxation

The strain status of the epilayer can be revealed through the alignement of the substrate reciprocal lattice point and that of the epilayer in a reciprocal space map (RSM), taking into consideration that the lattice parameter of the epilayer is changed to accommodate that of the substrate in case of fully strained. Figure 1.23 a) shows a 004 RSM from a 20-nm-thin GaP/Si sample.[79] The red cross and the black spot represent respectively the center of the Si and GaP reflection spots. They are well aligned in the lateral direction ($S_{//}$), indicating that the GaP epilayer is fully strained. If fully relaxed, the position of the GaP will be shifted towards the upper-left side, as marked by the black star. Indeed, the 004 RSM is sensitive to out-of-plane strain while the 224 RSM is sensitive to the in-plane lattice parameter. Figure 1.23 b) shows a 224 RSM of the same sample. Here we can also conclude that the epilayer is fully strained.

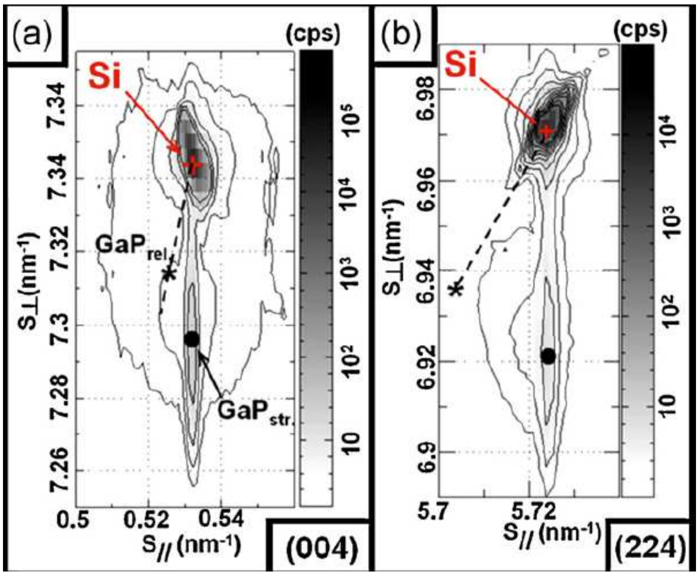

Figure 1.23 a) 004 RSM and b) 224 RSM on a 20-nm-thin GaP/Si sample. The calculated position of Si substrate, fully strained and totally relaxed GaP are marked respectively by red cross, black spot and black star. The alignement of Si center and GaP center in the $S_{//}$ direction indicate that the epilayer is fully strained.[79]

We can also estimate the strain status from 00L ω/2θ scans, by simply taking into account the lattice parameter of the epilayer in the out-of-plane direction. For example, as calculated in the section 1.1.2, the lattice constant of fully strained GaP is 0.5467 nm in the [001] direction, a little greater than the theoretical (fully relaxed) value 0.54506 nm. Figure 1.24 shows the ω/2θ scan profiles of specular 004 diffraction from a series of GaP/Si layers.[69] Knowing that the X-ray wavelength λ=0.1540562 nm, $2\theta_{relaxed}$ and $2\theta_{strained}$ are calculated to be respectively 68.84° and 68.61°, according to the Bragg's Law. The 2θ position of the fully relaxed GaP is indicated by a dashed line for easier determination: for samples whose GaP peak is located at the left side of the line, the strain is compressive and the epilayer is strained; for those with a GaP peak at the right side of the line, the strain is tensile and there is relaxation in the layer. Notice that the peak position of the 45 nm thin layer is found to be slightly less than the theoretical fully strained position 68.61°, this disagreement may be originated form the experimental adjustement.

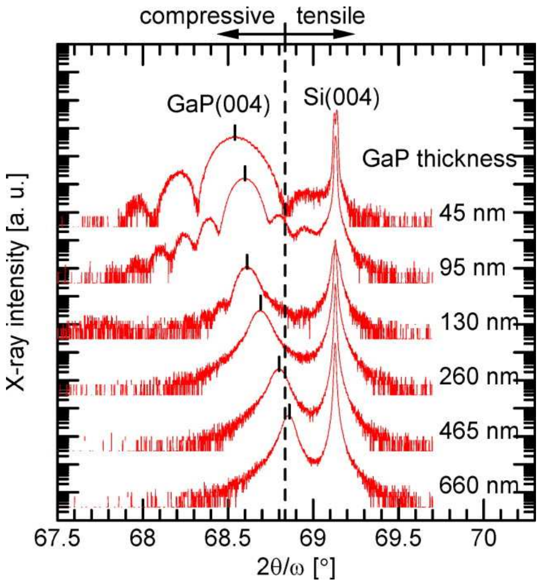

Figure 1.24 ω/2θ scan profiles of specular 004 diffraction from a series of GaP/Si samples.[69]

1.3.2 Evaluation of lattice misorientation

The heterepitaxial GaP on Si layers may consist of small “mosaic blocks” with rotational misorientation (or “tilt”) relative to one another, as shown in Figure 1.25 a). Therefore the normal directions to the crystallographic planes of same index in different blocks are distributed within a “tilt” angle[80]. These blocks are much larger than the spatial coherence length in XRD experiments (order of magnitude: 1 µm in this case) and thus scatter X-rays incoherently with respect to each other.[81,82] The reciprocal space ($S_{//}$, $S_{\perp}$) being defined along the directions parallel to the layer surface and its normal, a dispersion on $S_{\perp}$ is seen within a small angle, resulting in a broadening on the diffraction peak $\Delta\omega_M$, as depicted in the Figure 1.25 b), and this broadening contribution is more evident on high index reflections.[83] Whereas the broadening due to the crystallite size (here the average lateral size of the bloc) is constant on any reflections.

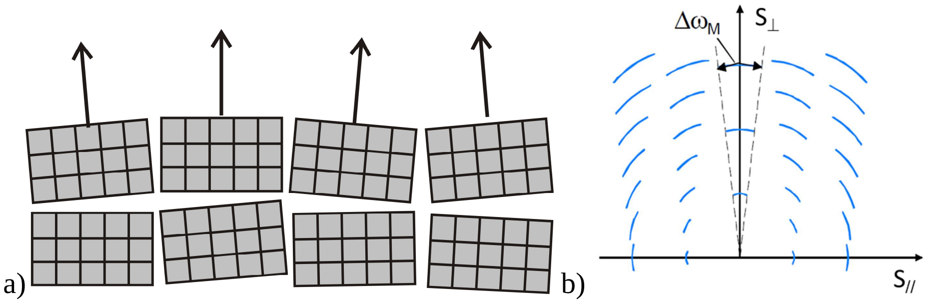

Figure 1.25 a) Schematic presentation of mosaic structure composed of disoriented small blocs b) Peak broadening due to mosaic tilt [84]

Therefore, the tilt angle along with the average crystallite size in the direction parallel to the layer surface can be evaluated via the decomposition of the ω scan peak broadening of 00L reflections, that is, the Williamson-Hall method, as proposed by Williamson and Hall in 1953. A more detailed derivation can be found in the APPENDIX of ref. [83].

1.3.3 Measurement of layer thickness

The layer thickness is another important parameter of the thin layer. The determination of layer thickness is based on the coherent interference between the layer surface and the layer/substrate interface. Considering an epitaxial layer with flat interface with good parallelism and few distortion, interference fringes can be observed in the scattering pattern. The layer thickness L can be determined using the he angular separation between the corresponding thickness fringes, which is given by the following expression, in the case of a specular reflexion:[85]

$$\Delta(\theta_m) = \lambda \frac{\sin\theta}{\sin(2\theta)L} \qquad \textit{Eq. 1–8}$$

Differentiating $S = \frac{2\sin\theta}{\lambda}$, one obtains:

$$\Delta S = \frac{2}{\lambda}\cos\theta\Delta\theta, \qquad \textit{Eq. 1–9}$$

Then, combining the (*Eq. 1-8*) and (*Eq. 1-9*) relationships:

$$\Delta S = \frac{2\sin\theta\cos\theta}{L\sin2\theta} = \frac{1}{L} \qquad \textit{Eq. 1–10}$$

Therefore:

$$m = LS_m + cte \qquad \textit{Eq. 1–11}$$

with m the fringe order and S_m its position.

Figure 1.26 shows a 004 ω/2θ scan profile of a 100-nm-thin GaPN/GaP sample[86]. This is a very typical profile of heteroepitaxial layer, basically composed of a substrate peak, a layer peak and the thickness fringes. The layer thickness measured from the figure is about 114 nm, a little bigger than the nominal 100 nm.

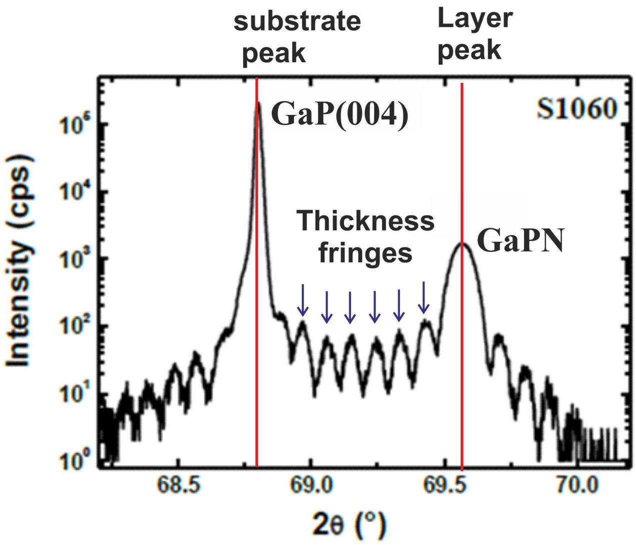

Figure 1.26 XRD 004 ω-2θ scan profile displaying thickness fringes, the layer thickness is measured to be 114 nm for a 100 nm-thin GaPN/GaP film.[86]

1.3.4 Observation of MTs in reciprocal space

All the above analyses are based on the study of the reciprocal lattice characteristics of the epilayer. Now let’s consider the MTs, being regarded as 180° rotation of the {111}-type nominal crystal planes along a [111] type axes. In reciprocal space, the twinning effect produces new reflection spots as schematically depicted in Figure 1.27. The green streaks correspond to the rotation of the nominal lattice point around the [11-1] axis, indicating the additional reflections due to the MT-A, whose boundaries are limited by (11-1) planes. The elongation of the spot along the [11-1] direction comes from the fact that the MT domain is a thin “platelet” with (11-1) boundaries. In the same way, the orange streaks correspond to the MT-C. The MT-B and the MT-D can be seen in the plane defined by the [001] and [1-10] vectors.

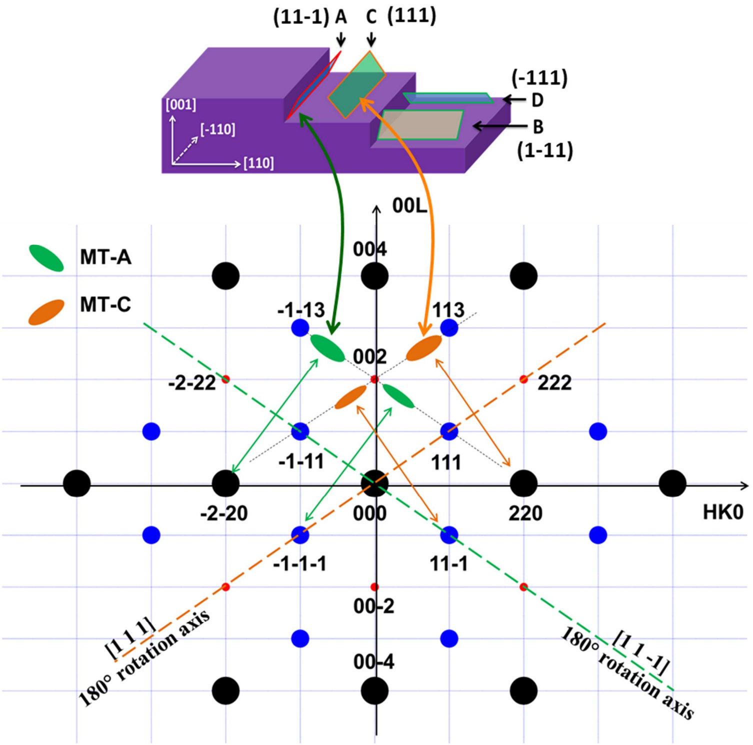

Figure 1.27 Reciprocal lattice points of GaP. The black, blue and red solid circles represent strong, medium and weak reflections. The green and orange ellipsoids represent respectively the MT-A and MT-C spots.

1.4 Summary

Perfect crystal doesn't exist. Variant crystalline defects can be generated in heteroepitaxially grown thin layers, involving strain and relaxation, misfit and treading dislocations, mosac tilt, microtwins and antiphase domains. The X-ray diffraction is shown to be a powerful technique in investigating the epilayer structure. Different techniques consisting of ω scan, ω/2θ scan, reciprocal space mapping, pole figure are widely used in measurement of strain status, mosaic tilt angle, epilayer thickness and other structural parameters. On this basis, we are able to develop analytical methods to evaluate the structural quality of the GaP/Si layers, especially the MT and APD densities. These analyses, combined with complementary microscopic measurements, lead to a complete understanding of structural qualities of the GaP/Si layers.

Chapter 2 GaP/Si growth and characterization techniques

This chapter presents the experimental supports of the thesis work. Firstly I will give a description on the GaP/Si samples growth, including the Si substrate, the Si surface preparation, the homoepitaxial growth of Si buffer layer and the heteroepitaxial growth of GaP layers. Then three X-ray diffraction measurement setups are presented: laboratory Bruker D8 Discover diffractometer on high resolution and low resolution mode and the beamline BM02 of European Synchrotron Radiation Facility. Finally, complementary techniques such as Atomic Force Microscopy, Transmission Electron Microscopy, Scanning Transmission Electron Microscopy and Scanning Tunneling Microscope are very simply introduced.

2.1 Growth of GaP/Si heterostructure

2.1.1 Vicinal Si substrate

The Si substrates used in this work are 2 inches n-type Si(001) wafers, containing two flats telling us the crystallographic orientation of the substrate, as shown in Figure 2.1 a). Two types of surfaces are used: the nominal Si surface with the [001] crystallographic direction parallel to the surface normal, ant the vicinal Si surface with 6 degrees miscut towards the [110] direction, as illustrated in Figure 2.1 b). The vicinal Si substrate is now widely studied since it has been shown that the APDs were formed due to polar on non-polar materials growth and could be partially avoided via double stepped Si(001) surface, realized by the miscut of a few degrees towards the [110] direction.[45,53,54]

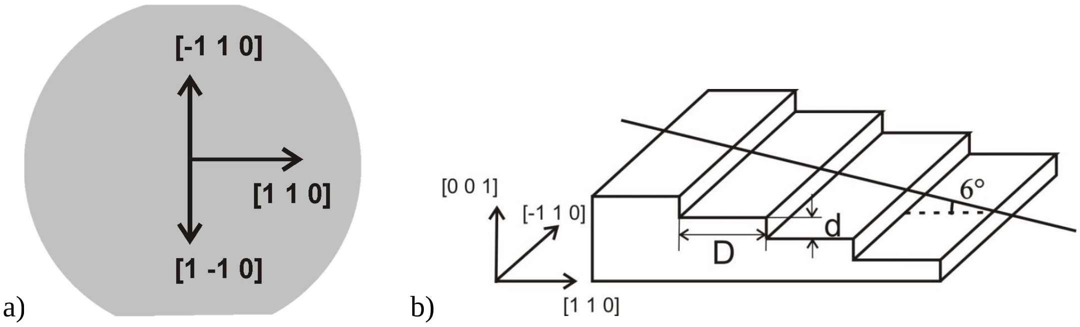

Figure 2.1 a) Schematic representation of the Si(001) wafer orientation. b) The vicinal substrate shows a miscut of 6° towards the [110] direction.

Indeed, on such a vicinal surface, both single-layer steps and double-layer steps can be formed. The relationship between the miscut angle α, the atomic step height d and the average terrace length D can be described as following:

$$tan(\alpha)=d/D. \qquad Eq.\ 2\text{–}1$$

Knowing that for single layers $d = \frac{a_0}{4}$ and for double layers $d = 2 \times \frac{a_0}{4}$, with a_0 = 0.5431 nm the lattice constant of silicon in the [001] direction. Then the terrace lengths D are calculated for different miscut angles and the results are listed in Table 2.1.

Table 2.1 Calculation of the terrace lengths D for Si substrate with different miscut angles

Miscut angle (°)	1	2	3	4	5	6
$D_{single\ layer}$ (nm)	7.779	3.888	2.591	1.942	1.552	1.292
$D_{double\ layer}$ (nm)	15.558	7.776	5.181	3.883	3.104	2.584

According to Chadi’s notation,[87] we distinct two types of steps for both single-layer (S) and double-layer (D), labeled by S_A, S_B, D_A and D_B. The subscript denotations indicate whether the Si-Si dimerization direction on the upper terrace near a step is perpendicular (A) or parallel (B) to the step edge, as depicted in Figure 2.2. On single stepped surface, we can observe an alternation of two domains: (1×2) for the terrace with Si-Si dimers perpendicular to the step edges and (2×1) for that with Si-Sidimers parallele to the step edges. Therefore, the surface with with D_A double steps represtes a single (1×2) domain and that D_B double steps represents a single (2×1) domain. The presence of single domain is the signature of double layer formation.

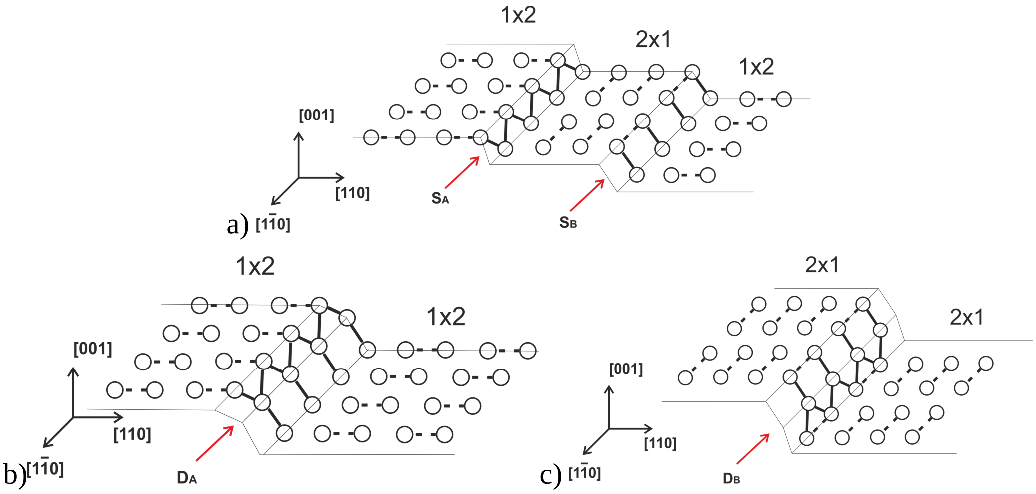

Figure 2.2 Illustration of Si surface presenting a) alternation of S_A and S_B single steps with (1×2) and (2×1) domains b) D_A double steps with single (1×2) domain and c) D_B double steps with (2×1) single domain. The dimerization direction on the upper terrace near a step is perpendicular (for S_A and D_A) or parallel (for S_B and D_B) to the step edge,

They also calculated the formation energies per unit length λ for the four types of steps:

$$\lambda(S_A) \approx (0.01 \pm 0.01eV)/a,$$

$$\lambda(S_B) \approx (0.15 \pm 0.03eV)/a,$$

$$\lambda(D_A) \approx (0.54 \pm 0.10eV)/a,$$

$$\lambda(D_B) \approx (0.05 \pm 0.02eV)/a.$$

We have $\lambda(D_B) < (\lambda(S_A) + \lambda(S_B)) < \lambda(D_A)$, therefore, D_B double steps with the surface dimerization parallel to the step edge are more energetically stable, which is also consistent with the calculation by Oshiyama[88] and the experimental observations.[89,90]

Althouth energetically favorable, the formation of D_B double steps strongly depends on the miscut angle and the surface preparation (chemical cleaning, thermal treatement and homoepitaxial growth of Si buffer layer, etc.)

Figure 2.3 shows the evolution of double steps formation as a function of miscut angle,[91] measures under the same thermal conditions (heated for 30 sec at 1525K). The closed squares represent the relative population of the (1×2) domain which decreases with the increase of miscut angle. The open squares represent the percentage of double steps, which increases witht the miscut angle. Both demonstrate that higher miscut angle facilitates the formation of D_B double steps.

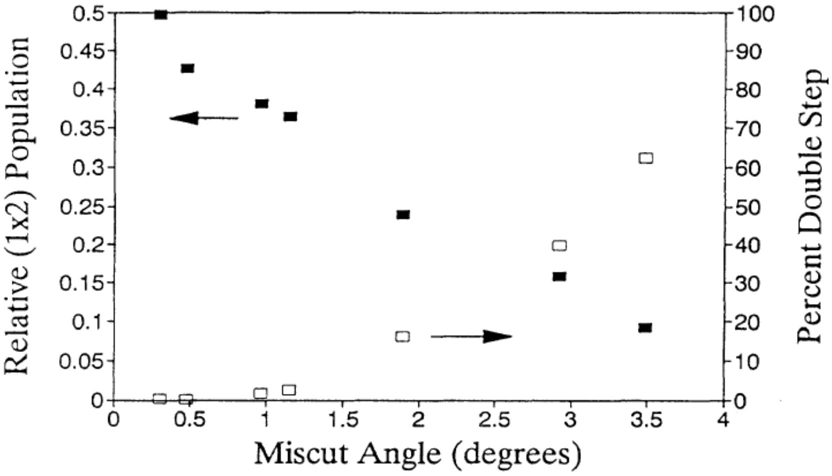

Figure 2.3 Relative population of the (1×2) domain (closed squares, left axis) and percentage of double steps (open squares, right axis) as a function of miscut angle. [91]

Actually, the 4 degrees miscut has already been studied in our laboratory[86,92] and it turned out to be not sufficient for obtaining a perfect double stepped surface, therefore, most of the samples studied in my thesis are grown on the Si(001) substrate misoriented of 6°. The Si surface cleaning procedures have been optimized by Tra Thanh Nguyen during his thesis (Foton, Insa Rennes)[86] and will be briefly introduced in the next part. The growth of Si buffer layer is one of the important parameters to be studied in this thesis and will be discussed in Section 4.2.2.

2.1.2 Si surface cleaning

Si is a very reactive material and contaminants such as carbon, oxide, metallic and organic impurities are easily formed on Si surface during the fabrication and storage process. Contaminants on the surface may act as a preferential nucleation site and result in high defect density in the compound semiconductor layer[93,94]. Smooth and contaminant-free Si surface is a key point to the successful epitaxial growth of III-V materials on Si to limit the defect generation. Evaluating the cleanliness of a chemical preparation is not straightforward. Fortunately the Chemical Vapor Deposition (CVD) technique is dramatically sensitive to substrate surface contamination. Even low contaminant density results in a highly rough and pitted surface after a homoepitaxial growth. The efficiency of the silicon surface preparation can be thus investigated by post-growth surface morphology characterization of silicon buffer layers.

Firstly a cleaning process based on the standard Radio Corporation of America (RCA) process[94] and called herein the “modified RCA process” has been applied. The main steps of the process are listed in Table 2.2.[95] The sample is firstly dipped in the NH_4OH-H_2O_2-H_2O solution for removing particles, small organic residues and most metallic impurities, then in the HF-H_2O solution and HCl-H_2O_2-H_2O solution for oxide removal, and finally in the HF-H_2O solution after an oxidation in UV/O_3 atmosphere for residual carbon removal. These last steps are repeated 5 times.

Table 2.2 Main steps of the modified RCA process, RT means room temperature.

Chemical environment	T(°C)	Time (min)	Effect
$NH_4OH : H_2O_2 : H_2O$ 10: 30: 200	70	10	Particles, organic, and metals (Cu, Ag, Ni, Co and Cd) removal; Fe and Al introduction.
DI water	RT	20	
HF : H_2O 12.5 : 237.5	RT	1	Oxide removal; Carbon and small amount of ions (especially Cu) introduction; Metallic residues removal; Oxide layer formation at surface.
HCl : H_2O_2 : H_2O 30 : 30 : 150	80	10	
DI water	RT	10	
HF : H_2O 12.5 : 237.5	RT	1	Oxide layer removal.
DI water	RT	10	
Oxydation in UV/O_3	RT	2	Carbon and Sulfur removal.
DI water	RT	3	
HF : H_2O 12.5 : 237.5	RT	1	
DI water	RT	3	
The last 4 steps are repeated 5 times using new HF solution with the same concentration. Finally, the wafer is immersed in a new HF bath and is loaded to the reactor.			

We have discussed and report the influence of the surface cleanness on the quality of the GaP layer and the GaP/Si interface.[96] As shown in the cross-sectional scanning electron microscopy (SEM) image (Figure 2.4 a)) the modified RCA process followed by 150 nm Si homoepitaxial layer leads to a pitted surface, displaying a flat bottom surface whose depth corresponds to the epitaxial layer thickness. The inclined edges of the groove, showing a constant angle value of 25° with the mean surface, indicate the (113) crystal facets. These grooves, also observed in the inserted AFM image, result in a very high r.m.s. surface roughness of 48 nm. This evidences the presence of contaminants at the substrate surface[97], which prevent any subsequent high-quality epitaxial growth.

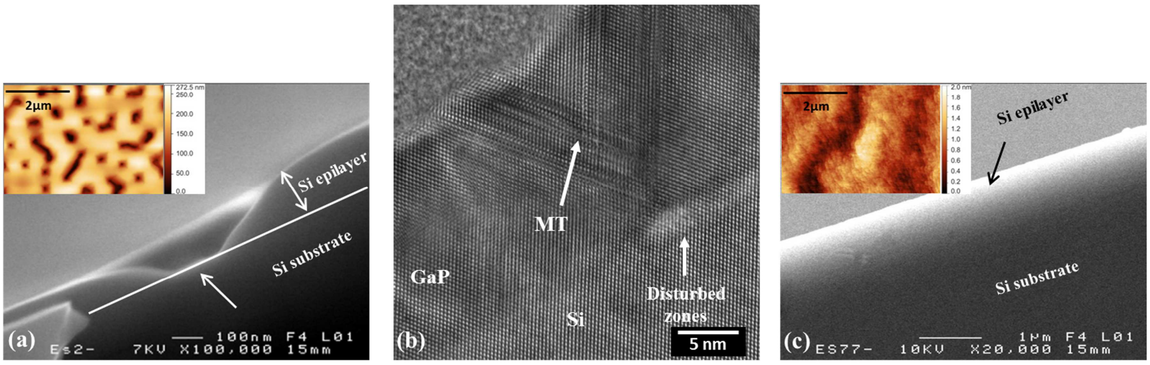

Figure 2.4 a) Cross-sectional SEM image and inserted AFM image of Si homoepitaxial layer grown on the Si substrate cleaned by modified RCA process; b) HRTEM images of a GaP epilayer grown on the Si substrate cleaned by modified RCA process; c) Cross-sectional SEM image and inserted AFM of Si homoepitaxial layer grown on the Si substrate cleaned by optimized HF cleaning process. [96]

Figure 2.4 b) presents the cross-sectional HRTEM image of a GaP layer grown directly on a Si substrate freshly chemically prepared by the modified RCA process. The GaP/Si interface is quite diffuse with localized bright areas which are attributed to the presence of contaminants at the Si surface. The nature of the contaminants has not been determined, but is usually assumed to be carbon or oxygen atoms.[98] This assumption is supported by various observations made at different scales on samples with different chemical preparations and different III-V regrowth conditions, but not shown here for clarity. In this situation, large packets of MTs are generated from these disturbed zones and emerge to the GaP surface, which has been also observed on different parts of different samples.

We attribute these observations to the numerous wet chemical steps used in the modified RCA process. This likely increases the exposure of the silicon surface to nonintentional contaminations, if the purity of the chemical solutions and the chemical environment is not perfectly controlled.

In order to limit the exposure of silicon to chemical solutions and improve the cleaning effect, a second method called “optimized HF process” has been developed, as described in Table 2.3. A first dipping in HF 1% bath for 90 seconds for native oxides removal is followed by an exposure under UV/O_3 during 10 minutes to remove carbon, organics and metal particles removal, but this second steps results in the SiO_2 layer formation. The process is finished by a final HF (1%) dipping for 90 seconds, in order to remove the SiO_2 layer and promote a hydrogen passivated surface that is believed inert to atmospheric contamination for 10 min or more[99]. This process is similar to that reported by Takahagi et al. who claimed successful achievement of clean and carbon-free silicon surface,[100] and already proved its efficiency for III-V/Si growth.[59,101] Figure 2.4 c) shows the cross-sectional SEM and AFM images of the Si homoepitaxial layer grown on the “optimized HF process” cleaned substrate. The epilayer is smooth without any detectable defects (pits, holes, grooves) and with a r.m.s. roughness around 0.3 nm. This indicates that the substrate surface was efficiently cleaned before Si growth.

Table 2.3 Main steps of the optimized HF cleaning process

Chemical environment	T	Time (min.)	Effect
HF 1%	RT	1.5	Native oxide removal
UV/O3	RT	10	Carbon, organics and metal particles removal; SiO2 layer formation
HF 1%	RT	1.5	SiO2 layer removal; Passivation of surface with hydrogen

All GaP/Si samples in this work are grown on the “optimized HF process” cleaned Si substrate, if not specially mentioned.

2.1.3 Heteroepitaxial growth of GaP thin layers on Si

The epitaxial growth is realized in an Ultra-High-Vacuum Chemical Vapor Deposition (UHVCVD) - Molecular Beam Epitaxy (MBE) cluster developed and installed in laboratory FOTON-OHM/INSA since 2010.[59] The Riber UHVCVD reactor dedicated to IV group element growth is connected by a UHV tunnel maintained at 10^{-9} Torr to the

Riber compact 21 solid source MBE chamber devoted to III-V compound growth, as shown in Figure 2.3. Both chambers are equipped with a Reflection High-Energy Electron Diffraction (RHEED) system composed of a RHEED Gun and a fluorescent screen, operating at 30 keV for UHVCVD and 12 keV for MBE, in order to monitor the growth in-situ.

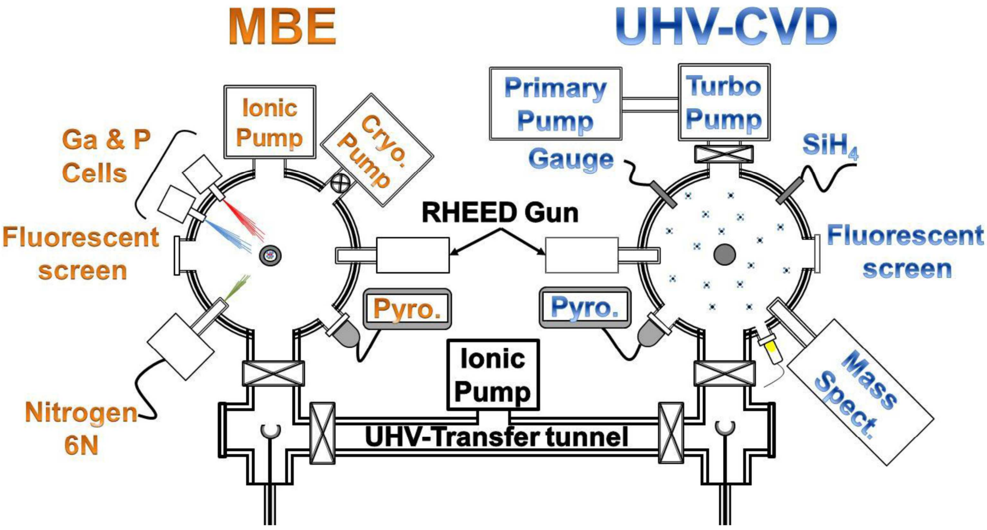

Figure 2.5 Schematic representation of the UHVCVD-MBE growth cluster. The UHVCVD reactor for group IV growth is linked to the MBE reactor for group III-V growth by a UHV transfer tunnel maintained at 10^{-9} Torr.[59]

For samples with GaP directly grown on Si, freshly prepared Si substrates are loaded into the MBE chamber, heated at 800°C during 5 minutes for dehydrogenation and cooled down to GaP growth temperature.

For samples with Si buffer layer prior to GaP growth, the substrates are introduced to the UHVCVD chamber after chemical preparation and heated to 800°C (heater on the sample holder) under a residual atmosphere of silane at about 10^{-6} torr. The homoepitaxial Si layer is deposited using silane (SiH_4) injected through a mass flow/Baratron flux/pressure controller and the pressure is fixed at 6.10^{-3} Torr, with 10 min annealing before cooling down. The Si/Si substrate is then transferred under UHV to the MBE growth chamber for GaP overgrowth.

The Ga is generated from conventional Knudsen effusion cells containing pure metal solid source and the P is provided by valved-cracker cells (P_4). Two growth modes are applied. The first one is the traditional Molecular Beam Epitaxy (MBE) growth where the Ga and the P are simultaneously supplied, and the growth rate is controlled by the Ga flux. The Ga and P flux have already been optimized before this thesis, so that for most samples described hereafter, the Ga flux is in the order of 1.1×10^{-7} torr and the P flux is in the order of 1.1×10^{-6} torr. The second mode is called Migration Enhansed Epitaxy (MEE) consisted of alternated Ga and P deposition. Two important characteristics of the MEE mode is the growth rate expressed by monolayer (ML) per second and the Ga amount per cycle that will be discussed in detail in Chapter 4.

2.2 X-ray diffraction setups

X-ray diffraction experiments have been carried out on lab setup and using Synchrotron Radiation at European Synchrotron Radiation Facility (ESRF) in Grenoble (France). Despite different X-ray sources and optical configurations, unique notation of surface azimuths has been defined to study the effects of substrate misorientation on MT formation: the first azimuth (noted hereafter as “az1” or “az ϕ = 0”) with the incident X-ray beams onto the (001) plane is parallel to the [-1-10] direction, and the second azimuth (noted as “az2” or “az ϕ = 90”) with the incident beams parallel to the direction [-110].

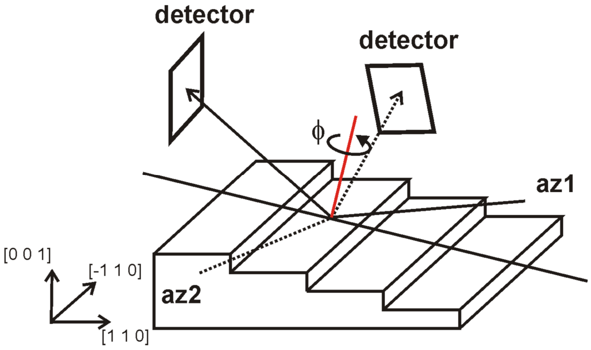

Figure 2.6 Notation of two azimuths: az1at ϕ=0° and az2 at ϕ=90°.

2.2.1 Laboratory X-ray diffraction

Laboratory X-ray diffraction experiments have been performed on a 4-circle Brucker D8 Diffractometer, at the Institut des Sciences Chimiques de Rennes of University of Rennes 1.

X-rays are generated from a Cu source and collimated by 1D Gobel Multi-layer Mirror placed on the linear focus window of a standard sealed tube. The feeding power is set at 40 kV/40 mA. Two different modes of this instrument have been applied for different type of measurements: a hith resolution mode and a low resolution mode.

Figure 2.7 illustrates the optical arrangement for the hith resolution mode. The source slit is placed at the exit of the source tube to reduce the horizontal width of the beam. A 4-

bounce Ge (022) asymmetric monochromator (Bartels) is used to reduce the divergence of the X-ray beam down to 0.008° and also to select the $K_{\alpha1}$ rays with a wavelength of 0.154056 nm. An Anti-scatter slit of 8 mm horizontal width and 15 mm vertical width, as well as a 2.5° Soller slits are used before the detector to reduce the background signal. The detector is a LynxEye^{TM}, 1 dimensional position sensitive detector (PSD) with 180 channels making a maximum of 13.5 mm in the horizontal direction (corresponding to a 2θ range of 2.6°).

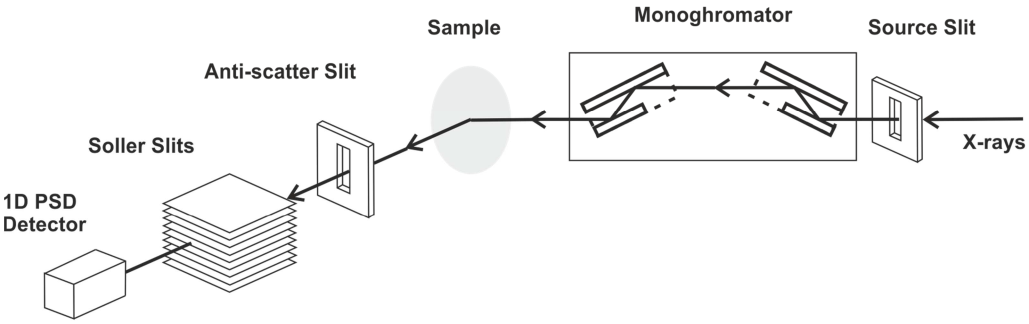

Figure 2.7 Optical arrangement for high resolution mode

Figure 2.8 represents the basic optical arrangement for low resolution mode. No monochromator is used, but instead, the beam size is limited in height and width to about 2×2 mm^2 by a cross slits system to produce a quasi-point beam and a Ni filter is placed before the detector to reduce the K_β pollution and to select the mean K_α rays with a wavelength of 0.154184 nm. In low resolution mode, the LynxEye detector is used in point detector mode, with an 8 mm width aperture in the horizontal direction and the full width aperture (about 15 mm) in the vertical direction.

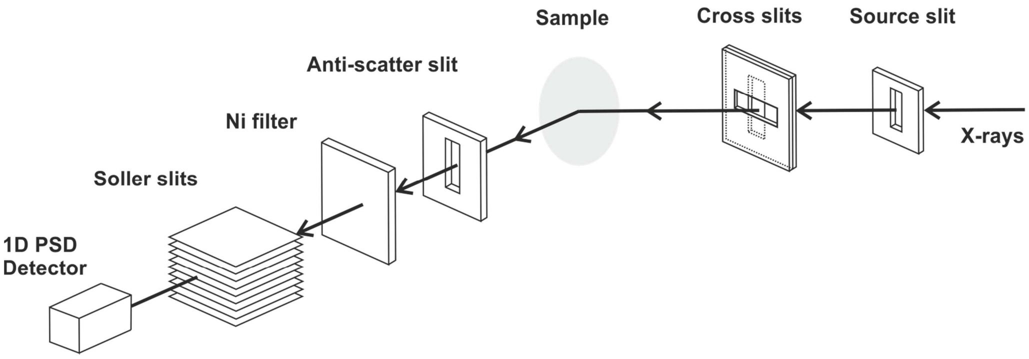

Figure 2.8 Optical arrangement for low resolution mode

The goniometer geometry is showed in Figure 2.9. The sample can be rotated around 3 circles and the detector can be rotated around 1 circle.

- Theta (θ): sample rotation around the vertical z axis, perpendicular to the incident beam which arrives from the direction x;
- Phi (ϕ): sample rotation around its normal
- Chi (χ): sample rotation around a horizontal axe, indicating the angle between the sample normal and the scattering plane (horizontal, and defined by Theta and 2Theta). The sample lies vertical at Chi=0° and horizontal at chi =90°.
- 2Theta (2θ): Detector arm rotation around the vertical z axe.

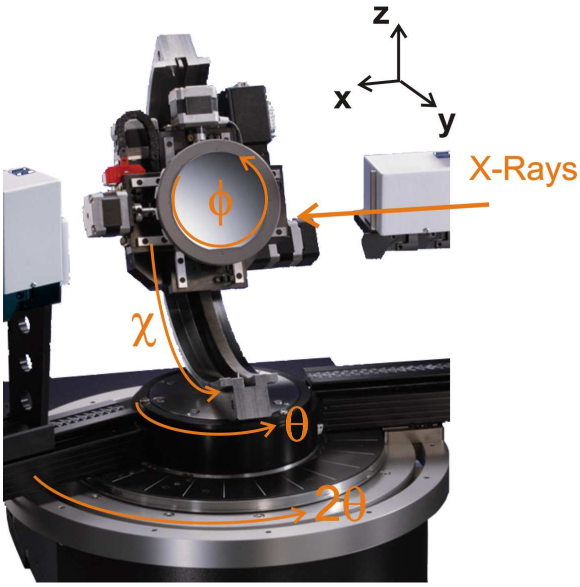

Figure 2.9 4-circle goniometer of the Brucker D8 Discover diffractometer with illustration of sample and detector motions

2.2.2 Synchrotron X-ray diffraction

Synchrotron X-ray diffraction experiments have been performed at BM02 - the D2AM French CRG Beamline. The beamline working energy is set at 16 keV, providing X-rays of wavelength 0.07749 nm, in order to reach the higher diffraction orders like 008 and 0010. Figure 2.10 presents the basic optic, consisting of a two crystal monochromator with sagittal focusing (mainly Si (111) but Si (311) is available), located between two cylindrically bent mirrors in a compact arrangement, with double focusing (3:1). The typical angular divergences are 3×10^{-4} rad at vertical direction and 3×10^{-3} rad at horizontal direction for a beam size of 3×30 mm^2 on the monochromator. The point focusing of the beam on the sample can be less than 0.3×0.3 mm^2.

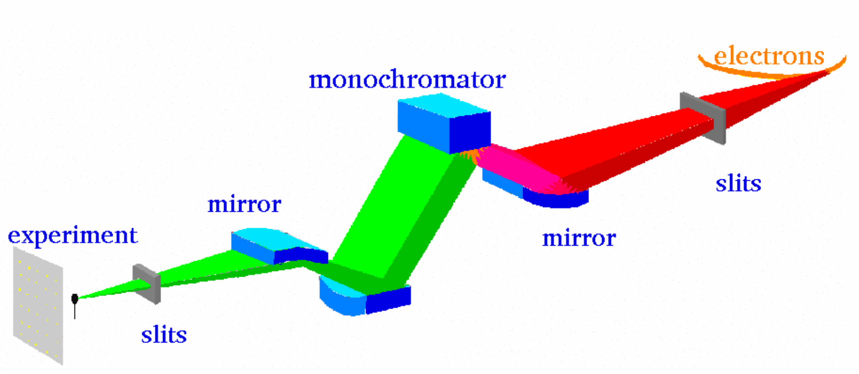

Figure 2.10 Sketch of the optic system on the BM02 - D2AM French CRG Beamline. Source: D2AM webpage

The beamline is equipped with a Kappa goniometer, allowing users to record data in and out of the polarization plane. Figure 2.11 gives a schematic representation of the goniometer overview. All the angular motions have a resolution lower than 0.001°, the confusion sphere being smaller than 50 µm.

The sample can be oriented through 4 circles of the instrument which can be defined both as physical axis or virtual Eulerian ones and the detection line uses 2 circles. The scattering plane is vertical.

- MU: sample rotation around a vertical axis (z).
- ETA: virtual eulerian angle: sample rotation around a horizontal axis perpendicular to the incident beam (y). Note that Tsz indicates the horizontal translation along y.
- CHI: virtual eulerian angle: sample rotation around x. The sample lies horizontal at chi=90 (its normal is z) and vertical at CHI=0 (its normal is then y).
- PHI: virtual eulerian angle: sample rotation around the sample normal. It is carried by CHI and ETA. At CHI=0, ETA and PHI axis are parallel and horizontal.
- KETA: physical rotation associated with ETA
- KPHI: physical rotation associated with PHI
- KAPP: physical rotation around the Kappa axis.
- NU: horizontal motion of the detector arm to allow measurement out of the polarization plane, its full use needs a special configuration of the experiment control program.
- DEL: vertical motion of the detector arm. It is carried by NU.

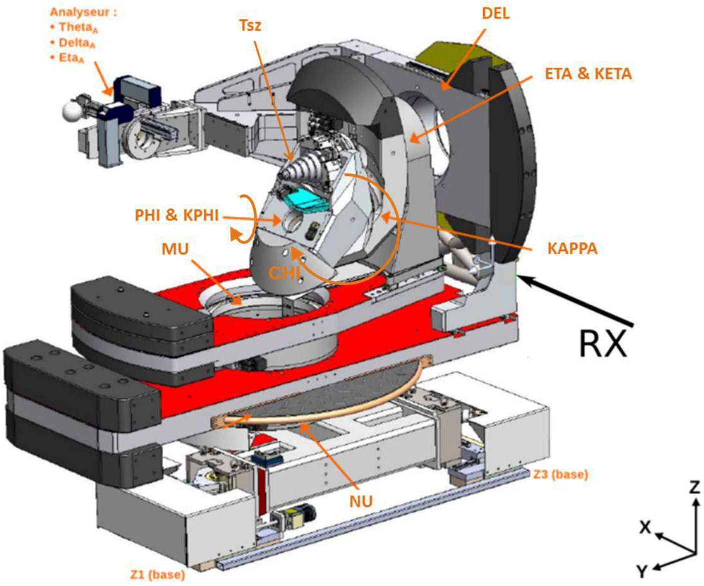

Figure 2.11 Sketch of the Kappa goniometer, at position CHI=0. The X-rays arrive from the direction parallel to x.

The detector used in this experiment is a XPAD3 hybrid pixel detector[102] designed with chips using IBM 0.25 μm technology. The wide Si detector is built with 8 modules, with each module consisting in 7 XPAD3 chips of 80×120 pixels. The pixel size is 130 ×130 μm^2. The counting rate is above 2×10^5 photons/pixel/s, corresponding to more than 2×10^7 photons/mm^2/s. The detector is combined with a pixel camera, allowing an acquisition of a reciprocal space images within only 300 seconds while it takes more than 5 hours on lab setup to acquire a similar image.

Figure 2.12 shows an initial image (on the GaP 004 reflection of a 45 nm-thin GaP/Si sample) taken on the detector. The whole image contains 1148 pixels in X direction and 576 pixels in Y direction. The transform of pixel to reciprocal space coordinate is necessary for appropriate data treatement. For example, one can use the following equations to convert X to the reciprocal space unit ΔS_x:

$$2\theta_{H=}\ actan((X-X_0)\cdot {}^{p}/_{D_{s-d}}) \qquad Eq.\ 2\text{–}2$$

$$\Delta S_x = 2sin\theta_H/\lambda \qquad Eq.\ 2\text{–}3$$

where θ_H is the angular difference between the detector center and the studied point, X the abscissa position of the studied point, X_0 the detector center abscissa, $D_{d\text{-}s}$ the distance between the detector and the sample center.

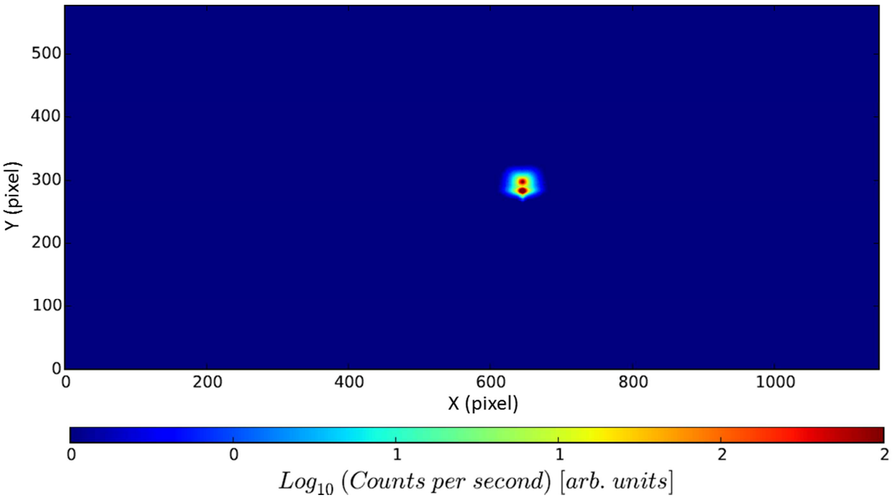

Figure 2.12 A typical initial image taken on the XPAD detector. This is an image on the GaP 004 reflection of a 45 nm-thin GaP/Si sample.

The detector to sample distance D_{d-s} is measured as following. Let's consider that the position (X,Y) of the incident beam spot moves vertically or horizontally with the motion of the detecter arm in vertical direction (DEL) or in horizontal direction (NU). By fixing a reference point O and taking several images on different DEL or NU positions, the D_{d-s} can be estimated as $D_{d-s} = {}^{d}/_{\tan(\delta)}$, where δ is the angular detector motion, and d the translation of the incident beam spot on the detector image, as illustrated in Figure 2.13.

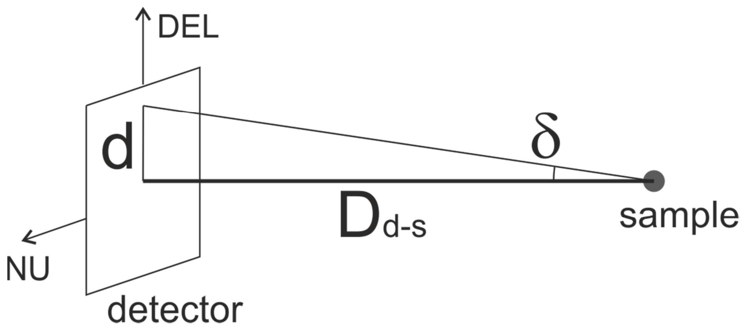

Figure 2.13 Illustration of the measurement of the distance between the detector and the sample center

2.3 Other analytical techniques

Complementary techniques such as Atomic Force Microscopy (AFM), Transmission Electron Microscopy (TEM), Scanning Transmission Electron Microscopy (STEM) and Scanning Tunneling Microscopy (STM) are used to give a complete characterization of sample structures.

2.3.1 AFM

AFM is a type of scanning probe microscopy. It is an important tool to study the sample’s surface morphology at a high resolution at the atomic scale. AFM operates in two basic modes: tapping mode and contact mode. The main difference is the manner of interaction between tip and the sample: repulsive force for contact mode, and alternation of repulsive and attractive forces for tapping mode. All of the measurements in this thesis have been performed on contact mode on a 2007 Veeco Innova AFM setup in laboratory FOTON-OHM, allowing 100×100 μm^2 images with maximum depth amplitude of about 6 µm.

2.3.2 TEM and STEM

TEM is a microscopy technique whose basic working principles are same as the optical microscopy but uses electron beams instead of light. The electron beams pass through the ultra-thin specimen, interact with the internal structure and are scattered by its crystallographic planes in diffraction conditions. An image is then constructed from the information contained in different electron waves, from which we distinguishe two imaging modes:

- Bright field (BF) mode deals with the transmitted direct beam (ie. weakened by the interaction with the specimen) selected by an aperture placed in the back focal plane of the objective lens. In this case, thick areas, heavy atoms and diffracting crystalline areas appear with dark contrast.
- Dark field (DF) mode deals with the scattered beams (or more properly diffracted beams since the scattering is coherent and elastic) selected by placing an aperture in the diffraction plane, the direct beam being blocked. Information on the planar defects or particle sizes can be extracted from the DF image.

Providing sensitive phase contrast, TEM has been widely employed for ex-situ analysis of crystal structures and defects. Moreover, since the wavelength of electrons controlled by acceleration energy is much shorter than the visible light, TEM may achieve resolution below 0.05 nm[103] at magnification of 50 million. This allows to examin the specimen at the atomic scale. The main disadvantage of TEM is that it requires burdensome sample preparation and heavy work in analysis of TEM images.

STEM is a type of TEM but uses a very small probe with focused electron beam to scan over the sample in a raster and the image is formed point by point. The two imaging modes are distinguished in the same way as in the TEM. However, the scattered beams in STEM are mostly incoherent and inelastic, and are selected depending on the angle with the direct beam. The High-Angle Annular Dark-Field (HAADF) imaging is a method which collects electrons of high scattering angle with an annular detector. This technique is highly sensitive to the atomic number of the atoms (Z-contrast) and hence gives information on the chemical composition of the specimen.

All TEM and STEM measurements in this work have been realized in collaboration with M. Bahri, G. Patriarche, L. Largeau at the Laboratoire de Photonique et Nanostructures (LPN) in Marcoussis, France, and

with A. Ponchet and J. Stodolna at the Centre d'Élaboration de Matériaux et d'Etudes Structurales (CEMES) in Toulouse, France.

2.3.3 STM

STM is also a microscopic imaging technique, working based on the quantum tunneling effect, usually made of tungsten. When the scanning probe is brought very close to the sample surface, the applied voltage allows the electrons to tunnel through the vacuum between the tip and the surface atoms, and to create tunneling current. The tunneling current is very sensitive to the distance between the tip and the sample. The surface morphology can be therefore recorded by keeping the probe at a constant height and measuring the variation of the current, or keeping the current constant and registering the probe height variation. The advantage of using STM is that it allows surface imaging at the atomic scale. The STM measurements presented in this thesis were performed in collaboration with S. Charbonnier and P. Turban at Institut de Physique de Rennes (IPR) in Rennes, France.

Chapter 3 Quantification of MT density for growth condition optimization

This chapter is dedicated to the development of methods to quantify the MT density using X-ray diffraction, aiming to improve the GaP/Si platform structural properties through the growth condition optimization. Firstly, a brief overview is given on previous synchrotron X-ray diffraction studies on non-optimized samples, displaying a high MT density. Then two methods are developed using an X-ray diffraction laboratory setup to, first, highlight the presence of MT and, second, quantify the MT volume fraction. These analyses, along with surface roughness measurements by AFM and TEM experiments, have allowed understanding the effect of the different growth parameters on the MT generation and, therefore, their successful elimination. Indeed, quasi MT-free GaP/Si pseudo-substrates have been obtained after growth optimization.

3.1 Previous MT study on non-optimized GaP/Si samples

The previous work on MT quantification was realized by Tra Thanh Nguyen during his thesis, in FOTON-OHM laboratory, and mainly based on synchrotron X-ray diffraction experiments.[104,105] Figure 3.1 is a detector image taken around the GaP 002 Reciprocal Lattice Node (RLN) for a sample of 20-nm-thin GaP/Si(001) 4°-off, with an exposure time of 300 seconds. The elongated spot corresponds to the reflection of MT-A. The integral widths deduced from cuts over the MT RLN in the longitudinal and transversal directions, as depicted by the dashed arrows in the figure, give correlation lengths of structural defects, uàsed to estimate the corresponding average MT sizes[105].

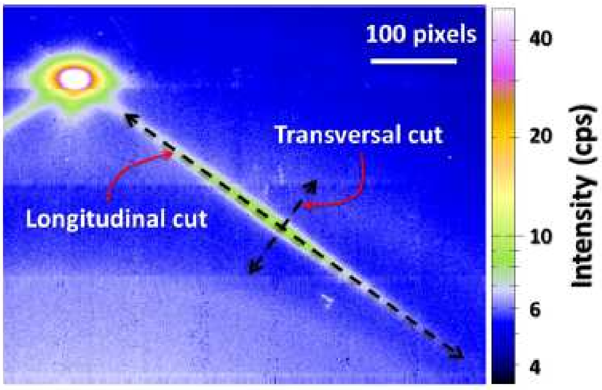

Figure 3.1 Evidence of MT reflection around the nominal GaP 002 reflection for a 20-nm-thin GaP/Si(001) 4°-off sample and illustration of correlation length measurement: longitudinal and transversal cuts through the MT streak are indicated by dashed lines with double sided arrows.

Moreover, for each variant, a series of 11 images have been captured at increasing ω value with a step size of 0.25°, leading to a ω scan around the center of the RLN ω_c. The step size is relatively large, in order to cover the thin and elongated MT spot. Figure 3.2 shows the ω scan images (detector imges) of MT-D for sample S1200, a 45-nm-thin GaP grown on Si(001) 6°-off (before growth parameter optimization). The intensity of MT RLN reaches the maximum at ω_c and keeps decreasing when the ω moves apart away from the center.

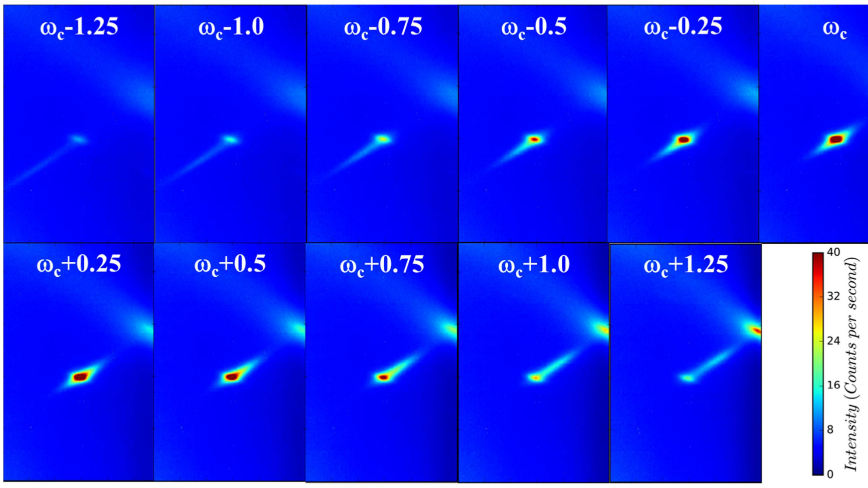

Figure 3.2 ω scan around the MT-D RLN of sample S1200, with a step size of 0.25°. The exposure time of each image is 20 seconds. The maximum intensity of the MT spot is seen at ω_C.

The integrated intensity of the MT RLN is considered to be proportional to the overall volume of MT inside GaP layer. Figure 3.3 a) shows the sum of the 11 images for every MT variant of S1200, so that the overall volume of the RLN is integrated. Strong reflection intensities are clearly evidenced on the 4 variants, indicating a high MT volume density. Anisotropy of MT intensities is observed, with MT-A the most intense, which could be attributed to the atomic steps on the substrate surface (see 3.4.1). Such non-optimized sample also displays rough surface (r.m.s. roughness = 7.1 nm) as measured by the 5×5 μm^2 AFM image in Figure 3.3 b). This roughness is correlated to the presence of a high density of emerging APBs, as described in the following chapter.

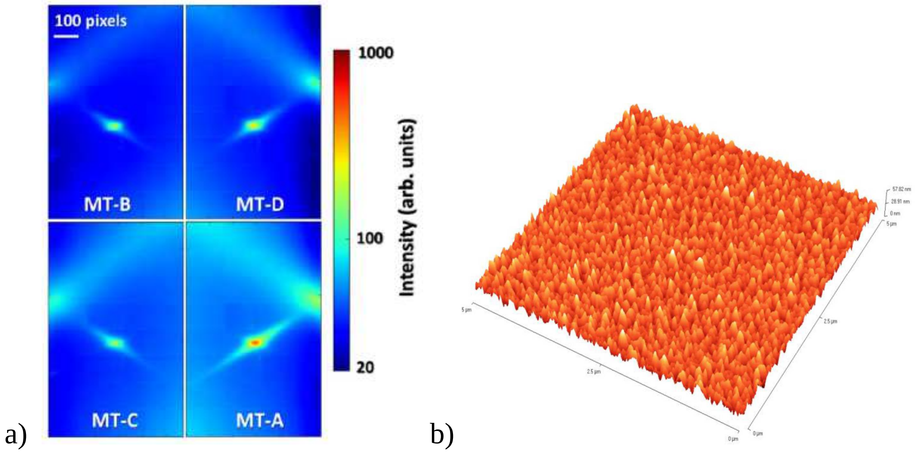

Figure 3.3 a) Sum of the 11 images for every MT variant of sample S1200 indicating high MT density, b) 5×5 μm^2 AFM image of the same sample, revealing a high surface roughness of 7.1 nm.

When comparing to laboratory X-ray experiments, synchrotron radiation has many advantages such as the possibility to vary the incident wavelength toward small ones that makes possible the study of higher diffraction orders like GaP 008 and GaP 0010, a very high brilliance suitable to visualize very low defect densities inside very thin samples, and rapid image acquisition within several minutes or even several seconds. For instance, these experiments have allowed us to study the very first stages of the GaP growth, at the level of the GaP/Si interface. Moreover, for practical reasons, and complementary to the synchrotron X-ray diffraction, we have developed new analytical methods for MT quantification using laboratory X-ray setup, in the light of the synchrotron analyses results.

3.2 Development of new quantification methods

3.2.1 Visualization and evaluation by pole figure method

a Performance of pole figure and visualization of MT

The pole figure method has been developed and already widely used to investigate the twin formation within epitaxial layers like YBaCuO/SrTiO$_3$(100)[106], InP/SrTiO$_3$[107], Ge/Si(001)[108], Si-C/Si(001)[109], epi-Si/Si(111)[110], and of course III-V/Si thin films.[73,111] Here we develop a new quantification method for MT density evaluation in the GaP/Si epilayers, using the pole figures. As described in Chapter 1 (Figure 1.14), the nominal GaP {111} planes are inclined by 54.7° from the (001) plane while the 4 MT variants planes are inclined by 15.9°. For GaP thicknesses below the critical one that is around 90 nm in the GaP/Si(001) case[69,72], we can consider that the GaP layers are fully strained when grown on the Si substrate. The principle of XRD pole figure method is to set the 2θ and ω angles to the strained GaP 111 Bragg position very close to the Si 111 position, especially since the detection angle of acceptance is large in the case of the pole figure experiments, allowing to harvest both the GaP 111 and Si 111 Bragg intensities at the same detector position. Then, the orientations of the (111) planes are determined by bringing them perpendicular to the scattering vector, using ϕ angular scans (polar angle) at successive χ values (sample inclination with respect to the incident X-ray beam), as depicted in Figure 1.18 c). The GaP and MT reflections are expected to be observed at χ around 54.7° and 15.9°, respectively, for samples grown on nominal Si(001) substrate.

Pole figures are performed on the D8 discover diffractometer using low resolution mode (see section 2.2.1 for optics and goniometer setup), with a beam sized 2×2 mm^2 and the detector widely opened in the out-of-plane direction, in order to integrate the maximum of the broadened MT signal. The sample's orientation is initially set at the azimuthal direction opposite to “az1”, with the incident X-ray beams parallel to the [110] direction.

Figure 3.4 a) shows a typical 111 pole figure taken for GaP thin layer grown on a nominal Si(001) substrate (that is, the (001) direction is the substrate surface normal). The pole figure is drawn using the ϕ and χ polar coordinates, such that ϕ represents the polar angle and χ the radial distance from the origin. The MT variants are observed on the pole figure around χ = 16°. The four spots near χ = 55° correspond to the GaP 111 nominal reflections. Actually, the low resolution XRD doesn’t allow separating the GaP and Si reflections, thus the diffracted intensity evidenced in the figure comes mainly from the Si substrate due to its far higher effective scattering volume as compared with the GaP thin layer. Figure 3.4 b) shows the pole figure for sample S1189, GaP layer grown on vicinal Si(001) 6°-off substrate. Due to the 6° misorientation, the MT-A and MT-C, as well as the corresponding 111 nominal reflections are shifted in χ by ± 6°, while a ϕ shift and MT reflections distortion are observed on MT-B and MT-D.

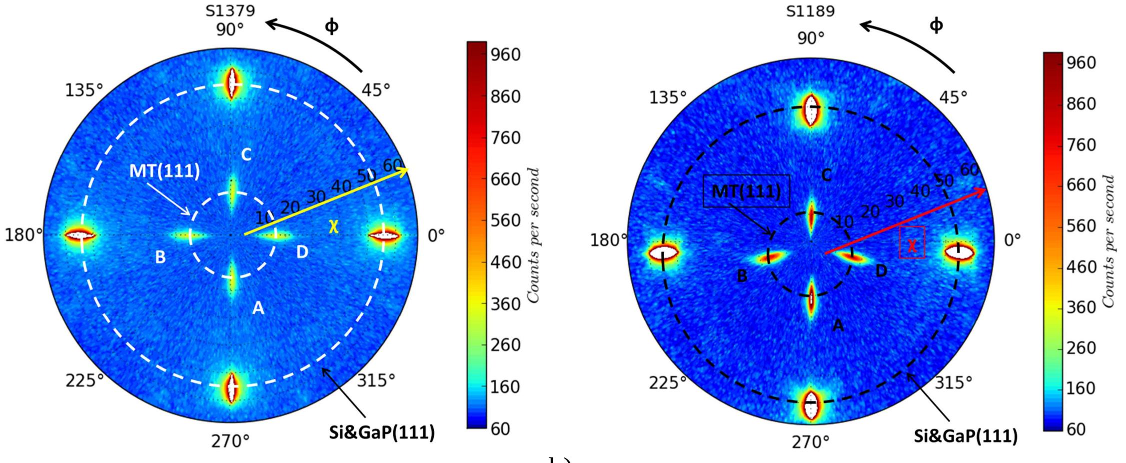

a) b)

Figure 3.4 Typical 111 pole figure for GaP/Si: a) on nominal Si(001) substrate, b) on vicinal Si(001) substrate misoriented of 6° towards the [110] direction

The pole figure intensity is normalized taking into account the intensity of the incident beam I_0. The integrated intensity of the MT spot (I_{MT}) is considered to be directly proportional to the MT volume in the GaP layer. The pole figure provides a visualization of MT volume level, thus permitting a rapid and qualitative comparison between samples of same thickness. For quantitative comparison or comparison between different thicknesses, quantification should be carried out, as described below.

b Quantification of MT density

We represent the pole figure in Cartesian coordinate system for easier integration, with ϕ as axis x and χ axis y, as shown in Figure 3.5. Two rectangular Regions of Interest (ROI) are defined around the reflection spot, to measure the mean background signal per pixel I_b and the MT intensity I_{MT}:

$$I_b = (I_2 - I_1)/(A_2 - A_1), \qquad \textit{Eq. 3–1}$$

$$I_{MT} = I_1 - A_1 \cdot I_b \,. \qquad \textit{Eq. 3–2}$$

where I_1 and I_2 are the total integrated intensity in the ROI, A_1 and A_2 the area of the two ROI. The ROI size must be carefully chosen, since too smaller regions don't permit the total integration of the MT signals and too large regions lead to an overvaluation of MT density as a result of integrating too large background signals (See Appendix A1). Indeed, the background signals should be carefully substracted before doing the integration.

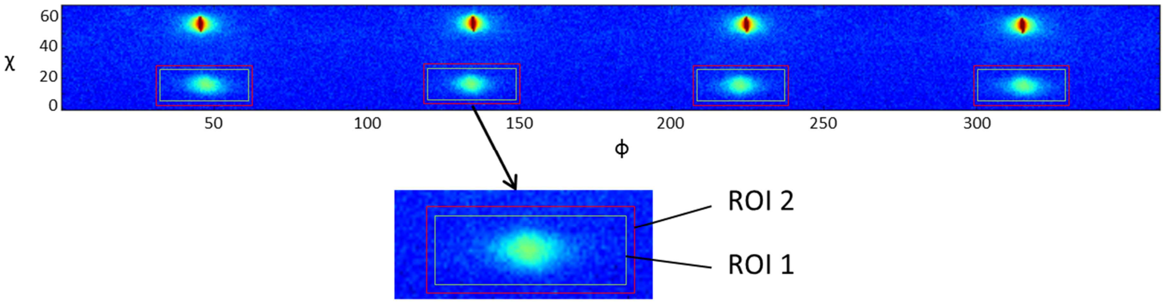

Figure 3.5 Illustration of ROI definition and MT intensity integration on the pole figure

The I_{MT} (normalized so that without unit) is indeed neither the intensity initially scattered by the MTs, nor the MT volume density. It can be seen as a merit factor directly proportional to the MT volume fraction. Figure 3.6 a) shows the I_{MT} measured from the pole figures for three non-optimized samples grown on Si(001) 6°-off substrate, using conventional MBE mode with a first 10-nm-thin layer grown at 350 °C followed by a 35-nm-thin layer grown at 500°C. The difference lies in the growth of a prelayer prior to the GaP growth: a Ga prelayer without Si buffer layer for S1200, a Si buffer layer followed by the Ga deposition for S1180, and a Si buffer layer followed by the P deposition for S1189. Figure 3.6 b) shows the quantification by synchrotron images for the same samples, referenced from the thesis of Tra Thanh Nguyen.[86]

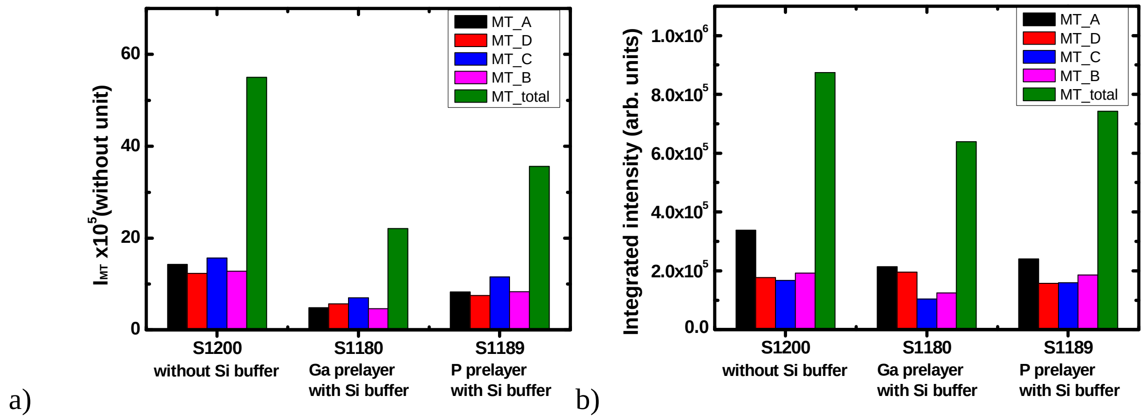

Figure 3.6 Measurement of MT intensity by a) laboratory pole figure (without correction) and b) synchrotron images, for samples S1200, S1180 and S1189.

One can find that the integrated intensity of MT reflection spots from both pole figures and synchrotron images provide an estimation of the total MT volume density and the same results remain when comparing the three samples: S1200>S1189>S1180. However, the anisotropy characteristics (relationship between variants) are not the same. Indeed, it has been reported in our previous work[59] and also by Skibitzki et al[73] that the MT densities in GaP layers grown on such vicinal Si substrate represent an anisotropy of A>C>B≈D. Indeed, this anisotropic phenomenon in GaP layers grown on vicinal substrate is due to the effect of the atomic steps, which will be discussed in the section 3.4.1. The synchrotron quantification (and also the rocking-curves that will be presented in the next part) shows a stronger intensity on MT-A than on MT-C, being consistent with the literature, while the pole figure quantification shows the contrast.

Two factors should be taken into consideration to correctly use the pole figures for MT density quantification. First, the layer thickness along with the incident and emergent beam angles determines the effective scattering volume, that is to say, the MT intensities measured on different variants correspond to different volumes of GaP layer. Second, the pole figures are not well centered due to the 6 degrees' miscut, so that the ϕ scans' linear speeds are not the same on the 4 MT variants that are located at different χ positions. As shown in Figure 3.7, the spot of MT-A is much smaller than that of MT-C, while in a nominal sample shown in Figure 3.5 the 4 MT spots exhibit the same shape. This indicates a signal loss on MT-A, since the scan over MT-A at χ=22° is 2.2 times much faster than that over the MT-C at χ=10°.

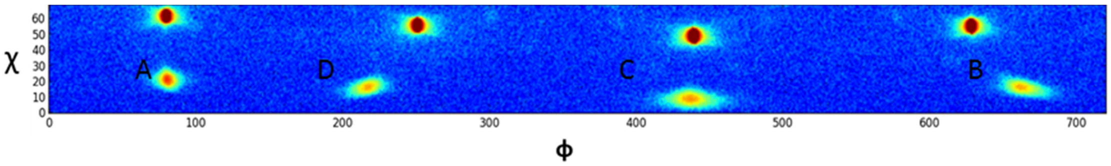

Figure 3.7 Pole figure represented in Cartesian coordinate system for GaP layer grown on vicinal Si substrate (S1189). The diffraction spot of MT-A is much smaller than the others, indicating a loss of signal due to the higher scan speed.

In the following, a more precise and reliable quantification method using rocking-curve measurements performed on each diffraction peak variant is described. Then corrections on pole figure quantification will also be presented.

3.2.2 Quantification by rocking-curve method

This method based on rocking-curve (RC) measurements also uses the low resolution diffraction setup. Indeed, rocking-curve scans have been carried out on, first, the four MT variants and, second, the nominal GaP 002 reflection, to quantitatively evaluate the absolute volume fractions of respectively MT and nominal GaP (See Appendix A2 for experimental details). Figure 3.8 shows an example of the RC scans performed on the MT variants of the sample S1180.

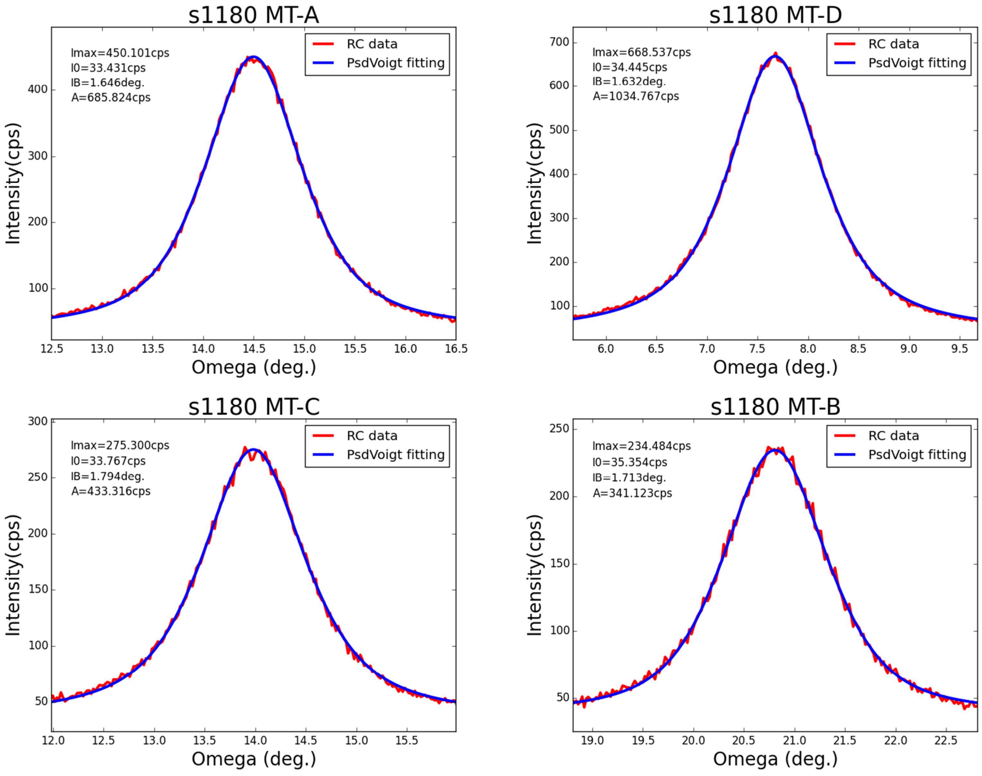

Figure 3.8 Rocking-curve scans on 4 MT variants of S1180 fitted with a Pseudo-Voigt function, for extraction of I_{max}, I_{bg} (“I0” in the figures), and IB.

The RC scan profiles are fitted by a Pseudo-Voigt function and the experimental integrated intensity (in counts) diffracted by MT or GaP of nominal orientation is measured from:

$$I_{int,exp} = (I_{max} - I_{bg}) \times (\frac{IB}{step\ size} \times step\ time)\ , \qquad \text{Eq. 3–3}$$

where I_{max} is the maximum measured intensity, I_{bg} is the average background intensity, IB is the integral breadth of the profile, step size is the scan increment and step time is the acquisition time for each scan step.

Next, the theoretical integrated intensity diffracted by a small single crystal rotated around the Bragg position can be calculated by the following equation, when absorption is neglected, as explained by B.E.Warren [112]:

$$I_{int,theo} = \frac{\Phi_0}{\dot{\omega}} r_0^2 \frac{V\lambda^3 F_T^2}{v_a^2} PL\ , \qquad Eq.\ 3\text{–}4$$

where Φ_0 is the intensity of the incident beam in counts/(second × unit area), $\dot{\omega}$ is the constant angular velocity of the crystal rotation, r_0 is the classical radius of electron and r_0^2 the scattering cross section of electron, V is the volume of the crystal, λ is the incident X-ray wavelength, v_a is the crystal unit cell volume, F_T^2 is unit cell structure factor taking into account the Debye-Waller factor, and PL is the Lorentz-polarization factor.

Then we consider the real case of an X-ray beam scattered by a monocrystalline thin layer sample, as shown in Figure 3.9.

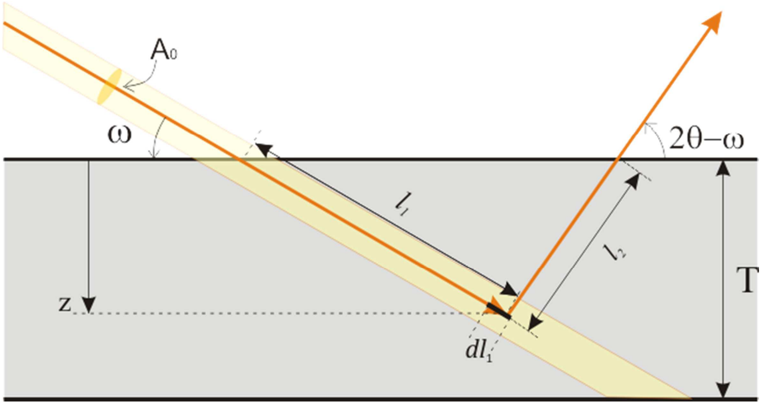

Figure 3.9 Sketch of effective scattering volume in a thin layer, with I_0 and A_0 the intensity and cross section of the incident X-ray beam, ω and 2θ–ω the incident and emergent angle and T the layer thickness.

We define I_0 and A_0 as the intensity and cross section of the incident X-ray beam, ω and (2θ–ω) as the incident and emergent angle, and T as the thickness of the thin layer.

The fact that the flux density reduces due to absorption before and after the elastic Bragg scattering gives rise to the effective scattering volume, i.e. V.

According to the Beer-Lambert law, the intensity diffracted by the elementary crystal volume $dV = dl_1 \times A_0$ located at a depth of z can be expressed by the following equation:

$$dI \propto I_0 e^{-\mu(l_1+l_2)} dV = I_0 e^{-\mu\left(\frac{z}{sin(\omega)}+\frac{z}{sin(2\theta-\omega)}\right)} A_0 \frac{dz}{sin(\omega)}, \qquad Eq.\ 3\text{–}5$$

Where l_1 and l_2 are the lengths of X-ray path and μ is the linear attenuation coefficient of the material. The integration of the equation on dz through T leads to the effective scattering volume of the crystal V:

$$V = A_0 \frac{sin(2\theta-\omega)}{\mu\,(sin\,\omega + sin(2\theta-\omega))}\left(1 - e^{-\mu T\left(\frac{1}{sin\,\omega}+\frac{1}{sin(2\theta-\omega)}\right)}\right). \qquad Eq.\ 3\text{–}6$$

In our study, the beam could be considered as unpolarized without the use of monochromator, the Lorentz-polarization factor is assumed to be $PL = \frac{1+\cos^2 2\theta}{2\sin 2\theta}$. Warren has detailed the calculation of F_T and we have applied the approximation of Kushwaha[113] for the Debye-Waller factor. These Debye-Waller corrections are indeed very small on 111 and 002 reflections (with a Debye-Waller factor between 0.970 and 0.985). This brings advantages for using these low angle reflections: for the MT evaluation, the 222 has a low unit cell structure factor that make the peak less intense, and 333 presents a much higher Debye-Waller factor correction; in the evaluation of GaP of nominal orientation, it is difficult to correctly integrate the 004 due to the Si substrate contribution and its thermal diffuse scattering (TDS) contribution (see APD study in Section 4.1.2) and the 006 is also less intense and affected by a larger Debye-Waller correction.

The final equation to calculate the theoretical diffracted intensity becomes:

$$I_{int,theo} = \frac{\Phi_0}{\dot{\omega}}\frac{A_0}{\mu}\frac{sin(2\theta-\omega)}{(sin\,\omega + sin(2\theta-\omega))}\left(1 - e^{-\mu T\left(\frac{1}{sin\,\omega}+\frac{1}{sin(2\theta-\omega)}\right)}\right) r_0^2 \frac{\lambda^3 F_T^2}{v_a^2}\frac{1+cos^2 2\theta}{2\,sin\,2\theta} Eq.\ 3\text{–}7$$

Finally, the $I_{int,exp}$ / $I_{int,theo}$ ratio is used to estimate the volume fraction of either one MT variant or the GaP of nominal orientation.

In ideal case, the total of these volume fractions should be 100%. Table 3.1 shows the rocking-curve quantification results on three samples: S1319, a 45-nm-thin GaP layer grown by MEE at 350°C, presenting very low MT density, and the previously introduced S1189 and S1180 with a very high MT density. The relative errors originate mainly from the fluctuation of the incident beam intensity during the experiment (of about ±10%).

Table 3.1 Volume fractions of MT variants and the GaP of nominal orientation (NO) measured from the rocking-curve scans for S1319, S1189 and S1180.

Sample	MT-A (%)	MT-D (%)	MT-C (%)	MT-B (%)	MT-S (%)	NO (%)	NO + MT-S (%)
S1319	0.4	0.2	0.3	0.4	1.3±1.0	110.3±12.1	111.6±13.1
S1189	7.8	5.3	5.2	6.4	24.6±2.5	69.2±7	93.8±10
S1180	4.6	3.8	3.0	3.4	14.8±1.6	62.1±7	76.91±9

These measurements lead to a total near the expected 100%, varying from 76.91±9% to 111.6±13%, and is less than 100% for samples of higher MT density (S1189 and S1180) while greater than 100% for S1319. Several phenomena may lead to such disagreements. Firstly, the very small intercrossing MT (especially in the case of high MT density, as evidenced in the cross-sectional STEM-bright field image in Figure 3.10) which is difficult to integrate correctly with a limited area point detector may lead to underestimate the MT volume fraction. Moreover, the presence of APDs (usual case in samples with high MT density), producing a strong effect on the broadening of the GaP 002 reflection that is only partially integrated (see Chapter 4 for detailed explanation), leads to an underestimation of the GaP of nominal orientation. These factors contribute to a sum lower than 100%. Contrarily, atoms located at boundaries of the MT and the GaP of nominal orientation are counted twince since they contribute both to the GaP and to the MT variants. This may yield to a total volume fraction higher than 100%. Thus, a more systematic study should be carried out to evaluate the sources of discrepancies.

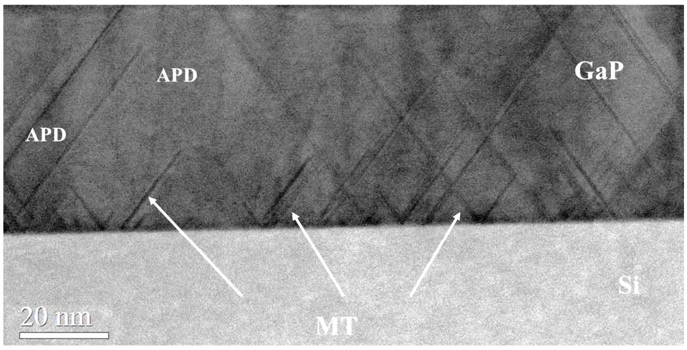

Figure 3.10 Cross-sectional STEM image evidencing the presence of intercrossing MTs in a sample with high MT density. (LPN)

3.2.3 Correction of pole figure quantification

Firstly, the MT intensities I_{MT} for each variant measured on the pole figure have been corrected with respect to the effective scattering volume calculated using Equation 3-6. This type of correction factors is constant for samples of same thickness. Then, considering that the rocking-curve method which takes into account the layer thickness, the effective scattering volume, the Debye-Waller factor, the Lorentz-polarization factor, etc, is accurate and reliable, another type of correction factors is deduced by comparing the quantifications from the pole figures (PF) to the rocking-curves (RC). Table 3.2 shows the calculation of the RC/PF ratios, based on three samples presenting large MT densities: S1180, S1189 and S1200, for which the measurements are more precise than other samples. The difference on the ratio RC/PF for different MT variant originates basically from the incident angle difference, and the slight difference on the same MT variant for different samples may come from the experimental adjustement. Then an average value is obtained for each variant, regarded as the correction factor that will be applied hereafter on all the samples quantified by the pole figure method. Indeed, the relative errors of about ±10% due to the fluctuation of the incident beam intensity are excluded in the table for clarity, since it doesn't affect the ratio RC/PF. After correction, all samples show an anisotropy of A > C.

Table 3.2 Calculation of the second type of correction factors for pole figure quantification, according to the rocking-curves. The final correction factors are the average RC/PF ratio of the three samples. Notice that all the values of PF quantification in the table are 10^5 times the original values, for easier representation.

Sample	S1180			S1189			S1200			
	PF	RC	RC/PF	PF	RC	RC/PF	PF	RC	RC/PF	**Corr. factor**
MT-A	4.83	4.6	**0.952**	8.25	7.8	**0.945**	14.22	13.1	**0.921**	**0.940**
MT-C	7.42	3.0	**0.404**	12.24	5.2	**0.425**	16.66	7.5	**0.451**	**0.427**
MT-B	4.76	3.4	**0.714**	8.64	6.4	**0.741**	13.29	9.5	**0.713**	**0.723**
MT-D	5.85	3.8	**0.650**	7.75	5.3	**0.684**	12.73	8.5	**0.667**	**0.667**

To summarize, two methods have been developed both using a lab XRD setup on low resolution mode. The pole figures allow a rapid visualization of the presence of MT, as well as quantification of MT density after corrections. The rocking-curve method is more accurate and leads an absolute quantification of the MT volume fraction in the thin GaP layer. The detection limit of the apparatus for both methods is estimated about 1.0 % in a 45-nm-thin GaP layers. Althouth it takes 14 hours to acquire a pole figure while the acquisition time reduces to about 6 hours for the RC method, the pole figure is more frequently used in the thesis, since on the one hand, it is very simple to carry out, requiring only a rough alignment of the z position (in the direction perpendicular to the sample surface), and on the other hand, it gives rapid feedback for comparison of the samples and then the optimization of the growth conditions.

3.3 Growth condition optimization towards the elimination of MT: application of the MT quantification methods

MT elimination is a key issue for the use of the GaP/Si pseudo-substrate as an appropriate platform for optoelectronic devices on silicon substrate, either lasers or photovoltaics, and is one of the main objects of this thesis work. In this part, I will describe the work on the growth parameter improvement thanks to the use of the MT quantification methods. Indeed, we have successfully improved the GaP/Si structural characteristics, in particular at the GaP/Si interface and at the GaP surface.

It has been demonstrated in previous work of the laboratory that the use of a Ga prelayer instead of a P prelayer leads to a reduction of the MT density.[86,114] Indeed, as argued by Grassman et al,[53] the use of Ga prelayer prevents the surface roughening caused by P and Si reaction.[115,116] In fact, the P deposited directly onto the Si surface forms Si-P heterodimers that will replace the Si-dimers, so that the Si surface atoms become adatoms incorporated into the GaP epitaxial layer during the growth, leading to a diffuse interface and then a rough epilayer surface.[117] Therefore, all the samples studied in my thesis are grown with a Ga prelayer. A first series of 45 nm GaP/Si 6°-off samples grown by MBE at different temperatures will be investigated to show the influence of this parameter on the surface roughness and MT formation. Secondly, the growth rate influence on the MT density will be studied. Then, I will show that a two-step procedure consisting of MEE technique at lower temperature followed by conventional MBE at higher temperature leads to a dramatic improvement of the structural properties. Finally, quasi free-of-MTs GaP layers with smooth surface are successfully achieved by applying all optimized parameters. Table 3.3 lists all the samples to be discussed in this Chapter, with the detail of their growth conditions.

Table 3.3 Samples studied in this chapter, with their detailed growth conditions. The common parameters such as Ga prelayer (otherwise mentioned) and substrate of Si(001) 6°-off are not shown in the table for clarity.

Sample	Thickness, mode, and temperature	Growth rates and Fluxes
S1180	(Si buffer layer) + 5 nm GaP by MBE at 350°C + 40 nm GaP by MBE at 480°C	Rate: 0.1 ML/s. Ga flux: $1.4\ 10^{-7}$ torr P flux: ~ $4\ 10^{-6}$ torr
S1189	(P prelayer) + 5 nm GaP by MBE at 350°C + 40 nm GaP by MBE at 480°C	
S1200	5 nm GaP by MBE at 350°C + 40 nm GaP by MBE at 480°C	
S1254	45 nm GaP by MBE at 350°C	Rate: 0.1 ML/s. Ga flux : 1.1×10^{-7}Torr, P flux :~ 10^{-6}Torr.
S1255	45 nm GaP by MBE at 400°C	
S1256	45 nm GaP by MBE at 450°C	
S1264	45 nm GaP by MBE at 500°C	
S1265	45 nm GaP by MBE at 550°C	
S1266	45 nm GaP by MBE at 600°C	
S1319	45 nm GaP by MEE at 350°C	Rate: 0.1 ML/sec. Ga amount per cycle: 0.9 ML Ga flux : 2.1×10^{-7}, P flux :~ 4.510^{-6}.
S1330	10 nm GaP by MEE at 350°C + 35 nm GaP by MBE at 500°C	For MEE: Rate : 0.1 ML/sec. Ga amount per cycle: 0.9 ML. For MBE: Rate: 0.2 ML/sec. Ga flux : 2.3×10^{-7}Torr, P flux :1.1×10^{-6}Torr.

3.3.1 Growth temperature

In this part, I report the study of S1254, S1255, S1256, S1264, S1265 and S1266, i.e. the 45-nm-thin GaP thin layers grown on Si(001) 6°-off substrate by conventional MBE technique at respectively 350°C, 400°C, 450°C, 500°C, 550°C and 600°C. Firstly XRD experiments including pole figures, $\omega/2\theta$ scans and ω scans are presented to show the influence of growth temperature on the structural quality of the GaP epilayer. Then a discussion on MT formation mechanism is given, related to the growth conditions.

a Reduction of MT density at higher growth temperature

In the XRD pole figures, the GaP layers grown at low temperature (< 500°C) present strong MT intensity while a dramatic reduction of MT intensity is observed for samples grown at temperatures higher than 500°C (Figure 3.11).

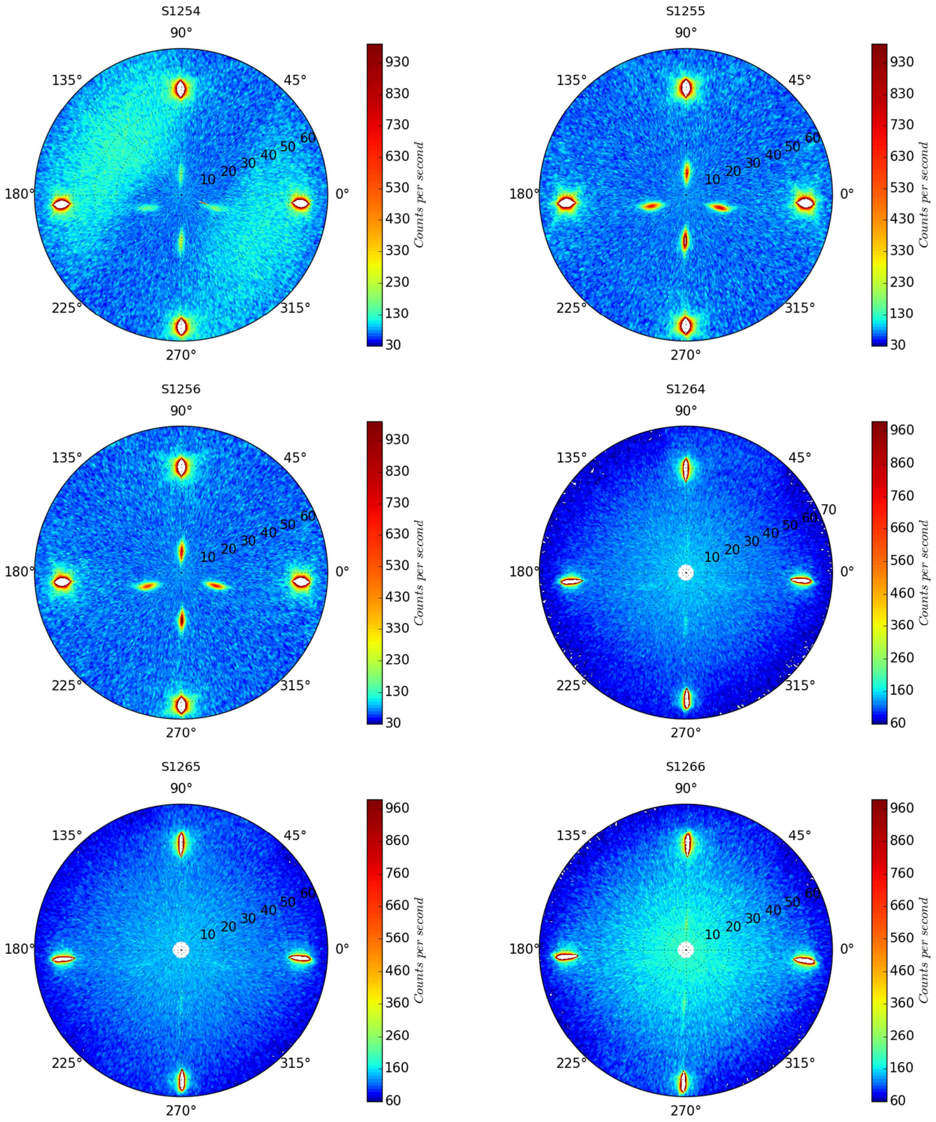

Figure 3.11 Pole figures on the 45-nm-thin GaP thin layers grown by MBE on Si(001) 6°-off at increasing temperatures, revealing a high intensity of MT reflections for samples grown below 500°C (S1254, S1255 and S1256) and a dramatic reduction of MT intensity for those grown above 500°C (S1264, S1265 and S1266).

Let us notice that the pole figure intensities are normalized with I_0. In Figure 3.11, the discrepancy between the signal-to-noise ratios is due to an optimization of this parameter for some samples (See Appendix A3 for details). Indeed, a part of the samples were analyzed after this improvement. However, this discrepancy does not jeopardize the following conclusions.

The MT volume fractions quantified from the pole figures for each variant of the samples have been corrected using the correction factors, and are shown in Figure 3.12. The total corrected volume fraction for theses samples are respectively 3.0%, 17.3%, 13.9%, 1.1%, 1.0%, and 1.4%. Samples grown at 400°C and 450°C present the highest MT density, and a dramatic reduction of MT density is seen when the growth temperature is increased above 500°C. The MT density anisotropy of MT-A > MT-C is observed on all samples.

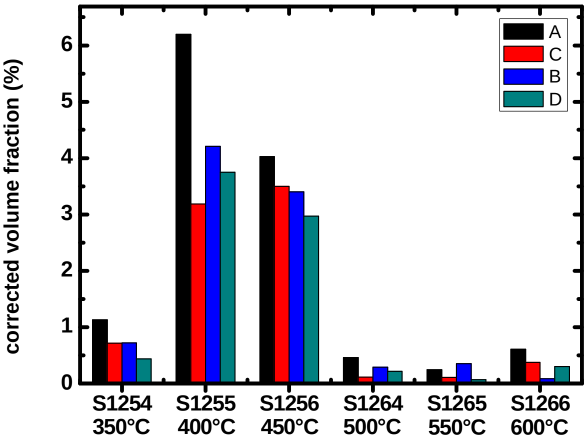

Figure 3.12 Corrected volume fractions of MT variants measured by pole figures, on samples grown by MBE at increasing temperatures, revealing a dramatic reduction of MT density at higher growth temperatures.

Assuming a thermally activated process following the Arrhenius law, the total MT density as a function of the growth temperature could be fitted with the following equation:

$$I(T) = I_0 - C \cdot exp\left(-\frac{E_a}{k_B T}\right), \qquad Eq. 3\text{–}8$$

Or equivalently:

$$ln\left(I_0 - I(T)\right) = lnC - \frac{E_a}{k_B T}, \qquad Eq. 3\text{–}9$$

where I_0 represents the volume fraction extrapolated at 0 K, C is a prefactor and E_a the activation energy of the growth mechanism considered.

Taking into consideration that the MT density for the sample grown at 350°C unexpectedly doesn't follow this relationship, and by assuming that from 500°C the MT density remains very low and constant, the activation energy is obtained only based on the samples grown at 400°C, 450°C, and 500°C. Firstly I_0 is estimated around 17, through the interpolation of the I(T) curve towards 0. Then a manual adjustment was performed to evaluate I_0, in order to make the curve $ln(I_0 - I(T))$ vesus (*1/T*) the most aligned and we find I_0 = 16.9. Figure 3.13 shows the plot of $ln(16.9 - I(T))$ as a function of (*1/T*) and the linear fit from which C and E_a are deduced to be respectively 1.17×10^5 and 0.697 eV. This value is in the range of the values usually measured for Ga adatom surface diffusion.[118] Indeed, the activation energy should drastically depend on the step edge density and on the exact configuration of the surface. Thus, a more systematic study should be carried out on different vicinal and nominal Si surfaces.

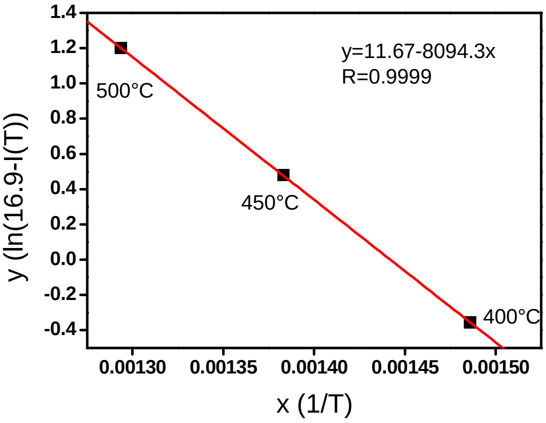

Figure 3.13 Total corrected volume fraction measured on pole figures for the samples grown at 400°c, 450°C and 500°C, as a function of the growth temperature. Linear Arrhenius fitting (red solid line) has found an activation energy E_a=0.697 eV.

Moreover, the overall crystalline quality of the GaP thin layer is improved at high temperature (above 500°C), as shown both by the XRD $\omega/2\theta$ scan analyses and the ω scans (Figure 3.14 a) and Figure 3.15). These scans are performed on the laboratory D8 diffractometer on hith resolution mode, using the copper wavelength (0.15406 nm).

Taking into account the wavelength and the GaP lattice constant in theoretical and fully strained cases (0.54506 nm and 0.54670 nm, respectively, as calculated in Chapter 1), the corresponding GaP 004 positions expressed on the diffraction vector modulus ***S*** are calculated to be 7.317 nm^{-1} and 7.339 nm^{-1}. At 500°C and higher temperatures, $\omega/2\theta$ scans (Figure 3.14 a)) display well-defined diffraction peak with a width limited by the layer thickness and not by the defect density. Besides, thickness fringes are also observed which is characteristic of a coherence length of the diffraction planes from the GaP/Si interface to the GaP surface. The GaP peaks are shifted to the left side (extra fully strained positions). This shift can originate from the experimental adjustment and is generally existent in the GaP/Si heterosystem with a 6° miscut along the [110] direction.

Assuming that $S_{//}$ and $S_{\perp}$ represent respectively the directions parallel and normal to the sample surface, the Si 004 RELP is located along the crystallographic [001] direction that is tilted of 6° with respect to the $S_{\perp}$, as depicted in Figure 3.14 b). Fully strained GaP, having the same lattice constant in the lateral direction as Si, is found below the Si 004 at the same $S_{//}$ position, while the relaxed GaP is located along the [001] direction. The GaP center positions for the ω/2θ scans were determined by doing a ω/2θ scan passing through the Si peak center. Possible shifts may be introduced during this procedure. In fact, RSMs are needed to tell the exact strain status of the GaP layer. For samples grown at lower temperature, the GaP layers are partially relaxed. In this case, broad and very weak GaP peaks are observed, which are signature of poor GaP layer structural quality.

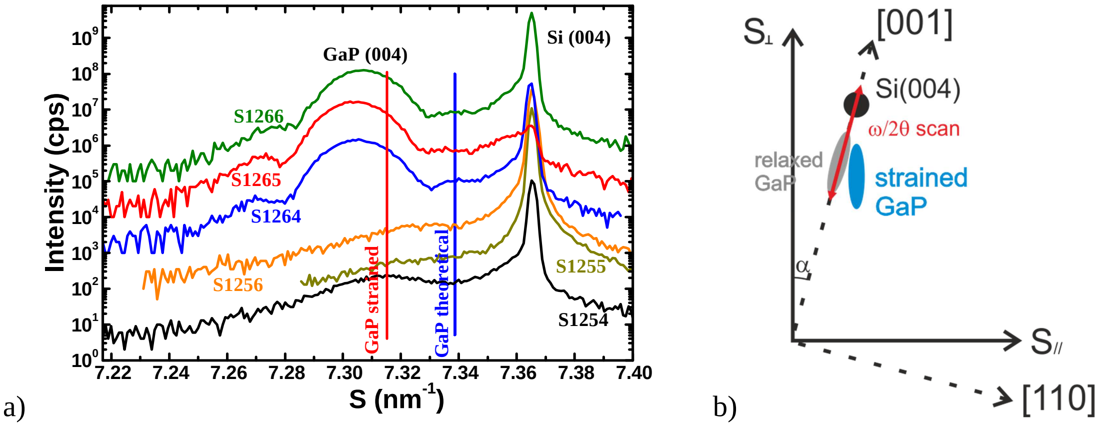

Figure 3.14 a) ω/2θ scans around the GaP 004 reflection for this series of samples: The vertical red line and blue line indicate the reciprocal space positions of the fully strained GaP and the theoretical one, respectively, b) illustration of RLN positions of the strained and relaxed GaP layer, with respect to the Si substrate.

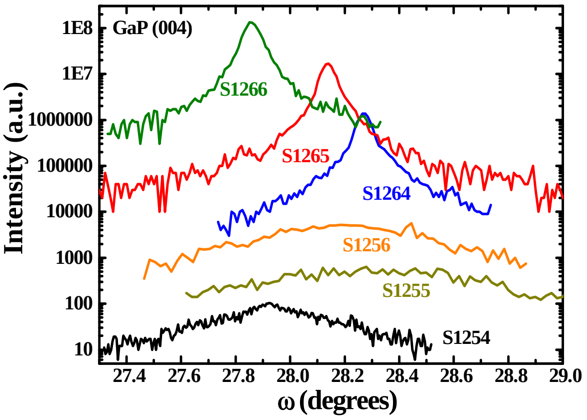

Figure 3.15 ω scans around GaP 004, with thinner peaks for the samples grown at higher temperature, indicating smaller lattice misorientation and defect density in the lateral direction.

In addition, as shown in Figure 3.15, the ω scan (or transverse-scan since the detector was opened at 0.375 nm with a very small angle of acceptance) profiles are thinner at high temperatures, indicating a smaller distribution of the lattice misorientation ("tilt", as introduced in Chapter 1) and smaller defect density in the lateral direction.

In brief, all the XRD measurements (pole figures, ω/2θ scans and ω scans) demonstrate better structural qualities for GaP/Si layers grown at higher temperatures.

However, higher growth temperature leads to a higher surface roughness. The r.m.s. roughness measured on 5×5 µm^2 AFM image is about 2.06 nm for S1254 grown at 350°C while up to 5.70 for S1266 when the growth temperature reaches 600°C (Figure 3.16). The acceptable roughness of the GaP/Si platform is considered to be of the order of 1 nm. The high surface roughness of the GaP/Si platform is detrimental for optoelectronic device applications since it makes the GaP/Si platform unsuitable for subsequent overgrowth of other III-V semiconductors, it is therefore of great importance to choose appropriate growth parameters to fulfill simultaneously the conditions of MT generation limitation and the minimization of surface roughness, as shown thereafter.

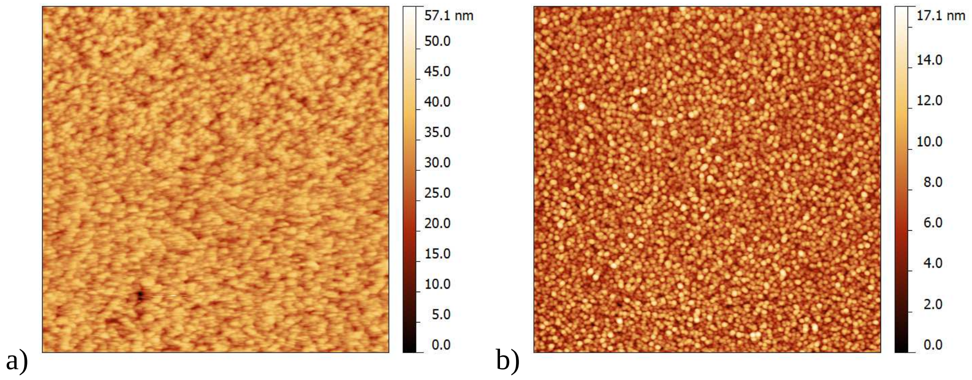

Figure 3.16 5×5 µm^2 AFM images of a) S1254 grown at 350°C and b) S1266 grown at 600°C, respectively showing a r.m.s. roughness of 2.06 nm and 5.70 nm for the two samples.

b Discussion on MT formation and prevention

The reduction of MT density at higher temperature has been experimentally proved, but the mechanism of MT formation and its relationship with the growth temperature still remains unknown. In closed packed alloy systems (FCC or HCP), twins can be formed during a deformation mechanism, from dislocations.[119,120] The dissociation of a dislocation into two Shockley partials[121] is energetically favored and provides a driving force for the generation of stacking faults.[122] The temperature dependent glide of partial dislocations on contiguous {111} planes forms twins.[123]

For highly strained layers like GaAs on Si, planar defects are believed to be formed due to the lattice mismatch induced interfacial stresses.[124,125] In our case (close packed FCC zinc blende GaP structure), misfit dislocations are absent within the critical thickness (about 90 nm[69,72]) since the lattice mismatch between GaP and Si is very small (~0.36% at room temperature) and the evolution of GaP lattice constant as a function of temperature can be neglected, verified by a calculation taking into account the linear expansion coefficient at $T > 300K$ (about 5.5×10^{-6}/K). The twins are believed to be formed during the heteroepitaxial layer growth, when growth mistakes occur on the {111} planes. Indeed, the growth of twins is commonly observed in semiconducting epitaxial layers.

In MBE growth mode, the Ga atoms are supplied together with the P atoms; GaP islands are formed at the initial stage.[126] Takagi et al[127] have experimentally evidenced using HRTEM technique the formation of 3D round-shaped GaP islands at the GaP/Si interface during the very first growth stage (5 eq-ML thick), as shown in Figure 3.17 a). As the growth continues (until 15 eq-ML thick), stacking faults are introduced in the process of coalescence by lateral expansion of isolated GaP islands as shown in Figure 3.17 b).

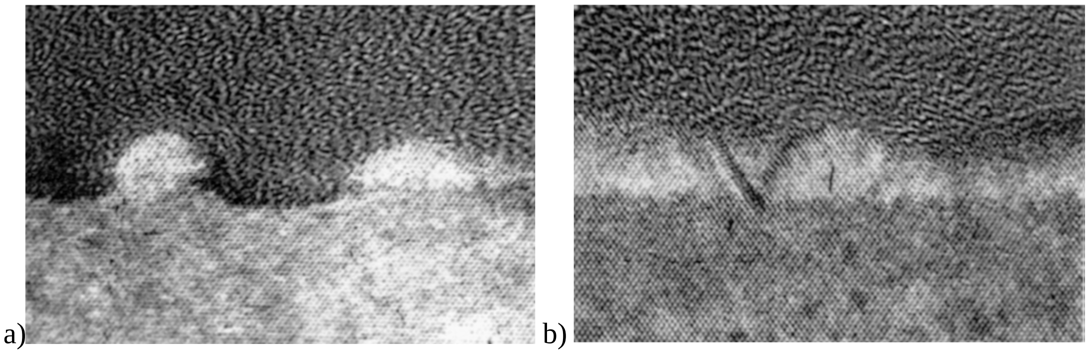

Figure 3.17 HRTEM images of GaP/Si grown by MBE, with a) 5 eq-ML thick layer, showing the formation of isolated round-shape GaP islands at the interface, b) 15 eq-ML thick layer, showing the generation of stacking faults at the interface during the expansion and coalescence of GaP islands.[127]

The generation of MTs has been attributed to the stacking errors on the {111} facet of the GaP islands, as argued by Ernst & Pirouz[128] and Narayanan[129]. At low temperature, the atoms arriving at the {111} facets are not able to incorporate the low energy configuration but rotate 90° and may occupy incorrect sites. Assuming that a {111} facet is terminated by atoms of A sites (seen as the first layer). When the atoms occupy the C sites instead of the expected B sites on the second layer, a stacking error occurs. If the atoms on the subsequent layers continue in the correct order, ABCA|CABC sequence is formed and results in an intrinsic stacking fault, as depicted in Figure 3.18. A single-layer twin is therefore created. Let's go back to the third layer. If the atoms are deposited on the B sites and then continue in the correct order, the stacking sequence becomes ABCA|C|BCABC, leading to an extrinsic stacking fault as if an additional C plane is inserted. A two-layer twin is formed. According to the calculation of Cohen and Carter,[130] the extrinsic and intrinsic staking fault energies of GaP were respectively 40.5±3 mJ/m^2 and 43.4±2 mJ/m^2. Extrinsic staking faults, leading to a faster MT formation and with lower formation energy, are therefore energetically favored.

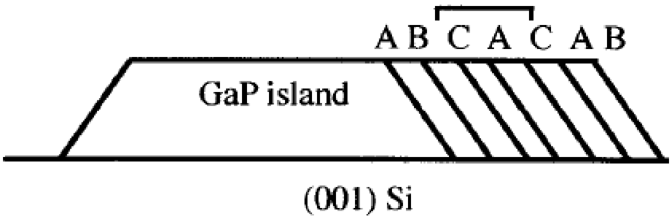

Figure 3.18 Formation of an intrinsic stacking fault on a {111} facet. [129]

The authors then suggested that firstly, the use of higher growth temperature, which allows the atoms to arrange themselves in low energy configurations, helps to reduce the MT formation, and secondly, low growth rate preventing the nucleation of GaP islands can also limit the MT density.

3.3.2 Migration Enhanced Epitaxy growth

The GaP growth rate can be controlled in the Migration Enhanced Epitaxy (MEE) mode which consists of alternated growth of Ga and P. The control of the Ga rate as well as the interruption time between the Ga and P depositions allows a pseudo-2D growth. Indeed, Takagi[127] et al has already shown the GaP layers free of islands and stacking faults, by using the MEE. In this section, I will show you the MT elimination in our GaP thin layers by the MEE growth mode.

Figure 3.19 a) shows the XRD pole figure performed on sample S1319, a 45-nm-thin GaP layer grown on a Si 6°-off substrate using the MEE growth technique at 350°C. When compared to the MBE-grown samples of same thickness and under same temperature (S1254), S1319 shows much lower MT intensity and smoother surface with a r.m.s. roughness of 0.97 nm, as measured from the 5×5 µm^2 AFM image (Figure 3.19 b)).

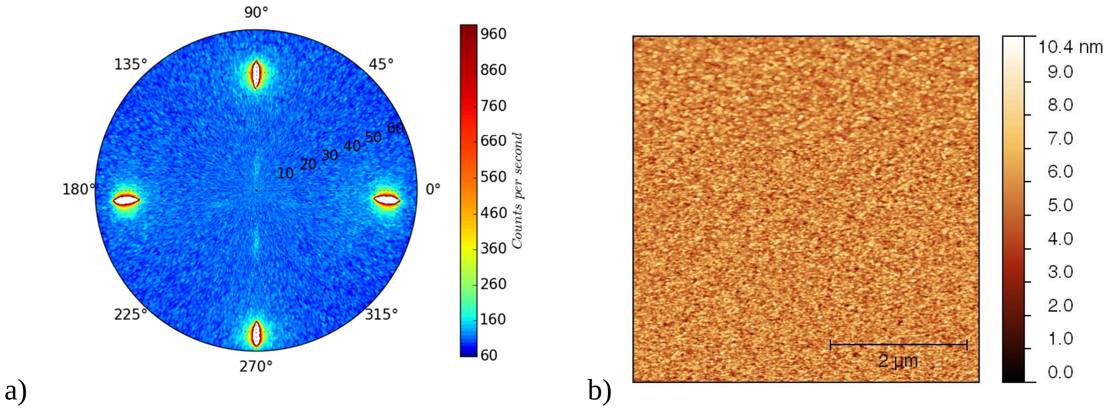

Figure 3.19 a) Pole figure and b) 5×5 µm^2 AFM image of S1319

However, since the MT reflection intensities are extremely weak, it is difficult to correctly integrate the MT signals on the pole figure. Here we can find another advantage of rocking-curve method over the pole figure: the capacity to accurately quantify the samples with lower MT density. Figure 3.20 represents the 4 rocking-curves taken around the 4 MT variants. The profiles show well-defined peaks and can be correctly fitted by Pseudo-Voigt functions.

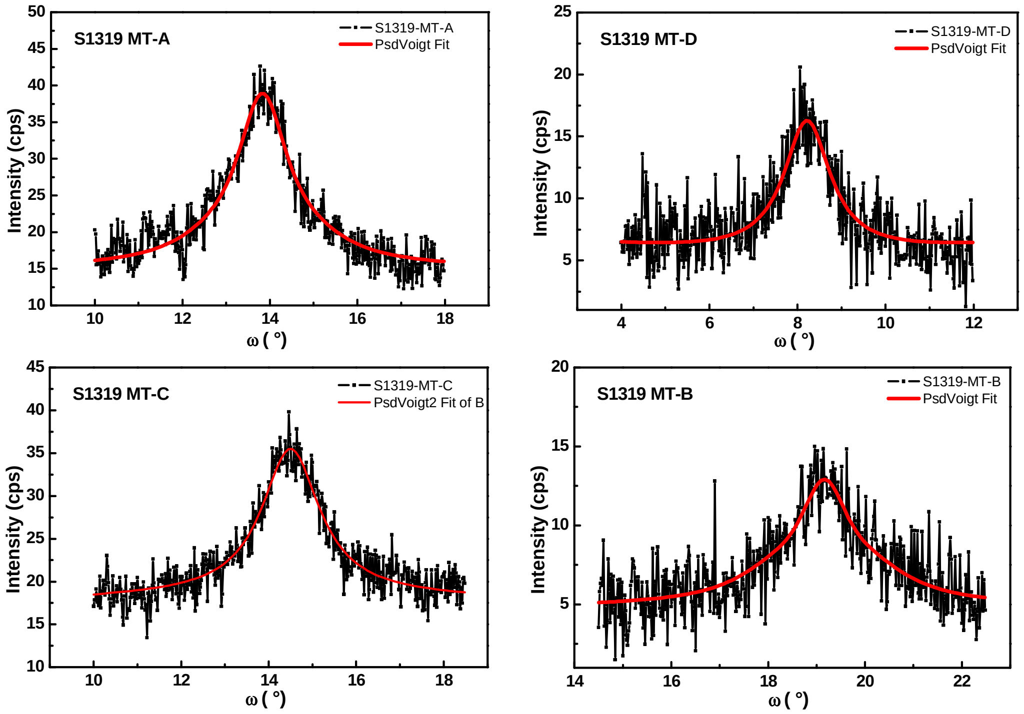

Figure 3.20 Rocking-curves of S1319 for the 4 MT variants, fitted by Pseudo-Voigt functions.

The volume fractions of each MT variants and the sum, calculated from the rocking-curves are shown in Table 3.1, used as an example to introduce the rocking-curve method. The total MT volume fraction of 1.3 ± 1% indicates a great improvement of the structural quality of the GaP layer by using the MEE growth mode instead of the MBE growth mode. Again, the most intense MT signal is seen on the variant A.

3.3.3 Two-step growth sequence

The two-step growth sequence inspired from the recipe of Grassman et al.[53], consists of a low temperature MEE growth to enhance the 2D nucleation at the early stage of growth, and a subsequent high temperature MBE growth to eliminate the remaining defects.[131–133] Indeed, the MEE is not suitable for the second sequence because firstly, it takes too much time (more than 4 hours) to grow a GaP layer of 45 nm at such a low growth rate (0.1 ML/sec.) and secondly, the 2D growth doesn't permit the annihilation of APDs which will be discussed in detail in the next Chapter. Sample S1330 is therefore designed using such two-step growth sequence as illustrated in Figure 3.21.

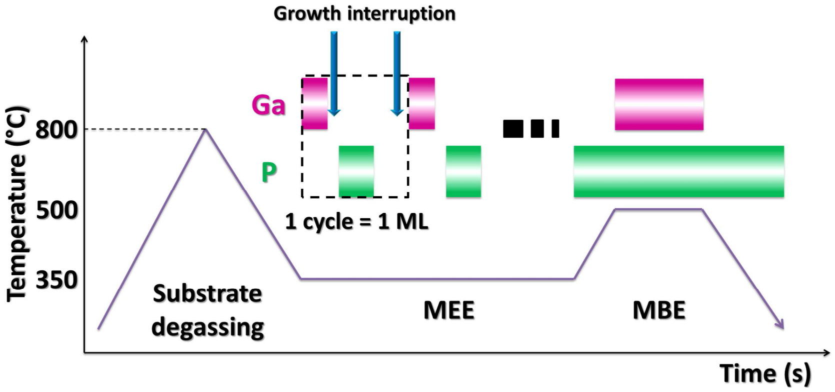

Figure 3.21 Illustration of the two-step growth procedure. MEE growth mode consists of alternated growth of Ga and P, leading to a good control of the Ga content and incorporation to obtain a pseudo-2D growth mode, followed by GaP overgrowth using conventional MBE mode.

The substrate is firstly heated to 800°C for degassing and ramped down to 350°C for the 40 ML (about 10 nm) MEE growth. One MEE cycle or monolayer (ML) consists of a first 0.9 ML Ga deposition at a growth rate of 0.1 ML/sec., followed by 4 sec. growth interruption and then an exposure to phosphorus overpressure for P deposition. Each MEE cycle is separated by 60 sec. growth interruption. Finally, a 35-nm-thin GaP layer is grown by MBE at 500°C. When compared to S1319, S1330 displays a slightly lower density of MT defects (volume fraction of about 1%) and a much smoother surface (r.m.s. = 0.3 nm), as measured in the pole figure and the 5×5 μm^2 AFM image shown in Figure 3.22. Indeed, the improvement of surface roughness is independent with the MT elimination and related to the APDs level[134,135] (see next Chapter).

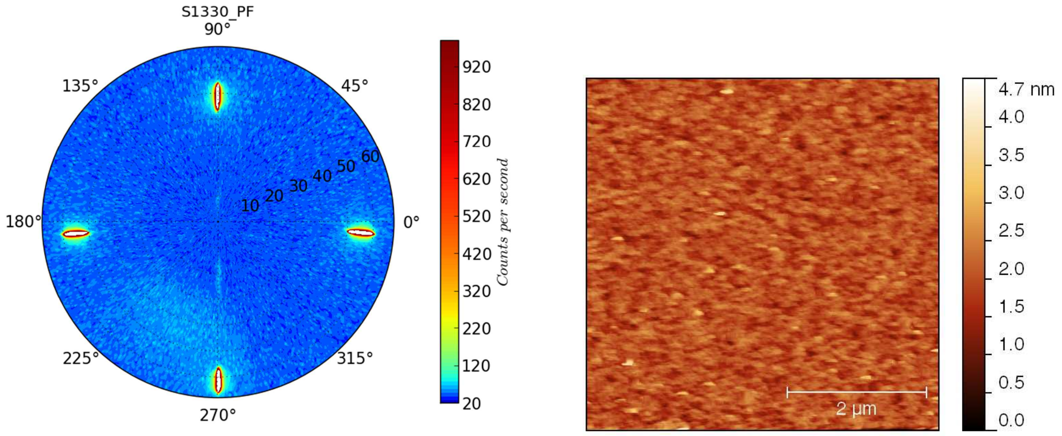

Figure 3.22 Structural characterization of S1330 by a) pole figure, showing very weak MT intensity, b) $5\times5\mu m^2$ AFM image, showing a smooth surface with a r.m.s. roughness of 0.3 nm.

Complementary MT analysis is given by cross-sectional HRTEM-BF images on S1319 and S1336 (grown under exactly the same conditions as S1330). The experiment has been carried out in collaboration with A. Ponchet and J. Stodolna at CEMES in Toulouse, France. Both S1319 and S1336 present some MTs generated at the GaP/Si interface. The MT density is slightly lower in S1336, confirming the results of the XRD analysis. Indeed, plan-view TEM observation on larger field showed a MT surface fraction of 5% for S1319 and 4% for S1336.

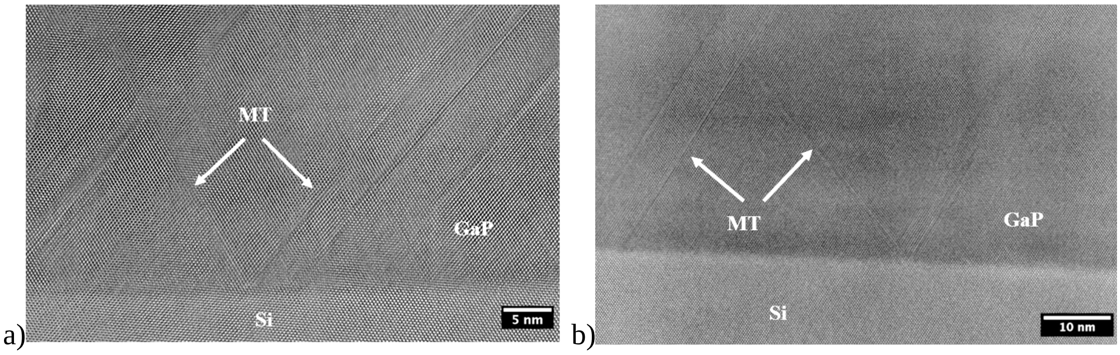

Figure 3.23 Cross-sectional HRTEM-BF image of a) S1319 and b) S1336. (CEMES)

However it has to be noticed that S1336 and S1319 are grown under the same conditions for the first 10 nm. Since the MTs are generated at the GaP/Si interface as confirmed by the HRTEM-BF images, and are strongly influenced by the initial growth stage, the slight improvement of the MT density seen on S1336 is probably due to the overgrowth by MBE: the intersection of MTs that prevents the propagation until the surface is enhanced on MBE mode and at higher temperature.

To conclude, the growth parameters involving temperature, MEE growth mode, and two-step growth sequence have been investigated on the reduction of MT density, with the help of the pole figure and rocking-curves method combined with complementary AFM and TEM images. We have successfully obtained GaP/Si pseudo-substrates displaying very low density of MTs and a smooth surface, grown by applying all optimized parameters (a first MEE layer starting with Ga dseposition and grown at 350 °C followed by a MBE layer grown at 500 °C).

3.4 Other discussions and comments on the MT formation and quantification

3.4.1 Anisotropy and influence of the Si surface atomic steps

Most of the samples studied in this thesis are grown on a Si substrate misoriented by 6° towards the [110] direction and as mentioned above, anisotropy has been observed along the atomic steps on the Si surface. Here we try to symmetrically investigate the dependence of anisotropy on growth parameters, especially the growth mode (MBE or MEE) and growth temperature.

Firstly; we define the anisotropy factor as the ratio of MT denstiy between the variant A and the variant C. Table 3.4 lists the MT volume fraction quantification of some representative samples and the calculation of anisotropy factor for each sample that is schematically represented in Figure 3.24.

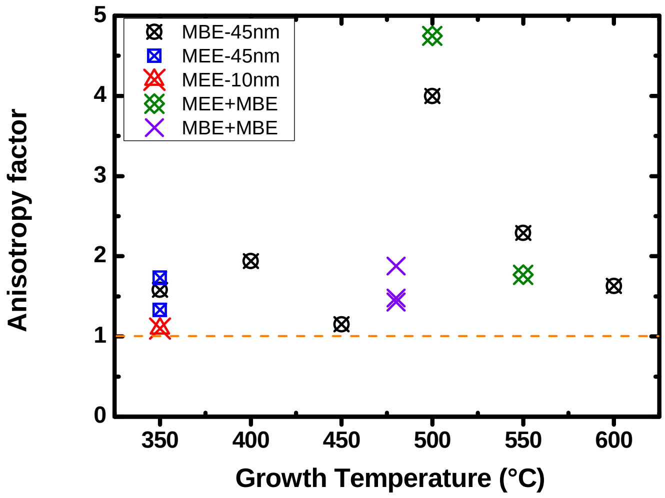

Figure 3.24 Anisotropy factors as a function of growth temperature

Table 3.4 MT volume fraction evaluated by pole figures (with correction) or rocking-curves, to study the relationship between the anisotropy and the growth conditions

Sample	Principal growth parameters	MT-A	MT-C	MT-B	MT-D	MT-total	Anisotropy factor
S1254	MBE, 350°C	1.13	0.71	0.72	0.44	3.00	1.58
S1255	MBE, 400°C	6.19	3.19	4.21	3.75	17.34	1.94
S1256	MBE, 450°C	4.02	3.50	3.40	2.97	13.89	1.15
S1264	MBE, 500°C	0.46	0.12	0.29	0.21	1.08	4.00
S1265	MBE, 550°C	0.24	0.11	0.35	0.07	0.77	2.29
S1266	MBE ,600°C	0.61	0.38	0.09	0.30	1.37	1.63
S1200	MBE, 350°C+480°C	13.37	7.11	9.61	8.49	38.58	1.88
S1189	MBE, 350°C+480°C	7.76	5.23	6.25	5.17	24.40	1.48
S1180	MBE, 350°C+480°C	4.54	3.17	3.44	3.90	15.05	1.43
S1330	MEE, 350°C+MBE, 500°C	0.47	0.10	0.13	0.08	0.78	4.76
S1319	MEE, 350°C (45 nm)	0.40	0.30	0.40	0.20	1.30	1.336
S1306	MEE, 350°C+MBE, 550°C	1.24	0.70	0.28	0.28	2.50	1.776
S1308	MEE, 350°C (10 nm)	7.99	7.26	6.27	7.81	29.33	1.106
S1322	MEE, 350°C (45nm)	7.05	4.07	5.81	5.3	22.23	1.736

From the above anayses, we find that all the anisotropy factors are greater than 1, indicating a higher MT density on MT-A than on MT-C, consistent with the literature.[59,73,111] Secondly, the evolution of anisotropy factor on MBE grown samples shows a peak value at 500°C. Samples grown at lower temperature, either by MBE or by MEE, shows a relatively weak anisotropy. Finally, samples grown under same temperature using same growth mode can present different anisotropy factors, that is to say, other parameters (especially Si surface preparation) can also influence the anisotropy characteristics (or kink density).

We attribute the anisotropic phenomenon to the role of atomic steps on MT generation and propose a kinetic mechanism of staking fault and MT formation from the step edges, after a discussion with A. Ponchet (CEMES, Toulouse, France). Assuming that the Si surface prior to the Ga growth is perfectly crystallized without any defects nor any contaminants, and only presents D_B double steps, as shown in the Figure 3.25 a). Only the Ga atoms being capable to form two Ga-Si bonds can be firstly incorporated, and perfectly cover the Si surface (Figure 3.25 b). Then one monolayer of P atoms is deposited, each form two P-Ga bonds (Figure 3.25 c). The growth continues with the correct deposition sequences and a perfect GaP/Si layer is formed without any defects. However, this is a hypothetical ideal case which cannot be true in reality.

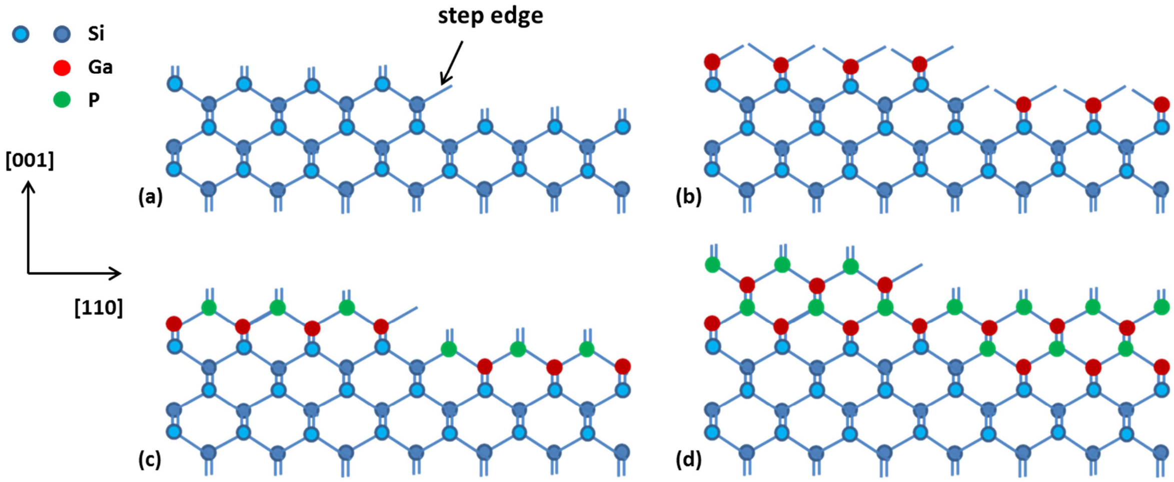

Figure 3.25 Illustration of GaP layer growth on a D_B-type Si surface. a) the D_B-type surface before growth, with Si dimers parallel to the step edges; b) the deposition begins with a perfect coverage of Ga atoms on the Si surface; c) a monolayer of P atoms are deposited and perfectly bonded to the Ga atoms; d) the growth continues correctly and no defect is formed.

Less ideally, we can assume that the Si surface is not perfectly covered by the Ga atoms and it is possible to adsorb atoms that from only one bond with the former layer. Taking into account that extra Ga atoms will from metallic droplets than can dissolve the Si,[136] no sufficient Ga atoms are supplied during the Ga deposition. The atoms diffuse on the terrace and preferentially migrate towards the bottom of the steps (notice that the atoms can less easily jump from one terrace to another due to the energy barriers of the step edge). Then a vacancy site is created at the top of the step edge, as shown in Figure 3.26 a). During the P deposition, one P atom can stay at the step edge as adsorbed atom, forming only one P-Ga bond with the Ga atom at his left side, since the right side is a vacancy (Figure 3.26 b)). It is then energetically possible that the P atom is rotated around itself (Figure 3.26 c)). In the following, a Ga atom arrives at the step edge and is adsorbed by the P atom (Figure 3.26 d)), rotated itself in order to form a stable double-bound with the newly coming P atom, as shown in Figure 3.26 e). Now, a stacking fault ABCA|C along with a single-layer twin is formed. However, if the growth continues with a repetition of step (b) to step (d), thicker twin domains can be created. Finally, a dislocation, whose Burgers vector corresponding to the difference between the adjacent Ga planes (here presented respectively by red and rose circles in Figure 3.26 f)), is introduced, in order to join the two domains. This mechanism proposes the formation of MT-C from the step edge. Further studies should be made, based on this mechanism and the Ga diffusion energies on Si surface and step edges, to interpret the relationship of anisotropy and the growth parameters.

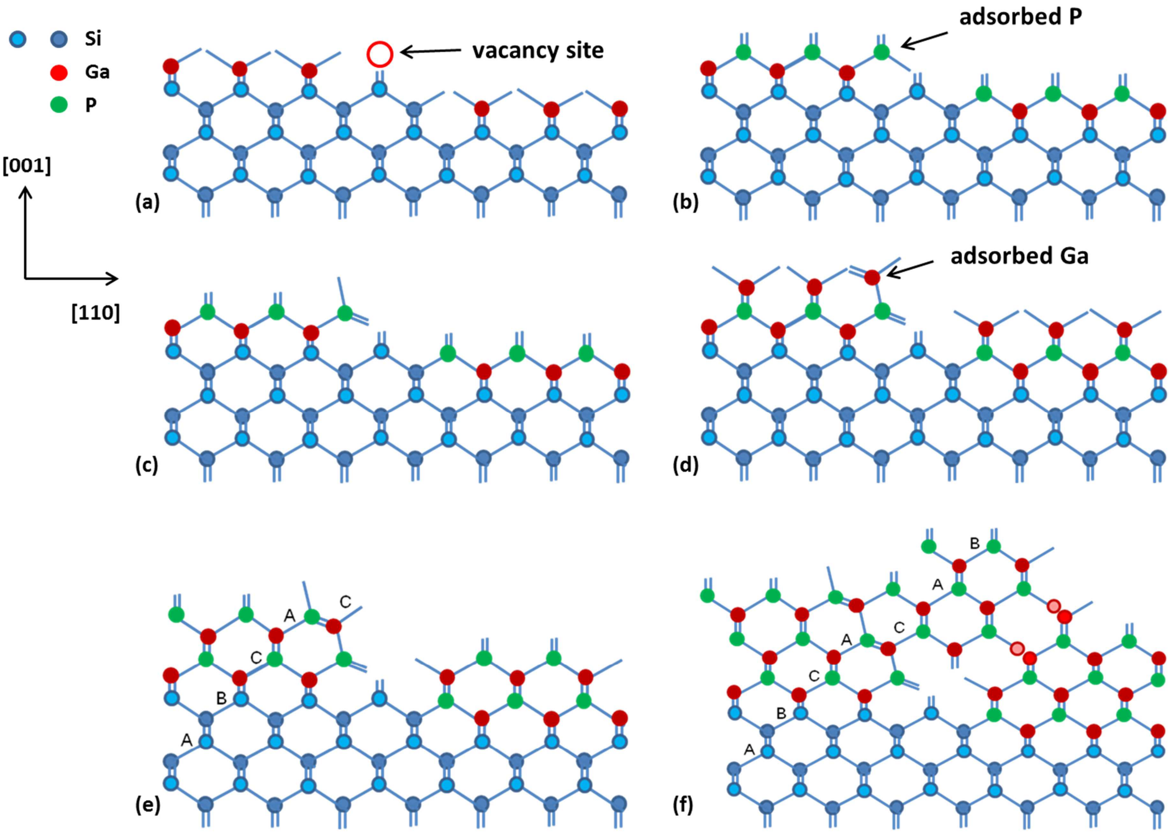

Figure 3.26 Formation of stacking fault and twin from the step edge. a) the deposition begin with the Ga atoms and the Si surface is partially covered by the Ga atoms with a vacancy site at the upper part of the step edge; b) a layer of P atoms are deposited with an adsorbed P atom at the step edge; c) the P atom is rotated round itself; d) a Ga atom is adsorbed by the P atom and rotated; e) the adsorbed Ga atom forms stable bonds with newly coming P atom, and a stacking fault along with a single layer twin is created; f) a dislocation is introduced to close the two domains.

3.4.2 Horizontal homogeneity of MT distribution

This is a complementary study to justify the lateral homogeneity of the structural quality (MT density distribution) of the GaP epilayers. Generally we set the sample in the way that X-rays arrive near the center of the sample surface to avoid the diffusion caused by beams outside the sample. However, sometimes the samples are already cut to half before XRD analysis. Hence it is of interest to verify the homogeneity of the thin layer quality, especially the MT density level in different surface position of the sample. To this end, rocking-curves on MT variants and GaP 002 have been carried out on S1189 at different surface positions. The lateral and longitudinal movement was guaranteed by the X and Y motors. The X-ray beam of about 2×2 mm^2 arrive around the center of the sample at (X=0, Y=0) with a foot print on the surface of about 8×2 mm^2 at the vertical position (χ=0°). But the foot print size changes when the sample inclines with respect to the arriving X-ray beams, which makes this study not very precise. Volume fractions of both MT and GaP of nominal orientation are measured and showed in Table 3.5.

Table 3.5 Volume fractions of both MT and GaP of nominal orientation for S1189 measured at different positions. Every measured term has a relative error estimated around ±10%.

(X,Y) position (mm)	MT-A	MT-D	MT-C	MT-B	MT-sum	NO-az1	NO-az2
(0, 0)	7.8	5.3	5.2	6.4	24.6	69.2	70.2
(0, 8)	8.2	5.3	5.0	6.2	24.7	69.1	70.2
(0, -8)	7.4	4.8	5.3	6.0	23.5	70.0	71.5
(8, 0)	7.6	5.0	5.5	6.3	23.9	71.0	72.0
(-8,0)	8.0	5.8	5.2	6.0	25.0	68.8	71.0

Several observations from the table are worth discussing. Firstly, the volume fractions at different positions of either every MT variant, the sum of all MT variants or the GaP of nominal orientation (NO) in two azimuths are very close to each other and within the 10% error bar. The sample can be considered as homogeneous at the scale of the XRD beam size. Secondly, where the MT volume fraction is slightly smaller, the GaP volume fraction is slightly greater. This may shows the validity of the “RC method”, considering that the sum of MT and NO volume fractions should always be identical and equal to 100% in ideal case.

3.5 Summary

We have developed two MT quantification methods using X-ray diffraction on lab setup. The pole figures for fast visualization and estimation of MT volume fraction after corrections, and the rocking-curves for absolute quantification of MT volume fraction. Based on previous non optimized samples and thorough XRD analyses, with complementary TEM and AFM analysis techniques, the GaP/Si platform structural properties have been significantly improved, after an optimization procedure involving growth temperature, MEE growth procedure and two-step growth sequence. GaP layers quasi-free of MTs are obtained at the first 40 ML GaP grown by MEE at 350°C and 40 nm overgrowth GaP layer by MBE at 500°C. The sample surface is almost smooth with a r.m.s. of only 0.3 nm, suitable for the subsequent growth of an optoelectronic heterostructure.

MT formation mechanism has been discussed along with the experimental results and based on the assumptions proposed in literature. On MBE growth mode and at low temperature, the 3D nucleation of GaP islands is believed to dominate the MT formation, when the atoms are deposited in incorrect sequences or during the coalescence of these nucleis. MT density has been dramatically reduced at low temperature by using MEE since the growth rate can be carefully controlled to promote a quasi 2D growth that eliminate a large amount of 3D GaP islands. Residual MT is suppressed by a further optimization of growth parameters such as the Ga amount per MEE cycle at the initial growth stage and will be presented in the next Chapter. The anisotropy of MT density (MT-A>MT-C) due to the atomic steps is seen on all the samples grown on vicinal Si substrate. We proposed a hypothetic mechanism of GaP deposition on bi-stepped Si surface, to explain the stacking fault and twin formation at the step edge. Thermodynamic studies on Ga diffusion energies at the Si surface and the Si step edges are necessary for further study of this mechanism.

Chapter 4 Evaluation of APD density for growth condition optimization

In the last chapter, I have presented some analytical methods for MT quantification which has enabled the structural quality improvement of the heteroepitaxial GaP layer, with a dramatic lowering of the MT density, by optimizing the growth conditions involving growth temperature, MEE procedure and two-step growth sequence. This chapter deals with another type of defects: the APDs (separated by the APBs). Firstly, analytical methods for APD density evaluation using both laboratory setup and synchrotron XRD are described. Then, a deep APD analysis based on the XRD methods combined with TEM, AFM and STM images will be carried out on several samples. This study shows a large impact of the substrate surface preparation (physical, chemical and Si buffer layer) and growth parameters (growth temperature, Ga coverage, AlGaP marker layers) on APD density and configuration. The APD formation and annihilation mechanisms related to the growth conditions are also discussed.

4.1 XRD methods for APD density evaluation

APD density can be characterized by the lateral correlation length $\xi_{x\text{-APD}}$, which is defined as the mean distance between the APBs along the in-plane direction (perpendicular to the growth direction), provided that the APD sizes are relatively homogenous. Samples with higher APB density generally show shorter lateral correlation lengths. Characterization of APD based on XRD measurements has already been presented[137] and widely used in thin films[138,139], including GaP/Si[132,140,141]. In this work, XRD reciprocal space maps (RSMs) are carried out around 00L Bragg reflections, using both laboratory XRD setup and synchrotron radiation, for extraction of the transverse scans to study the lateral structure of the GaP epilayer.

4.1.1 RSM recorded on laboratory XRD setup

The RSMs have been carried out around the 002, 004 and 006 reflections at the laboratory D8 diffractometer on high resolution mode (see Section 2.2.1 for setup details). The PSD detector was used in 1D mode for faster acquisition. 2θ and ω angles being initially set at the Bragg positions, conventional $\omega/2\theta$ scans were performed and recorded at successive ω position.

Figure 4.1 illustrates the X-ray scattering geometry for the RSM of GaP/Si(001) misoriented by 6° toward the [110] direction. $\boldsymbol{k_i}$ and $\boldsymbol{k_f}$ are the reduced scattering vectors along respectively the incident and scattered directions, with $|\boldsymbol{k_i}| = |\boldsymbol{k_f}| = 1/\lambda$. The scattering vector $\boldsymbol{S}$ is defined as $\boldsymbol{k_f} - \boldsymbol{k_i}$ and collinear with [001]. The in-plane direction ($\boldsymbol{S_x}$) is coplanar with the scattering plane defined by $\boldsymbol{k_i}$ and $\boldsymbol{k_f}$, and parallel to the projection of $\boldsymbol{S}$ ([001] vector) onto the sample surface. The out-of-plane direction ($\boldsymbol{S_z}$) is the growth direction that is normal to the sample surface. At this azimuthal scattering condition, the incident X-ray beams are parallel to the [-1-10] direction and the 00L reflections are nearly specular (not strictly specular) since the 6° miscut results on a shift of ω (i.e. $\omega = \theta + 6°$), which also allows the highest transverse resolution (when the miscut results in a non-zero value of the χ angle, a significant broadening of transverse scans is indeed observed due to a rotation of the linear beam footprint). The advantage of using such (S_x, S_z) coordinates in this azimuthal condition is that the epilayer reciprocal lattice node (RLN) falls at the same S_x position as the substrate RLN. The elongation of the RLN along the S_z direction is inversely proportional to the layer thickness and is accompanied by thickness fringes (also called pendellosung fringes), in case of high structural perfection of the thin epitaxial layer (sharp interface, flat surface, low plastic relaxation, low defect density, etc.). The extraction of "transverse scans" along S_x also allows the measurement of the defects correlation length in the in-plane direction with a high sensitivity without resolution loss, by integrating the intensities within a certain height along S_z (here 0.03 nm^{-1} in reciprocal space, as depicted on the RSMs in Figure 4.2).

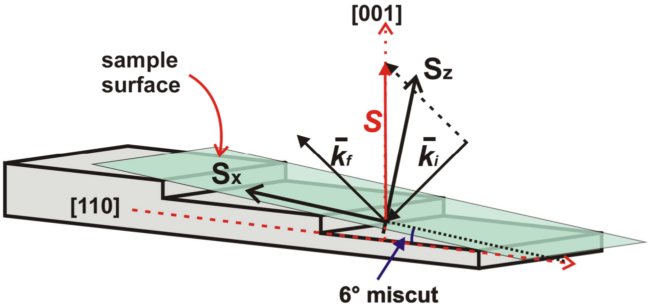

Figure 4.1 Illustration of the scattering geometry on GaP/Si(001) misoriented by 6° toward the [110] direction, with incident X-ray beams along the [-1-10] direction and the nominal Bragg position is found at $\omega = \theta+6°$.

Figure 4.2 shows typical RSMs around the 002, 004 and 006 nearly specular reflections of the GaP/Si heteroepitial system, obtained on sample S1330 (a 10-nm-thin MEE GaP layer grown at 350 °C followed by 35-nm-thin MBE GaP layer grown at 500 °C). The experimental angular coordinate have been converted into the surface azimuth coordinate (S_x, S_z) using the following relationship:

$$\begin{cases} S = \frac{2sin(\theta)}{\lambda} \\ S_x = S \cdot sin(6°) \\ S_z = S \cdot cos(6°) \end{cases} \qquad \textit{Eq. 4–1}$$

The RLN broadening of the GaP peak along S_z is mainly due to the finite layer thickness (Scherrer law). The diffuse broadening observed along the S_x direction is believed to correspond mainly to the mosaic tilt and threading defects that break the long-range order in this direction. The 004 RSM exhibits both GaP and Si peaks (Si is forbidden reflection and generally very weak on 002 and 006), with the GaP peak lying at the same S_x value than Si, indicating the absence of plastic relaxation. The Si CTR is tilted with respect to the S_z direction due to the substrate's 6° miscut. The 006 diffraction spot shows a much lower intensity with respect to the 002, due to the loss of intensity at high incident angle. The intensity integration has been performed at the center of the GaP CTR within a 0.03nm^{-1} high band to extract the transverse scans, as illustrated in Figure 4.2 by the red rectangles.

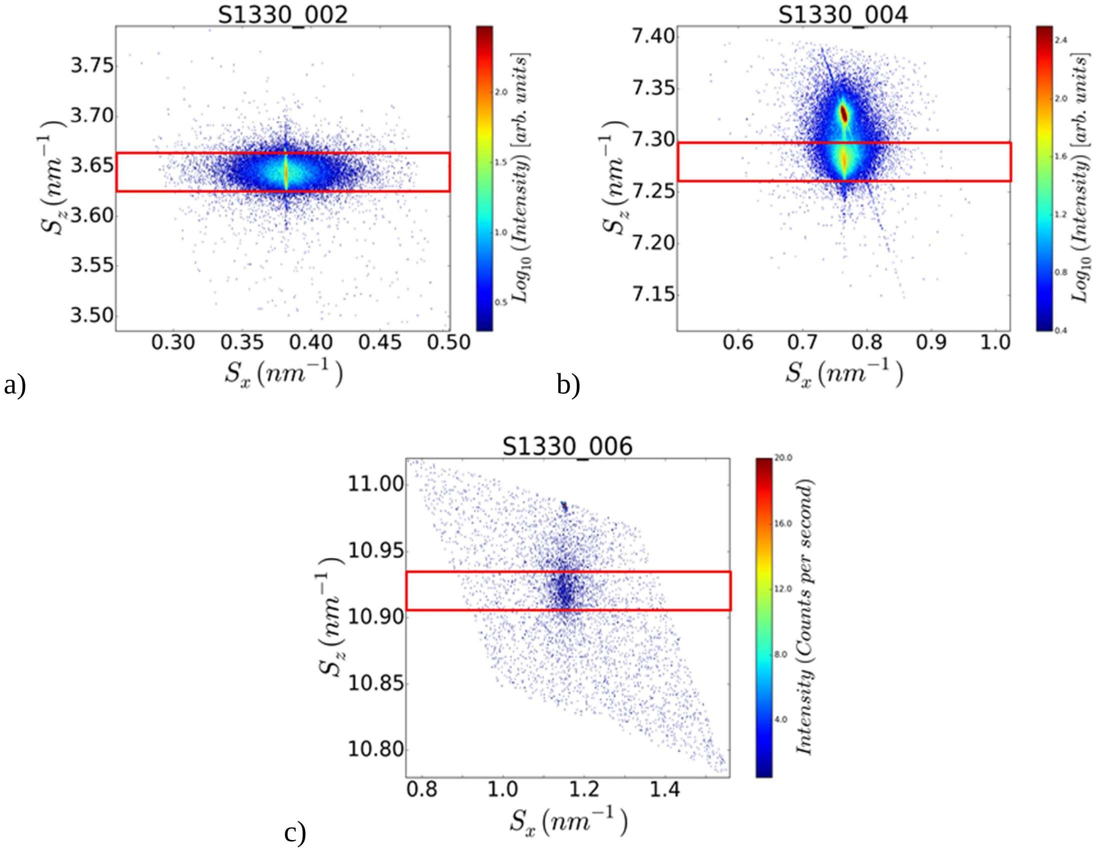

a)

b)

c)

Figure 4.2 Laboratory XRD RSM around 002, 004 and 006 nearly specular reflections for S1330. The red line rectangles indicate the S_z boundaries for transverse scan extraction, corresponding to 0.03 nm^{-1} height centered on the GaP CTR in S_z direction.

Figure 4.3 shows the transverse scans extracted from the above RSMs. The abscissa axis is expressed on ΔS with the profile peak located at $\Delta S = 0$. Both 002 and 004 transverse scans display two-component line-shapes: a resolution-limited thin peak due to the long-range structural correlation length (characteristic of a heteroepitaxial thin layer) and a diffuse-scattering broad component from the shorter-range correlation length. The integral breadth (IB) of the thin peak indicates a very regular lattice spacing and good parallelism of the epitaxial GaP atomic planes, over a relatively long in-plane distance. The broad "diffuse" peak is attributed to a limitation of the in-plane correlation length due to structural defects at a shorter range, as already investigated in the mosaic epitaxial GaP thin films [69,142]. The thin peak intensity decreases with respect to the diffraction order and is lacking on the 006 transverse scan that displays a broad peak profile with a poor resolution due to the weak intensity. The profiles are fitted by two-component (or single on 006) Pseudo-Voigt functions[143], respectively for the resolution-limited thin component and the broad component. The IBs of the broad peaks, as well as the thin peak and broad peak areas are extracted for further analysis.

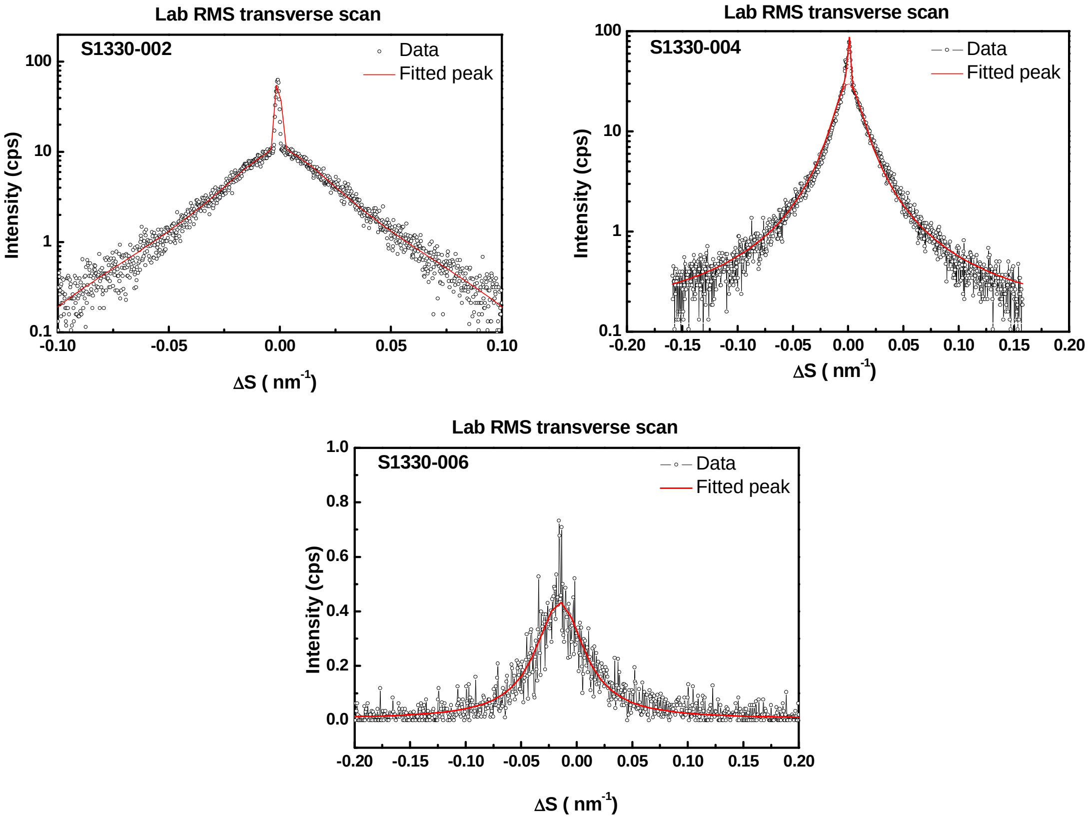

Figure 4.3 Transverse scans extracted from the 002, 004 and 006 nearly specular RSMs shown in Figure 4.2, fitted by Pseudo-Voigt functions. 002 and 004 transverse scans display two-component line-shape while the thin peak is lacking on the 006 transverse scan.

4.1.2 Reciprocal space images by synchrotron X-rays

Reciprocal space images around the 00L reflections were recorded using synchrotron radiation at the BM02 beamline (see Section 2.2.2 for beamline configuration). The use of a 2D XPAD detector combined with a CCD camera allows the acquisition of a reciprocal space image within only 300 seconds while it takes more than 5 hours on lab setup to acquire such an image. Another advantage of synchrotron X-ray diffraction is that we were able to use smaller wavelength (λ=0.07749 nm at 16 keV in our case), that makes it possible to study high diffraction orders like 008 and 0010.

Figure 4.4 shows the detector images of the sample S1330 at the nominal Bragg positions of the nearly specular 002, 004, 006, 008 and 0010 reflections, taken in the azimuthal condition “az1” with the incident X-ray beams along the [-1-10] direction.

Therefore, the nominal incidence angles for these reflections are respectively θ+6°. The images are expressed in pixel in both horizontal (X) and vertical (Y) directions, with each pixel size p = 130 μm. This basically determines the detection resolution in reciprocal space (0.00327 nm^{-1}), according to the Equation 2-2 and 2-3.

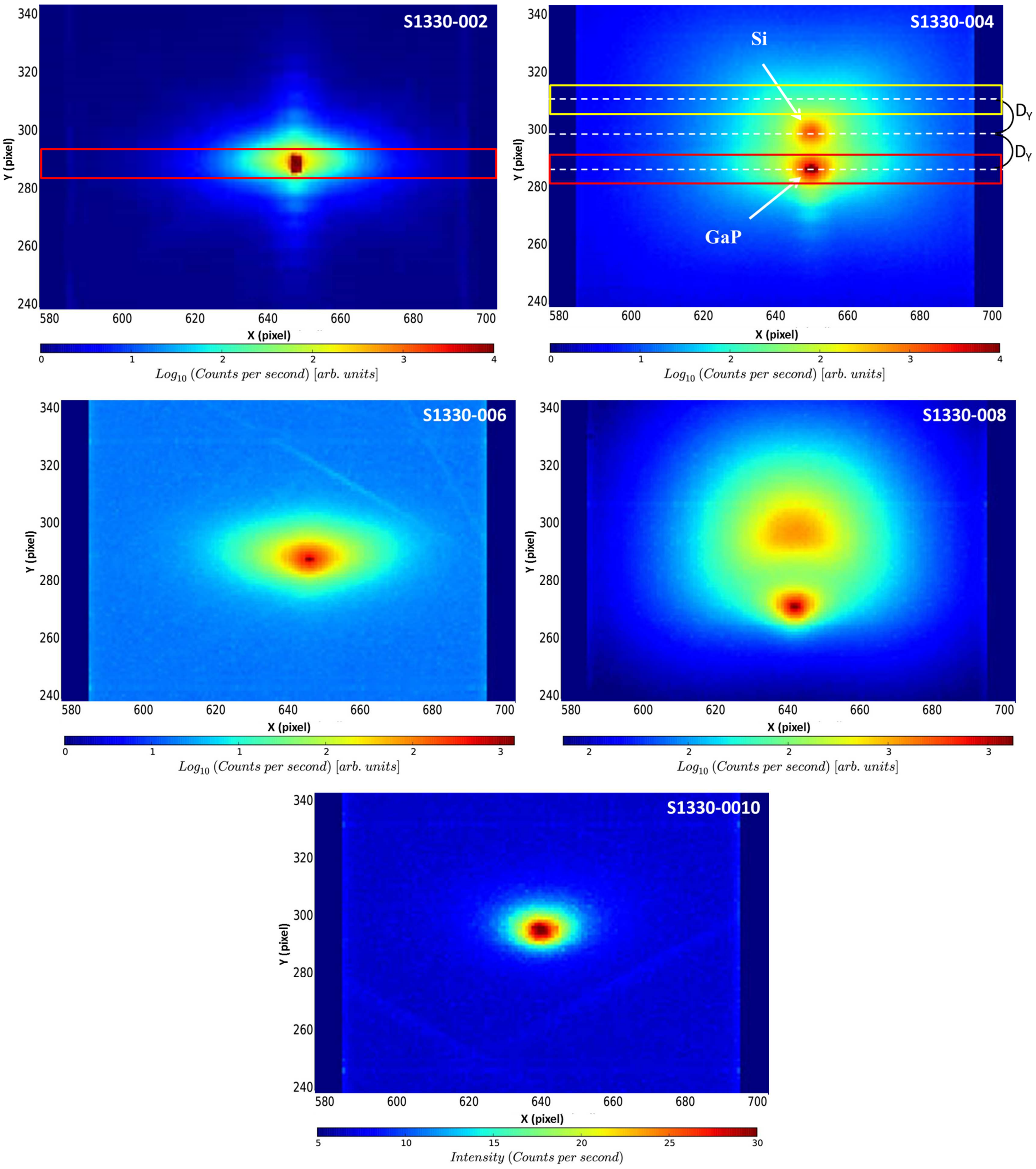

Figure 4.4 Detector images of S1330 at the center of the nominal Bragg positions of the nearly specular 002, 004, 006, 008 and 0010 reflections, carried out on the BM02 beamline at ESRF. Red line rectangle and yellow line rectangle indicate the vertical boundaries for transverse scan extraction and Si diffuse contribution extraction, respectively. Equidistance white dashed lines on 004 indicate the center of respectively the diffuse extraction, Si peak and the GaP peak.

An intense thin peak is obviously visual at the center of the 002 and 004 spots, due to the long-range order in the lateral direction, as described above. Lateral streaks with weak thickness fringes are observed on the 002 image, signature of the coherent interference of the X-rays between the GaP/Si interface and the epilayer surface. Both observations indicate a high crystalline quality of the epilayer. Notice that these streaks are absent on the lab 002 RSM of the same sample, probably because the fringes are too weak to be acquired on lab setup, or because the Sollers slits are so large that integrate all divergent signals in the vertical direction.

Indeed, an ω scan have been carried out on each 00L reflection, around their nominal Bragg position, with a step size of 0.1°, in order to record a 3D pattern in reciprocal space. A reconstruction of the 3D RLN is necessairy to obtain the informations along the H, K, L directions and to make an exact analysis of the peak broadening. The following preliminary study is carried out based only on the above detector images centered on the Bragg positions.

Transverse scans have been extracted by integrating the intensity at the center of the GaP scattering spot within a 10 pixel high band, as indicated by the red rectangle in Figure 4.4 a), corresponding to 0.0327 nm^{-1} in reciprocal space. Notice that on 004 and 008 strong reflections, the intense Si peak is very close to the GaP peak and brings a diffuse contribution (which can be due to the Thermal Diffusion Scattering-TDS). This diffuse contribution should be subtracted. Assuming that it is symmetric along the vertical direction, a same integration has been made at the same position on the other side of the Si peak (as depicted by the yellow rectangle in Figure 4.4 b)) and was regarded as the diffuse of Si on the GaP peak. Indeed, a simulation of the TDS should be done to verify the symmetry of the diffuse and for a more precise subtraction.

This effect is very weak on lab RSMs since the distance between the Si peak and the GaP peak is sufficiently large along the S_z direction, due to a greater wavelength (λ = 0.1541 nm) on lab setup.

For this experiment, the detector to sample distance $D_{d\text{-}s}$ is measured to be 513.2 mm ± 1.5%. The abscissa of the transverse scan patterns (pixel) along the horizontal direction is converted to the reciprocal space unit ΔS using the relationship described in Chapter 2 (Equation 2-2 and 2-3).

The corresponding transverse scans are shown in Figure 4.5. When compared to the laboratory transverse scans shown in Figure 4.3, the two-component shape is observed not only on the 002 and 004 reflections, but also on the 006 and 008 reflections (although relatively weaker). These scans each are fitted by two-component Pseudo-Voigt functions. The 0010 scan displays a well-defined single broad peak that is correctly fitted by a single Pseudo-Voigt function. The Si diffuse contributions as well as the peaks before subtraction are also shown on the 004 and 008 profiles. We can find that the Si diffuse brings stronger influence on the broad peak rather than on the thin one.

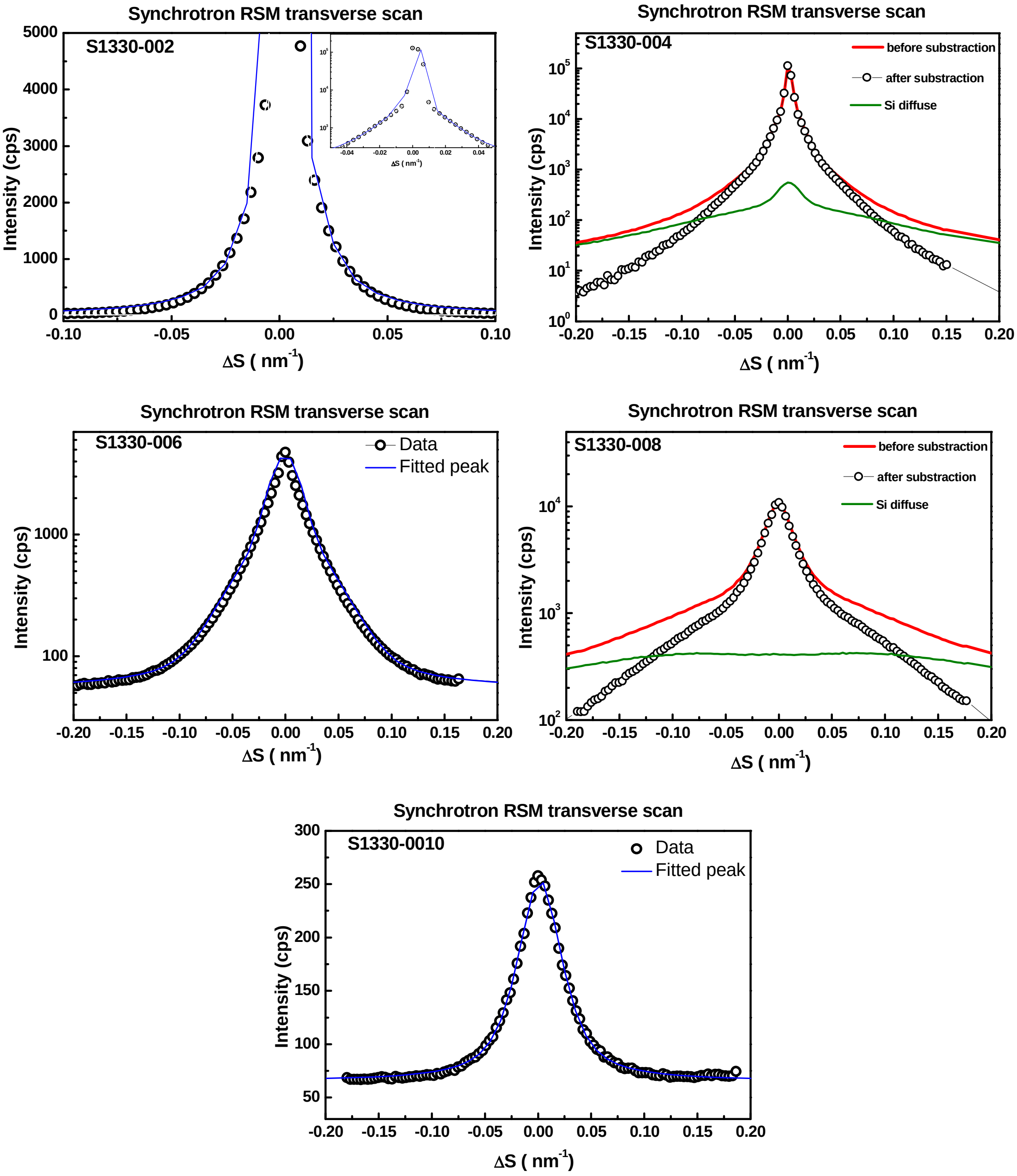

Figure 4.5 Transverse scan profiles extracted from the synchrotron reciprocal images for S1330, fitted by Pseudo-Voigt functions. The Si diffuse contribution strongly influences the broad peak of GaP 004 and 008 reflections.

4.1.3 Transverse scan analysis

Let's first investigate the scattered intensity I (from the amplitude A) of the transverse scans around a Bragg reflection whose scattering vector is $\boldsymbol{S}$, for a zinc blende GaP structure presenting only main phases and antiphases. All structure factors and form factors are considered as real and can be simply added. For strong reflections like 004:[144]

$$A_{Total}(S) \approx F_{Total}(S) \cdot F_{SR}(S) \qquad \textit{Eq. 4–2}$$

$$F_{Total}(S) = (F_{MP}(S) + F_{APD}(S)) \qquad \textit{Eq. 4–3}$$

$$A_{Total}(S) \approx (F_{MP}(S) + F_{APD}(S)) \cdot F_{SR}(S) \qquad \textit{Eq. 4–4}$$

where $F_{Total}(S)$, $F_{MP}(S)$, and $F_{APD}(S)$ are form factors of respectively the whole layer, the main phase and the antiphase. $F_{SR}(S) = 4(f_{Ga}(S) + f_P(S))$ is the unit cell structure factor of main phase on strong reflection with $f_{Ga}(S)$ and $f_P(S)$ respectively the atomic scattering factor of Ga and P. Assuming that the only difference between the APD and the main phase is that the Ga atoms and P atoms exchange their positions, the $F_{SR}(S)$ remains the same value for the antiphases. Therefore, the presence of APD has no influence on the final scattered intensity by strong reflections.

For weak reflections like 002, the unit cell structure factor of the main phase is $F_{APR}(S) = 4(f_{Ga}(S) - f_P(S))$, and that of the antiphase is opposite. Thus the scattered amplitude becomes:

$$A_{Total}(S) \approx (F_{Total}(S) - 2F_{APD}(S)) \cdot F_{APR}(S), \qquad \textit{Eq. -4–5}$$

Finally, the scattered intensity around the weak reflection is proportional to:

$$I \approx \left(F_{Total}{}^2 - 4F_{Total} \cdot F_{APD} + 4F_{APD}{}^2\right) \cdot F_{APR}{}^2 \qquad \textit{Eq. 4–6}$$

From the above equation, we can find that, firstly, the diffracted intensities of weak reflections are strongly influenced by APD with an enhancement of a factor 4 from the term $4F_{APD}^2$, and secondly, the thin peak due to lateral correlations in long-range distances, remains on weak reflections with the term F_{Total}^2, when APD density is not too large.

Hence, the broad component of the transverse scan around the weak reflections like the 002 is mainly attributed to APDs, and the broadening on the strong reflections like 004 is considered to be originated from other defects like MTs or SFs (staking faults), provided that the 004 peak width is much lower than the 002 and 006 ones. Two different methods have been developed to evaluate the crystalline perfection and APD size: the Quality factor and the Williamson-Hall-like analysis.

a Quality Factor

We define the Quality Factor (**QF**) as the area ratio of the thin component to the broad component:

$$QF = \frac{A_{thin}}{A_{broad}}. \qquad Eq.\ 4\text{–}7$$

Higher QF indicates better crystalline quality with fewer planar defects along the lateral direction.

b Williamson-Hall-like plot

A more precise evaluation has been carried out based on the Williamson-Hall-like evaluation method.[82,83,145] N. Herres[83] has attributed the line profile broadening to three mechanisms: the mosaicity tilt, the average crystallite size, and the inhomogeneous strain. However, in our case, broadening due to inhomogeneous strain along the longitudinal direction does not affect the lateral transverse scans [146]. Therefore, we take into account only the tilt of the crystallites relative to the sample surface (ΔM), and the lateral correlation length (ξ_x) corresponding to mean size of defects. The transverse scan broadening due to the mosaicity tilt, noted $\beta_{\Delta M}$, is given by $\beta_{\Delta M} = \Delta M \cdot S$, with S the scattering vector modulus, and can be modeled by a Gaussian shape (β_G). The broadening due to the lateral correlation length, noted β_x, is considered to be $\beta_x = 1/\xi_x$ according to Scherrer's law, and can be modeled by a Lorentzien function (β_L). The transverse scan being regarded as Voigt function (a linear composition of a Gaussian profile and a Lorentzien one), its peak broadening (β) is expressed by the following parabolic relationship [147]:

$$\beta^2 = \beta_L \beta + \beta_G^2 . \qquad Eq.\ 4\text{–}8$$

Note that here "IB" is used as the abbreviation of "integral breadth" that is measured from the experimental profile and is a unique value for one peak. However, the notation "β" is used to expresse the "broadening" that can be dissociated into multiple components originated from the mosaicity tilt, the twist, or the defects and having different shapes (Gaussian or Lorentzien).

By applying the relationships of $\beta = IB(S)$, $\beta_{\Delta M} = \Delta M \cdot S$ and $\beta_x = 1/\xi_x$, the last equation becomes:

$$\left(\frac{IB(s)}{S}\right)^2 = \frac{1}{\xi_x}\frac{IB(s)}{S^2} + \Delta M^2 \qquad Eq.\ 4\text{–}9$$

where IB(S) is the measured broad peak IB of the transverse scans for different diffraction order reflections (i.e. 002, 004 or 006).[146] Then, if we plot $(\frac{IB(s)}{s})^2$ as a function of $\frac{IB(s)}{s^2}$, one should obtain a straight line, with ΔM and ξ_x respectively given by the intercept and the slope. We call this a "Williamson-Hall-like" (WHL) plot [145].

In practical case, the strong reflection points are usually not aligned with the weak ones since they are sensitive to different types of defect. Therefore, ΔM and $\xi_{x\text{-APD}}$ are extracted from the 002 and 006 transverse scan broadenings that are considered mainly due to the APD defect contribution as explained above. The extracted $\xi_{x\text{-APD}}$ corresponds to the average APD size in the lateral direction in the case of low defect density of other nature. It also corresponds to the mean distance between two antiphase boundaries (APB), in the case of a high APB density[141] and equilibrium between phase and antiphase domains. Moreover, since the ΔM in the crystal remains the same when performing 004 RSM, the straight line connecting the 004 point and the intercept allows the extraction of the defect correlation length related to other type of planar defects (ξ_x). The detailed transverse scan analyses (IBs, QF, WHL plots) will be shown along with the samples for growth condition optimization.

4.2 Growth condition optimization towards APB density reduction

Since we have focused on the structural improvement of the GaP/Si platform rather than on the XRD technique itself, we present the studies of MTs and APDs in two separate chapters. However, both defects are generated from the interface, and we believe that the effect of growth parameters on MT elimination and on APD density reduction is not independent from one to another. In the last chapter, we have found that a two-step growth sequence, using first a MEE technique followed by a MBE one (along with appropriate growth temperatures) have led to a dramatic lowering of the MT density (< 1% as volume fraction for a 45-nm-thin GaP layer) with an appropriate surface smoothness (0.3 nm r.m.s.). In this section, a more general study will be reported to minimize the APD density, based on the previously optimized parameters (growth temperature, two-step sequence), the substrate surface preparation, and other growth conditions like the Ga coverage, use of

AlGaP maker layers etc. Table 4.1 lists the main samples studied in this chapter, along with their detailed growth parameters.

Table 4.1 The main samples studied in this chapter, with their detailed growth conditions. The common parameters such as substrate of Si(001) 6°-off, surface cleaning using the "optimized HF" procedure, and the Ga prelayer and are not shown in the table for clarity.

Sample	Thickness, mode, and temperature	Ga amount per cycle for MEE *
S1319	45 nm GaP by MEE at 350°C	0.9 ML
S1330	10 nm GaP by MEE at 350°C + 35 nm GaP by MBE at 500°C	0.9 ML.
S1296	5 nm GaP by MEE at 350°C	1.1 ML.
S1297	5 nm GaP by MEE at 350°C	0.85 ML.
S1298	5 nm GaP by MEE at 350°C	0.93 ML.
S1480	10 nm GaP by MEE at 350°C + 35 nm GaP by MBE at 500°C	0.75 ML for the first three cycles and 0.9ML for the rest
S1477	10 nm GaP by MEE at 350°C + 4 × (2 nm $Al_{0.2}$GaP by MEE + 50 nm GaP by MBE at T), with T=500°C, 535°C, 565°C and 600°C	0.75 ML for the first three cycles and 0.9ML for the rest
* 1. For MEE: Growth rate = 0.1 ML/sec. 2. For MBE: Growth rate = 0.2 ML/sec., Ga flux = 2.3×10^{-7}Torr, P flux = 1.1×10^{-6}Torr.		

4.2.1 Annihilation of APD at high growth temperature

a Reduction on APD density evidenced by TEM images

This study has been carried out on a series of 20-nm-thin GaP layers grown on Si(001) substrate 4° off along the [110] direction, by MEE at respectively 350 °C, 400 °C, and 580 °C. Here I present the APD characterization using TEM imaging. The experiment has been carried out in collaboration with A. Ponchet and J. Stodolna at CEMES in Toulouse, France. The images have been recorded using a Philips CM30 in high resolution or conventional mode with an acceleration voltage of 300 kV. The specimens were prepared by mechanical polishing and ion thinning. Figure 4.6 shows the plan-view TEM dark field (DF) images of the samples. The black contour lines in the image indicate the emerging APB and the black spots likely correspond to the projection of self-annihilated APB. We can find from the images that the APB density decreases and the APD size increases when the growth temperature increases. XRD studies[95] revealed that the correlation lengths of APDs are respectively 17.4 nm, 17.2 nm and 22.5 nm for these samples, also indicating larger APDs at higher temperature (>500°C). The reduction of APD density at higher temperature can be explained by the fact that the emerging APBs lying on {110} planes tend to kink to the{111} planes or {112} planes, leading to a self-annihilation[50,148–150] (see detailed discussion in the Section 4.3).

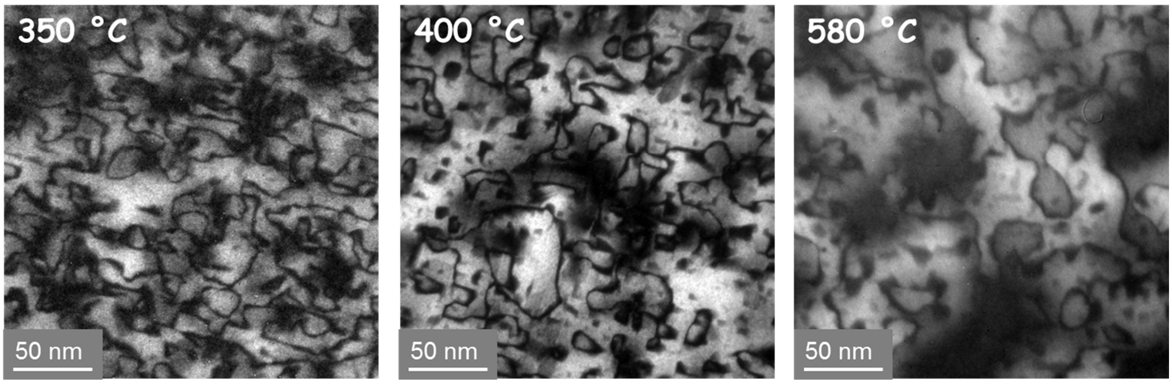

Figure 4.6 Plan-view TEM DF images for the 20-nm-thin GaP/Si 4°off grown by MEE mode at increasing temperatures. (CEMES)

Although higher growth temperature lowers both APD and MT density (synchrotron XRD studies showed the absence of MT at 580 °C[86]), the surface roughness increases, as shown in the cross-sectional TEM DF images of the three samples (Figure 4.7). For the sample grown at 350 °C, the surface is relatively flat, with a slight undulation caused by the emergent APBs. For sample grown at 400 °C, the domains become larger and the surface undulation becomes sharper. At 580 °C, in addition to the emergent APBs, deep grooves forms at the top of the APD annihilation regions, leading to a very rough surface.

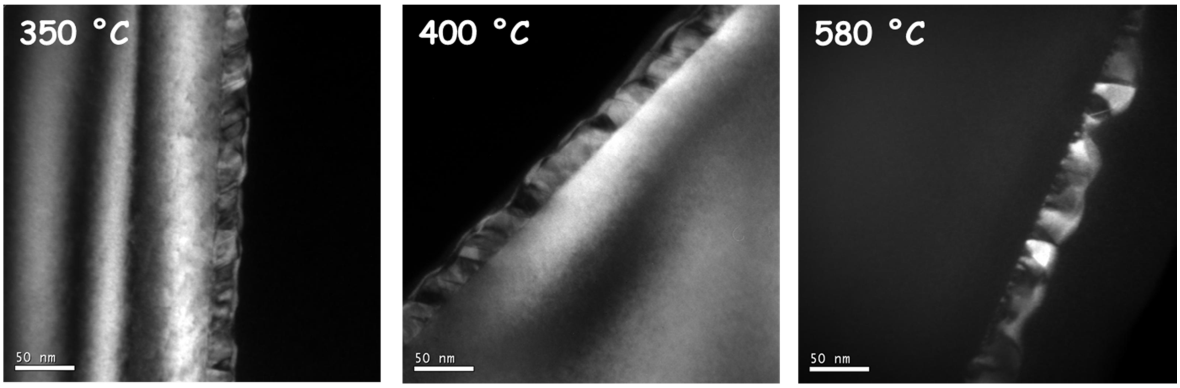

Figure 4.7 Cross-sectional TEM DF images of the 20-nm-thin GaP/Si 4°off grown on MEE mode at increasing temperatures. (CEMES)

Indeed, the TEM technique has been long ago developed and widely used to investigate the planar defects such as APDs in epitaxial layers.[148,149,151] The TEM DF technique is very sensitive to the presence of APDs, with a typical black and white contrast (one phase domain to the other). Figure 4.8 shows two magnified TEM DF images, clearly evidencing two types of APDs: the triangle shaped self-annihilated APDs (SA-APD) are formed at the GaP/Si interface and annihilated within the layer, while the emerging APDs (E-APD) cross through the whole layer up to the layer surface. It is also evidenced that the surface roughness is closely related to a high density of APDs, especially the emerging APDs.

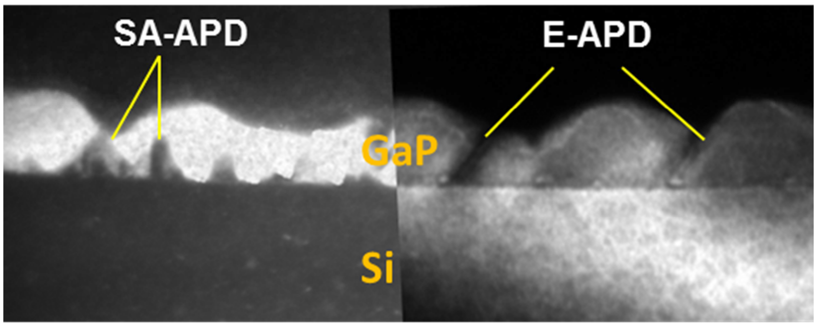

Figure 4.8 Evidence of two types of APDs by cross-sectional TEM DF image. (CEMES)

The TEM technique is a powerful technique for obtaining local information at the sample surface or in a cross section, and is capable to visualize both self-annihilated APBs and emerging APBs. XRD transverse scan analysis, on the other hand, allows statistical evaluation of defect density in large volume, but can’t distinguish the two types of APBs. XRD measurement combined with TEM images and other microscopy techniques guarantees a complete study of sample structural quality.

b Investigation of surface roughness related to APDs

It is very interesting that the density of both MT and APDs is reduced at higher temperature but the surface roughness increases, since the surface roughness is proved to be directly related to the APDs and hence is expected to be lowered down when APD density decreases. Indeed, this phenomenon can be explained by the deep grooves due to the APDs annihilation as seen in Figure 4.8.

This suggestion is consistent with the AFM observations on the series of 45-nm-thin GaP layers grown by MBE at increasing temperatures (350 °C, 500 °C, and 550 °C) that have been presented to demonstrate the MT density evolution as a function of growth temperature (see Section 3.3.1). Figure 4.9 shows the 5×5 μm^2 AFM images and the height analysis profiles extracted along the [110] direction for these samples.

For the sample grown at 350°C, small GaP domains in the order of 100 nm are homogeneously distributed with an average pit depth of about 8 nm, leading to an r.m.s. roughness of 2.06 nm. For the sample grown at 500°C, the average size of GaP domains along the [110] direction is much larger, in the order of 200 nm. 6 pits with an average depth of 35 nm are observed in a surface of 5×5 μm^2. The mean r.m.s. roughness is measured to be 2.60 nm. When the temperature increases to 550°C, larger GaP domains are formed with a pit density of 4 pits/5×5 μm^2, signature of larger APD domains. The pit depth is about 41 nm and the r.m.s. roughness is 4.35 nm. Observations in larger zones (50×50 μm^2) were also performed and the above results remained.

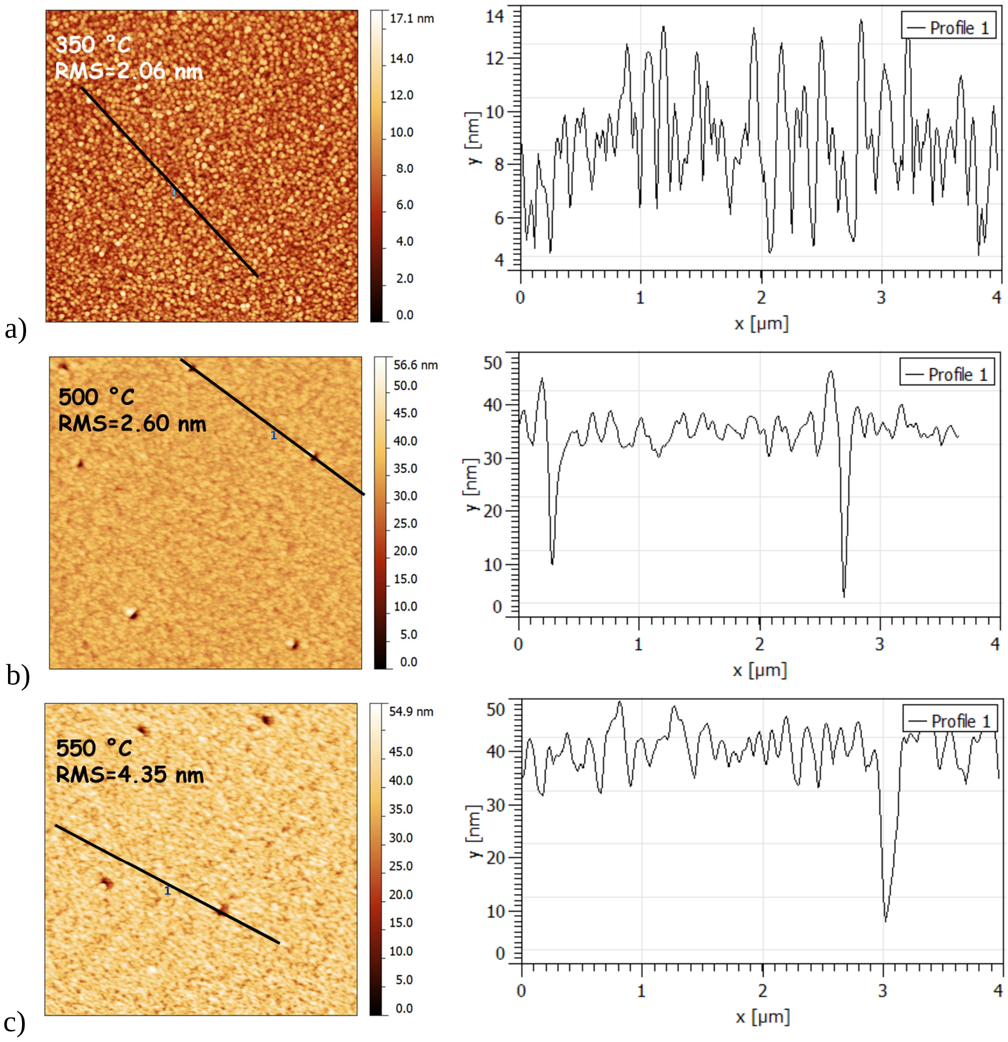

Figure 4.9 5×5 μm^2 AFM images and height profiles extracted along the [110] direction for a series of 45-nm-thin GaP/Si samples grown by MBE at 350 °C, 500 °C and 550 °C.

c APD annihilation using two-step growth sequence

The two-step growth sequence is believed to reduce the emerging MTs and APDs during the second growth phase at higher temperature,[53,131–133] and has shown its efficiency in structural quality improvement in the last chapter. Here we will present its effect on APDs density reduction. Firstly let's look at the sample S1319, a 45-nm-thin GaP/Si 6°-off sample grown using the one-step MEE procedure at 350°C. Figure 4.10 represents the detector images acquired at the center of the 00L nominal Bragg positions, at the Beamline BM02 under the same experimental conditions as S1330 (Figure 4.4).

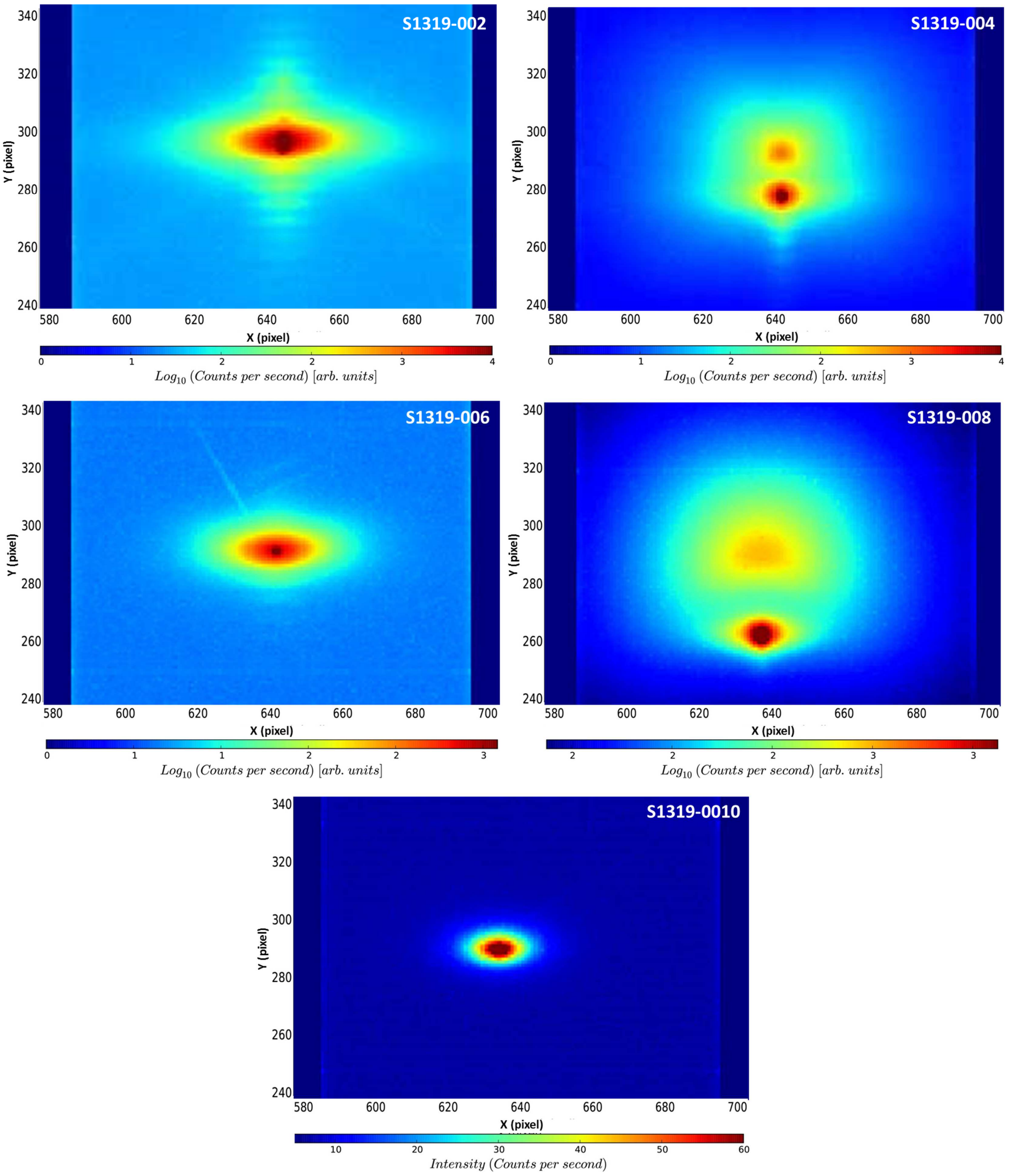

Figure 4.10 Detector images of S1319 centered at the nominal Bragg positions of the nearly specular 002, 004, 006, 008 and 0010 reflections, carried out on the BM02 beamline at ESRF.

The incident X-ray beams are in the direction [-1-10] (azimuth “az1”). The main characteristics observed on S1330, such as the intense thin peak, the lateral streaks on 002 reflection and the Si diffuse contribution on strong reflections, remain on this sample.

The transverse scans have been extracted and fitted using the same method as the sample S1330. The profiles are not shown here for clarity. Figure 4.11 shows the results of the transverse scans analysis for S1319 based on the detector images on two azimuths. The IB of the broad peaks as a function of diffraction order is displayed in Figure 4.11 a). The IBs for the same diffraction in two azimuthal directions are close to each other, suggesting that the defect size anisotropy along the [110] direction is not very evident. The 002, 006 and 0010 IBs are roughly of similar values, that is to say, the broadening is mainly due to the defect-induced correlation length which is constant on all the 00L reflections, rather than the mosaicity tilt that is proportional to diffraction order, as explained by Herres.[83] The 008 peak is much broader than the 004 one, probably because of the intensity loss at higher diffraction. Figure 4.11 b) shows the evolution of QF as a function of diffraction order. The higher QF on the 004 strong reflection implies that the APD contribution is dominant on weak reflections and these reflections can be treated separately in the WHL analysis.

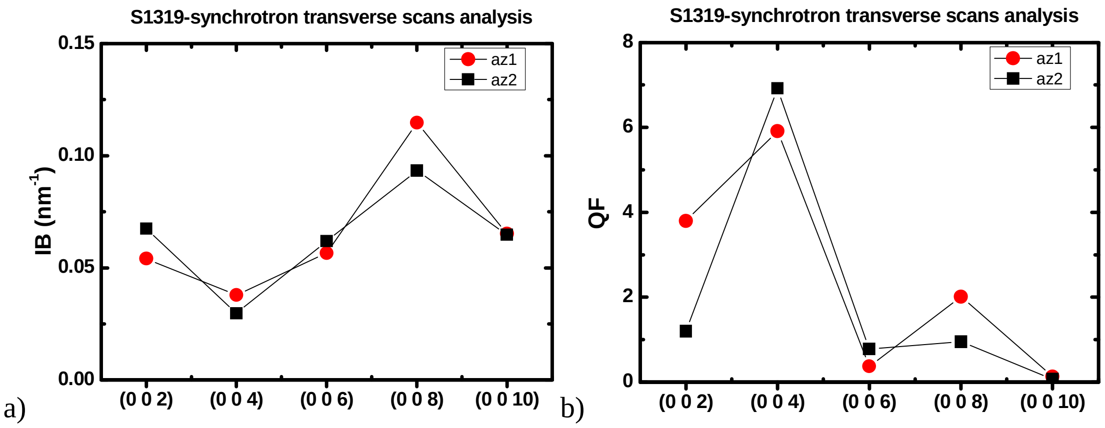

Figure 4.11 IB and QF as a function of diffraction order, deduced from the transverse scans of S1319 extracted from the detector images.

Corresponding WHL plots are shown in Figure 4.12, also for two azimuths. The error bars are evaluated taking into account both the fluctuation of the incident X-ray beam intensity (about 10%) and the Pseudo-Voigt Fitting. The 002, 006 and 0010 weak reflection points are well aligned in two azimuths. The mosaic tilt angles are deduced to be respectively 0.0014° and 0°. $\xi_{x\text{-}APD}$, the lateral correlation length related to APDs, is measured to be 18.6±0.2 nm and 14.8±0.2 nm, respectively for two azimuths. These results, along with the slightly higher QF on 002 at “az1”, suggest a privileged APD annihilation along the [110] direction. The correlation length ξ_x due to other defects is deduced only from the 004 reflection, taking into consideration the eventual intensity loss on the 008 peak.

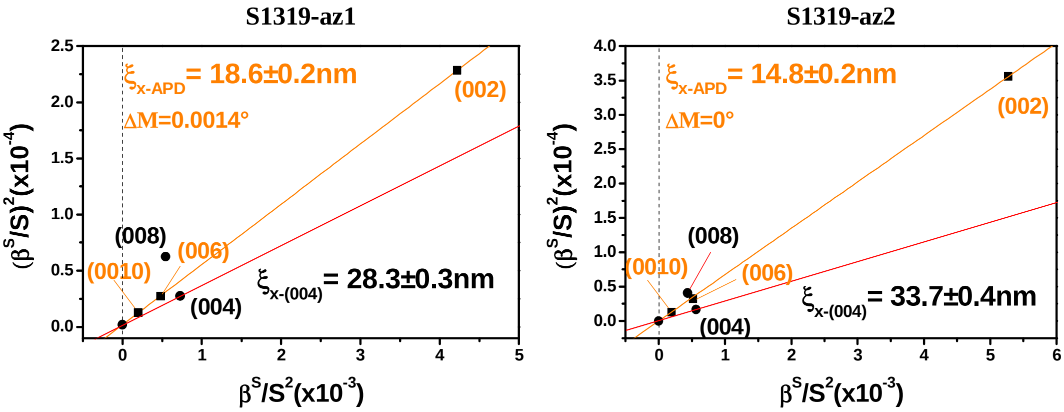

Figure 4.12 WHL plots of S1319 for synchrotron image analysis at two azimuths

For S1330, we have already shown the lab RSMs and synchrotron detector images taken at “az1” as well as the corresponding transverse scans (Figure 4.2 to Figure 4.5). The synchrotron images for “az2” is not shown here for clarity, but it has to be mentioned that the 0010 reflection is of very weak intensity and exhibits a peak that cannot be correctly fitted by the Pseudo-Voigt function (Figure 4.13). Therefore, the 0010 reflections at both azimuths are not taken into account in the transverse scan analyses for this sample.

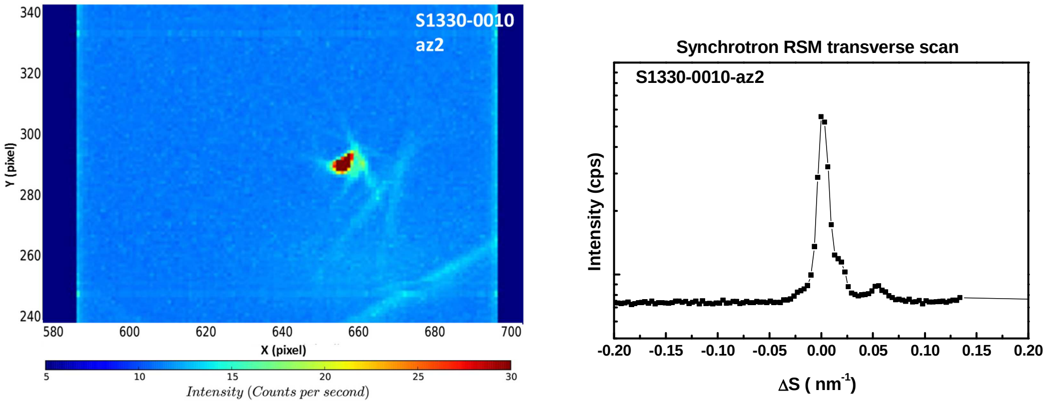

Figure 4.13 Synchrotron reciprocal space image around the GaP 0010 reflection at the azimuth “az2”, displaying an irregular shaped diffraction spot. The extracted transverse scan doesn’t permit a correct Pseudo-Voigt fitting.

Figure 4.14 shows the evolution of IBs and QFs as a function of diffraction order for both synchrotron measurements and the laboratory measurement, for sample S1330. When compared to the sample S1319, we find that the differences of IBs on same diffraction order are greater in two azimuths, indicating a more evident anisotropy. This is confirmed by the WHL plot analysis which reveals that the lateral correlation lengths $\xi_{x\text{-APD}}$ are respectively 31.2±0.2 nm and 22.5±0.2 nm for two azimuths, as shown in Figure 4.15, signature of privileged APD annihilation along the [110] direction. The 008 reflections always present larger peaks than the 004. The QFs on 002 of S1330 is much larger than that of S1319, suggesting a better crystalline quality with weaker APD densities. This is also confirmed by the greater $\xi_{x\text{-APD}}$ values deduced from the WHL plot.

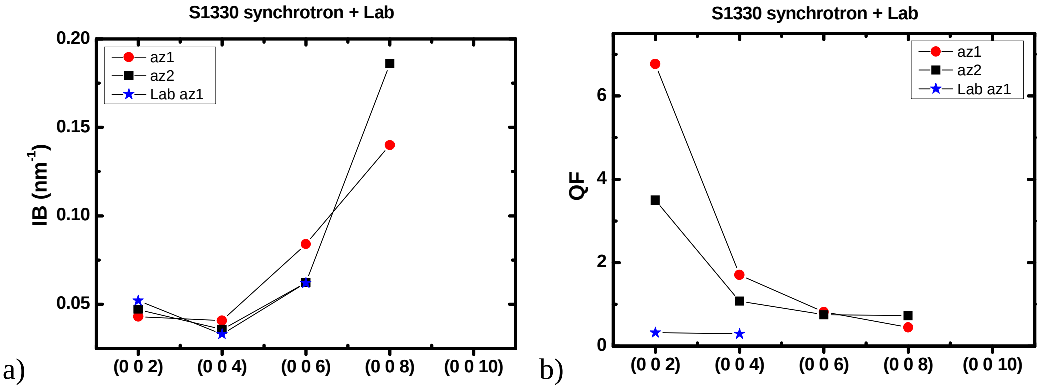

Figure 4.14 Transverse scan analysis of S1330 at two azimuths for synchrotron measurements and at “az1” for laboratory measurement: IB and QF as a function of diffraction order.

The $\xi_{x\text{-APD}}$ in both azimuths of S1330 are greater than S1319, indicating a reduction of APB density in both directions. Besides, the correlation length of other defects deduced from the 004 peak is much larger than S1319 at “az2”, showing an improvement of defect elimination using the two-step growth procedure, although it is impossible to extract the ξ_x at “az1”, since the straight line linking the 004 point and the ΔM point gives a line without slope.

Finally, a large difference is seen between the results extracted from laboratory RSMs and the synchrotron images at the same azimuth: both QF and $\xi_{x\text{-APD}}$ measured on lab setup are smaller. This is due to the difference in X-ray beam characteristics and instrumental configurations (lateral divergences leading to different beam coherence lengths). Different samples are therefore comparable only under the similar experimental conditions.

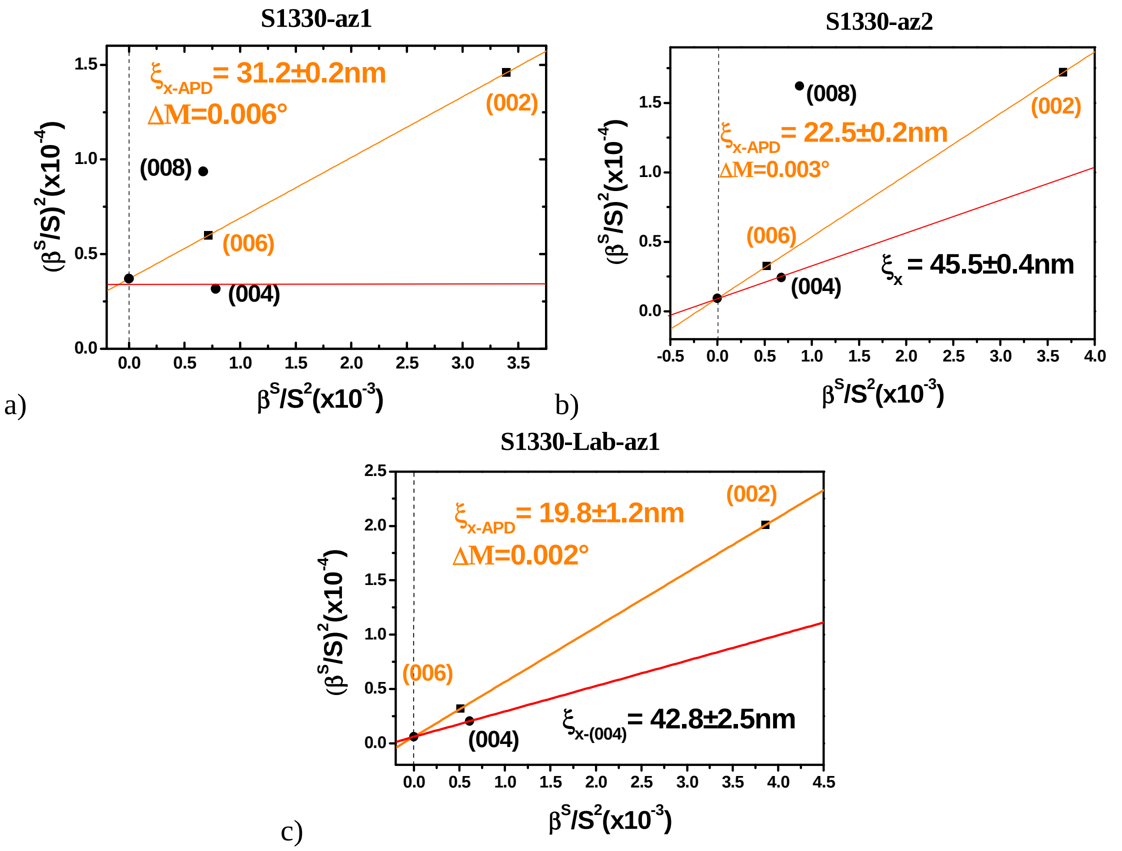

Figure 4.15 Williamson-Hall-like plot of S1330 deduced from transverse scans extracted from a) Synchrotron detector images at azimuth "az1", b) Synchrotron detector images at azimuth "az2" and c) Laboratory RSMs at azimuth "az1"

Since the WHL analysis gives an evaluation of mean distance between APBs but doesn't permit distinguishing the emerging APD and the self-annihilated APDs, cross-sectional STEM Bright Field (BF) images are used for complementary visualization of the APDs with high resolution. The APBs constituted of "III-III' or "V-V" atomic bonds are regarded equivalent to stacking faults and evidenced by diffusion contrast in the STEM-BF imaging. The experiments have been carried out in collaboration with M. Bahri, G. Patriarche, L. Largeau from LPN in Marcoussis, France (OPTOSI ANR project). Figure 4.16 shows two STEM-BF images of S1330. Although an APD is self-annihilated, the annihilation occurs very close to the epilayer surface, making the APD passing through almost the whole layer (Figure 4.16 a)). Emerging APBs are clearly shown in Figure 4.16 b), resulting in pits on the layer surface. The average distance between the emerging APBs are estimated in the order of 20 nm, consistent with the XRD measurement.

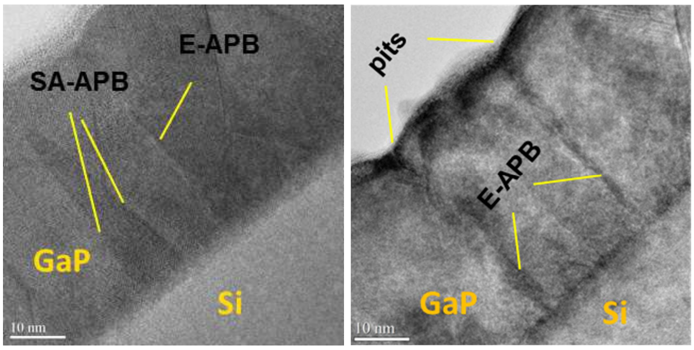

Figure 4.16 Cross-sectional STEM-BF image of S1330 for a) evidence of two types of APB, and b) showing surface pits originating form E-APB. (LPN)

In brief, higher growth temperature (especially on the overgrowth stage of the two-step sequence), contributes to an annihilation of APDs, but however leads to surface roughness due to the pits resulted from the APDs. In order to lower the defect densities and to increase the surface smoothness, it was of great importance to avoid or annihilate completely the APDs as close as possible to the GaP/Si interface by choosing appropriate growth parameters, as shown hereafter.

4.2.2 Limitation of the APD formation at the interface

As well known, the APDs are formed during the polar on non-polar growth and are favored either 1) by the single atomic steps at the substrate surface[67] or 2) by a non-ideal Ga coverage on the Si surface (non-uniform Ga coverage leading to coverage of P in some places on the Si terrace). Theoretically, one can avoid the APD appearance by 1) obtaining a Si substrate bi-stepped surface and 2) an ideal Si coverage by only one species (Ga in our case). In addition, it has been proposed that contaminations (like carbon) at the substrate surface before GaP growth can also contribute to APD formation.[45,152,153] Therefore, the surface preparation[154,155] and the Ga coverage are two essential parameters to be controlled, in order to limit the APD formation.

a Si surface preparation

It was suggested that the APDs could be partially avoided via double stepped Si(001) surface, realized on a vicinal Si substrate with a miscut of a few degrees towards the [110] direction and a step bunching obtained with an annealing procedure.[45,54,75,156] On this basis, most of the samples studied in this thesis are grown on a Si(001) substrate misoriented of 6° towards the [110] direction. However, such a Si surface always presents an unintentional additional miscut, disturbing the expected regular and periodic bi-atomic steps. Carbon also affects the Si surface reconstruction.[157] Careful chemical cleanness, thermal treatment, and homoepitaxial growth of Si buffer layers are needed to obtain a bistepped GaP/Si interface.

It has already described in Section 2.2 that using the “HF optimized” cleaning procedure leads to a smooth and defect free surface. Here, we focus on the GaP/Si interface quality without any Si buffer layer at first. The STEM-HAADF imaging strongly depends on atomic number Z[158,159] and thus has been used to observe the GaP/Si interface as well as the Ga and P atoms arrangement. Figure 4.17 a) shows the high resolution cross-sectional STEM-HAADF image of the sample with the GaP layer directly deposited on the Si surface prepared by the modified RCA process. The GaP/Si interface is diffuse and waviness. Figure 4.17 b) shows the interface for the sample with GaP grown on the Si substrate cleaned by the “HF optimized” process. The interface is more clearly distinguished. But no periodic atomic steps can be observed.

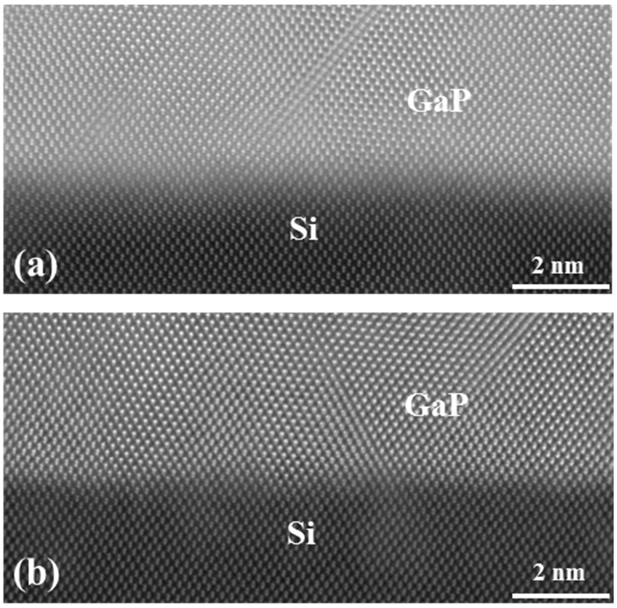

Figure 4.17 Cross-sectional HRSTEM-HAADF images of (a) GaP epilayer directly grown on the modified RCA process prepared Si surface, (b) GaP epilayer directly grown on the “optimized HF” process prepared Si surface. (CEMES)

Then, a homoepitaxial Si buffer layer has been deposited on the chemically cleaned Si substrate at 800°C using silane (at a 6.10^{-3} Torr pressschroederure) in the UHVCVD growth chamber and transferred under UHV to the MBE growth chamber for GaP overgrowth. The GaP/Si interface of the sample with a Si buffer layer prior to the GaP growth is clearly sharp and displays an appearing periodicity of 6 to 7 atoms, as shown in Figure 4.18.

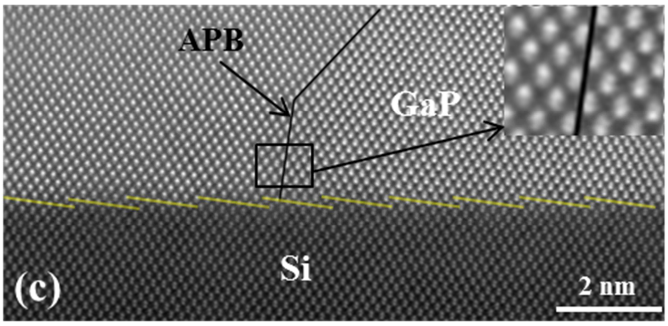

Figure 4.18 Cross-sectional HRSTEM-HAADF image of GaP epilayer grown on the optimized HF process prepared Si surface, with a homoepitaxial Si buffer layer prior to the GaP growth. Inset is the magnified image of the enclosed zone, showing the inversion of Ga-P dumbells from one side of an APB to the other side. (CEMES)

Indeed, a surface reconstruction has been observed by RHEED during the growth. A 2×n pattern is observed, as shown in Figure 4.19 a). Figure 4.19 b) illustrates the beam direction with respect to the sample misorientation. The 2× pattern is observed when the electron beam is parallel to the [110] direction (perpendicular to the step edges) and the ×n pattern is observed in the [1-10] direction (parallel to the step edges), with n the number of atoms on the terraces along the [110] direction, already widely discussed in the literature.[160]

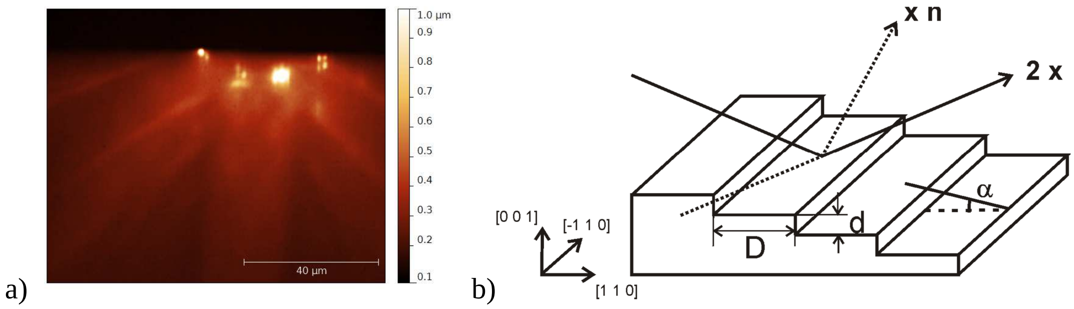

Figure 4.19 a) RHEED Pattern showing a 2×n pattern observed during the homoepitaxial growth of Si buffer layer, b) Illustration of RHEED beam directions with respect to the atomic steps on the Si surface

The mean value of n can be roughly calculated with n = L/l, where L and l represent the diffraction spots interval from respectively the surface lattice and the terrace length along [110] direction[161]. Figure 4.20 shows the cross profile of peak analysis from the RHEED pattern. The average values of L and l are measured to be 57.4 and 8.1 (arbitrary units) respectively, giving rise to n ~ 7, corresponding to a terrace length of 2.69 nm.

As calculated in Table 2.1, the theoretical terrace length for a bi-stepped Si(100) surface is 2.58 nm, each step terrace thus containing on average 6.7 atoms.

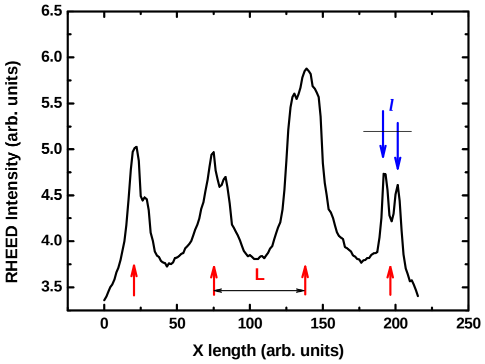

Figure 4.20 RHEED pattern cross profile analysis for measurement of average L and l values. Red upward pointing arrows indicate the diffraction spots from the surface lattice along [1 1 0] direction and blue downward pointing arrows indicate the diffraction spots from the steps length.

Therefore, both the measurements from the RHEED pattern and the theoretical calculation confirm the observation on the HRSTEM-HAADF image, and indicate the presence of bi-atomic steps. However, despite the obtaintion of a bi-stepped GaP/Si interface, APBs are still visible in the GaP/Si sample with a Si buffer (see the black solid line in Figure 4.18 and corresponding inset). APBs can be evidenced by specific contrasts in atomic resolved images, as reported for instance by Narayanan[162] using HRTEM and Bayer[163] using HRSTEM HAADF technique. Here, as in ref.[164,165], the inserted magnified image shows clearly the inversion of the Ga-P dumbbells from one side of the APB to the other side. Notice that the APB is generated on the terrace but not at the step edge, which confirms the importance of controlling the initial group III or group V coverage of the Si surface before any III-V growth, even if performed on a bi-stepped Si surface.

b Ga coverage at the initial growth stage

A set of 20 ML (about 5 nm-thin) GaP layers grown by MEE at 350°C on Si substrate misoriented by 6°, with a difference on the Ga coverage per MEE cycle (S1297 with 0.85 ML Ga, S1298 with 0.93 ML Ga and S1296 with 1.1 ML Ga) have been used to study the effect of the Ga amout at the very first growth stage.

Firstly MTs are studied by synchrotron XRD method, since the scattering intensities by 5-nm-thin GaP layers are so weak that cannot be correctly integrated on lab setup. Figure 4.21 shows the synchrotron detector images around the 002 reflection at azimuth “az1”, with indicent X-ray beams along the [-1-10] direction and the nominal Bragg positions at $\omega = \theta + 6°$. The exposure time is 300 seconds.

MT signals are very weak on S1296 (with 1.1 ML of Ga), a little stronger on S1298 (with 0.93 ML of Ga) but not observed on S1297 (with 0.85 ML of Ga). The surface roughness measured by AFM images reveals that S1298 presents a most smooth surface, with a r.m.s. value of only 0.26 nm[166]. Indeed, the total Ga amount per cycle is considered to have a strong effect on the epilayer's smoothness and the defect level, since an excess Ga tend to form metallic droplets and induce the melt-back etching of the Si surface[164,167], or promote 3D GaP islands at the Si surface,[65] where treading defects were generated.

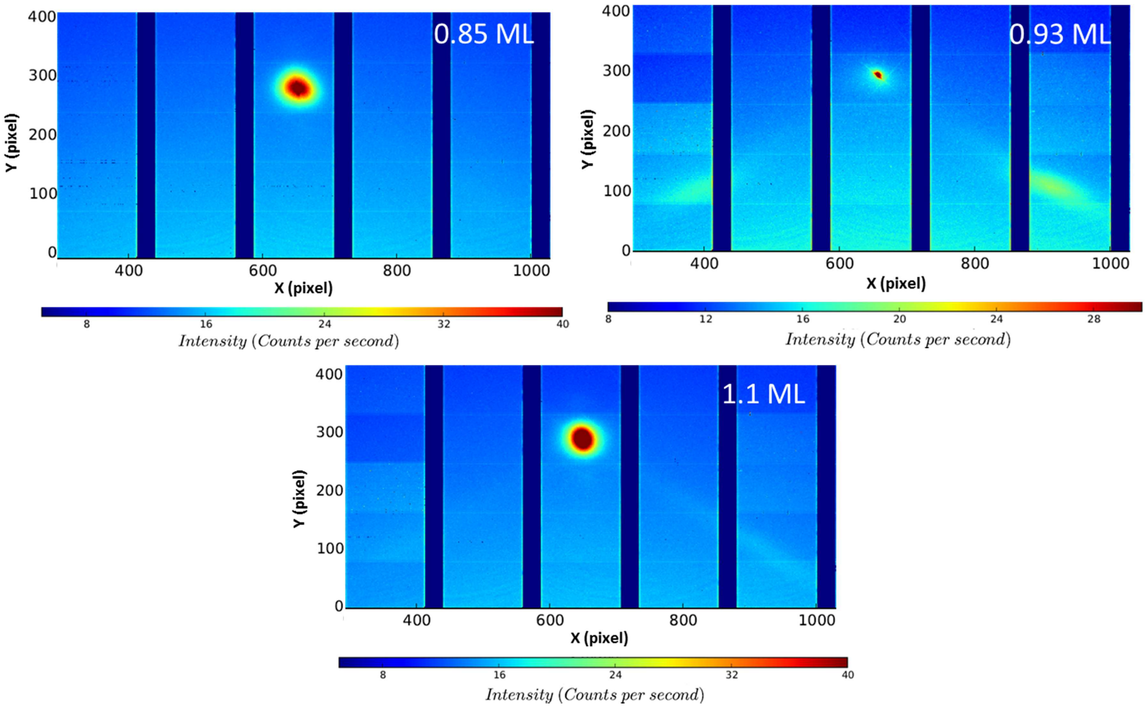

Figure 4.21 Detector images around GaP 002 carried out at the BM02 beamline at ESRF, evidencing weak MT signal on S1296 (1.1ML) and S1298 (0.93ML), but no MT signal is observed on S1297 (0.85 ML).

Transverse scans were extracted using the same method as S1330. However, since the 006 reflections are too weak to provide an effective evaluation of IB, the evaluation of APD-induced correlation length $\xi_{x\text{-}APD}$ was performed only on the GaP 002 peak broadening, using the following equation instead of the WHL method, assuming that the mosaicity tilt can be neglected.

$$IB = 1/\xi_{x\text{-}APD} \qquad \text{Eq. 4–10}$$

Table 4.2 lists the IBs, QFs as well as the deduced $\xi_{x\text{-}APD}$ values for the three samples. Note that the lateral experimental resolution for the transverse scans is 0.00327 nm^{-1} in reciprocal space. All samples show a very short $\xi_{x\text{-}APD}$ (in the order of 10 nm), indicating high density of APDs.

Table 4.2 Integral breadth, correlation length and QF deduced from GaP 002 reflection for S1296, S1297 and S1298

	Ga Coverage (ML)	az1 //[-1-10]			az2 // [-110]		
		IB (nm^{-1})	$\xi_{x\text{-}APD}$ (nm)	QF	IB(nm^{-1})	$\xi_{x\text{-}APD}$ (nm)	QF
S1297	0.85	0.094	10.70±0.08	49.3±1.3	0.155	6.47±0.05	6.8±0.3
S1298	0.93	0.148	6.67±0.08	1.1	0.221	4.53±0.07	0.6
S1296	1.1	0.116	8.64±0.04	0.4	0.128	7.82±0.04	0.2

The most remarkable observation on these samples is the strong anisotropy of crystalline quality (represented by the QF value) along the two azimuthal directions for sample S1297 (0.85 ML Ga). The anisotropy indeed depends also on the Ga coverage. Figure 4.22 shows the detector images centered on the GaP 002 reflection for sample S1297 at two azimuths. An intense central peak is seen at both azimuths, and “az1” displays very thin diffuse along the horizontal direction while a round-shape diffuse spot is observed at “az2”. The diffraction CTR is larger in the vertical direction when compared to the 45-nm-thin samples, due to their smaller layer thickness.

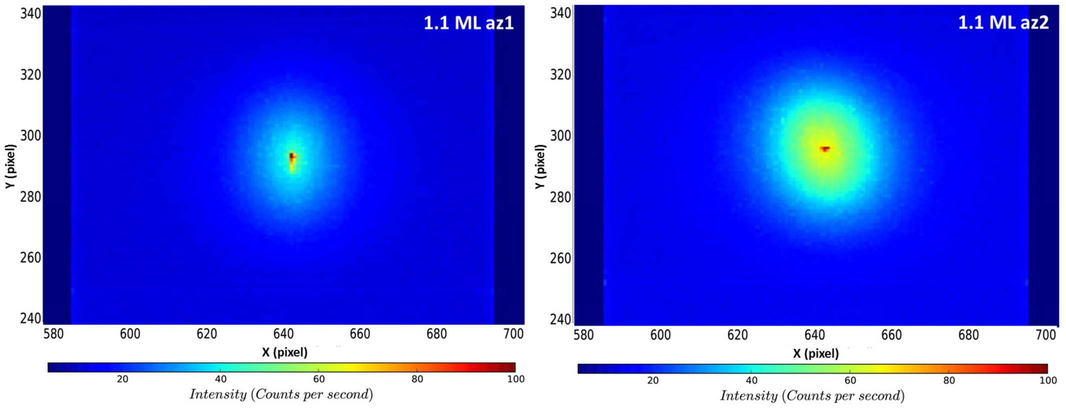

Figure 4.22 Synchrotron detector images of S1297 (0.85 ML) at two azimuths, displaying a strong anisotropy.

Both transverse scans display a two-component line shape, as shown in Figure 4.23. The thin peak is more intense at “az1” and the broad peak is more diffuse at “az2”, leading to a QF of 49.3 for “az1”, more than 7 times larger than the other azimuth.

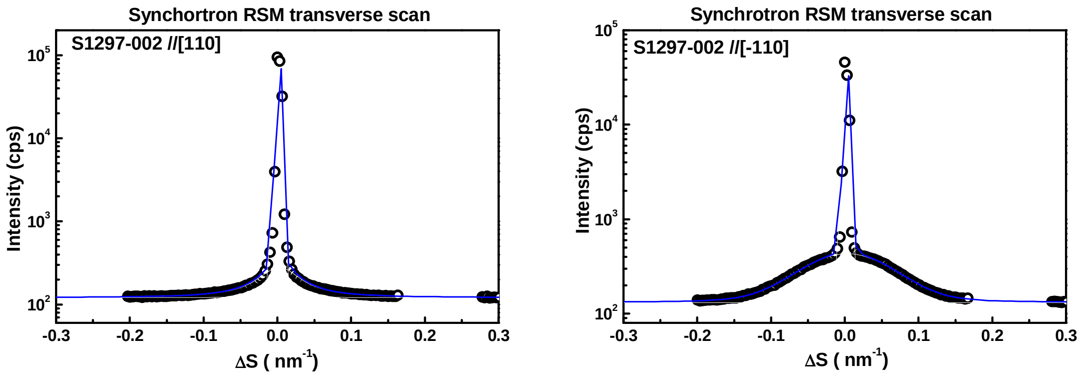

Figure 4.23 Transverse scan profiles extracted from the synchrotron reciprocal images for S1297 at two azimuths, fitted by Pseudo-Voigt functions.

Then let's look at the diffraction image around GaP 002 on S1296 with 1.1 ML Ga (Figure 4.24). The visual intense points at the center of the GaP spots correspond to only two-pixel width and can't be considered as a thin component. The diffuse in lateral direction at "az1" is much weaker than that at "az2", but their IBs are very close to each other as shown in Table 4.2. The QF of "az1" is only twice larger than that of "az2". In brief, this sample also shows anisotropy along two azimuthal directions, but the anisotropy is less distinct than on S1297 with 0.85 ML Ga.

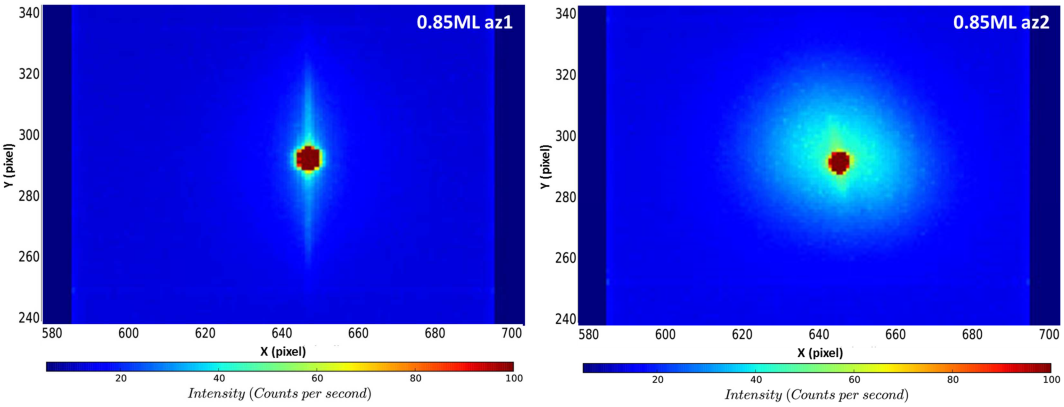

Figure 4.24 Synchrotron detector images of S1296 (1.1 ML) at two azimuths.

c Optimized two-step growth sequence

As demonstrated above, the Ga coverage at the initial stage strongly affects the formation of both MTs and APDs. Sample grown with smaller Ga coverage (here 0.85 ML) is free of MTs within the detection limit of the synchrotron experiment and shows better crystalline quality with a much higher QF along the [110] direction (along the atomic steps), although the smoothest surface is obtained with 0.93 ML of Ga coverage. The anisotropy is firstly related to the substrate vicinality and then to the role of Ga coverage, which will be discussed as APD formation and annihilation mechanism in the section 4.3.

On this basis, we have made a slight change to the initial growth stage of the sample S1330: each of the first 3 MEE cycles consists of 0.75 ML instead of 0.9 ML Ga deposition followed by 60 seconds growth interruption and then the P deposition. The other parameters remained unchanged, that is, a total 10-nm-thin GaP layer grown by MEE at 350°C followed by 35 nm GaP growth by MBE at 500°C, which has led to sample S1480. S1480 displays a high structural quality. The MT volume fraction evaluated by pole figure (Figure 4.25 a)) turns out to be less than 1% and the surface smoothness measured on 5×5μm^2 AFM image (Figure 4.25 b)) is about 0.4 nm.

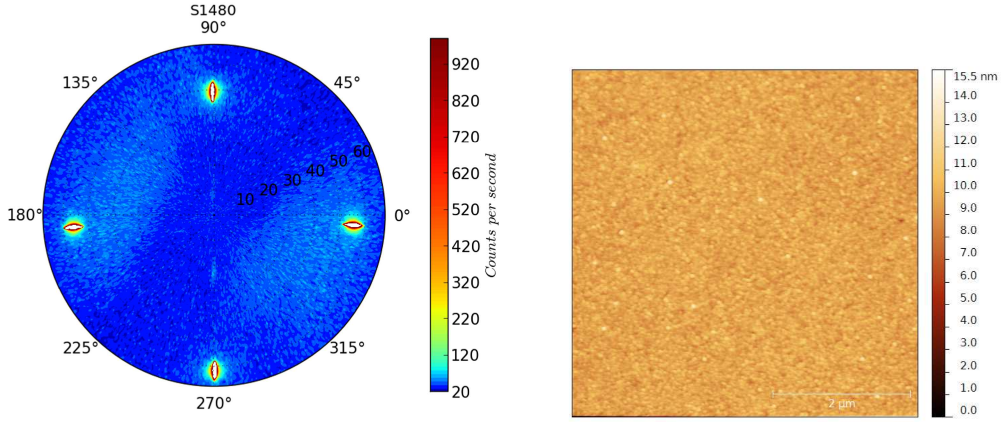

Figure 4.25 a) Pole figure of S1480, showing very weak MT intensity, b) 5×5μm^2 AFM image of AFM, the r.m.s. roughness is measured to be 0.4 nm.

Figure 4.26 presents the cross-sectional HRSTEM-BF images of the S1330 and the S1480. Several single isolated MTs are generated at the interface of S1330 (Figure 4.26 a)), while no MT is observed on S1480, which is also confirmed by observations on larger scales in different parts of the sample. This observation is in good agreement with what has been observed by Volz et al.,[50] who already showed that an excessive initial Ga coverage increased the number of generated defects. With these growth conditions, the TEM imaging at large field of view allows to give an estimation of the linear density of MTs as low as 5 MTs/μm on S1480.

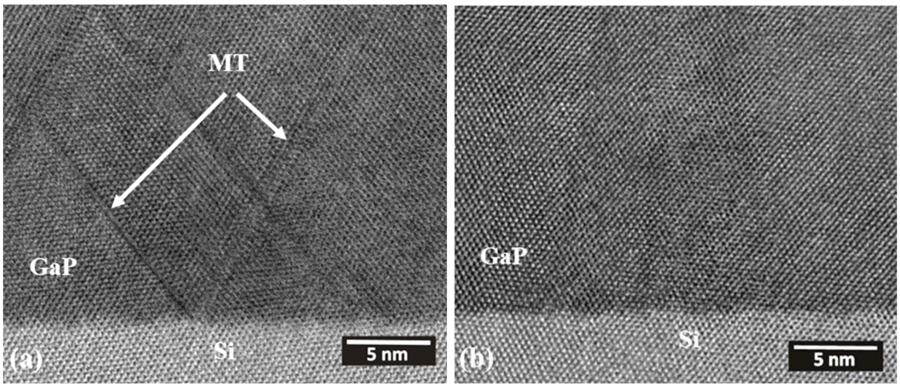

Figure 4.26 Cross-sectional HRSTEM-BF images of a) S1330 and b) S1480. (LPN)

Figure 4.27 shows the RSMs around the GaP 002, 004 and 006 nearly specular reflections taken on lab setup on S1480. Integrations along S_x direction have been performed to extract the transverse scans but are not shown here for clarity.

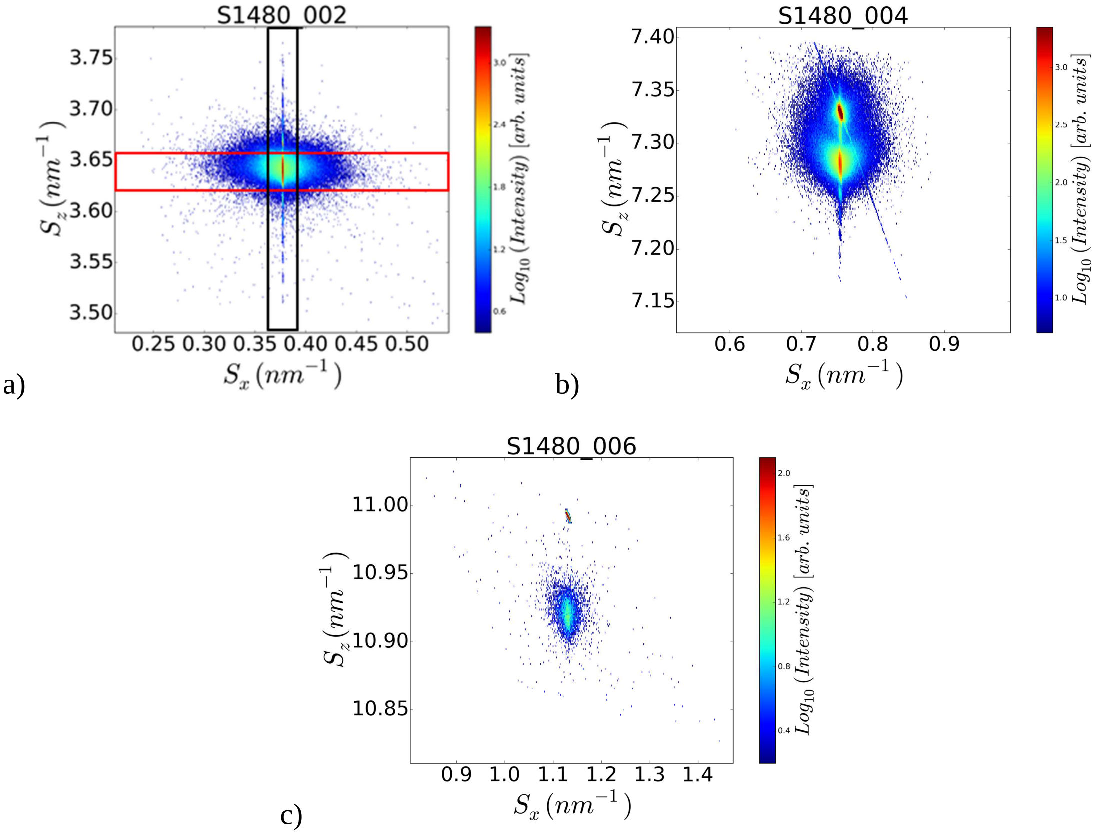

a)

b)

c)

Figure 4.27 RSMs around GaP 002, 004 and 006 nearly specular reflections of S1480.

Figure 4.28 shows the results of the transverse scan analyses. IBs deduced from the broad peaks are respectively 0.037 nm^{-1}, 0.018 nm^{-1} and 0.034 nm^{-1} for 002, 004 and 006 reflections. The QF value for 002 is estimated at 0.98, much higher than that of S1330 measured under the same conditions (0.21), which can be considered as a signature of a better crystallographic quality with fewer defects. WHL analysis (Figure 4.28 b)) gives the $\xi_{x\text{-APD}}$ and ξ_x values of 27.0±1.8 nm and 55.6±3.3 nm, also larger than those of S1300 obtained in the same experimental conditions (19.8±1.2 nm, and 42.8±2.5 nm). That is to say, both APD and other type of defects have been reduced by the optimization of MEE procedure at the initial growth stage.

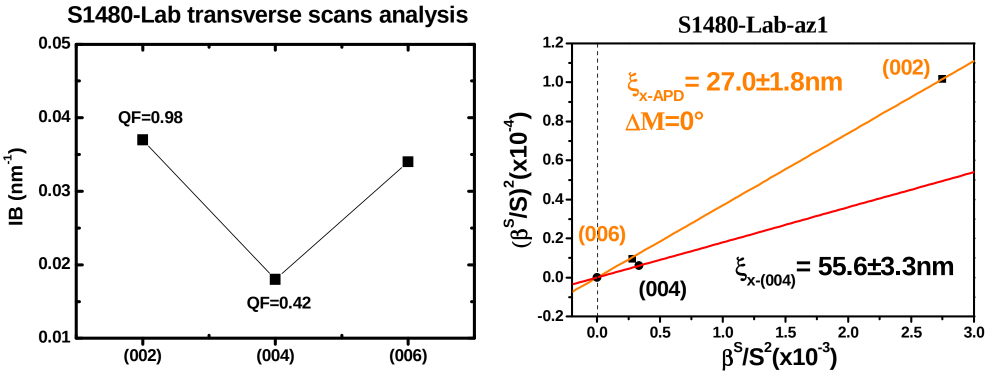

Figure 4.28 Laboratory RSMs transverse scan analyses for S1480: a) IB and QF as a function of the diffraction order, b) WHL plot revealing $\xi_{x\text{-APD}}$ = 27.0±1.8 nm ξ_x 55.6±3.3 nm.

Furthermore, the CTR along the S_z direction on the 002 RSM of S1480 represents regular fringes, as shown in Figure 4.27 a), which is missing on sample S1300. The integration along S_z direction at the central S_x position within a small width allows an extraction of the S_z profile (Figure 4.29 (a)). Distinct and regular thickness fringes are evidenced on the profile, indicating good structural quality of the thin epitaxial layer (low defect density, and low surface and interface roughness).

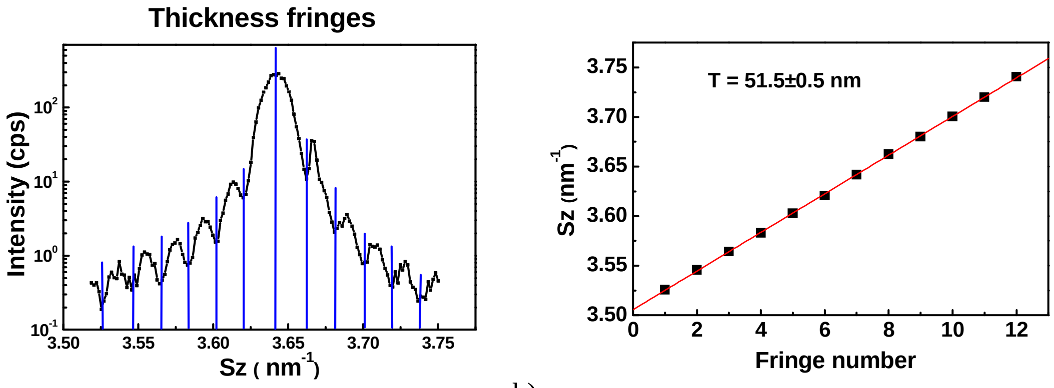

a) b)

Figure 4.29 Sz profile extracted from laboratory GaP 002 RSM, evidencing thickness fringes and the measurement of layer thickness from the fringes.

The S_z position of the fringe valleys are quoted and represented as a function of the fringe numbers (Figure 4.29 b)). The points are fitted by a straight line whose slope is considered to be inversely proportional to the correlation length of the crystallographic planes along the growth direction, that is, the layer thickness. Therefore, the layer thickness is calculated to be 51.1±0.5 nm, a little bit larger than the nominal layer thickness of 45 nm.

Complementary observations are provided by cross-sectional STEM-BF image (Figure 4.30). Some APBs are generated at the interface and are self-annihilated in the layer within about 20 nm. APBs threading to the surface result in some small pits but the surface is relatively smooth. The mean APB distance is estimated on the order of 30 nm, in good agreement with the XRD analysis. Several MTs are also observed originated from the GaP/Si interface. These observations confirm the relevance and reliability of our XRD method showing the strong advantages of a nondestructive method without sample preparation and with statistical averaging other a large area. However, this STEM-BF picture shows the presence of very thin MT that could not be detected by using either rocking-curve or pole figure method on our XRD setup.

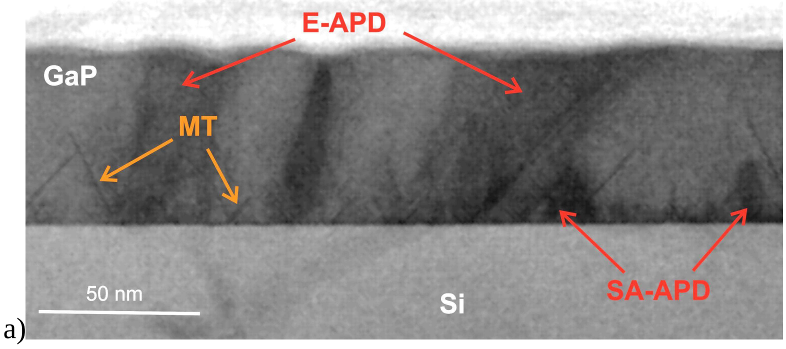

Figure 4.30 Cross-sectional STEM-BF image of S1480. (LPN)

To conclude, sample S1480, with a 0.75 ML Ga coverage for the first three MEE cycles exhibits a better crystalline quality than S1300 (with 0.9 ML Ga coverage). The APDs formation can be avoided by bi-atomic steps and an ideal Ga coverage on the Si surface. Nevertheless, we can never guarantee the ideal “mono” coverage in the epitaxial growth even if the growth procedure is started by one ML of Ga.

Despite the improvement of structural properties by limiting the formations of APDs from the interface, especially along the [110] direction, optimization of GaP/Si interface quality and Ga coverage don’t allow the subsequent annihilation of the already formed APDs. There are still some APBs emerging to the surface in optimized sample (S1480), as shown in Figure 4.30. Other solutions should be therefore found to force the annihilation of the APDs during the growth.

4.2.3 APD annihilation by AlGaP marker layers

It is very important but also very difficult to control the initial growth stage to prevent the APD formation. Besides, we have also worked on the annihilation of APDs in case where the APDs are already formed. The sample S1477 has been grown using the same procedure as S1480 for the first 10-nm growth, followed by successive 50-nm-thin MBE GaP layers grown at increasing temperatures: 500 °C, 535 °C, 565 °C and 600 °C. Each MBE layer was separated by a 2-nm-thin AlGaP marker grown at the same temperature as the following GaP layer. Figure 4.31 gives a schematic representation of the S1477 growth architecture. The initial purpose of these markers was to “mark” the boundaries between the different growth temperatures and, therefore, to study by TEM the effect of these growth parameters.

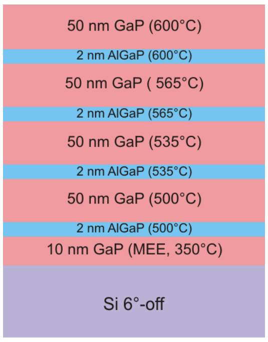

Figure 4.31 Sketch of the growth procedure of S1477

MT density evaluation has been carried out by pole figure. No visible MT signal is observed as shown in Figure 4.32. There are two possibilities: either the MTs have been totally eliminated, or reduced down to the diffractometer detection limit (less than 0.3% in volume fraction).

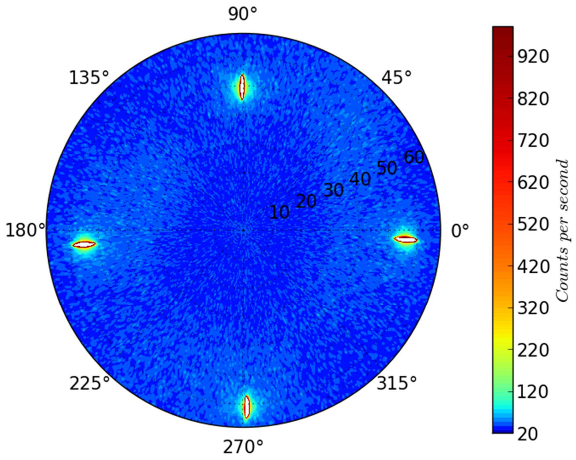

Figure 4.32 Pole figure on sample S1477 where no MT signal is observed

Figure 4.33 shows the 5×5 μm^2 AFM image and the height profiles along the [110] (profile 1) and [1-10] (profile 2) directions. The r.m.s roughness is measured to be 3.32 nm, larger than that of the sample S1480 grown under the same conditions as S1477 for the first 10 nm but followed directly with a 40-nm-thin GaP layer grown at 500°C. The average pit depth is about 10 nm, with several deep grooves (up to 30 nm) in a 5×5 μm^2 region. The GaP domains are distributed homogeneously along the two directions, without distinct anisotropy. Thus the surface roughness might be attributed to the atomic mobility at the epilayer surface that is enhanced by the high overgrowth temperature, rather than to the APDs, since most APDs are proved to be annihilated within the first 10 nm as shown after.

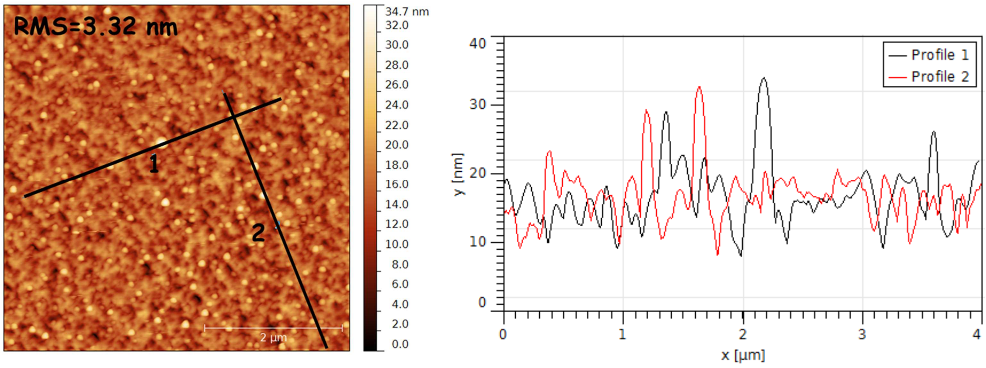

Figure 4.33 5×5μm^2 AFM image S1477 showing surface r.m.s. roughness of 3.32 nm, and the height profiles along the [110] and the [1-10] directions.

Laboratory XRD RSMs around the GaP 002, 004 and 006 nearly specular reflections have been carried out and are presented in Figure 4.34. Note that the overall thickness is larger than the critical one so that the layer is partially relaxed as indicated by the slight S_x shift of the GaP peak center with respect to the Si peak. The GaP CTRs are less elongated in the S_z direction when compared to the 45-nm-thin samples, since S1477 has a much greater thickness 410 nm.

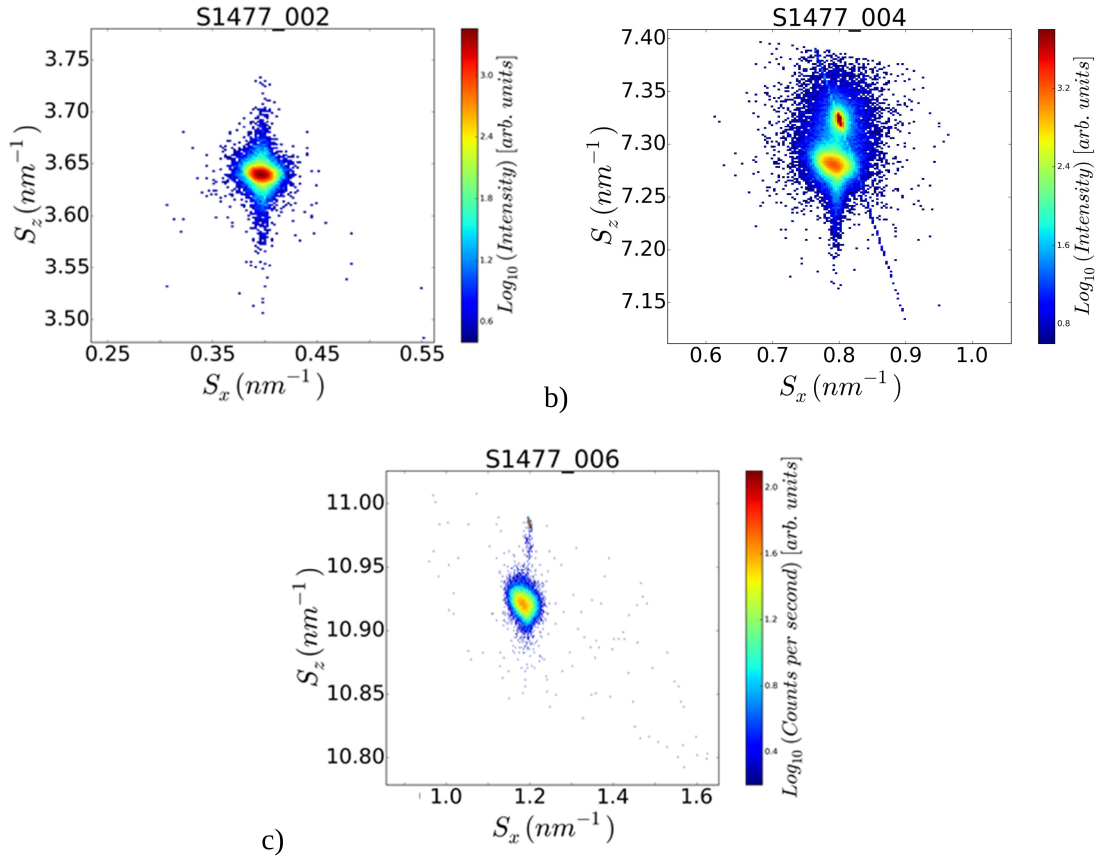

a) b) c)

Figure 4.34 Lab RSMs on 002, 004 and 006, reflections for S1477

The corresponding transverse scans are extracted, fitted, and presented in Figure 4.35. The 002 scan shows a two-component shape, with a thin component relatively larger when compared to S1330 and S1480, probabely due to the relaxation induced dislocations. Only one peak can be observed on the 004 and 006. If we compare the IBs and QFs of S1477 with the other two samples, we can find that S1477 shows thinnest 002 and 006 peaks, signature of larger APD-induced correlation lengths. But its 004 peak broadening is much larger than the other samples, and also much larger than its own 002 and 006 peaks. The larger thin peak on 002, the lack of thin peak on 004, and the IB value on the 004, are probably due to the partial relaxation of the GaP layer.

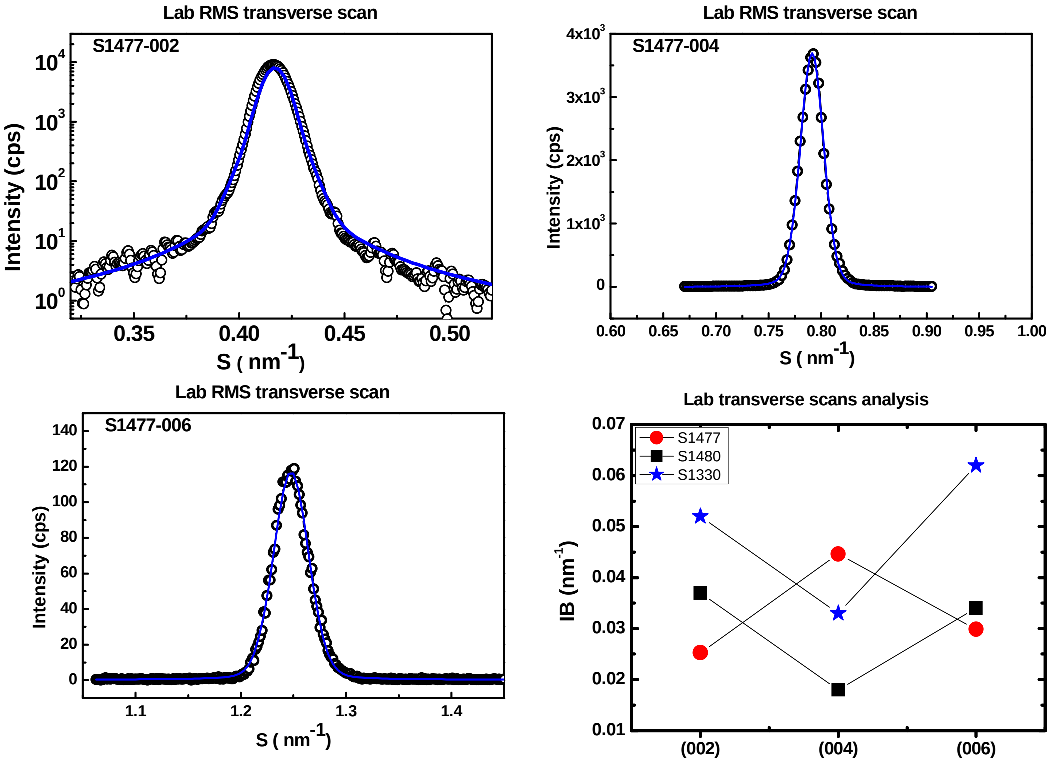

Figure 4.35 Transverse scans extracted from the lab RSMs, fitted by Pseudo-Voigt functions, and the evolution of IBs as a function of diffraction orders for S1477, S1480 and S1330

Figure 4.36 shows the WHL plot of S1477. The lateral correlation length related to APDs ($\xi_{x\text{-APD}}$) and other defects (ξ_x) are estimated to be 48.6±3 nm and 64.3±4 nm, larger than that of all the previous samples, showing the best structural properties from the XRD analysis point of view, on both MT and APB density.

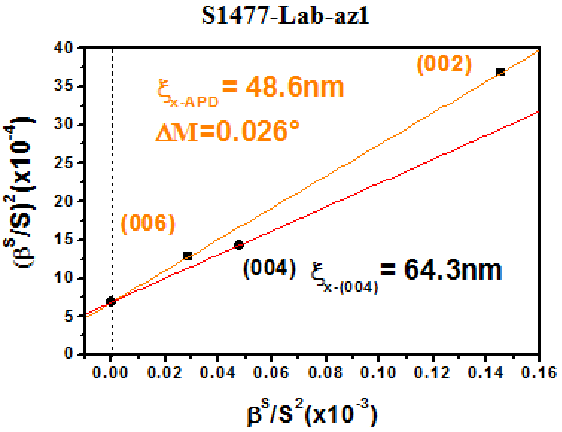

Figure 4.36 WHL plot of S1477

It must be noticed that these analyses by XRD are less precise than on other samples, due to the partial relaxation. Indeed, the distribution of strain and mosaicity tilt can be measured by using a quick scanning X-ray diffraction microscopy technique (called K-map) developed at the ID01 beamline at ESRF,[168–170] which will be briefly introduced as perspectives works of this thesis.

Figure 4.37 shows the cross-sectional STEM-BF image of S1477. The AlGaP layers are almost parallel to the GaP/Si interface, indicating a 2D growth until the layer surface. A large density of APBs is generated at the GaP/Si interface but most APBs are annihilated within the first 10 nm. The measurement of average APB density from larger field of observation shows 10 APBs /µm above the first AlGaP marker and 3 APBs /µm above the second one.

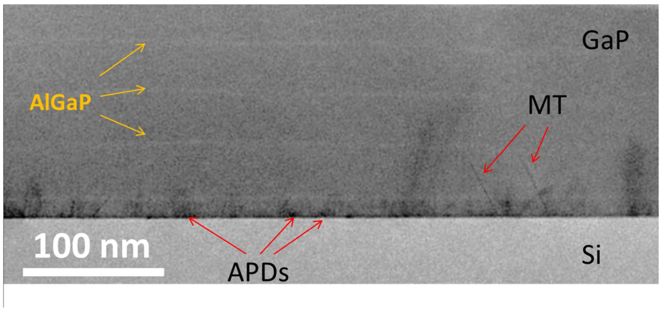

Figure 4.37 STEM-BF image of S1477. (LPN)

In order to confirm the reproducibility of the APD annihilation by using the AlGaP marker layers, a second sample has been produced using the same recipe as S1477 and was analyzed by TEM imaging. Figure 4.38 shows the TEM-DF image of this sample. A large density of APDs is formed at the interface but more than 80% are annihilated within the first 10 nm.

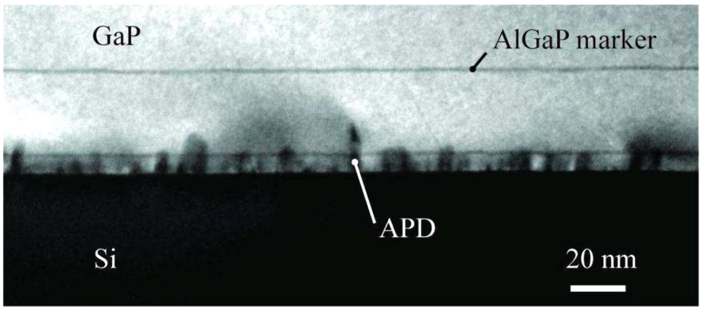

Figure 4.38 TEM-DF image showing a huge density of APDs formed at the interface and annihilated within 10 nm. (CEMES)

Moreover, a third sample grown under the same conditions has been studied using the STM. The 400×400 nm^2 tunnel current image shows a flat GaP surface without grooves, indicating a complete annihilation of APBs, as shown in Figure 4.39 (left). The surface topography image on a 75×75 nm^2 surface (right) evidences that all the GaP surface dimers are oriented along the [110] direction, parallel to the expected atomic step edges, signature of the presence of single domain and the bi-atomic steps.

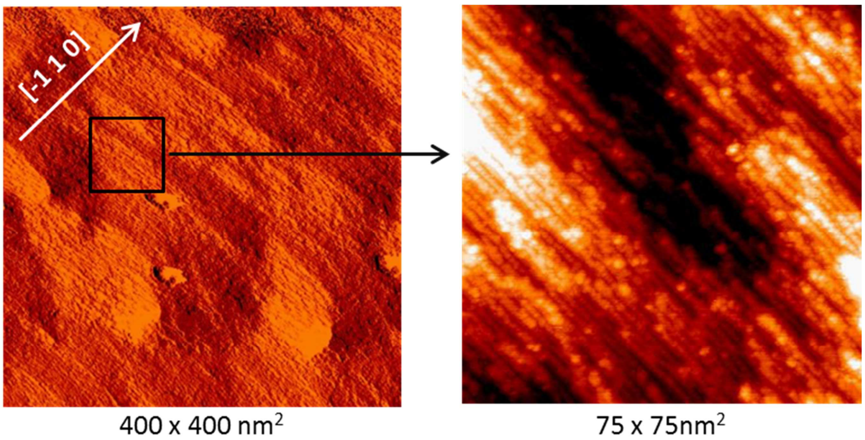

Figure 4.39 400×400 nm^2 STM tunnel current image and 75×75 nm^2 surface topography image of the sample grown using the same recipe as S1477.

4.2.4 Conclusions

Firstly we have presented that the APD density was reduced by using higher growth temperature, either on MBE mode, MEE mode or the two-step sequence. Then we have demonstrated the limitation of APD formation from the interface during the very early stage of growth, by optimizing the Si surface preparation and the Ga coverage. A strong anisotropy of APD size and structural quality was observed on sample grown with low Ga coverage (0.85 ML). Finally, we showed a reproducible annihilation of already formed APDs by overgrowth at higher temperatures separating by AlGaP marker layers. Recent sample is free of MTs and has a very weak APD density.

4.3 Discussions and hypothesis on APD annihilation

In the last section, the APD prevention and annihilation were experimentally reported, along with optimization of growth parameters such as temperature, Si surface preparation, Ga coverage and the use of AlGaP marker layers. Nevertheless, the mechanisms are not very clear. This part is dedicated to a discussion, based on the literature and our experimental results, to achieve a better understanding of the APD formation and annihilation.

4.3.1 Propagation of APBs in low index {11n} planes

From the Figure 4.38, we can find that the annihilated APDs have different shapes and heights. Indeed, a triangle shaped self-annihilated APD has its boundaries lying only on the {111} planes as illustrated in Figure 4.40 a), and the emerging APBs are lying on the {110} planes as indicated by line AB in Figure 4.40 b). The other lines show that the APD of any other shape may have boundaries lying on various crystallographic lattice planes: CD parallel to {100}, DE parallel to {112} and EF parallel to {113}. It is obvious that the propagation of APBs in lower index {11n} planes leads to a faster annihilation of APD, close to the interface.

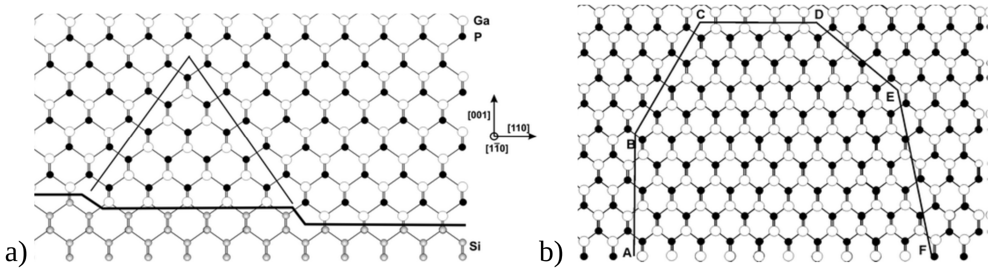

Figure 4.40 APBs in zinc blende structure on different crystallographic planes: AB parallel to {1 1 0}, BC: parallel to {111} CD: parallel to {100}, DE: parallel to {112}, EF: parallel to {113}[95]

Indeed, the {110} and {111} configurations are extrema situations and all other APB planes can be regarded as a composition of the two cases, as depicted in the model proposed by Lin et al. (Figure 4.41[171]). The lower index planes have a lower ratio of {110} to {111} terraces.

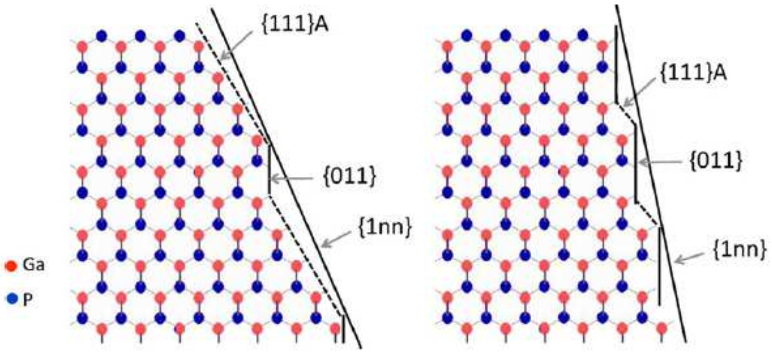

Figure 4.41 Illustrations of {1nn} APBs that consist of {110} and {111}A terraces. The ratio of {110} to {111}A terrace determines the APB plane and the proportion of Ga-Ga to P-P bonds.[171]

This decomposition was energetically proved true. The formation energies of the APBs were calculated by Rubel[172], using the ab initio Density Functional Theory (DFT). He found that the {110} APBs had a lowest formation energy (34 mV/A^2) and {111}

APBs had the highest (53 mV/A^2). The formation energies of {113} APBs and {112} APBs are located between the two values and are very close to each other.

From another point of view, all APBs have a ratio of Ga-Ga and P-P bonds depending on which plane they are located.[173] The {110} APBs composed of equal number of Ga-Ga bonds and P-P bonds are stoichiometric, with a ratio of 0.5. The APBs lying on {111} and {100} planes consist only Ga-Ga bonds or P-P bonds, with a ratio of 1 or 0. Although the {110} APBs are most stable at equilibrium position, the MBE deposition is well-known "far-from-equilibrium" deposition technique that prevents the atoms to migrate to the thermodynamically equilibrium positions. Assuming that there is an energetic preference for Ga-Ga bonds to P-P bonds, during the growth, Ga-Ga bonds were favored. Thus, lower-index planes, with a higher ratio of {111} to {110} planes, present higher proportion of Ga-Ga to P-P bonds, are favored for the APB propagation, leading to a fast annihilation.

This hypothesis can probably give an explanation to the APD annihilation by using the MBE overgrowth at higher temperature (for the two-step sequence). Indeed, the MEE growth at low temperature and lower growth rate is expected to provide a quasi-equilibrium 2D growth, in the purpose of preventing defect formation.

4.3.2 Post-growth annealing

Guo et al [79] have reported a APB-modified thermodynamic equilibrium mechanism to explain the APB migration. As mentioned above, O. Rubel[172] reported that the {110} APBs are most energetically stable at equilibrium, but the MBE growth is "far-from-equilibrium". The sample was therefore assumed to have APBs distributed statistically over all the {111} and {110} planes. During the post-growth annealing, the unstable APBs are first expected to kink toward the stable {110} position, as shown in Figure 4.42 a). On the other hand, the surface mobility enhanced by higher temperature make the atoms locate at the top of the APB to migrate towards more stable positions such as a vacancy on the top of the surface. These two effects will act as digging the GaP layer along the APB. As a consequence, anti-phase and main phase will be separated. A deep trench is created at the place of the APB, as shown in Figure 4.42 b). The APD is annihilated when this process takes place at its two sides. This mechanism can also be used to explain the APD annihilation and the high surface roughness on the samples grown at higher temperature.

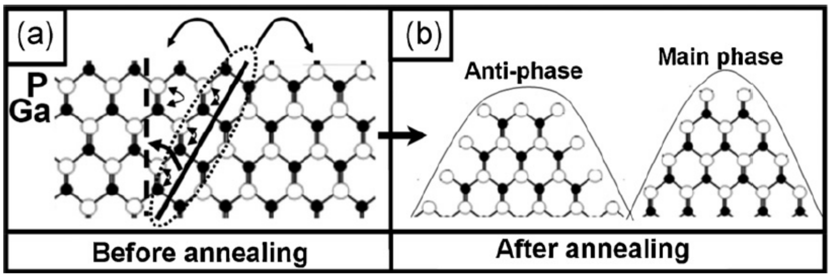

Figure 4.42 APB-modified thermodynamics mechanism: (a) the atoms on unstable APBs tend to migrate towards the more stable {110} APB positions, or other stable crystalline sites. (b) Crystalline islands of anti-phase and main phase with deep trenches are formed. [79]

4.3.3 Growth of main phase GaP over small APDs

Another proposition to the APD annihilation is the growth of main phase GaP over the small APDs due to the growth rate difference between them. The GaP main domain preferentially exhibits a P-stable 2×4 surface.[174] Assuming that the Ga adatom diffusion length is longer along the direction parallel to the P dimer bonding, Ga adatoms have a longer diffusion length in the [1-10] direction within an APD and along the [110] direction in the main phase. The difference of the diffusion length could result in different growth rates, so that the surrounding regions overgrow the APDs along the direction [110]. If the Si surface is covered by the main phase GaP nuclei and small APDs (as observed in our samples with low Ga coverage along the step direction), the APBs can serve as energy barriers preventing the migration of Ga adatoms from one domain to another, as illustrated in Figure 4.43 a). The larger surface of the main phase results in a longer diffuse length for the Ga atoms and keeps the growth rate difference on the two sides of the APBs. Finally, the APD is covered by the surrounding main phases. A trench may occur at the top of the annihilated APD (Figure 4.43 b))

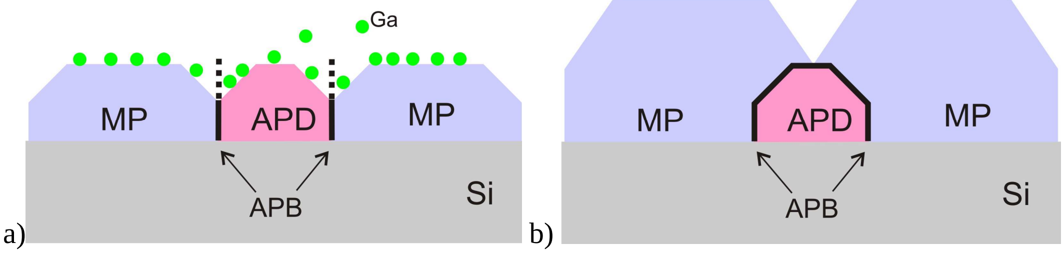

Figure 4.43 Illustration of the main phases overgrowing the small APD

4.3.4 Other important observations and possible interpretations

The height of the self-annihilated APDs was proposed to depend on their basal width, shown in TEM images[136] and according to DFT calculation[172]. On the one hand, when two APBs are close to each other with Ga-Ga bonds for one APB and P-P bonds for the other, the opposite charge distribution creates an attractive potential between the two APBs and lowers the formation energy. In this case, the {111} APBs are most favored, leading to a fast annihilation of the small APDs. On the other hand, it is energetically possible for the distant APBs growing in {110} planes to be kinked in the {112} or {113} planes, but it is hard to give preference to one or another since the formation energies of the two planes are very close to each other.

This proposition might be useful in the interpretation of the preferred APD annihilation along the [110] direction, and the strong anisotropy on the sample grown with lower Ga coverage in the first MEE cycles.

Figure 4.44 shows the cross-sectional STEM-BF image of S1632, GaP layers grown under the same conditions as S1477 on a nominal Si(001) substrate. The APDs formed at the interface are of greater size than in S1477. The facet inclined of 27.5° from the GaP (001) planes, corresponding to the (113) planes, is believed to be an APB, and results in the parallel facets (113) at the surface seen in the STM image. This also shows that the surface roughness is depending on APDs.

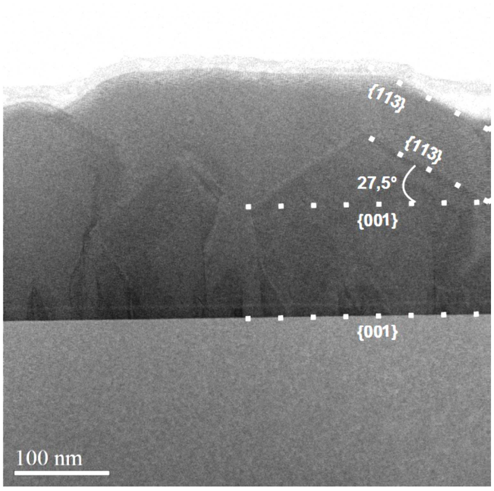

Figure 4.44 Cross-sectional STEM-BF image S1632, GaP layers grown on nominal Si. (LPN)

The presence of facets can also be observed on the STM image, as shown in Figure 4.45. The STM images have been performed in collaboration with P. Turban and S. Charbonnier at IPR in Rennes, France. The (113) boundaries can be found at the sample surface, and are related to the high density of APDs leading to the large surface roughness. A favored direction of the trenches and the (113) facets formation are observed along the [110] direction, corresponding to a higher APBs density in the [1-10] (or [-110]) direction.

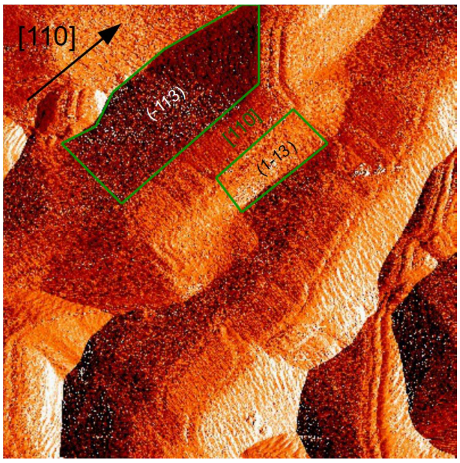

Figure 4.45 600×600 nm^2 STM image showing the preference of facet formation in the direction perpendicular to the steps

In the case of non-perfect coverage of initial Si surface by the Ga atoms (0.75 ML coverage here), the P atoms can be deposited directly on the Si surface and form an APD. The APD size is determined by the distance between non-covered regions, which can be influenced by the Ga diffusion length. It is therefore energetically possible to form smaller APDs along the atomic steps, since the step edges, serving as energy barriers, limit the Ga diffusion along the [110] direction.

The APD size can be also affected by the Ga amount during the initial deposition stage. A comparison between the 0.9 ML Ga coverage (S1330) and 0.75 ML Ga coverage (S1480) by cross-sectional STEM-BF images is shown in Figure 4.46. Very large APDs are generated from the GaP/Si interface of S1330 and no evident annihilation process has occurred, while several smaller APDs formed at the interface of S1480 are annihilated during the growth.

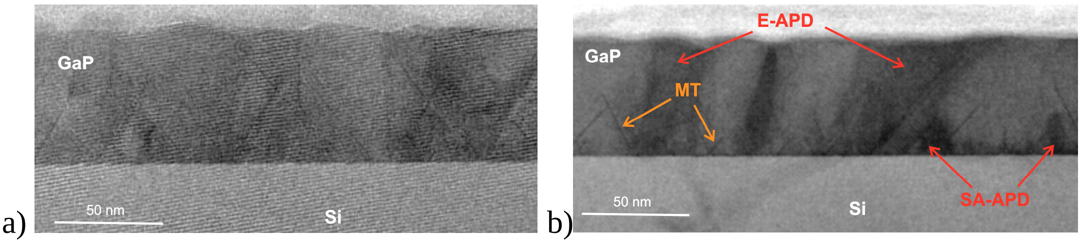

Figure 4.46 Cross-sectional STEM-BF image of a)S1330 (0.9 ML Ga) and b)1480 (0.75 ML Ga). (LPN)

4.4 Summary

We have presented the APD analyses based on transverse scans extracted from reciprocal space maps, using both laboratory and synchrotron XRD setups. The quality factor (QF) is considered to indicate the crystalline quality of the GaP layer (defect density, residual strain, etc.). The Williamson-Hall-like method is used to deduce the mosaicity tilt related to the crystallite misorientation with respect to the layer surface and the lateral correlation length which is related to the mean size of APDs, provided that the APD sizes are relatively homogenous and that other defects such as MTs are at a very low density. With the help of the XRD analyses along with surface roughness and morphology study by AFM and STM, and the local APD quantification by different TEM techniques, we have successfully optimized the parameters to achieve a great structural quality improvement. Growth temperature, substrate surface preparation, Ga amount per MEE cycle at the initial growth stage and AlGaP marker layers are shown to strongly affect the APD formation at the GaP/Si interface and the residual APD annihilation.

Abrupt GaP/Si interface of high quality displaying periodic bi-steps has been achieved by homoepitaxial growth of a Si buffer layer on the carefully prepared Si substrate surface, promising for limitation of the APD formation from the GaP/Si interface, but the presence of residual APBs indicates the importance of the control of other growth parameters. GaP layers with very low MT density (1% volume fraction), quite large APD sizes (about 27 nm) and smooth surface (r.m.s. of 0.4 nm) has been achieved by an optimized two-step sequence composed of: i) 10 nm GaP growth by MEE at 350°C (first 3 cycles with 0.75 monolayer (ML) of Ga/cycle + 37 cycles with 0.9 ML of Ga), and ii) 40 nm GaP growth at 500°C, using standard continuous MBE. Reproducible effective APD annihilation (more than 80%) has been observed within the first 10 nm on sample grown using the recipe of the optimized two-step sequence for the first 10 nm, followed by four 50 nm GaP growth by MBE at increasing temperatures, every two GaP layers separated by an AlGaP marker layer. This sample presents no MT and 3 antiphase boundaries (APB) per micron at the upper part of the layer as observed by TEM image.

The APD annihilation has been proposed to depend on the formation energies of the APBs in different planes. At higher temperature, the atoms in unstable APBs planes tend to migrate towards the more stable positions, either to the stable {110} APB planes or to the Si surface, leading to a digging effect and a deep trench at the initial APB position, resulting in a high surface roughness of the epilayer. The strong anisotropy observed at the vicinal Si surface in case of low Ga coverage can be explained by the assumption that smaller APDs are formed along the steps direction ([110] direction) due to the limitation of Ga diffusion along by the step edges. Smaller APBs can be then rapidly annihilated along the {111} APB planes close to the interface, or covered by the overgrowth of the surrounding main phase domains. In contrary, larger APDs observed on nominal Si surface or in the case of more Ga coverage, tend to annihilate along the {112} or {113} APB planes.

Chapter 5 General conclusions and perspective works

5.1 Summary and conclusions

This thesis is focused on the structural analysis of the GaP/Si heteroepitaxial layers and the quantitative evaluation of the crystal defects such as microtwins (MT) and antiphase domains (APD) in GaP layers, mainly by using X-ray diffraction techniques, combined with complementary microscopy techniques. The final purpose is the growth of a low defect GaP/Si platform, suitable for a subsequent active zone growth (either for light emission or absorption). The thesis work is presented in two main parts concerning respectively the study of microtwins and antiphase domains.

In the first part, rocking-curve and pole figure integration methods have been employed for absolute quantification of MT volume fraction in the GaP layer. These analyses, along with surface roughness measurements by AFM and local evidence of MTs by TEM experiments, have allowed understanding the effect of the different growth parameters on the MT generation and, therefore, their successful elimination. The GaP/Si platform structural properties have been significantly improved, after an optimization procedure involving growth temperature, MEE growth procedure and two-step growth sequence. It has been proved that higher growth temperature and the MEE procedure help limiting the MT formation at the interface. The growth of first 40 ML GaP by MEE at 350°C followed by 40 nm overgrowth of GaP layer by MBE at 500°C has led to GaP layers quasi-free of MTs (with a volume fraction less than 1%) presenting a smooth surface (with a r.m.s. of only 0.3 nm).

MT formation mechanism has been discussed along with the experimental results and based on the assumptions proposed in literature. Under MBE continuous growth mode and at low growth temperature, the 3D nucleation of GaP islands is believed to favor the MT formation, as the atoms are not mobile enough to arrange themselves into correct positions or during the coalescence of these nuclei. MT density has been dramatically reduced at low temperature by using MEE, since the low growth rate carefully controlled by the Ga deposition flux promotes a quasi 2D growth that eliminate a large amount of 3D GaP islands. Anisotropy of MT volume fraction along the [110] direction due to the atomic steps has been observed on all studied samples, and can be explained kinetically by the lack of perfect coverage of the Ga prelayer which may introduce stacking faults at the step edges. This effect is enhanced at lower growth temperature and an activation energy is evaluated through a model implying surface diffusion of gallium atoms, based on the evolution of MT density as a function of growth temperature.

In the second part, we have presented the APD analyses, based on transverse scans extracted from reciprocal space maps, using both laboratory and synchrotron XRD setups. The quality factor (QF) is considered to indicate the crystalline quality of the GaP layer (defect density, residual strain, etc.). The Williamson-Hall-like method is used to deduce the mosaicity tilt related to the crystallite misorientation with respect to the layer surface and the lateral correlation length which is related the mean size of APDs, provided that APD sizes are relatively homogeneous and that other defects such as MTs are at a very low density.

These XRD analyses combined with AFM and TEM allowed a very efficient optimization of the growth parameters. Growth temperature, substrate surface preparation, Ga amount per MEE cycle at the initial growth stage and AlGaP marker layers are shown to strongly affect the APD formation at the GaP/Si interface and the residual APD annihilation.

Abrupt GaP/Si interface of high quality displaying periodic bi-steps (Figure 5.1) has been achieved by homoepitaxial growth of a Si buffer layer prior to the GaP growth, on the carefully prepared Si substrate surface. Such an interface is promising for limitation of the APD formation from the GaP/Si interface. However, the presence of residual APBs (the inversion of Ga-P dumbells seen in the inset) suggests the importance of the control of other growth parameters.

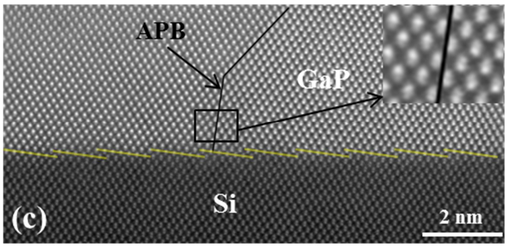

Figure 5.1 Cross-sectional HRSTEM-HAADF image of GaP grown on the optimized HF process prepared Si surface, with a homoepitaxial Si buffer layer prior to the GaP growth.

GaP layers with very low MT density (1% volume fraction), quite large APD sizes (about 27 nm) a smooth surface (r.m.s. of 0.4 nm) has been achieved by an optimized two-step sequence composed of: i) 10 nm GaP growth by MEE at 350°C (first 3 cycles with 0.75 monolayer (ML) of Ga/cycle + 37 cycles with 0.9 ML of Ga), and ii) 40 nm GaP growth at 500°C, using standard continuous MBE. Reproducible effective APD annihilation (more than 80%) has been observed within the first 10 nm (Figure 5.2 a)) on sample grown using the recipe of the optimized two-step sequence for the first 10 nm, followed by four 50 nm GaP growth by MBE at increasing temperatures, every two GaP layers separated by a AlGaP marker layer. This sample presents no MT (Figure 5.2 b)) and 3 antiphase boundaries (APB) per micron at the upper part of the layer as observed by TEM image.

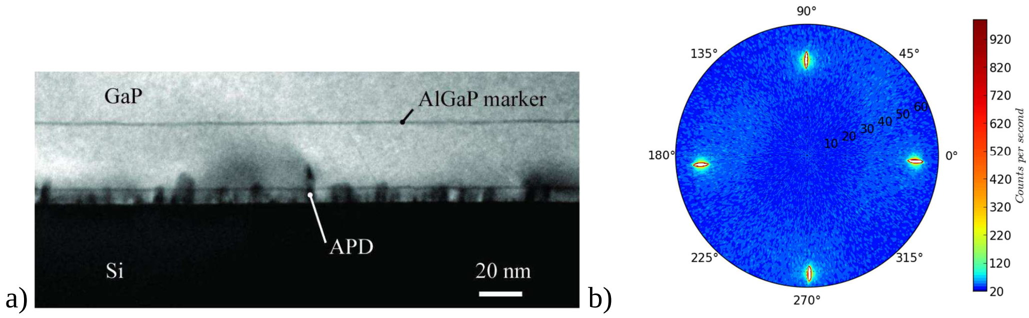

Figure 5.2 a) STEM-BF image and b) pole figure of the recent optimized sample, showing the annihilation of huge density of APDs within 10 nm, and the lack of MT.

The APD annihilation has been proposed to depend on the formation energies of the APBs in different planes. At higher temperature, the atoms in unstable APBs planes tend to migrate towards the more stable positions, either to the stable {1 1 0} APB planes or to the Si surface, leading to a digging effect and a deep trench at the initial APB position, resulting in a high surface roughness of the epilayer. The strong anisotropy observed at the vicinal Si surface in case of low Ga coverage can be explained by the assumption that smaller APDs are formed along the steps direction ([1 1 0] direction) due to the limitation of Ga diffusion along by the step edges. Smaller APBs can be then rapidly annihilated along the {1 1 1} APB planes close to the interface, or covered by the overgrowth of the surrounding main phase domains. In contrary, larger APDs observed on nominal Si surface or in the case of more Ga coverage, tend to annihilate along the {1 1 2} or {1 1 3} APB planes.

As a conclusion, combined structural analyses allowed, during this thesis, an optimization of the growth conditions for the fabrication of a GaP/Si platform. This platform now presents very low interfacial defect density and a quasi defect free surface (low roughness, low density of emerging defects), which can serve as template for photonic and photovoltaic applications.

5.2 Perspective works

In this part, I present some perspective works based on experiments carried out on the ID01 microdiffraction beamline at ESRF, Grenoble, France. Two different scan techniques have been used during this first experiment, providing new analytical means to a complete structural evaluation of the GaP/Si platform. In the following, I will present some rough conclusions on coherent diffraction imaging experiments, prior to a more complete and thorough analysis which will be done soon.

5.2.1 Attempts of Coherent Bragg Imaging

The Coherent Bragg Imaging has been performed at the ID01 ESRF beamline[175] using a highly coherent X-ray beam. The working energy is fixed at 8 keV (X-ray wavelength $\lambda = 0.15498$ nm). The X-ray beam was focused using a tungsten Fresnel zone plate (FZP) to a size of 500 nm in width and 250 nm in height. A 2D detector[176] of 516×516 pixels with 55×55 μm^2/pixel was located at 52.8±0.5 cm from the sample, giving rise to a resolution in reciprocal space of about 0.039 nm^{-1}. The interest of using highly coherent X-rays is multifold. It can be very efficient as an ultimate X-ray imaging technique either in Bragg scattering or small angle scattering. Coherent Bragg scattering imaging can be performed for samples with low defect density, enabling a spatial resolution below the beam size.[177,178] It has been first demonstrated on academic cases such as gold microcrystals more than 15 year ago,[179] and these techniques combined with ultimate brilliances achievable on the last generation synchrotrons now open the route for structure resolution of single molecules (see for instance ref.[180]) that can disentangle the double problem of crystallization of large molecules and static or dynamic disorder.[181] Such phase retrieval technique has been also successfully employed for analysis of antiphase boundaries in GaN nanowires[182] and FeAl alloys[183].

Attempts of Coherent Bragg Imaging were performed around the GaP 002 nearly specular reflection with the incident X-ray beams in the [-1-10] direction and the nominal Bragg position $\omega = \theta + 6°$, on newly optimized sample S1480 and S1477 (See Table 4.1 for detailed growth conditions). A spiral real-space scan[177,184] was carried out, composed of

250 scanning points on the sample surface, with a length step of 100 nm in both pix (along the crystallographic [110]) and piy (along [-110]) directions, to ensure a full coverage of the selected region. Notice that the size of the initial beam was up to 300 × 100 nm^2, the footprint on the sample was therefore 300×300 nm^2. At every scanning point (pix, piy), a detector image was recorded. Figure 5.3 shows three typical detector images for sample S1477. The detector coordinate (x, y) is expressed on pixel, with the pixel size of 55 μm. x and y corresponds respectively to the [-110] and [001] directions. The acquisition time of each figure is 10 seconds. Phase retrieval for the different spiral scans on this sample failed since there was no convergence. This has been attributed to a too large defect density (small APD size compared to the scattering volume, for instance).[185]

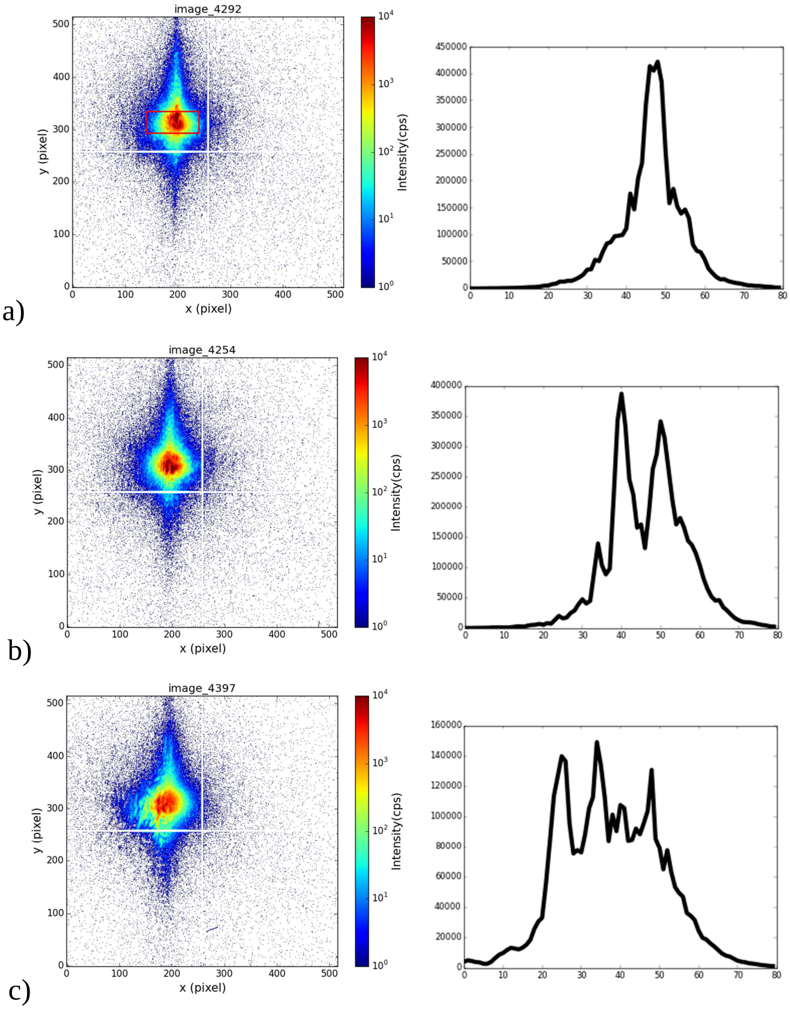

Figure 5.3 Three typical detector images in a spiral scan on the GaP 002 reflection

Nevertheless, we tried to exploit this first experiment in a different way. Intensities have been summed up within 40 pixels in y direction, in the x range of 80 pixels, around the center of the spot, as depicted by the red rectangle in Figure 5.3 a) that indicate the integration limits. The extracted diffraction profile along the x direction of the camera is shown at the right side, and it presents a single very sharp peak (in image 4292 Figure 5.3a). In image_4254 (Figure 5.3 b)), the central spot is splitted into an interference pattern which yields two smaller spots in the lateral direction, leading to the extracted profile displaying two nearly intense peaks. The image_4397 in Figure 5.3 c) shows an interference pattern consisting of diffuse and slightly distorted central spot, and the corresponding profile has at least three principle peaks.

These observations are consistent with the simulation results. A preliminary simulation of the scattering intensity on a 2D GaP structure in the lateral direction shows a profil of a thin peak without splitting, as depicted by the violet curve in Figure 5.4. If an APB is introduced at the center of the structure, the scattering profile exhibits a completely splitted pattern as shown by the blue curve. The displacement of 300 points of the APB apart away from the center makes the splitting effect weaker (red curve) and the profil becomes a broad peak without splitting if the APB is too far from the center (black curve).

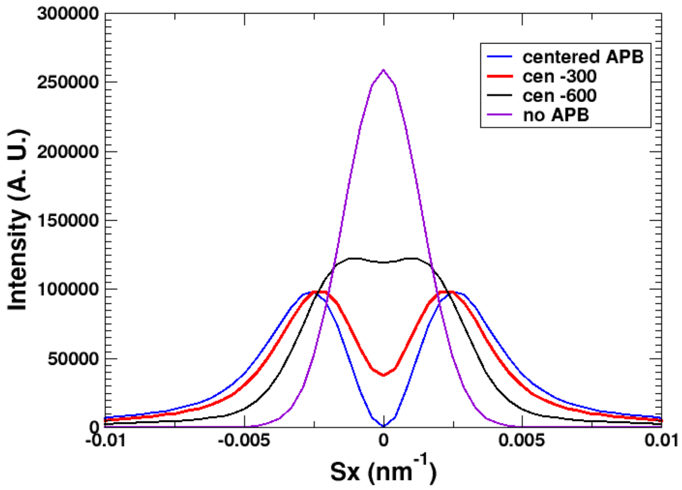

Figure 5.4 Simulation of the scattring intensity by a 2D GaP structure in the lateral direction, showing a central thin peak if there is no APB and a totally splitted one if there is an APB at the center. The splitting effect becomes weaker if the APB is displaced apart away from the sturcure center.

The complete spinal scan is displayed by putting the extracted profiles at the corresponding (pix, piy) positions (Figure 5.5). The assembly of profiles presenting similar shapes in a small region indicates that the micro-domain of the sample displays homogeneous structural characteristics. For example, a region of splitted peaks is encircled by red lines, probably indicating the presence of an APB or an APD inside this area. The blue lines encircle the single sharp peaks, signature of domains presenting a lower defect density. The spiral scan allows evaluate the local distribution of structural quality.

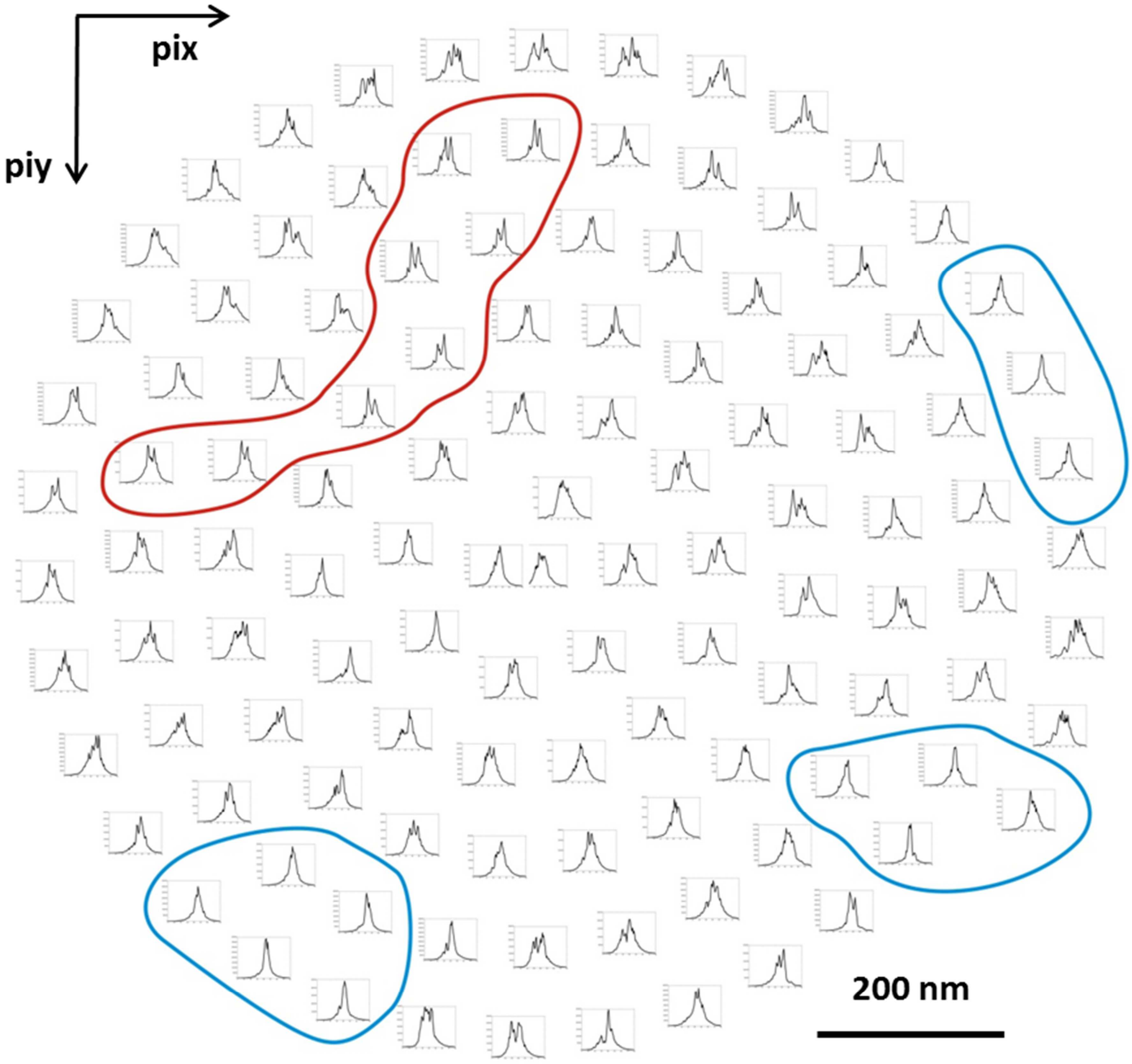

Figure 5.5 Complete spiral scan of S1477 around the GaP 002 reflection

The spiral scan of the sample S1480, also on the nearly specular GaP 002 reflection, taken at the same conditions as S1477, shows a totally different aspect. The profiles within the whole scanning region present very similar shapes, as shown in Figure 5.6. Indeed, phase retrieval on this sample shows no contrast, indicating huge and homogeneous density (at the scan range) of small sized defects within the whole studied zone.

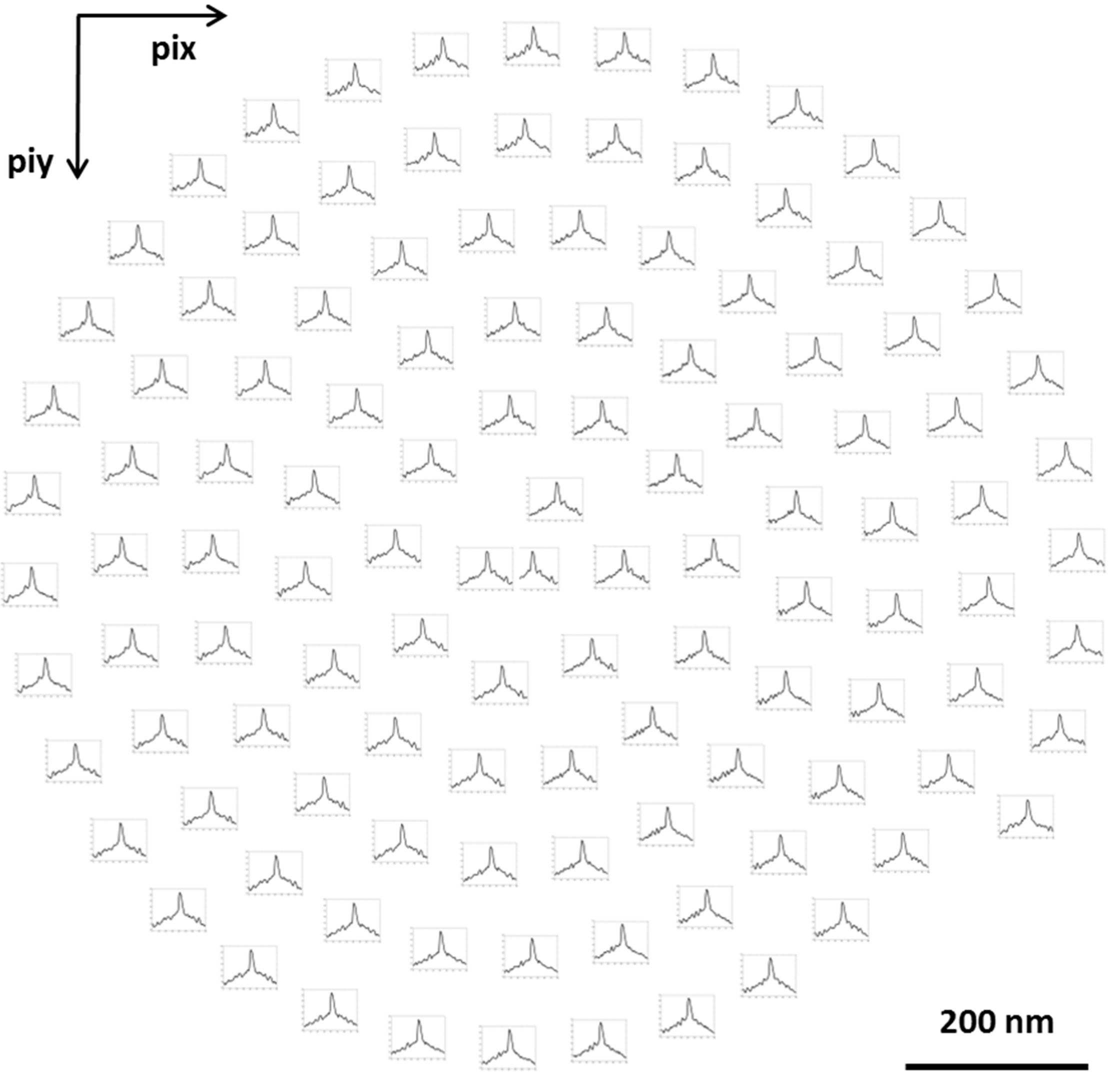

Figure 5.6 Complete spiral scan of S1488 around the GaP 002 reflection

Figure 5.7 shows a typical detector image and the extracted profiles for this sample. Here we can find that, compared to the sample S1477, this diffraction spot is more diffuse in the lateral direction, but with an intense central peak. The extracted profil in linear scale visualize the intense central peak and that in logarithm scale highlihgts the diffuse part.

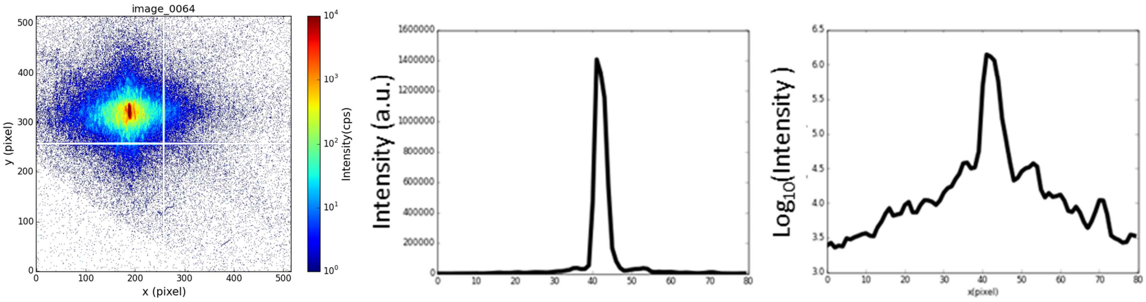

Figure 5.7 Typical detector image centered on the GaP 002 reflection for S1480, and the extracted profiles in linear scale and logarithm scale

5.2.2 Quick scanning X-ray diffraction microscopy

K-map is a quick Scanning X-ray Diffraction Microscopy technique developed at the ID01 beamline, using a partially coherent but highly brilliant X-ray beam with a vertical size of 100 nm and horizontal size of about 300 nm. The principle is doing an ω rocking scan around its nominal GaP position at every surface point (pix, piy), over a small region of the sample surface, in order to construct a 3D reciprocal space map for every scanned point.[168] It allows studying the structural inhomogeneity involving lattice strain and lattice misorientation ("tilt"). [169,170,186]

In our experiment, K-maps were carried out on the sample S1477. The incident X-ray beams are in the [-1-10] directions so that the nominal Bragg positions are ω = θ+6°. Figure 5.8 shows one of the original images acquired by the detector at the GaP 002 center. Firstly five Regions of Interest (ROI) have been defined, with ROI 1 covering the whole diffraction spot, ROI 2 covering the peak center, ROI 3 and ROI 4 respectively for the left side and right side diffuse, and finally ROI 5 for measuring the upper diffuse part.

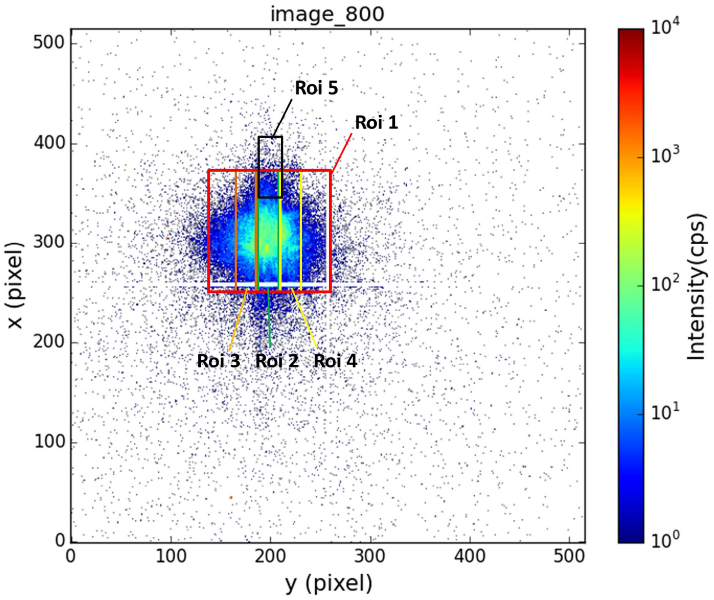

Figure 5.8 A typical detector image obtained at the center of the nominal GaP 002 (with ω = θ+6°), and the definition of Regions of Interest.

The K-maps are reconstructed by representing, for each ω position, over each ROI, the distribution of scattering intensities in real space coordinate (pix, piy). Figure 5.9 shows the 7×3 μm^2 GaP 002 Kmaps for the sample S1477 at ω=22.254°, over ROI 1. Note that the incident X-ray beams are in the [-1-10] direction and the nominal Bragg position of the GaP 002 is 22.51°.

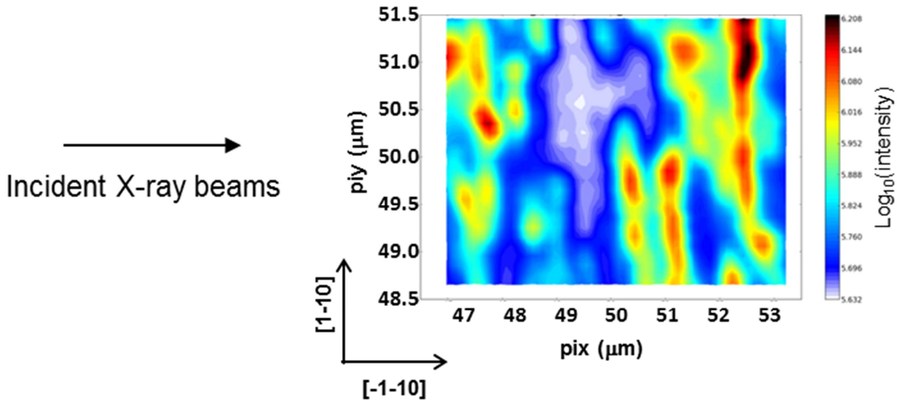

Figure 5.9 7×3 µm^2 GaP 002 K-map for the sample S1477 at ω=22.254°, over ROI 1.

The real-space step size is 100 nm in both directions, leading to a total number of 2100 original detector images recorded for single K-map. The final number of images for one complete K-map experiment depends on the number of omega positions in the rocking scan. For example, 10500 images are stored for a rocking scan with only 5 different omega positions. Based on these images, we can reconstruct a 3D pattern in reciprocal space for each (pix, piy) position, which permits obtaining the spatial distribution of the strain and the tilt in the studied zone, called the strain map and the tilt map. Here I present only some observations and rough analyses.

Figure 5.10 shows the GaP 002 K-maps for S1477 at ω = 22.254°, over the five ROIs. A strong inhomogeneity of scattering intensity is observed on all of the five maps, indicating inhomogeneous crystalline quality of the sample (deformation, strain, tilt and defect density).

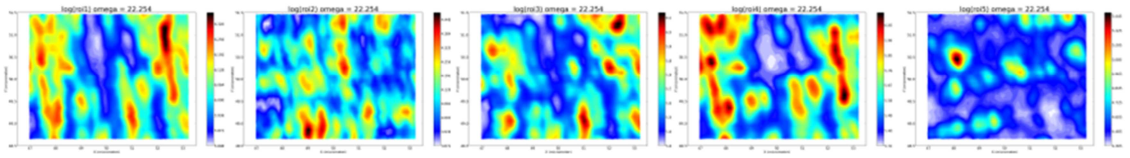

Figure 5.10 7×3 µm^2 GaP 002 K-maps for S1477 over the 5 ROI (from left to right: ROI 1, ROI 2, ROI 3, ROI 4 and ROI 5), at ω=22.254°.

Vertically oriented intense bands are observed over ROI 1 (covering the whole spot), signature of anisotropy along two directions, consistent with the observations in Chapter 3 and Chapter 4. The left side (ROI 3) and right side (ROI 4) of the spot display totally different intensity distribution, probably due to the inhomogeneous distribution of tilt.

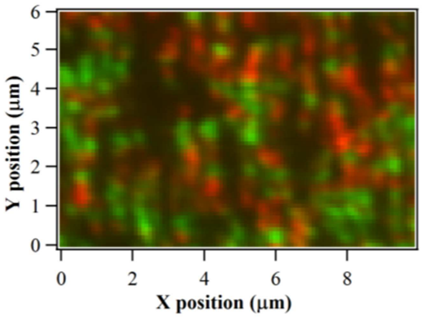

Figure 5.11 ROI 3 (red channel) and ROI 4 (green channel) from Figure 5.10, showing a spatial separation.

On the Figure 5.11**,** ROI 3 and ROI 4 signals are superimposed, with red channel representing ROI 3 and the green channel representing ROI 4, showing a lateral separation of the signals. This suggests that the intense signals are more likely originated from a contribution of microtilt rather than a Bragg broadening induced by APB or APD. This microtilt configuration is may be related to the strain around annihilating APD. A thorough analysis must be carried out to conclude on this point.

We can also compare the K-maps over a chosen ROI (for example the ROI 1), at different ω positions, as shown in Figure 5.12.

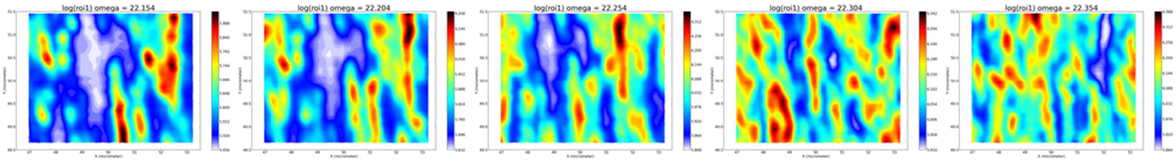

Figure 5.12 7×3 µm^2 GaP 002 K-maps for S1477 over ROI 1, at five different ω positions (from left to right: 22.154°, 22.204, 22.254°, 22.304° and 22.354°).

Firstly, the anisotropy phenomenon is always observed, with intense thin bands along the [1-10] direction (perpendicular to the atomic steps), probably related to the longer defect-induced correlation length in this direction. Secondly, intense signals in some part of the studied zone remain from one ω position to another. In other words, the corresponding rocking-scan at this spatial point should display a large intense component, signature of a poor crystal quality (large treading defect density, lattice plane distortion, tilt, etc.), as explained in the chapter 4. For the zones displalying weak intensities, intense peak is absent, suggesting a larger density of defects (widely scattered intensity) or larger lattice tilt. However, it is not evident to have informations on tilt and lattice plane distortion in case of large APD density since the 002 reflection is very sensitive to the APDs.

In brief, the crystalline quality of the sample S1477 is very inhomogeneous, consistent with the spatial spiral scan. K-maps around the GaP 004 strong reflection and further studies with reconstruction of 3D pattern in reciprocal space are essential for obtaining the strain map and the tilt map.

5.3 Suggestions for future works

1. For growth of a GaP/Si platform, it should be of great interest to study the samples grown on the bi-stepped Si surface, using optimized two-step sequence, in order to limit the APD formation from the very initial growth stage, and combined with the use of AlGaP marker layers for annihilation of residual APDs.

2. It is important to study the Ga diffusion energy on the Si surface by molecular dynamics simulations, as a function of temperature, growth rate, Ga coverage, presence of bisteps, etc, in order to understand the effect of different growth parameters on the MT and APD formation and finally their elimination.

3. For X-ray diffraction measurements, an evaluation method should be developed to quantify the APD volume fraction, based on X-ray diffraction experiments, theoretical calculation, and simulation.

4. Coherent X-ray diffraction imaging should give exploitable results on newer samples with low APD density. This would be particularly interesting, combined with cathodoluminescence analysis, in the case of GaP/Si-based microdisk resonators (Figure 5.13) for the development of novel integrated optical functions.[187]

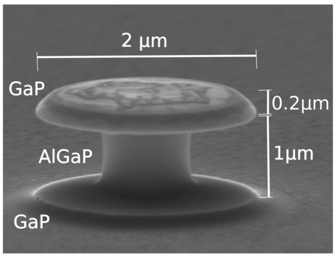

Figure 5.13 SEM image of a 200 nm thick active microdisk, including 5 layers of 3 nm thick GaPN/GaP quantum wells, on an AlGaP pedestal grown on GaP substrate.

Appendices

A1 The choice of appropriate integration size

This is a complementary study. The MT density quantification by pole figure is not enough accurate concerning the variants anisotropy. Let’s now look back to the analysis on S1189. The relationship of MT density for each variants is C>A>B>D from the pole figure but A>B>C≈D from both Synchrotron images and the rocking-curves. We have found that this disagreement was influenced by the sizes of the integration regions.

Figure A1.1 shows pole figures in Cartesian coordinates of two samples regarded as references for samples of high (S1189) and low (S1306) MT density respectively. Black rectangles indicate the ROI for intensity integration. ROI of different sizes are used to adapt to the MT spot shape, in order to cover all MT single with a minimum background signal.

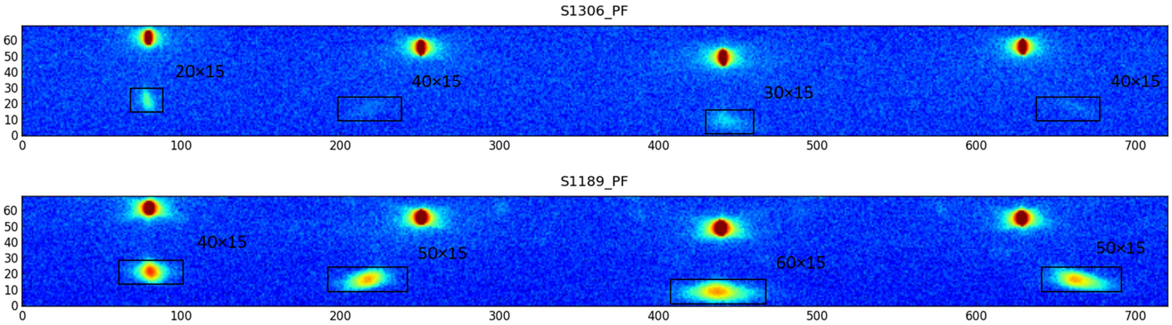

Figure A1.1 Poles figures of S1306 and S1189, with black rectangles indicating adequate ROI size for each MT variant

As the comparison between samples requires integration uniformity, the same ROI size shoulde be used for all the MT reflections. Figure A1.2 compares the MT densities extracted from the pole figures using different ROI sizes. With the variation of the ROI size, the relative variation of I_{MT} (calculated according to the Equation 3.2) is more evident in S1306 than in S1189, probabely due to the too weak MT signal with respect to the background noise covered by the ROI.

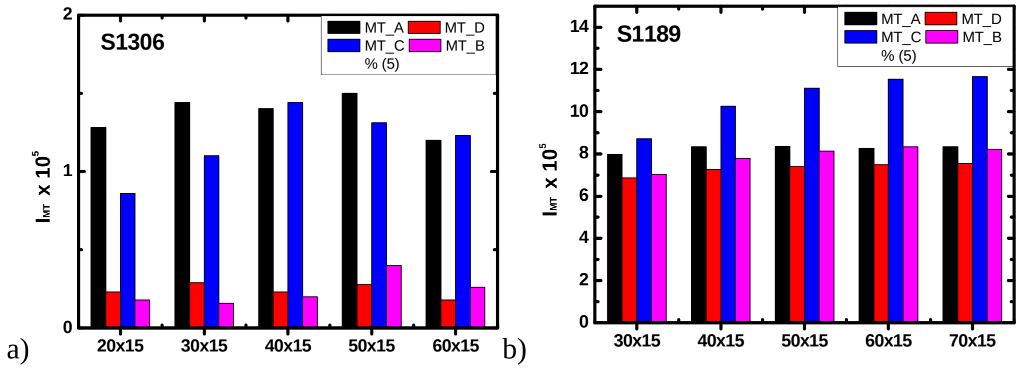

Figure A1.2 MT variants anisotropy measured on pole figure with different ROI sizes for S1306 and S1189

Nevertheless, the ROI size doesn't change the total MT density relationship between different samples. Figure A1.3 compares five typical samples with I_{MT} ranging from 0.1 to 55, measured at different ROI sizes, showing always S1200 > S1322 > S1308 > S1306 > S1319. It is more evident on samples presenting high MT density that I_{MT} increases when ROI size increases. A magnification of ×20 or ×10 has been applied on samples with low MT density for better visualization of this evolution (Figure A1.3 right). The 60×15 has finally been chosen as the ROI size for all samples to ensure an entire integration of MT reflections. However, too much background signal around the smaller and weaker MT reflections is counted as MT signal, making the quantification less reliable.

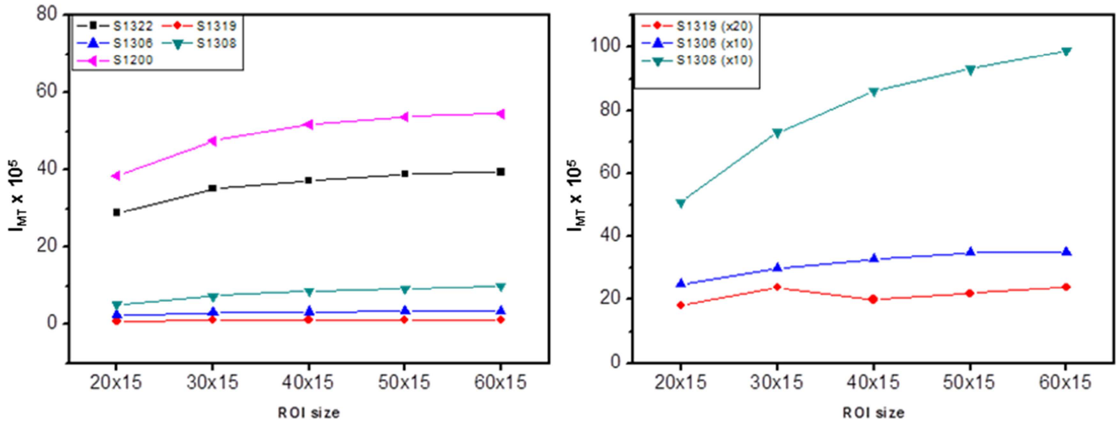

Figure A1.3 MT density (I_{MT}) measured for different samples with different ROI sizes.

A2 Performance of rocking-curve scans for MT quantification

Four rocking-curve (RC) scans are performed respectively on the four MT variants, with 2θ fixed at the GaP 111 Bragg position (i.e. $2\theta_B = 28.44°$) and the sample rotated on ω axis around its Bragg position ω_B ($\omega_B = \theta_B$ without miscut). The 6 degree's substrate miscut is taken into account by a ω shift for MT-B and MT-D (i.e. $\omega = \theta_B \pm 6°$ with $\chi = 16°$), and by χ shift for MT-A and MT-C (i.e. $\chi = 16° \pm 6°$ with $\omega = \theta_B$). In addition, one RC scan around the nominal GaP 002 reflection is carried out to measure the volume fraction of the GaP of nominal orientation. The motors positions for each of the RC scans are listed in table A2.

Table A2 Rocking-curves scan motor positions

	2θ (°)	ϕ (°)	χ (°)	ω scan center (°)
MT-D	28.44	0	16	8.22
MT-C	28.44	90	10	14.22
MT-B	28.44	180	16	20.22
MT-A	28.44	270	22	14.22
GaP 002	32.86	0	0	10.43

A3 Improvement of the Signal-to-noise ratio for low resolution lab XRD setup

At the beginning of the development of the pole figure method, two cross-pasted slits opened at about 2 mm were used at the place of the cross-superimposed slits to produce the quasi-point beam. No Sollers Slit was used after the sample. Then since we would like to adjust the slit opening, the present superimposed slits were designed and fabricated. With the improvement of sample quality and decrease of MT signal intensity, it was indispensable to improve the Signal-to-noise ratio (SNR) in pole figures and rocking-curve scans. The test was realized with the sample S1189. Rocking-curves around the MT-A have been performed when changing the vertical slit height, with or without the Sollers Slit. The table A3 shows the results of the test. The incident beam intensity I_0 was measured on the detector on 0D mode and opened at 2 mm and the MT rocking-curve is recorded with an opening of 8 mm to ensure the entire capture of intensity. I_{max} corresponds to the maximum value of the MT profile peak, and the I_{bg} represents the mean background noise intensity.

Table A3 Measurement of incident beam intensity, maximum MT signal and background noise for different slit configuration

Vertical slit height	Sollers Slit	I_0 (Mcps)	I_{max} (cps)	I_{bg} (cps)	SNR
2mm	No	92.2	1118	90	12.4
2mm	Yes	51.94	560	35	16.0
5mm	No	182.02	2276	195	11.8
5mm	Yes	110.67	1130	70	16.1

From the table, we can easily find that the minimum of the background noise intensity and the optimal SNR is achieved when the vertical slit height is set at 2 mm with the use of Sollers Slit.

References

1. Miller, D. A. B. Device Requirements for Optical Interconnects to Silicon Chips. *Proc. IEEE* **97,** 1166–1185 (2009).
2. Jalali, B. *et al.* Advances in silicon-on-insulator optoelectronics. *IEEE J. Eelected Top. Quantum Electron.* **4,** 938–947 (1998).
3. Soref, R. A., Schmidtchen, J. & Petermann, K. Large single-mode rib waveguides in GeSi-Si and Si-on-SiO2. *IEEE J. Quantum Electron.* **27,** 1971–1974 (1991).
4. Splett, A., Schuppert, B., Petermann, K. & Burbach, G. Low loss singlemode optical waveguides with large cross-section in silicon-on-insulator. *Electron. Lett.* **27,** 1486–1488 (1991).
5. Soref, R. A. & Lorenzo, J. P. Single-crystal silicon: a new material for 1.3 and 1.6 μm integrated-optical components. *Electron. Lett.* **21,** 953–954 (1985).
6. Soref, R. A. & Larenzo, J. All-silicon active and passive guided-wave components for λ = 1.3 and 1.6 μm. *IEEE J. Quantum Electron.* **22,** 873–879 (1986).
7. Dehlinger, G. *et al.* Intersubband Electroluminescence from Silicon-Based Quantum Cascade Structures. *Science* **290,** 2277–2280 (2000).
8. Boyraz, O. & Jalali, B. Demonstration of a silicon Raman laser. *Opt Express* **12,** 5269–5273 (2004).
9. Walters, R. J., Bourianoff, G. I. & Atwater, H. A. Field-effect electroluminescence in silicon nanocrystals. *Nat Mater* **4,** 143–146 (2005).
10. Loncar, M., Doll, T., Vuckovic, J. & Scherer, A. Design and fabrication of silicon photonic crystal optical waveguides. *J. Light. Technol.* **18,** 1402–1411 (2000).
11. Almeida, V. R., Xu, Q., Barrios, C. A. & Lipson, M. Guiding and confining light in void nanostructure. *Opt Lett* **29,** 1209–1211 (2004).
12. Vlasov, Y. A., O'Boyle, M., Hamann, H. F. & McNab, S. J. Active control of slow light on a chip with photonic crystal waveguides. *Nature* **438,** 65–69 (2005).
13. Liu, A. *et al.* A high-speed silicon optical modulator based on a metal-oxide-semiconductor capacitor. *Nature* **427,** 615–618 (2004).
14. Shin, J.-S. & Kim, J. T. Broadband silicon optical modulator using a graphene-integrated hybrid plasmonic waveguide. *Nanotechnology* **26,** 365201 (2015).
15. Chong, L. *et al.* High performance silicon waveguide germanium photodetector. *Chin. Phys. B* **24,** 38502 (2015).
16. Michel, J., Liu, J. & Kimerling, L. C. High-performance Ge-on-Si photodetectors. *Nat Photon* **4,** 527–534 (2010).
17. Richter, A., Steiner, P., Kozlowski, F. & Lang, W. Current-induced light emission from a porous silicon device. *Electron Device Lett. IEEE* **12,** 691–692 (1991).
18. Qin, G. G. & Jia, Y. Q. Mechanism of the visible luminescence in porous silicon. *Solid State Commun.* **86,** 559–563 (1993).
19. Bisi, O., Ossicini, S. & Pavesi, L. Porous silicon: a quantum sponge structure for silicon based optoelectronics. *Surf. Sci. Rep.* **38,** 1–126 (2000).

20. Franzò, G., Coffa, S., Priolo, F. & Spinella, C. Mechanism and performance of forward and reverse bias electroluminescence at 1.54 μm from Er-doped Si diodes. *J. Appl. Phys.* **81,** 2784–2793 (1997).
21. Vinh, N. Q., Ha, N. N. & Gregorkiewicz, T. Photonic Properties of Er-Doped Crystalline Silicon. *Proc. IEEE* **97,** 1269–1283 (2009).
22. Pavesi, L., Dal Negro, L., Mazzoleni, C., Franzo, G. & Priolo, F. Optical gain in silicon nanocrystals. *Nature* **408,** 440–444 (2000).
23. Pavesi, L. & Turan, R. *Silicon Nanocrystals; Fundamentals, Synthesis, and Applications*. (Wiley-VCH Verlag GmbH & Co. KGaA, 2010).
24. Godefroo, S. *et al.* Classification and control of the origin of photoluminescence from Si nanocrystals. *Nat Nano* **3,** 174–178 (2008).
25. Cheng, K.-Y., Anthony, R., Kortshagen, U. R. & Holmes, R. J. High-Efficiency Silicon Nanocrystal Light-Emitting Devices. *Nano Lett.* **11,** 1952–1956 (2011).
26. Franzò, G. *et al.* Electroluminescence of silicon nanocrystals in MOS structures. *Appl. Phys. A* **74,** 1–5 (2002).
27. Fujii, M., Yoshida, M., Kanzawa, Y., Hayashi, S. & Yamamoto, K. 1.54 μm photoluminescence of Er3+ doped into SiO2 films containing Si nanocrystals: Evidence for energy transfer from Si nanocrystals to Er3+. *Appl. Phys. Lett.* **71,** 1198–1200 (1997).
28. Priolo, F. *et al.* Role of the energy transfer in the optical properties of undoped and Er-doped interacting Si nanocrystals. *J. Appl. Phys.* **89,** 264–272 (2001).
29. Iacona, F. *et al.* Electroluminescence at 1.54 μm in Er-doped Si nanocluster-based devices. *Appl. Phys. Lett.* **81,** 3242–3244 (2002).
30. Irrera, A. *et al.* Influence of the matrix properties on the performances of Er-doped Si nanoclusters light emitting devices. *J. Appl. Phys.* **107,** 54302 (2010).
31. Liu, J. *et al.* Tensile-strained, n-type Ge as a gain medium formonolithic laser integration on Si. *Opt Express* **15,** 11272–11277 (2007).
32. Morse, M., Dosunmu, O., Sarid, G. & Chetrit, Y. Performance of Ge-on-Si p-i-n Photodetectors for Standard Receiver Modules. *Photonics Technol. Lett. IEEE* **18,** 2442–2444 (2006).
33. Mitze, T. *et al.* Hybrid integration of III/V lasers on a silicon-on-insulator (SOI) optical board. in *Group IV Photonics, 2005. 2nd IEEE International Conference on* 210–212 (2005). doi:10.1109/GROUP4.2005.1516455
34. Pasquariello, D. & Hjort, K. Plasma-assisted InP-to-Si low temperature wafer bonding. *IEEE J. Sel. Top. Quantum Electron.* **8,** 118–131 (2002).
35. Schjolberg-Henriksen, K., Moe, S., Taklo, M. M. V., Storås, P. & Ulvensoen, J. H. Low-temperature plasma activated bonding for a variable optical attenuator. *Sens. Actuators Phys.* **142,** 413–420 (2008).
36. Fischer, R. *et al.* Growth and properties of GaAs/AlGaAs on nonpolar substrates using molecular beam epitaxy. *J. Appl. Phys.* **58,** 374–381 (1985).
37. Sakai, S., Soga, T., Takeyasu, M. & Umeno, M. Room-temperature laser operation of AlGaAs/GaAs double heterostructures fabricated on Si substrates by metalorganic chemical vapor deposition. *Appl. Phys. Lett.* **48,** 413–414 (1986).
38. Fischer, R. *et al.* Low threshold laser operation at room temperature in GaAs/(Al,Ga)As structures grown directly on (100)Si. *Appl. Phys. Lett.* **48,** 1360–1361 (1986).

39. Kataria, H. *et al.* Towards a monolithically integrated III–V laser on silicon: optimization of multi-quantum well growth on InP on Si. *Semicond. Sci. Technol.* **28,** 94008 (2013).
40. Sarkar, A., Kimukin, I., Edgar, C. W., Yi, S. & Islam, M. S. Heteroepitaxial growth dynamics of InP nanowires on silicon. *J. Nanophotonics* **2,** 21775-21775–15 (2008).
41. Mano, T., Fujioka, H., Ono, K., Watanabe, Y. & Oshima, M. InAs nanocrystal growth on Si (100). *Appl. Surf. Sci.* **130–132,** 760–764 (1998).
42. Cirlin, G. E. *et al.* Formation of InAs quantum dots on a silicon (100) surface. *Semicond. Sci. Technol.* **13,** 1262 (1998).
43. Zhao, Z. M. *et al.* Growth and characterization of InAs quantum dots on Si(0 0 1) substrates. *J. Cryst. Growth* **271,** 450–455 (2004).
44. Balakrishnan, G. *et al.* Growth mechanisms of highly mismatched AlSb on a Si substrate. *Appl. Phys. Lett.* **86,** 34105 (2005).
45. Fang, S. F. *et al.* Gallium arsenide and other compound semiconductors on silicon. *J. Appl. Phys.* **68,** R31–R58 (1990).
46. Bartenlian, B. *et al.* Nucleation and growth of gallium arsenide on silicon. *Appl. Surf. Sci.* **56–58,** 589 – 596 (1992).
47. Yonezu, H. Control of structural defects in group III–V–N alloys grown on Si. *Semicond. Sci. Technol.* **17,** 762 (2002).
48. Moon, S. Y. *et al.* Dislocation-Free InxGa1-xP1-yNy/GaP1-zNz Double-Heterostructure Light Emitting Diode on Si Substrate. *Jpn. J. Appl. Phys.* **44,** 1752 (2005).
49. Furukawa, Y. *et al.* Growth of Si/III–V-N/Si structure with two-chamber molecular beam epitaxy system for optoelectronic integrated circuits. *J. Cryst. Growth* **300,** 172–176 (2007).
50. Volz, K. *et al.* GaP-nucleation on exact Si (001) substrates for III/V device integration. *J. Cryst. Growth* **315,** 37–47 (2011).
51. Kunert, B., Volz, K., Koch, J. & Stolz, W. Direct-band-gap Ga(NAsP)-material system pseudomorphically grown on GaP substrate. *Appl. Phys. Lett.* **88,** 182108 (2006).
52. Kunert, B. *et al.* Correlation between hetero-interface properties and photoluminescence efficiency of Ga(NAsP)/(BGa)P multi-quantum well structures on (001) Si substrate. *J. Cryst. Growth* **315,** 28 – 31 (2011).
53. Grassman, T. J. *et al.* Control and elimination of nucleation-related defects in GaP/Si(001) heteroepitaxy. *Appl. Phys. Lett.* **94,** 232106 (2009).
54. Grassman, T. J. *et al.* Nucleation-related defect-free GaP/Si(100) heteroepitaxy via metal-organic chemical vapor deposition. *Appl. Phys. Lett.* **102,** 142102 (2013).
55. Ratcliff, C., Grassman, T. J., Carlin, J. A. & Ringel, S. A. High temperature step-flow growth of gallium phosphide by molecular beam epitaxy and metalorganic chemical vapor deposition. *Appl. Phys. Lett.* **99,** 141905 (2011).
56. Guo, W. *et al.* First step to Si photonics: synthesis of quantum dot light-emitters on GaP substrate by MBE. *Phys. Status Solidi C* **6,** 2207–2211 (2009).
57. Robert, C. *et al.* Room temperature operation of GaAsP(N)/GaP(N) quantum well based light-emitting diodes: Effect of the incorporation of nitrogen. *Appl. Phys. Lett.* **98,** 251110 (2011).
58. Durand, O. *et al.* Monolithic Integration of Diluted-Nitride III–V-N Compounds on Silicon Substrates: Toward the III–V/Si Concentrated Photovoltaics. *Energy Harvest. Syst.* **1,** 147 (2014).

59. Quinci, T. *et al.* Defects limitation in epitaxial GaP on bistepped Si surface using UHVCVD–MBE growth cluster. *J. Cryst. Growth* **380,** 157–162 (2013).
60. Ehrhart, P. *Properties and interactions of atomic defects in metals and alloys*. (Springer, 1991).
61. Watkins, G. D. Native Defects and their Interactions with Impurities in Silicon. in *Symposium E:Defects and Diffusion in Silicon Processing* **469,** (1997).
62. Taylor, G. I. The Mechanism of Plastic Deformation of Crystals. Part I. Theoretical. *Proc. R. Soc. Lond. Math. Phys. Eng. Sci.* **145,** 362–387 (1934).
63. Callister, W. D. J. *Fundamentals of Materials Science and Engineering*. (John Wiley & Sons, Inc, 2005).
64. Pohl, U. W. *Epitaxy of Semiconductors*. (Springer Berlin Heidelberg, 2013).
65. Yamane, K., Kawai, T., Furukawa, Y., Okada, H. & Wakahara, A. Growth of low defect density GaP layers on Si substrates within the critical thickness by optimized shutter sequence and post-growth annealing. *J. Cryst. Growth* **312,** 2179 – 2184 (2010).
66. Holt, D. B. Antiphase boundaries in semiconducting compounds. *J. Phys. Chem. Solids* **30,** 1297–1308 (1969).
67. Kroemer, H. Polar-on-nonpolar epitaxy. *J. Cryst. Growth* **81,** 193–204 (1987).
68. Ayers, J. E. *Heteroepitaxy of semiconductors : theory, growth, and characterization*. (CRC Press, 2007).
69. Takagi, Y., Furukawa, Y., Wakahara, A. & Kan, H. Lattice relaxation process and crystallographic tilt in GaP layers grown on misoriented Si(001) substrates by metalorganic vapor phase epitaxy. *J. Appl. Phys.* **107,** 63506 (2010).
70. Matthews, J. W. & Blakeslee, A. E. Defects in epitaxial multilayers: I. Misfit dislocations. *J. Cryst. Growth* **27,** 118–125 (1974).
71. Samonji, K. *et al.* Reduction of threading dislocation density in InP-on-Si heteroepitaxy with strained short-period superlattices. *Appl. Phys. Lett.* **69,** 100–102 (1996).
72. Soga, T., Jimbo, T. & Umeno, M. Dislocation generation mechanisms for GaP on Si grown by metalorganic chemical vapor deposition. *Appl. Phys. Lett.* **63,** 2543–2545 (1993).
73. Skibitzki, O. *et al.* GaP collector development for SiGe heterojunction bipolar transistor performance increase: A heterostructure growth study. *J. Appl. Phys.* **111,** 73515 (2012).
74. Morizane, K. Antiphase domain structures in GaP and GaAs epitaxial layers grown on Si and Ge. *J. Cryst. Growth* **38,** 249–254 (1977).
75. Grassman, T. J. *et al.* Toward metamorphic multijunction GaAsP/Si photovoltaics grown on optimized GaP/Si virtual substrates using anion-graded GaAsyP1-y buffers. in *Photovoltaic Specialists Conference (PVSC), 2009 34th IEEE* 002016–002021 (2009). doi:10.1109/PVSC.2009.5411489
76. Tea, E. *et al.* Theoretical study of optical properties of anti phase domains in GaP. *J. Appl. Phys.* **115,** 63502 (2014).
77. Bauer, G., Li, J. H. & Holy, V. High Resolution X-ray Reciprocal Space Mapping. *Acta Phys. Pol. A* **89,** 115 (1996).
78. Birkholz, M. *Thin Film Analysis by X-Ray Scattering*. (Wiley-VCH Verlag GmbH & Co. KGaA, 2005).
79. Guo, W. *et al.* Thermodynamic evolution of antiphase boundaries in GaP/Si epilayers evidenced by advanced X-ray scattering. *Appl. Surf. Sci.* **258,** 2808 – 2815 (2012).

80. Ayers, J. E., Ghandhi, S. K. & Schowalter, L. J. Crystallographic tilting of heteroepitaxial layers. *J. Cryst. Growth* **113,** 430–440 (1991).
81. Darwin, C. G. The reflexion of X-rays from imperfect crystals. *Philos. Mag. Ser. 6* **43,** 800–829 (1922).
82. Miceli, P. F. X-ray scattering from rotational disorder in epitaxial films: *Phys Rev B* **51,** 5506 (1995).
83. Herres, N. *et al.* Effect of interfacial bonding on the structural and vibrational properties of InAs/GaSb superlattices. *Phys Rev B* **53,** 15688–15705 (1996).
84. Herres, N. X-ray diffractometry on (Al,Ga,In)-nitride layers.ppt. in (2001).
85. Holý, V., Pietsch, U. & Baumbach, T. *High-Resolution X-Ray Scattering from Thin Films and Multilayers*. **149,** (Springer Berlin Heidelberg, 1999).
86. Nguyen Thanh, T. Silicon photonics based on monolithic integration of III-V nanostructures on silicon (Thesis). (Insa de Rennes, 2013).
87. Chadi, D. J. Stabilities of single-layer and bilayer steps on Si(001) surfaces. *Phys Rev Lett* **59,** 1691–1694 (1987).
88. Oshiyama, A. Structures of Steps and Appearances of {311} Facets on Si(100) Surfaces. *Phys. Rev. Lett.* **74,** 130–133 (1995).
89. Bringans, R. D., Uhrberg, R. I. G., Olmstead, M. A. & Bachrach, R. Z. Surface bands for single-domain 2 × 1 reconstructed Si(100) and Si(100):As. Photoemission results for off-axis crystals. *Phys. Rev. B* **34,** 7447–7450 (1986).
90. Chabal, Y. J. & Raghavachari, K. Surface Infrared Study of Si(100)-(2×1)H. *Phys. Rev. Lett.* **53,** 282–285 (1984).
91. Swartzentruber, B. S., Kitamura, N., Lagally, M. G. & Webb, M. B. Behavior of steps on Si(001) as a function of vicinality. *Phys. Rev. B* **47,** 13432–13441 (1993).
92. Guo, W. Heterogeneous MBE growth of GaP on Silicon and nanostructure for integrated photonics (Thesis). (Insa de Rennes, 2010).
93. Ishizaka, A. & Shiraki, Y. Low Temperature Surface Cleaning of Silicon and Its Application to Silicon MBE. *J. Electrochem. Soc.* **133,** 666–671 (1986).
94. Kern, W. The Evolution of Silicon Wafer Cleaning Technology. *J. Electrochem. Soc.* **137,** 1887 (1990).
95. Németh, I. Transmission electron microscopic investigations of heteroepitaxial III/V semiconductor thin layer and quantum well structures (Thesis). (Philipps Universitat Marburg, 2008).
96. Ping Wang, Y. *et al.* Abrupt GaP/Si hetero-interface using bistepped Si buffer. *Appl. Phys. Lett.* **107,** (2015).
97. Chollet, F., André, E., Vandervorst, W. & Caymax, M. Si(100) epitaxy by low-temperature UHV-CVD: AFM study of the initial stages of growth. *J. Cryst. Growth* **157,** 161 – 167 (1995).
98. Nayak, S., Savage, D. E., Chu, H.-N., Lagally, M. G. & Kuech, T. F. In situ RHEED and AFM investigation of growth front morphology evolution of Si(001) grown by UHV-CVD. *J. Cryst. Growth* **157,** 168 – 171 (1995).
99. Meyerson, B. S. Low-temperature Si and Si:Ge epitaxy by ultrahigh-vacuum/chemical vapor deposition: Process fundamentals. *IBM J. Res. Dev.* **34,** 806–815 (1990).

100. Takahagi, T., Nagai, I., Ishitani, A., Kuroda, H. & Nagasawa, Y. The formation of hydrogen passivated silicon single-crystal surfaces using ultraviolet cleaning and HF etching. *J. Appl. Phys.* **64,** 3516–3521 (1988).
101. Madiomanana, K. *et al.* Silicon surface preparation for III-V molecular beam epitaxy. *J. Cryst. Growth* **413,** 17–24 (2015).
102. Berar, J.-F. *et al.* {XPAD3} hybrid pixel detector applications. *Nucl. Instrum. Methods Phys. Res. Sect. Accel. Spectrometers Detect. Assoc. Equip.* **607,** 233–235 (2009).
103. Erni, R., Rossell, M. D., Kisielowski, C. & Dahmen, U. Atomic-Resolution Imaging with a Sub-50-pm Electron Probe. *Phys. Rev. Lett.* **102,** 96101 (2009).
104. Nguyen Thanh, T. *et al.* Synchrotron X-ray diffraction analysis for quantitative defect evaluation in GaP/Si nanolayers. *Thin Solid Films* **541,** 36–40 (2013).
105. Nguyen Thanh, T. *et al.* Quantitative study of microtwins in GaP/Si thin film and GaAsPN quantum wells grown on silicon substrates. *J. Cryst. Growth* **378,** 25–28 (2013).
106. He, Y.-L., Wang, G.-C., Drehman, A. J. & Jin, H.-S. X-ray pole-figure analyses of YBa2Cu3O7 thin film on SrTiO3(100) prepared by rf diode sputtering. *J. Appl. Phys.* **67,** 7460–7466 (1990).
107. Cheng, J. *et al.* Twin formation during the growth of InP on SrTiO3. *Appl. Phys. Lett.* **94,** 231902 (2009).
108. Zaumseil, P., Yamamoto, Y., Bauer, A., Schubert, M. A. & Schroeder, T. X-ray characterization of Ge epitaxially grown on nanostructured Si(001) wafers. *J. Appl. Phys.* **109,** 23511 (2011).
109. Zheng, X. H. *et al.* Comprehensive analysis of microtwins in the 3C–SiC films on Si(0 0 1) substrates. *J. Cryst. Growth* **233,** 40–44 (2001).
110. Zaumseil, P. & Schroeder, T. A complex x-ray characterization of heteroepitaxial silicon/insulator/silicon(111) structures. *J. Appl. Phys.* **104,** 23532 (2008).
111. Devenyi, G. A. *et al.* The role of vicinal silicon surfaces in the formation of epitaxial twins during the growth of III-V thin films. *J. Appl. Phys.* **110,** 124316 (2011).
112. Warren, B. E. *X-Ray Diffraction.* (Dover Publications, INC., 1990).
113. Kushwaha, M. . Compressibilities, Debye-Wailer factors, and melting criteria for II-VI and III-V compound semiconductors. *Phys. Rev. B* **24,** 2115–2120 (1987).
114. Cornet, C. Contribution to the study of monolithic integration of III-V semiconductors on silicon in the pseudomorphic approach for photonics and photovoltaics. (HDR). (Insa de Rennes, 2015).
115. Curson, N. J. *et al.* STM characterization of the Si-P heterodimer. *Phys. Rev. B* **69,** 195303 (2004).
116. Nakada, Y., Aksenov, I. & Okumura, H. Scanning tunneling microscopy studies of formation of 8×5 reconstructed structure of Ga on the Si(001) surface. *J. Vac. Sci. Technol. B* **17,** 1–6 (1999).
117. Bachmann, K. J., Rossow, U., Sukidi, N., Castleberry, H. & Dietz, N. Heteroepitaxy of GaP on Si(100). *J. Vac. Sci. Technol. B* **14,** 3019–3029 (1996).
118. Itoh, M. & Ohno, T. Absence of a step-edge barrier on a polar semiconductor surface with reconstruction. *Phys. Rev. B* **62,** 1889–1896 (2000).
119. Mahajan, S. Critique of mechanisms of formation of deformation, annealing and growth twins: Face-centered cubic metals and alloys. *Scr. Mater.* **68,** 95–99 (2013).

120. Christian, J. W. & Mahajan, S. Deformation twinning. *Prog. Mater. Sci.* **39,** 1–157 (1995).
121. Kaiser, U., Khodos, I. I., Kovalchuk, M. N. & Richter, W. Partial dislocations and stacking faults in cubic SiC. *Crystallogr. Rep.* **46,** 1005–1013 (2001).
122. Hong, H. U. *et al.* Localized microtwin formation and failure during out-of-phase thermomechanical fatigue of a single crystal nickel-based superalloy. *Int. J. Fatigue* **69,** 22–27 (2014).
123. Kovarik, L. *et al.* Microtwinning and other shearing mechanisms at intermediate temperatures in Ni-based superalloys. *Prog. Mater. Sci.* **54,** 839–873 (2009).
124. Hull, R. & Fischer-Colbrie, A. Nucleation of GaAs on Si: Experimental evidence for a three-dimensional critical transition. *Appl. Phys. Lett.* **50,** 851–853 (1987).
125. Biegelsen, D. K., Ponce, F. A., Smith, A. J. & Tramontana, J. C. Initial stages of epitaxial growth of GaAs on (100) silicon. *J. Appl. Phys.* **61,** 1856–1859 (1987).
126. Yonezu, H., Furukawa, Y. & Wakahara, A. III–V epitaxy on Si for photonics applications. *J. Cryst. Growth* **310,** 4757 – 4762 (2008).
127. Takagi, Y., Yonezu, H., Samonji, K., Tsuji, T. & Ohshima, N. Generation and suppression process of crystalline defects in GaP layers grown on misoriented Si(100) substrates. *J. Cryst. Growth* **187,** 42–50 (1998).
128. Ernst, F. & Pirouz, P. Formation of planar defects in the epitaxial growth of GaP on Si substrate by metal organic chemical-vapor deposition. *J. Appl. Phys.* **64,** 4526–4530 (1988).
129. Narayanan, V., Sukidi, N., Bachmann, K. J. & Mahajan, S. Origins of defects in self assembled GaP islands grown on Si(001) and Si(111). *Thin Solid Films* **357,** 53–56 (1999).
130. Cohen, D. & Barry Carter, C. Evaluation of the extrinsic and intrinsic stacking-fault energies of GaP. *Philos. Mag. A* **79,** 1805–1815 (1999).
131. Bi, W. G., Mei, X. B. & Tu, C. W. Growth studies of GaP on Si by gas-source molecular beam epitaxy. *J. Cryst. Growth* **164,** 256 – 262 (1996).
132. Dixit, V. K. *et al.* Effect of two-step growth process on structural, optical and electrical properties of MOVPE-grown GaP/Si. *J. Cryst. Growth* **310,** 3428–3435 (2008).
133. Lin, A. C., Harris, J. S. & Fejer, M. M. Two-dimensional III-V nucleation on Si for nonlinear optics. *J. Vac. Sci. Technol. B* **29,** 03C120 (2011).
134. Takano, Y. *et al.* High-Temperature Growth of GaP on Si Substrates by Metalorganic Vapor Phase Epitaxy. *Jpn. J. Appl. Phys.* **48,** 11102 (2009).
135. Brammertz, G. *et al.* Selective epitaxial growth of GaAs on Ge by MOCVD. *J. Cryst. Growth* **297,** 204–210 (2006).
136. Beyer, A. *et al.* Influence of crystal polarity on crystal defects in GaP grown on exact Si (001). *J. Appl. Phys.* **109,** 83529 (2011).
137. Edmunds, I. G., Hinde, R. M. & Lipson, H. Diffraction of X-Rays by the Alloy AuCu3. *Nature* **160,** 304 (1947).
138. Kirste, L., Pavlov, K. M., Mudie, S. T., Punegov, V. I. & Herres, N. Analysis of the mosaic structure of an ordered (Al,Ga)N layer. *J. Appl. Crystallogr.* **38,** 183–192 (2005).
139. Neumann, D. A., Zabel, H., Fischer, R. & Morkoç, H. Structural properties of GaAs on (001) oriented Si and Ge substrates. *J. Appl. Phys.* **61,** 1023–1029 (1987).
140. Jussila, H. *et al.* Structural study of GaP layers on misoriented silicon (001) substrates by transverse scan analysis. *J. Appl. Phys.* **111,** 43518 (2012).

141. Létoublon, A. *et al.* X-ray study of antiphase domains and their stability in MBE grown GaP on Si. *J. Cryst. Growth* **323,** 409 – 412 (2011).
142. Durand, O. *et al.* Studies of PLD-grown ZnO and MBE-grown GaP mosaic thin films by x-ray scattering methods: beyond the restrictive ω rocking curve linewidth as a figure-of-merit. in **7940,** (PROC. of SPIE, 2011).
143. Young, R. A. & Wiles, D. B. Profile shape functions in Rietveld refinements. *J. Appl. Crystallogr.* **15,** 430–438 (1982).
144. Nguyen Thanh, T. *et al.* Structural and optical analyses of GaP/Si and (GaAsPN/GaPN)/GaP/Si nanolayers for integrated photonics on silicon. *J. Appl. Phys.* **112,** 53521 (2012).
145. Williamson, G. K. & Hall, W. H. X-ray line broadening from filed aluminium and wolfram. *Acta Metall.* **1,** 22–31 (1953).
146. Durand, O., Letoublon, A., Rogers, D. J. & Teherani, F. H. Interpretation of the two-components observed in high resolution X-ray diffraction ω scan peaks for mosaic ZnO thin films grown on c-sapphire substrates using pulsed laser deposition. **519,** 6369 – 6373 (2011).
147. Halder, N. C. & Wagner, C. N. J. Separation of particle size and lattice strain in integral breadth measurements. *Acta Crystallogr.* **20,** 312–313 (1966).
148. Németh, I., Kunert, B., Stolz, W. & Volz, K. Heteroepitaxy of GaP on Si: Correlation of morphology, anti-phase-domain structure and MOVPE growth conditions. *J. Cryst. Growth* **310,** 1595 – 1601 (2008).
149. Németh, I., Kunert, B., Stolz, W. & Volz, K. Ways to quantitatively detect antiphase disorder in GaP films grown on Si(001) by transmission electron microscopy. *J. Cryst. Growth* **310,** 4763 – 4767 (2008).
150. Wong, C. S. *et al.* Structural investigation of MOVPE-grown GaAs on Ge by x-ray techniques. *Semicond. Sci. Technol.* **27,** 115012 (2012).
151. Kuan, T. S. & Chang, C.-A. Electron microscope studies of a Ge–GaAs superlattice grown by molecular beam epitaxy. *J. Appl. Phys.* **54,** 4408–4413 (1983).
152. Liliental-Weber, Z., Weber, E. R., Parechanian-Allen, L. & Washburn, J. On the use of convergent-beam electron diffraction for identification of antiphase boundaries in GaAs grown on Si. *Ultramicroscopy* **26,** 59–63 (1988).
153. Barrett, C. S. C. *et al.* Quantitative correlation of interfacial contamination and antiphase domain boundary density in GaAs on Si(100). *J. Mater. Sci.* **51,** 449–456 (2015).
154. Supplie, O. *et al.* Formation of GaP/Si(100) Heterointerfaces in the Presence of Inherent Reactor Residuals. *ACS Appl. Mater. Interfaces* **7,** 9323–9327 (2015).
155. Supplie, O. *et al.* Atomic scale analysis of the GaP/Si(100) heterointerface by in situ reflection anisotropy spectroscopy and ab initio density functional theory. *Phys. Rev. B* **90,** 235301 (2014).
156. Warren, E. L. *et al.* Growth of antiphase-domain-free GaP on Si substrates by metalorganic chemical vapor deposition using an in situ AsH3 surface preparation. *Appl. Phys. Lett.* **107,** 82109 (2015).
157. Butz, R. & Lüth, H. The surface morphology of Si (100) after carbon deposition. *Surf. Sci.* **411,** 61–69 (1998).
158. Pennycook, S. J. & Boatner, L. A. Chemically sensitive structure-imaging with a scanning transmission electron microscope. *Nature* **336,** 565–567 (1988).

159. Pennycook, S. J. & Jesson, D. E. High-resolution incoherent imaging of crystals. *Phys. Rev. Lett.* **64,** 938–941 (1990).
160. Crook, G. E., Däweritz, L. & Ploog, K. In situ monitoring of step arrays on vicinal silicon (100) surfaces for heteroepitaxy. *Phys Rev B* **42,** 5126–5134 (1990).
161. Zhu, J., Brunner, K. & Abstreiter, G. Step characterization on vicinal Si surfaces by reflection high-energy electron diffraction at arbitrary azimuths. *Appl. Surf. Sci.* **137,** 191 – 196 (1999).
162. Narayanan, V., Mahajan, S., Bachmann, K. J., Woods, V. & Dietz, N. Antiphase boundaries in GaP layers grown on (001) Si by chemical beam epitaxy. *Acta Mater.* **50,** 1275 – 1287 (2002).
163. Beyer, A. *et al.* Atomic structure of (110) anti-phase boundaries in GaP on Si(001). *Appl. Phys. Lett.* **103,** 32107 (2013).
164. Beyer, A. *et al.* GaP heteroepitaxy on Si(001): Correlation of Si-surface structure, GaP growth conditions, and Si-III/V interface structure. *J. Appl. Phys.* **111,** 83534 (2012).
165. Reis, R. dos *et al.* Direct atomic imaging of antiphase boundaries and orthotwins in orientation-patterned GaAs. *Appl. Phys. Lett.* **102,** 81905 (2013).
166. Ping Wang, Y. *et al.* Quantitative evaluation of microtwins and antiphase defects in GaP/Si nanolayers for a III–V photonics platform on silicon using a laboratory X-ray diffraction setup. *J. Appl. Crystallogr.* **48,** 702–710 (2015).
167. Yamane, K. *et al.* Growth of pit-free GaP on Si by suppression of a surface reaction at an initial growth stage. *J. Cryst. Growth* **311,** 794–797 (2009).
168. Chahine, G. A. *et al.* Imaging of strain and lattice orientation by quick scanning X-ray microscopy combined with three-dimensional reciprocal space mapping. *J. Appl. Crystallogr.* **47,** 762–769 (2014).
169. Chahine, G. A. *et al.* Strain and lattice orientation distribution in SiN/Ge complementary metal–oxide–semiconductor compatible light emitting microstructures by quick x-ray nano-diffraction microscopy. *Appl. Phys. Lett.* **106,** 71902 (2015).
170. Zoellner, M. H. *et al.* Imaging Structure and Composition Homogeneity of 300 mm SiGe Virtual Substrates for Advanced CMOS Applications by Scanning X-ray Diffraction Microscopy. *ACS Appl. Mater. Interfaces* **7,** 9031–9037 (2015).
171. Lin, A. C., Fejer, M. M. & Harris, J. S. Antiphase domain annihilation during growth of GaP on Si by molecular beam epitaxy. *J. Cryst. Growth* **363,** 258 – 263 (2013).
172. Rubel, O. & Baranovskii, S. D. Formation Energies of Antiphase Boundaries in GaAs and GaP: An ab Initio Study. *Int. J. Mol. Sci.* **10,** 5104 (2009).
173. Matsushita, T., Yamamoto, T. & Kondo, T. Epitaxial Growth of Spatially Inverted GaP for Quasi Phase Matched Nonlinear Optical Devices. *Jpn. J. Appl. Phys.* **46,** L408 (2007).
174. Wood, C. E. C., Singer, K., Ohashi, T., Dawson, L. R. & Noreika, A. J. A pragmatic approach to adatom-induced surface reconstruction of III-V compounds. *J. Appl. Phys.* **54,** 2732–2737 (1983).
175. ID01 - Microdiffraction imaging. Available at: http://www.esrf.eu/UsersAndScience/Experiments/XNP/ID01. (Accessed: 15th November 2016)
176. Ponchut, C. *et al.* MAXIPIX, a fast readout photon-counting X-ray area detector for synchrotron applications. *J. Instrum.* **6,** C01069 (2011).

177. Favre-Nicolin, V. *et al.* Analysis of strain and stacking faults in single nanowires using Bragg coherent diffraction imaging. *New J. Phys.* **12,** 35013 (2010).

178. Abbey, B. From Grain Boundaries to Single Defects: A Review of Coherent Methods for Materials Imaging in the X-ray Sciences. *JOM* **65,** 1183–1201 (2013).

179. Robinson, I. K., Vartanyants, I. A., Williams, G. J., Pfeifer, M. A. & Pitney, J. A. Reconstruction of the Shapes of Gold Nanocrystals Using Coherent X-Ray Diffraction. *Phys. Rev. Lett.* **87,** 195505 (2001).

180.Aquila, A. *et al.* The linac coherent light source single particle imaging road map. *Struct. Dyn.* **2,** 41701 (2015).

181. Tokuhisa, A., Jonic, S., Tama, F. & Miyashita, O. Hybrid approach for structural modeling of biological systems from X-ray free electron laser diffraction patterns. *J. Struct. Biol.* **194,** 325–336 (2016).

182. Labat, S. *et al.* Inversion Domain Boundaries in GaN Wires Revealed by Coherent Bragg Imaging. *ACS Nano* **9,** 9210–9216 (2015).

183. Stadler, L.-M. *et al.* Coherent x-ray diffraction imaging of grown-in antiphase boundaries in Fe65Al35. *Phys. Rev. B* **76,** 14204 (2007).

184. Kalender, W. A. Technical foundations of spiral CT. *Semin. Ultrasound CT MRI* **15,** 81–89 (1994).

185. Fernández, S. *et al.* X-ray nanodiffraction in forward scattering and Bragg geometry of a single isolated Ag–Au nanowire. *Thin Solid Films* **617, Part A,** 9–13 (2016).

186. Schroeder, T. Merging Si microelectronics with Ge photonics: On advanced synchrotron micro-XRD techniques for local and global Ge heteroepitaxy approaches.ppt. in (E-MRS Spring Meeting 2015 Symposium DD, 2015).

187. Guillemé, P. Investigation of the optical properties of GaP microdisks for optical functions integrated on silicon.ppt. in (Compound semiconductor week 2015, 2015).

Résumé de Thèse

L'épitaxie hétérogène de semi-conducteurs III-V sur le silicium a été largement étudiée dans le cadre de l'intégration monolithique de la photonique à faible coût sur le silicium. Cependant, les forts désaccords de maille entre la plupart des matériaux III-V et le silicium conduisent à une forte densité de dislocations. Pour surmonter ce problème, la croissance de GaP sur Si (avec un faible désaccord de maille de 0,37% à la température ambiante) a été proposée pour réaliser une plate-forme efficace permettant l'intégration d’autres semi-conducteurs III-V sans défaut. Néanmoins, les défauts cristallins tels que les domaines d’inversion et les micro-macles peuvent être générés à l’interface du GaP/Si.[1–3] Ces défauts modifient largement les propriétés et diminuent les performances des dispositifs optoélectroniques. Leur densité doit donc être fortement limitée afin d’assurer des performances et la fiabilité de ces dispositifs.

Cette thèse est centrée sur le développement des méthodes d’analyse structurale des micro-macles et des domaines d’inversion, basées sur la diffraction des rayons X (DRX) et combinées à des techniques de microscopie (TEM, AFM, STM). L’objectif est d’obtenir une plate-forme GaP/Si plane et sans défaut cristallin, via l’optimisation des paramètres de croissance. Le Chapitre 1 présente les différents types de défauts dans la couche hétérogène comme les dislocations, les micro-macles, les domaines d’inversion, la contrainte et désorientation de maille cristalline, etc. Le chapitre 2 présente les méthodes expérimentales utilisées pour la croissance hétérogène de couches GaP, ainsi que les techniques analytiques (DRX, AFM, TEM, STM). Les chapitres 3 et 4 présentent au travers d’études expérimentales poussées respectivement sur les micro-macles et les domaines d’inversion, l’optimisation des recettes de croissance ayant permis d’obtenir une plate-forme GaP/Si quasiment sans défaut.

Dans cette thèse, la croissance de couches minces GaP sont réalisées sur des substrats Si(001) vicinaux désorientés de 6 degrés vers la direction [1 1 0]. La surface du substrat est nettoyée par un processus optimisé, qui consiste à une première immersion du substrat dans une solution de HF à 1% pendant 90 secondes pour l'élimination des oxydes locaux, et ensuite l'exposition sous atmosphère d’UV/O_3 pendant 10 minutes pour l’élimination du carbone, des composés organiques et des particules métalliques. Le processus se termine par l'immersion dans une nouvelle solution HF (1%) pendant 90 secondes, afin d'éliminer la couche de SiO_2 formée dans l'étape précédente, et de créer une surface passivée d'hydrogène qui peut résister à la contamination atmosphérique pendant 10 minutes ou plus[4]. Le substrat traité avec ce processus présente une surface très lisse (avec une rugosité de 0.3 nm) avec une très faible densité de défauts.

La croissance par l'épitaxie est réalisée sur le « cluster » de croissance « Ultra High Vacuum Chemical Vapor Deposition (UHV CVD) - Molecular Beam Epitaxy (MBE) » installé dans notre laboratoire.[5] Pour la croissance de GaP directement sur Si (sans « buffer » Si), le substrat est introduit dans la chambre de MBE tout de suite après le nettoyage, et chauffé à 800 ° C pendant 5 minutes pour la déshydrogénation puis refroidi à la température de croissance de GaP. La couche GaP est déposée à partir d'une source solide en métal pur pour l'élément galium et des cellules P_4 pour l'élément phosphore. Pour les échantillons avec une pré-couche de Si avant la croissance de GaP, le substrat est introduit dans la chambre UHVCVD après le nettoyage. La couche de Si est déposée à 800 °C en utilisant le silane (SiH_4) (à une pression de 10^{-6} torr). Le substrat Si/Si est ensuite transférée sous UHV à la chambre de MBE pour la surcroissance de GaP.

Nous avons d'abord développé deux méthodes d'analyse de micro-macles par la diffraction des rayons X, en utilisant un diffractomètre de laboratoire en mode « basse résolution ».[6] Les rayons X sont générés à partir d'un tube scellé standard à cible de cuivre. Dans ce mode, le faisceau est partiellement monochromatisé autour du doublet Kalpha (lambda=0.15418nm) par la présence d'un miroir parabolique multicouche et d'un filtre de nickel. La taille du faisceau est limitée en hauteur et en largeur à environ 2×2 mm^2 par un système de fentes croisées pour produire un faisceau quasi-ponctuel. Le détecteur est utilisé en mode de détection ponctuel avec une large ouverture (d'une largeur de 8 mm et d'une hauteur d'environ 15 mm) pour pouvoir collecter la quasi-totalité du signal diffusé par les micro-macles.

Dans l'espace réel, les plans {111} de GaP nominal sont inclinés de 54,7 ° par rapport aux plans (001), et les plans de micro-macles sont inclinés de 15,9 °. La figure de pôle est réalisée en fixant les angles 2θ et ω à la position Bragg de GaP 111 (ce qui est très proche de la position Si 111). La figure 1 représente une figure de pôles typique obtenue pour un échantillon de couche mince GaP déposée sur un substrat de Si désorienté de 6°. Les taches de diffusion de GaP (Si) ont observées à χ autour de 54,7 ° et les quatre variants de micro-macles sont visualisées à χ autour de 16 °. Les variants A et C ainsi que les taches de GaP nominal sont décalés de ± 6° en χ du fait du miscut, tandis que les variants B et D sont légèrement distordus et déplacés en ϕ.

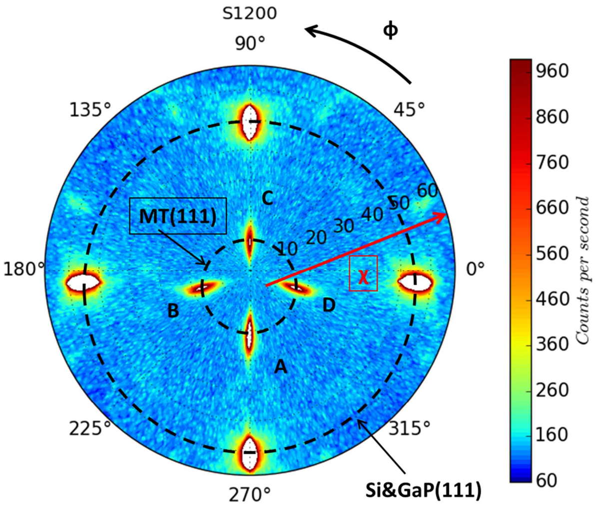

Figure 1 Représentation d'une figure de pôle typique pour un GaP/Si désorienté.

En supposant que les intensités intégrées des taches sont directement proportionnelles au volume de micro-macles qui se présente à l'intérieur de la couche de GaP, la figure de pôle donne un moyen très simple et illustratif pour visualiser la présence de micro-macles, connaître le niveau de sa densité et comparer rapidement différents échantillons. Cependant, pour évaluer quantitativement la fraction volumique de micro-macles, une méthode plus fiable basée sur des mesures « rocking-curve » est exploitée.

Le balayage de type « rocking-curve » est réalisé pour chaque variant en faisant varier l'angle ω autour de la position centrée, après avoir centré les angles χ, ϕ et 2θ. Ensuite, la valeur théorique de l'intensité diffractée est obtenue par calcul. Le rapport entre la valeur expérimental à la valeur théorique donne la faction volumique de micro-macles dans la couche. Le même type de mesure est réalisé autour de la tâche GaP 002, pour évaluer la fraction volumique de la phase nominale (non maclée). Dans le cas « idéal », la somme des deux fractions volumique doit être égale à 100%.

Grâce à ces deux méthodes, nous avons pu quantifier la fraction volumique de micromacle de manière assez précise et optimiser les conditions de croissance pour l'amélioration de caractéristique structurale de la couche GaP/Si. Une première série de six échantillons de 45 nm GaP élaborés sur Si désorienté de 6° par MBE à différentes températures de croissance montre une réduction importante de densité de micro-macles au-dessus de 500°C qui confirme ce qui a été reporté dans la litérature[7,8] Un scénario de formation des micro-macles est proposé via la formation de lacunes ainsi qu'une énergie d'activation mise en jeu pour éviter ce phénomène. Cependant, la croissance à haute température génère une surface très rugueuse qui ne peut être utilisée ensuite pour la réalisation de dispositifs. Une procédure de croissance dite « MEE » (Migration Enhanced Epitaxy qui consiste à déposer de manière alternée Ga et P) a été développée et optimisée par caractérisation DRX et AFM. Les échantillons « MEE » présentent après optimisation et pour une même épaisseur déposée, un volume maclé beaucoup plus faible et une surface beaucoup plus lisse que les meilleurs échantillons réalisés par MBE classique à même température de croissance. Enfin, la structure de la couche GaP/Si a été optimisée par une séquence de croissance de deux étapes: une première croissance de 40 monocouches de GaP à 350 °C (basse température) par la MEE suivie d'une deuxième croissance de 40 nm de GaP à 500 °C (haute température) par la MBE. La figure 2 a) représente la figure de pôle de cet échantillon (S1330), où l'intensité de micro-macles est très faible. La faction volumique de micro-macles est évalué à inférieur à 1% (la limite de résolution de ces méthodes par diffraction des rayons X à base résolution). La rugosité surfacique de cet échantillon est mesurée à 0.3 nm (la limite de sensibilité de cette technique d'AFM est de l'ordre de 0.15 nm) par l'image d'AFM comme présenté dans la figure 2 b).

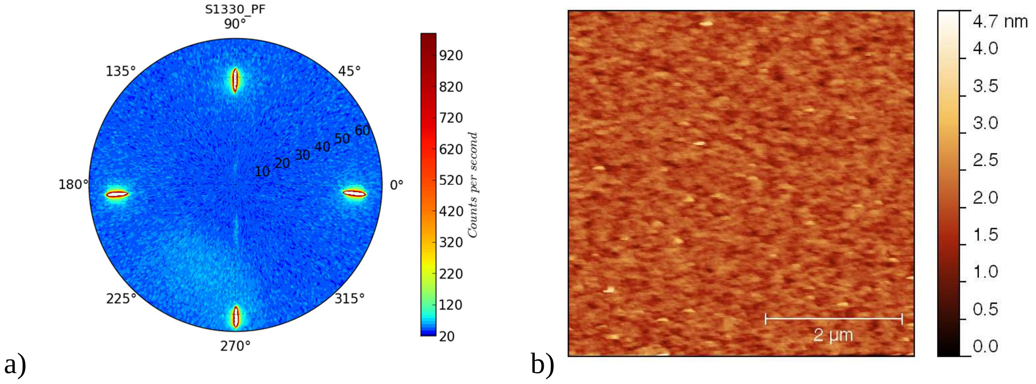

Figure 2 a) la figure de pôle et b) l'image AFM de l'échantillon S1330, après l'optimisation des paramètres de croissance vers l'élimination des micro-macles.

Dans la partie suivante (chapitre IV), je présente l'évaluation des domaines d'inversion par la diffraction des rayons X en laboratoire et sur synchrotron. La diffraction au laboratoire est réalisé en mode dit « haute-résolution » avec l'utilisation d'un monochromateur permettant d'obtenir une longueur d'onde de 0,154056 nm et de réduire la divergence du faisceau to about 0.008 degrés. Les expérimentations au synchrotron ont été réalisées sur la ligne de lumière BM02 de l'ESRF (European Synchrotron Radiation Facility) à Grenoble, France. Nous avons travaillé à 16 keV pour pouvoir atteindre des réfections plus lointaines dans l'espace réciproque et limiter la diffusion par l'air. Le faisceau ponctuel (0.3×0.3 mm^2) et très intense (de l'ordre de 10^{11} coups/seconde) ainsi qu'un détecteur 2D à pixels hybride (XPAD 3) a été utilisée pour la capture d'image.

La figure 3 représente les cartographies de l'espace réciproque centrées sur les positions de GaP 00L obtenue en laboratoire sur S1330. L'intégration suivant la direction S_z (comme indiqué par les rectangles rouges) nous a permis d'extraire les « scans » transverses, qui présentent deux composantes: une composante fine correspondant à la longueur de corrélation cristalline à longue distance (donnée par le substrat) et une composante large venant des petites longueurs de corrélations dues à la présence de défauts[9]

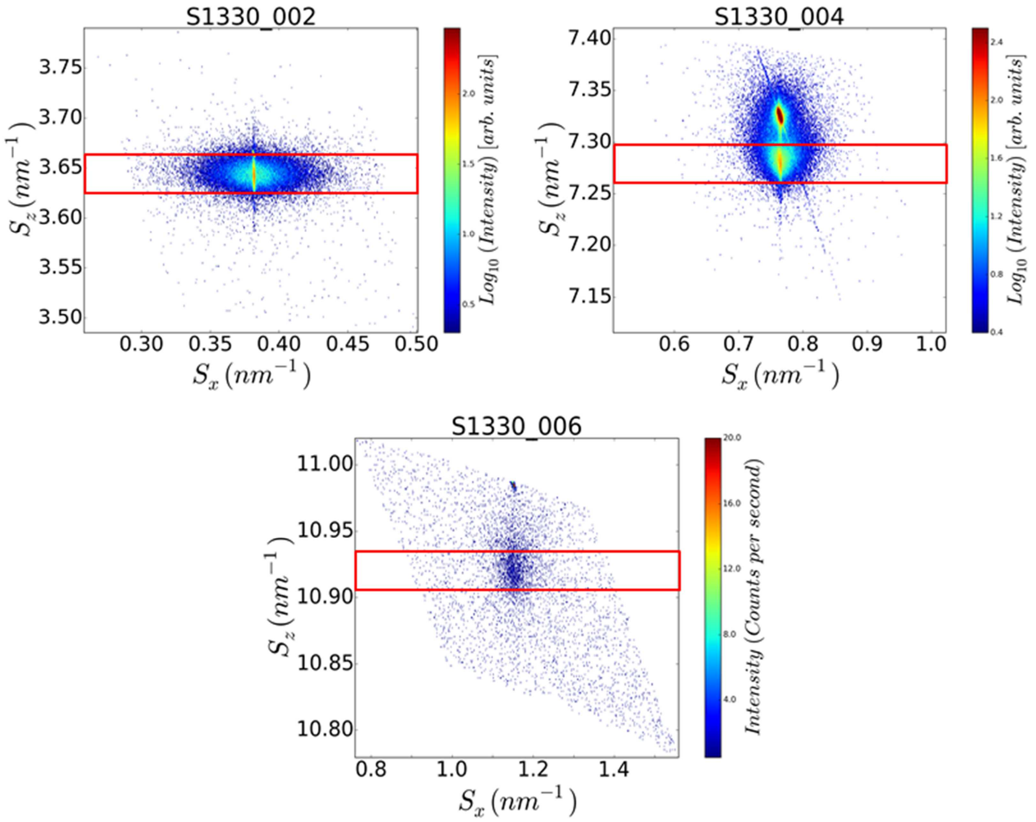

Figure 3 Les cartographies de l'espace réciproque de S1330 centré sur la position de GaP 002, 004 et 006, obtenue par la diffraction de rayons X en haute résolution sous conditions de laboratoire, pour l'évaluation des domaines d'inversion par la méthode « Williamson Hall like ».

Le facteur de qualité (QF) définie comme le ratio de l'aire entre la composante fine et la composante large, est un indicateur de qualité cristalline de l'échantillon. En plus, les micro-désorientations (micro-mosaïcité) des plans cristallins peut aussi impliquer un élargissement du pic large. Ainsi, nous avons développé une méthode dite "Williamson-Hall like", pour dissocier l'élargissement dû à la mosaïcité et celui dû à la longueur de corrélation des défauts. Cette méthode nous a permis d'évaluer la longueur de corrélation liée aux domaines d'inversion, qui correspond à la distance moyenne entre deux parois d'inversion (pour une polarité moyenne proche de 0). Pour cet échantillon, la longueur de corrélation est mesurée à 19.8 nm à partir de ces cartographies.

Grâce à cette méthode d'évaluation, et avec les images de TEM, une optimisation a été effectuée sur la quantité Ga au stade initial de croissance. La procédure de croissance de l'échantillon S1480 est basée sur celle de S1330, mais avec une couverture de Ga à 0,75 monocouche par cycle pour les 3 premiers cycles (au lieu de 0,9 pour S1330). L'amélioration des propriétés structurales est évidente, avec une densité de macles plus faible et une longueur de corrélation des APDs plus grande (27 nm). Finalement, une optimisation plus poussée avec l'annihilation des parois d'inversion a été observée sur l'échantillon S1477, qui a été réalisé en utilisant le même procédé de croissance que le S1480 pour la première couche de 10 nm, suivie par 4 couches de GaP de 50 nm d'épaisseurs épitaxiées à 4 températures croissantes (500 °C, 535 °C, 565 °C et 600 °C). Chaque couche est séparée par une couche de marqueur d'AlGaP de 2 nm d'épaisseur. La figure 4 montre l'architecture de la croissance de S1477.

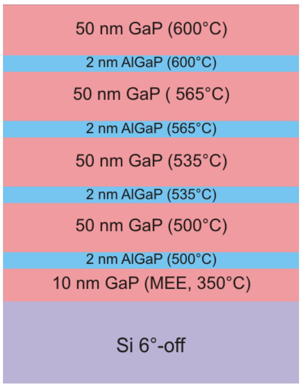

Figure 4 Illustration schématique de l'architecture de la croissance de S1477

Cet échantillon est considéré comme une « référence ». Aucun signal de micro-macle n'est présent sur la figure de pôles (la figure 5 a)), indiquant une densité très faible (inférieur à environ 0.3% de fraction volumique). La longueur de corrélation des domaines d'inversion mesurée par la méthode « Williamson Hall like » est d'environ 48,6 nm, beaucoup plus grand que les autres échantillons. De plus, une relaxation plastique partielle de l'échantillon a été observée en DRX et contribue aussi à l'élargissement des pics de Bragg. On ne peut pas donc se baser sur cette seule observation pour estimer la largeur moyenne des APD ou la distance moyenne entre APB. La figure 5 b) montre une image de STEM du S1477. Une forte densité de parois d'inversion est générée à l'interface de GaP on Si, mais la plupart des parois sont annihilés au sein de la première 10 nm. La densité moyenne des parois est environ 10 parois/µm à partir de la première couche d'AlGaP et 3 parois/µm au-dessus de la seconde.

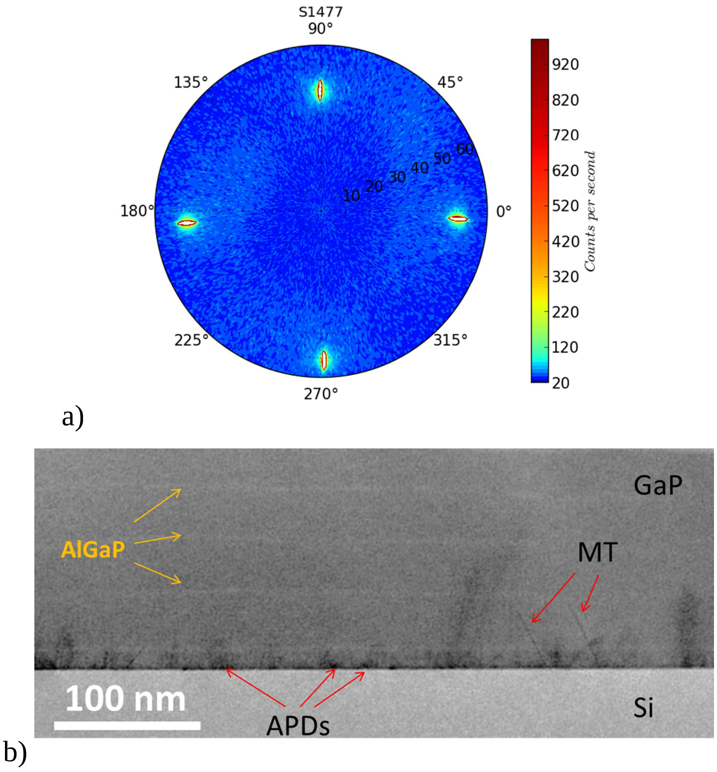

figure 5 La figure de pôle du S1477, sans aucun signal de micro-macle ; b) l'image STEM en champ blanc du S1477, montant une annihilation de grande densité des parois d'inversion à partir de la première couche de marqueur d'AlGaP.

Les domaines d'inversion sont générés à partir de l'interface GaP/Si et la formation des domaines d'inversion est favorisée par la présence des mono-marches atomiques sur la surface du substrat. Un scénario d'annihilation des domaines d'inversion et une étude a été sur l'amélioration de la qualité de l'interface ont été apportée à la fin du chapitre. Une interface très claire avec des doubles marches atomiques a été obtenue, après la croissance par l'épitaxie homogène d'une couche de Si sur le substrat nettoyé par un processus optimisé, avant la déposition de la couche de GaP, comme présenté sur la figuer 6. Cependant, les parois d'inversion sont encore générées malgré la présence de doubles marches atomiques, cela indique que le contrôle des autres paramètres de croissance est aussi important pour définitivement éliminer ces défauts.

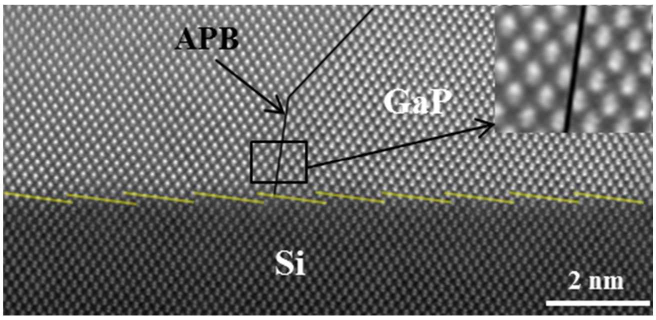

Figure 6 L’image STEM-HAADF de l’interface de GaP/Si, avec une couche de Si avant la croissance de GaP. [10]

En conclusion, les méthodes d’analyse structurale des défauts développées en utilisant la diffractions des rayons X, combinées avec d’autre techniques, nous ont permis d’optimiser les conditions de croissance pour éliminer les micro-macles et les domaines d’inversion et réaliser une plate-forme GaP/Si à l’état de l’art.

Références :

1. Nguyen Thanh, T. et al. Synchrotron X-ray diffraction analysis for quantitative defect evaluation in GaP/Si nanolayers. Thin Solid Films 541, 36 – 40 (2013).
2. Nguyen Thanh, T. et al. Quantitative study of microtwins in GaP/Si thin film and GaAsPN quantum wells grown on silicon substrates. J. Cryst. Growth 378, 25 – 28 (2013).
3. Guo, W. et al. Thermodynamic evolution of antiphase boundaries in GaP/Si epilayers evidenced by advanced X-ray scattering. Appl. Surf. Sci. 258, 2808 – 2815 (2012).
4. Meyerson, B. S. Low-temperature Si and Si:Ge epitaxy by ultrahigh-vacuum/chemical vapor deposition: Process fundamentals. IBM J. Res. Dev. 34, 806–815 (1990).
5. Quinci, T. et al. Defects limitation in epitaxial GaP on bistepped Si surface using UHVCVD–MBE growth cluster. J. Cryst. Growth 380, 157 – 162 (2013).
6. Ping Wang, Y. et al. Quantitative evaluation of microtwins and antiphase defects in GaP/Si nanolayers for a III–V photonics platform on silicon using a laboratory X-ray diffraction setup. J. Appl. Crystallogr. 48, 702–710 (2015).
7. Ernst, F. & Pirouz, P. Formation of planar defects in the epitaxial growth of GaP on Si substrate by metal organic chemical-vapor deposition. J. Appl. Phys. 64, 4526–4530 (1988).
8. Narayanan, V., Sukidi, N., Bachmann, K. J. & Mahajan, S. Origins of defects in self assembled GaP islands grown on Si(001) and Si(111). Thin Solid Films 357, 53 – 56 (1999).
9. Durand, O., Letoublon, A., Rogers, D. J. & Teherani, F. H. Interpretation of the two-components observed in high resolution X-ray diffraction ω scan peaks for mosaic ZnO thin films grown on c-sapphire substrates using pulsed laser deposition. 519, 6369 – 6373 (2011).
10. Ping Wang, Y. et al. Abrupt GaP/Si hetero-interface using bistepped Si buffer. Appl. Phys. Lett. 107, 191603 (2015).

Personal biography

PUBLICATIONS

Y. Ping Wang, J. Stodolna, M. Bahri, J. Kuyyalil, T. Nguyen Thanh, S. Almosni, R. Bernard, R. Tremblay, M. Silva, A. Letoublon, T. Rohel, K. Tavernier, L. Largeau, G. Patriarche, A. Le Corre, A. Ponchet, C. Magen, C. Cornet, O. Durand, Abrupt GaP/Si hetero-interface using bistepped Si buffer, *Applied Physics Letters*, 2015, 107 (19), pp.191603.

O. Durand, S. Almosni, **Y. Ping Wang**, C. Cornet, A. Létoublon, C. Robert, C. Levallois, L. Pedesseau, A. Rolland, J. Even, J. Jancu, N. Bertru, A. Le Corre, F. Mandorlo, M. Lemiti, P. Rale, L. Lombez, J. Guillemoles, S. Laribi, A. Ponchet, J. Stodolna, Monolithic Integration of Diluted-Nitride III–V-N Compounds on Silicon Substrates: Toward the III–V/Si Concentrated Photovoltaics, *Energy Harvesting and Systems*, 2014, 1 (3-4), pp.147-156.

T. Quinci, J. Kuyyalil, T. Nguyen Thanh, **Y. Ping Wang**, S. Almosni, A. Létoublon, T. Rohel, K. Tavernier, N. Chevalier, O. Dehaese, N. Boudet, J. Bérar, S. Loualiche, J. Even, N. Bertru, A. Le Corre, O. Durand, C. Cornet, Defects limitation in epitaxial GaP on bistepped Si surface using UHVCVD-MBE growth cluster, *Journal of Crystal Growth*, 2013, 380, pp.157-162.

Y. Ping Wang, A. Létoublon, T. Nguyen Thanh, M. Bahri, L. Largeau, G. Patriarche, C. Cornet, N. Bertru, A. Le Corre, O. Durand, Quantitative evaluation of microtwins and antiphase defects in GaP/Si nanolayers for a III–V photonics platform on siliconusing a laboratory Xray diffraction setup, *Journal of Applied Crystallography*, 2015, 48 (3), pp.702-710.

INVITED TALKS

O. Durand, S. Almosni, **Y. Ping Wang**, C. Cornet, A. Létoublon, C. Levallois, A. Rolland, J. Even, N. Bertru, A. Le Corre, P. Râle, L. Lombez, J.-F. Guillemoles, A. Ponchet. Monolithic integration of GaAsPN dilute-nitride compounds on silicon substrates: toward the III-V/Si tandem solar cell, *SPIE Photonics West conference* , San Francisco, USA, February 2015.

O. Durand, **Y. Ping Wang**, S. Almosni, M. Bahri, J. Stodolna, A. Létoublon, N. Bertru, A. Le Corre, A. Ponchet, G. Patriarche, L. Largeau, C. Magen, J. Gauthier, C. Robert, C. Levallois, J. Even, A. Rolland, Ch. Cornet, P. Râle, L. Lombez, J.-F. Guillemoles, Thorough structural and optical analyses of GaP-based heterostructures monolithically grown on silicon substrates for photonics on Si applications: toward the laser on silicon and high efficiency photovoltaics on silicon, *6th International Workshop on "Advanced optical and X-ray characterization techniques of multifunctional materials for information and communication technologies, health and renewable energy applications"*, Bucharest, Romania, Sep 2014.

C. Cornet, C. Robert, T. Nguyen Thanh, **Y. Ping Wang**, S. Almosni, M. Perrin, A. Létoublon, J. Even, P. Turban, A. Balocchi, X. Marie, N. Bertru, O. Durand, A. Le Corre, Intégration optique par croissance directe de nanostructures III-V sur silicium, *14èmes Journées Nano, Micro et Optoélectronique (JNMO),* Evian, France, May 2013.

COMMUNICATIONS WITH INTERNATIONAL AUDIENCE

Y. Ping Wang, A. Létoublon, T. Nguyen Thanh, M. Bahri, et al., Quantitative evaluation of microtwins and antiphase defects towards a GaP/Si platform for monolithic integrated photonics, *European Materials Research Society 2015 Spring Meeting (E-MRS 2015),* Lille, France, May 2015.

Y. Ping Wang, A. Létoublon, T. Nguyen Thanh, J. Stodolna, N. Bertru, A. Le Corre, A. Ponchet, C. Magen, N. Boudet, J. Micha, J. Even, C. Cornet, O. Durand, Quantitative evaluation of microtwins and antiphase defects in GaP/Si nanolayers for III-V photonics platform on silicon, *XTOP 2014: 12th Biennal Conference on Hith resolution X-Ray Diffraction and Imaging,* Villard de Lans, France, Sep 2014.

Y. Ping Wang, J. Stodolna, T. Nguyen Thanh, A. Létoublon, J. Kuyyalil, N. Bertru, A. Le Corre, A. Ponchet, C. Magen, C. Cornet, O. Durand, Abrupt heterointerface and low defect density in GaP/Si nanolayers, *Compound Semiconductor Week 2014*, Montpellier, France, May 2014.

Y. Ping Wang, J. Stodolna, T. Nguyen Thanh, A. Létoublon, J. Kuyyalil, N. Bertru, A. Le Corre, A. Ponchet, C. Magen, J. Even, C. Cornet, O. Durand, Low cristalline defect density in GaP/Si nanolayers, *European Materials Research Society 2014 Spring Meeting (E-MRS 2014),* Lille, France. 2014, May 2014

O. Durand, S. Almosni, P. Râle, J. Rodière, **Y. Ping Wang**, A. Létoublon, H. Folliot, A. Le Corre, C. Cornet, A. Ponchet, L. Lombez, J.-F. Guillemoles, Advanced concepts of III-V-based Solar Cells heterostructures: towards III-V/Si CPV on Si substrates and hot-carrier solar cells on InP substrates, *European Materials Research Society 2014 Spring Meeting (E-MRS 2014)*, Lille, France, May 2014.

O. Durand, S. Almosni, C. Robert, T. Nguyen Thanh, **Y. Ping Wang**, C. Cornet ,A. Létoublon, C. Levallois, L. Pedesseau, J. Even, J. Jancu, N. Bertru, A. Le Corre, A. Bondi, P. Râle, L. Lombez, J.-F. Guillemoles, E. Tea, S. Laribi, J. Stodolna, A. Ponchet, N. Boudet, Monolithic integration of diluted-nitride III-V-N compounds on silicon substrates : toward the III-V/Si Concentrated Photovoltaics, *International Symposium on Inorganic and Environmental Materials*, Rennes, France, Oct 2013.

O. Durand, T. Nguyen Thanh, **Y. Ping Wang**, A. Létoublon, C. Cornet, A. Le Corre, Advanced X-ray analyses on epitaxially-grown thin films for optoelectronic applications, *15th International Conference of Physical Chemistry - ROMPHYSCHEM-15*, Bucharest, Romania, Sep 2013.

C. Cornet, C. Robert, S. Almosni, T. Nguyen Thanh, T. Quinci, **Y. Ping Wang**, A. Létoublon, M. Perrin, J. Even, N. Bertru, A. Balocchi, P. Barate, X. Marie, O. Durand, A. Le Corre, GaAsPN compounds for Si photonics, *International Workshop "Silicon & Photonics"*, Rennes, France, Jun 2013.

S. Almosni, C. Cornet, T. Quinci, T. Nguyen Thanh, J. Kuyyalil, C. Paranthoën, P. Râle, L. Lombez, J.-F. Guillemoles, J. Stodolna, A. Ponchet, C. Robert, **Y. Ping Wang**, A. Létoublon, N. Boudet, C. Levallois, N. Bertru, O. Durand, A. Le Corre, UHVCVD-MBE growth cluster for III-N-V/Si solar cells, *Compound semiconductors week, ISCS,* 2013, Kobe, Japan, May 2013.

S. Almosni, C. Cornet, T. Quinci, T. Nguyen Thanh, J. Kuyyalil, P. Râle, L. Lombez, J.-F. Guillemoles, J. Stodolna, A. Ponchet, C. Robert, **Y. Ping Wang**, A. Létoublon, N. Boudet, C. Levallois, N. Bertru, O. Durand, A. Le Corre, UHVCVD-MBE growth for tandem solar cells, *Photovoltaic technical conference - thin film & advanced silicon solutions 2013*, Aix-en-Provence, France, May 2013.

J. Kuyyalil, T. Nguyen Thanh, T. Quinci, C. Cornet, A. Létoublon, **Y. Ping Wang**, J. Stodolna, F. Demangeot, A. Ponchet, N. Bertru, O. Durand, A. Le Corre, Growth of GaP on biatomic Si steps using a UHVCVD-MBE cluster, *euro-MBE conference*, Levi, Finland, Mar 2013.

COMMUNICATIONS WITH NATIONAL AUDIENCE

Y.Ping Wang, A. Létoublon, T. Nguyen Thanh, C. Cornet, N. Bertru, N. Blanc, N. Boudet, J. Stodolna, A. Ponchet, S. Charbonnier, P. Turban, J. Even, A. Le Corre and O. Durand, Influence des premiers stades de croissance cristalline GaP/Si sur la morphologie des domaines d'antiphase, *X1ème colloque rayons X et matière,* Grenoble, France, Dec 2015.

O. Durand, S. Almosni, **Y. Ping Wang**, C. Cornet, A. Létoublon, C. Levallois, L. Pedesseau, A. Rolland, J. Even, N. Bertru, A. Le Corre, A. Ponchet, P. Râle, L. Lombez, J.-F. Guillemoles, Epitaxie cohérente de composés GaP et GaAsPN à azote dilué sur substrats de Si pour l’élaboration de cellules PV tandem III-V/Si, *Matériaux 2014*, Montpellier, France, Nov 2014.

C. Cornet, P. Guillemé, J. Gauthier, C. Robert, J. Stodolna, **Y. Ping Wang**, A. Létoublon, A. Ponchet, M. Bahri, G. Patriarche, L. Largeau, Y. Dumeige, P. Feron, C. Levallois, Y. Léger, O. Durand, Intégration pseudomorphique dans la filière GaP/Si pour les applications lasers sur puce, *Journées thématiques du GDR Ondes GT2*, Orsay, France, Nov 2014.

Y. Ping Wang, T. Nguyen Thanh, A. Létoublon, C. Cornet, N. Bertru, N. Boudet, J. Stodolna, A. Ponchet, J. Even, A. Le Corre, O. Durand, Analyse quantitative par diffraction des rayons X des défauts plans dans GaP/SI pour la photonique sur Si, *Colloque annuel du GDR CNRS Pulse*, Toulouse, France, Oct 2014.

S. Almosni, C. Robert, C. Cornet, T. Nguyen Thanh, **Y. Ping Wang**, P. Râle, L. Lombez, J.-F. Guillemoles, A. Létoublon, C. Levallois, N. Bertru, A. Le Corre, O. Durand, Development of GaAsPN alloy for its integration in III-V/Si tandem solar cell, *Workshop on above 25% efficiency solar cells via low cost approaches,* Palaiseau, France, Jul 2014.(Poster)

S. Almosni, C. Robert, C. Cornet, T. Nguyen Thanh, **Y. Ping Wang**, P. Râle, L. Lombez, J.-F. Guillemoles, A. Létoublon, C. Levallois, N. Bertru, O. Durand, A. Le Corre, Optimisation des propriétés structurale de l'interface GaP/Si et des propriétés électroniques de cellules solaires

GaAsPN/GaP pour la fabrication de cellule tandem, *Journées nationales du Photovoltaïque JNPV 2013*, Dourdan, France, Dec 2013.

T. Quinci, R. Varache, **Y. Ping Wang**, C. Cornet, A. Létoublon, D. Munoz, M. Baudrit, O. Durand, A. Le Corre, New concept of photovoltaic heterostructure GaP/c-Si : AFORS-HET simulation and first pseudomorphic approach, *Journées nationales du Photovoltaïque JNPV 2013*, Dourdan, France, Dec 2013.

A. Létoublon, T. Nguyen Thanh, **Y. Ping Wang**, S. Almosni, C. Cornet, N. Bertru, N. Boudet, J. Stodolna, A. Ponchet, E. Tea, J. Even, S. Laribi, A. Le Corre, O. Durand, Analyse quantitative de la perfection cristalline de nanocouches épitaxiales GaP/Si, *Xème colloque rayons X et matière*, Nantes, France, Nov 2013.

Y. Ping Wang, T. Nguyen Thanh, A. Létoublon, C. Cornet, N. Bertru, N. Boudet, J. Stodolna, A. Ponchet, J. Even, A. Le Corre, O. Durand, Analyse quantitative des micromacles dans des nanocouches épitaxiales GaP/Si pour la photonique sur silicium, *Xème colloque rayons X et matière*, Nantes, France, Nov 2013.(Poster)

J. Stodolna, F. Demangeot, A. Ponchet, N. Bertru, O. Durand, C. Cornet, J. Kuyyalil, A. Le Corre, A. Létoublon, T. Nguyen Thanh, **Y. Ping Wang**, N. Boudet, Etude par TEM et DRX des défauts cristallins dans des couches épitaxiées par MBE de GaP sur Silicium (001), *Colloque annuel du GDR CNRS Pulse*, Aix-en-Provence, France, Jul 2013.

C. Cornet, O. Durand, A. Létoublon, C. Robert, T. Nguyen Thanh, S. Almosni, T. Quinci, **Y. Ping Wang**, J. Kuyyalil, L. Pedesseau, M. Perrin, C. Levallois, S. Richard, J. Burin, Y. Léger, H. Folliot, J. Even, J. Jancu, S. Loualiche, N. Bertru, A. Le Corre, Emetteurs/absorbeurs optiques sur silicium : intégration pseudomorphique de semi-conducteurs III-V, *Séminaires de l'institut de physique de Rennes*, Rennes, France, 2012.

INSA de RENNES
Service des Formations

AVIS DU JURY SUR LA REPRODUCTION DE LA THESE SOUTENUE

Titre de la thèse:
Structural analyses by advanced X-ray scattering on GaP layers epitaxially grown on silicon for integrated photonic applications

Nom Prénom de l'auteur : WANG YANPING

Membres du jury :
- Madame FONTAINE Chantal
- Monsieur PATRIARCHE Gilles
- Monsieur DURAND Olivier
- Monsieur LETOUBLON Antoine
- Monsieur THOMAS Olivier
- Monsieur DECOBERT Jean
- Monsieur RENARD Charles

Président du jury : PATRIARCHE

Date de la soutenance : 17 Juin 2016

Reproduction de la these soutenue

Thèse pouvant être reproduite en l'état
~~Thèse pouvant être reproduite après corrections suggérées~~

Fait à Rennes, le 17 Juin 2016

Signature du président de jury

G. Patriarche

Le Directeur,

M'hamed DRISSI

Résumé

Cette thèse porte sur le développement des méthodes d’analyse structurale de la couche mince de GaP epitaxiées sur le substrat de silicium par l’épitaxie par jets moléculaires (MBE), basées sur la diffraction des rayons X (DRX) et combinées à des techniques complémentaires telles que la microscopie électronique en transmission (TEM), la microscopie à force atomique (AFM) et la microscopie à effet tunnel (STM). Le travail est centré sur la caractérisation quantitative de la densité des défauts cristallins comme les micro-macles et les domaines d’inversion présents dans la couche ainsi que l’évaluation de la qualité de surface et l’interface. L’objectif ultime est d’obtenir une plate-forme GaP/Si parfaitement cristallisée sans défaut, via l’optimisation des paramètres de croissance.

Nous avons mis en place et utilisé deux méthodes de quantification des micro-macles par diffraction des rayons X (DRX) en condition de laboratoire : les figures de pôles pour la visualisation rapide et l'évaluation de la densité des micro-macles et les « rocking-curves » permettent une extraction précise de la faction volumique de macles. Les propriétés structurales de la plate-forme de GaP/Si ont été considérablement améliorées, après une procédure d'optimisation impliquant la température de croissance, une procédure de croissance alternée (MEE) et une séquence de croissance en deux étapes. Un échantillon quasiment sans micro-macles a été obtenu par le dépôt de 40 monocouches de GaP par MEE à 350 °C suivi d’une surcroissance de 40 nm de GaP par MBE continue, à 500 °C. La surface de l'échantillon est lisse avec une rugosité de 0.3 nm.

L'évaluation des domaines d’inversion par DRX a été effectuée sur les cartographies de l’espace réciproque centrées sur les réflexions GaP de type 00L, en laboratoire et sur une ligne synchrotron. Les balayages « transverses » extraits à partir des cartographies de l’espace réciproque sont analysés via une méthode dite "Williamson-Hall like", afin d'obtenir la "mosaïcité" qui est reliée à la micro-désorientation des petits domaines cristallins et la longueur de corrélation latérale correspondant à ces petits domaines. La distance moyenne entre parois de domaines d’inversion est ensuite estimée à partir de cette mesure. En utilisant cette méthode d'analyse et les techniques microscopiques, une optimisation plus poussée a été effectuée sur la dose de Ga au stade initial de croissance, l'utilisation de couches de marqueur AlGaP et l’homoépitaxie d’une couche de silicium avant le GaP. Enfin, nous avons obtenu un échantillon ne présentant pas de signal de micro-macle détectable en conditions standard de laboratoire, et une très faible densité de domaines d’inversion. Nous avons aussi observé une interface de GaP/Si présentant visiblement des bi-marches atomiques régulières, sur un échantillon avec une couche de silicium déposée avant la croissance du GaP.

Abstract

This thesis deals with the development of structural analyses methods of the GaP thin layers heterogeneously grown on the Si substrate by Molecular Beam Epixay (MBE), based on X-ray diffraction (XRD) analyses, combined with complementary techniques such as transmission electron microscopy (TEM), atomic force microscopy techniques (AFM) and scanning tunneling microscope (STM). The main work is centered on the quantitative characterization of crystalline defect such as micro-twins and anti-phase domains, and the evaluation of the surface and interface quality. The ultimate goal is to achieve a perfectly crystallized GaP/Si platform without any defect, through the optimization of the growth conditions.

We have applied two micro-twin quantification methods using a XRD lab setup. Pole figure method for fast visualization and evaluation of micro-twin density and rocking curves integration for a more precise absolute quantification of the micro-twin volume fraction. The GaP/Si platform structural properties have been significantly improved, after an optimization procedure involving growth temperature, MEE (Migration Enhanced Epitaxy) growth procedure and a two-step growth sequence. GaP layers quasi-free of MTs are obtained, with a r.m.s. roughness of only 0.3 nm.

The APD evaluation by XRD has been performed on reciprocal space maps (RSM) centered on the 00L GaP reciprocal space lattice points either in lab setup or on synchrotron. Analysis of the transverse scans extracted from such RSM through the “Willamson-Hall like” method permits obtaining the “mosaicity” that is related to the micro-orientation of the small crystalline domains in the GaP layer, and the lateral correlation length which is considered to be related to the mean distance between two APBs, provided that this distance is approximately homogenous and corresponding to the mean APD size, and the density of other defects are very weak so that their influence can be neglected. Using this analytical method and the microscopic techniques, further optimization has been carried out on Ga amount at the initial growth stage, the use of AlGaP marker layers and the homoepitaxie of Si buffer layer. Finally, sample with none MT signal and very low density of APD has been achieved. Moreover, an abrupt GaP/Si interface displaying regular and double atomic steppes is observed on sample with a Si buffer layer prior to the GaP growth.

N° d’ordre : **16ISAR 10 / D16 - 10**
Institut National des Sciences Appliquées de Rennes
20, Avenue des Buttes de Coësmes - CS 14315 - F-35043 Rennes Cedex
Tél : 02 23 23 82 00 – Fax : 02 23 23 83 96